STATUS AND PERSPECTIVES OF THE FRENCH CRG-IF INTERFACE BEAMLINE BM32

REPORT FOR THE BEAMLINE REVIEW PANEL OF MAY 25 and 26, 2010

APRIL 2010

G. Renaud, O. Ulrich, F. Rieutord, M. De Santis , J.-S. Micha, O. Robach, X. Biquard, H. Tolentino

Contents

Overview: role and impact of the beamline

The French CRG Interface (IF) Beam Line (BM 32) is dedicated to study the physics and chemistry of surfaces, interfaces, thin films and nanostructures and to mechanical properties at the micron scale. It was one of the first beamlines available to users, in 1994. It first held three experimental stations that were used alternatively, one equipped with a multipurpose goniometer (GMT), one dedicated to X-ray absorption spectroscopy (XAS) experiments, and one devoted to surface X-ray diffraction in ultra-high vacuum (UHV) called INS (In situ Nanostructures and Surfaces). In 2000, the XAS station moved to a new, dedicated beamline BM30B (CRG-FAME). In 2006, the beamline optics has been completely refurbished with two vertically focusing mirrors in addition to a two crystals sagitally focusing monochromator. In addition to the “standard” monochromatic mode, a white beam microfocus configuration has been added producing a sub-micrometric beam in the GMT hutch. In parallel, a micro-diffraction setup has been developed.

The goniometer of the GMT station has three main characteristics, which makes it unique for some investigations. The goniometer is very accessible and versatile, so that many different scattering experiments can be performed, bulk or surface sensitive, with the sample surface either horizontal or vertical. Different sample environments such as a cryostat and a small vacuum chamber are available. Several others have already been used: magnet and cold finger, Langmuir trough, dilution fridge etc... A specific feature is the possibility to deviate the beam downwards for studying liquid surfaces, and the availability of well adapted cells for these measurements. Although such equipment is now available on other stations, in particular on the Troïka Beamline, the advantages of the IF beamline are the very clean X-ray beam with low background, and the possibility to work at much higher energies (up to 30 keV), which is necessary for studies of interfaces between dense materials (liquid/liquid or liquid/solid). Because of its very versatile design, the GMT instrument is a user-oriented facility that fits the needs of a wide community. The research on the GMT diffractometer includes studies of « soft » and « hard » condensed matter.

A new instrument for Laue microdiffraction was added in 2006, to be used in alternance with the GMT goniometer in the same hutch. A white (5-30 keV) microbeam (0.5x0.5 µm2) arrives on the surface of the polycrystalline sample, under an angle of 40°. Each illuminated crystallite produces a Laue pattern, that is collected onto a 2D detector located near $2\theta=90°$, and then analyzed for local orientation and deviatoric strain. Sample scanning then provides 2D maps of these parameters. The technique is well fitted to the characteristics of an ESRF BM beamline source and it is actually one of the very few white sub-micrometer beam setup in Europe. The technique is not limited to thin films and allows the study of the near surface region of bulk polycrystalline materials. The setup brought several new users from materials science on the beamline. The possibility to obtain the 2D strain distribution, with a submicron space resolution (at least in 2D), in fine-grained polycrystals, attracted specialists of mechanics trying to elucidate the micro-scale physical origins of materials mechanical properties. Another strong area of activity is the in-situ study of poly- or single-crystalline objects of micrometer dimensions, while they are submitted to mechanical stress, electrical testing, or thermal annealing. This is to investigate how the small size of the objects and their confinement inside foreign materials affect their functional properties. The setup is now in a state of routine use, and new equipment is being installed to upgrade it (faster detectors, better focussing optics, wire-scanning system to add spatial resolution along the beam). A suite of data treatment software has been developed ("LaueTools") now available as open-source on SourceForge. Actions were also taken for communication toward the user community. A first workshop was organized in 2006, to present the new setup to potential users, and discuss the applications of the technique to various fields. This was important as the technique is relatively recent (1999) and the setup was the first of this kind in Europe. A second workshop was organized in 2009, this time about data analysis. The new software was presented and specialists of plasticity were invited to discuss the issues of interpreting spot shapes in terms of dislocation densities.

The INS station is based on a UHV diffractometer devoted to Surface X-Ray Diffraction (SXRD), Grazing Incidence X-ray Scattering at wide (GIXS) and Small (GISAXS) angles, X-ray reflectivity and Surface X-ray Absorption Spectroscopy (S-XAS) on surfaces and interfaces, and during thin film and nanoparticle growth. The main advantages with respect to other existing stations are the possibility to perform *in situ* deposition with up to seven sources in the X-ray chamber, as well as a very good RHEED system and Auger analysis under grazing incidence, which can be operated simultaneously with x-ray measurements during deposition or annealing.

With these three instruments, the beamline has a large impact in the French research community in nanoscience. In addition, both instruments serve each year as a support for practicals and tutorials dedicated to student during their Master at the local Grenoble University, and for HERCULES (the Higher European Research Course for Users of Large Experimental Facilities) students. The local team is then involved in the corresponding teaching. Note also that a course on surface X-ray diffraction was organized within the CNRS training framework, on the INS instrument.

Organization, committees and funding

The IF CRG beamline is part of a program established in 1991 by the two French research agencies: CNRS (Centre National de la Recherche Scientifique) and CEA (Commissariat à l'Energie Atomique). Two CRG beamlines - IF and D2AM – have been operational since 1994. A third beamline has a split radiation fan with one branch –FIP- operational since 1999, and the second branch equipped with the FAME beamline. A CRG/French Council with representatives of the two agencies is responsible for the financial, personnel and scientific policy of the entire program. The program is executed locally by a "structure d'exploitation" regrouping the three Department Heads of "Institut Néel (CNRS)", "Service de Physique des Matériaux et Microstructure" (INAC CEA-Grenoble) and "Institut de Biologie Structurale" (CEA-CNSR lab.), all established at Grenoble. The Grenoble University is also participating through a Contract for supplying student training every academic year. The personnel working on the beam lines are employed by these local laboratories. As a consequence the concept of in-house research is slightly different from the one at ESRF. The beamline and instrument scientists perform research programs of their own laboratory. The facilities of the three labs (infrastructure, workshop, design, secretary...) are available.

About 20% of the total available beam time is reserved for upgrade, maintenance and in-house research. One third of the remaining beam time is reserved for to the European community, and is allocated by European committees through the usual application for beam time at the ESRF. The 2/3 of remaining beamtime is open to the entire French community. The beam time is allocated through applications and reviewing by an *ad hoc* Committee in a way similar to the ESRF. Two Committees for the two main scientific areas, Physics and Chemistry of Materials (PCM), and Biology were established. The PCM Committee, the only one concerned with IF beam line, has 9 French members from various scientific areas (surfaces and interfaces, nanophysics, hard condensed matter, soft condensed matter, earth science) and selects the applications once a year in November. At this time the results from the ESRF international Committee allocations are known. The available user beam time is calculated applying the rules observed at ESRF: time is reserved for in-house research, buffer between experiments and maintenance

The two scheduling periods of the ESRF have been followed during the first operation year. However the amount of user time on each instrument was too small on a six months basis and since that time a one-year period has been preferred. In-house research is reviewed as well by the Committee.

Funding of the equipment has been initially provided by CNRS, CEA, Ministry of Research, Grenoble University, Région Rhônes Alpes and Conseil Régional. The construction cost of the beamline was 17.8 MF (Millions of French Francs), excluding salaries of the staff members, which are paid by CNRS or CEA. CNRS and CEA share the operational cost on a 60-40 basis. In 2009, for instance, the IF beam line has a budget of 200 kEuros (recurrent cost including reimbursement to ESRF, and investment). It decomposes into 52 k€ of recurrent cost refunded to ESRF, 24 k€, 15 k€ and 30 k€ of recurrent cost on the beamline, the GMT and the INS stations respectively, and 20 k€ and 30 k€ for new developments on the beamline and the experimental stations respectively. Large investments, *e.g.* in new detectors had to be asked separately.

The refurbishment project has been conducted together with the build-up of the white-beam microdiffraction setup. The overall cost of the project (900k€) was shared between the CEA (200k€) and the CNRS (200k€), with a strong contribution from the applied research division of the CEA through the basic technological research (RTB) program (500k€). These contributions allowed a renewal of the beamline optical elements and the design of a micro-diffraction setup prototype.

Then the development of the microdiffraction instrument was further carried out (new detectors, new optics, postdoc) thanks to a grant (580k€) from the French national research agency (ANR). (MiDiFabl project within the PNano program (2007-2010)).

The gas distribution system to perform UHV-CVD with silane, germane and ethene in the INS instrument has been funded by the Grenoble Nanoscience Fondation (250 k€) and by the CEA-INAC (100 k€). The Nanoscience Fondation also granted a bursary for an 18 month postdoc starting in April 2010.

Beamline staff and organization

The staff on the beamline is provided by CNRS and CEA. It comes from the Institut Néel for the CNRS side and from the Institut Nanoscience et Cryogénie for the CEA. No scientific staff is working for the IF beamline at 100% of their time as they are all involved in research projects at from their own laboratory. A postdoctoral fellow (T. Schülli) has been hired for 18 month before being hired on a permanent position. He then left to the ESRF to take the responsibility of the ID01 beamline. He has recently been replaced by another postdoc. In addition, 18 month contract for a postdoc has been allocated by the Nanoscience Fundation to start the UHV-CVD setup on the INS instrument.

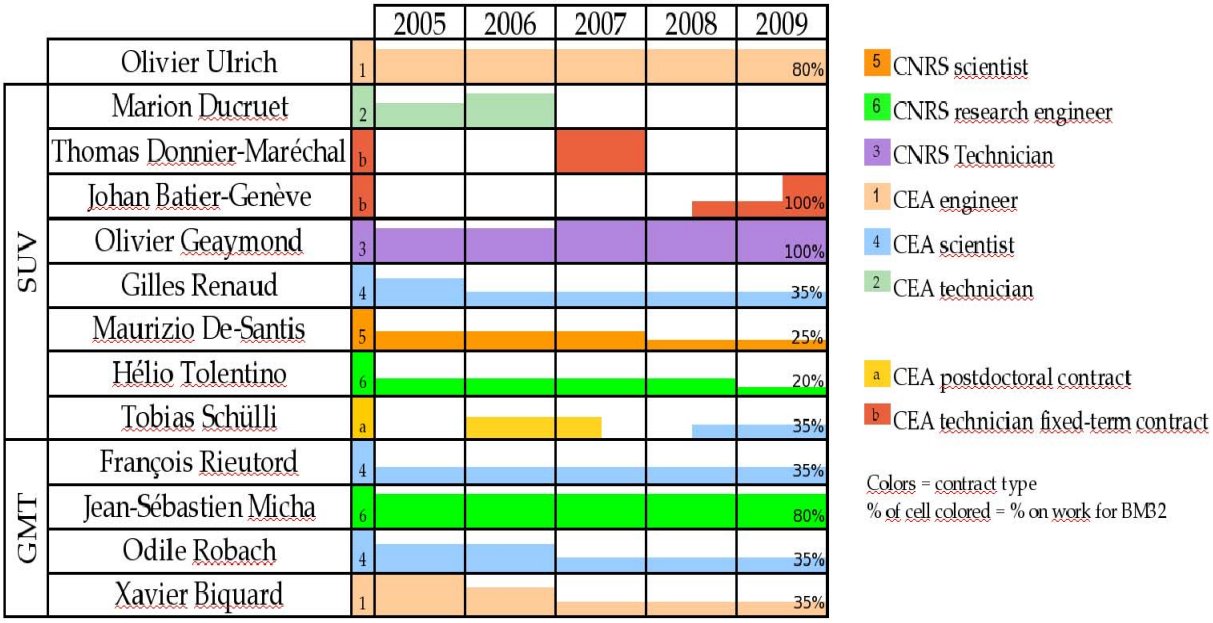

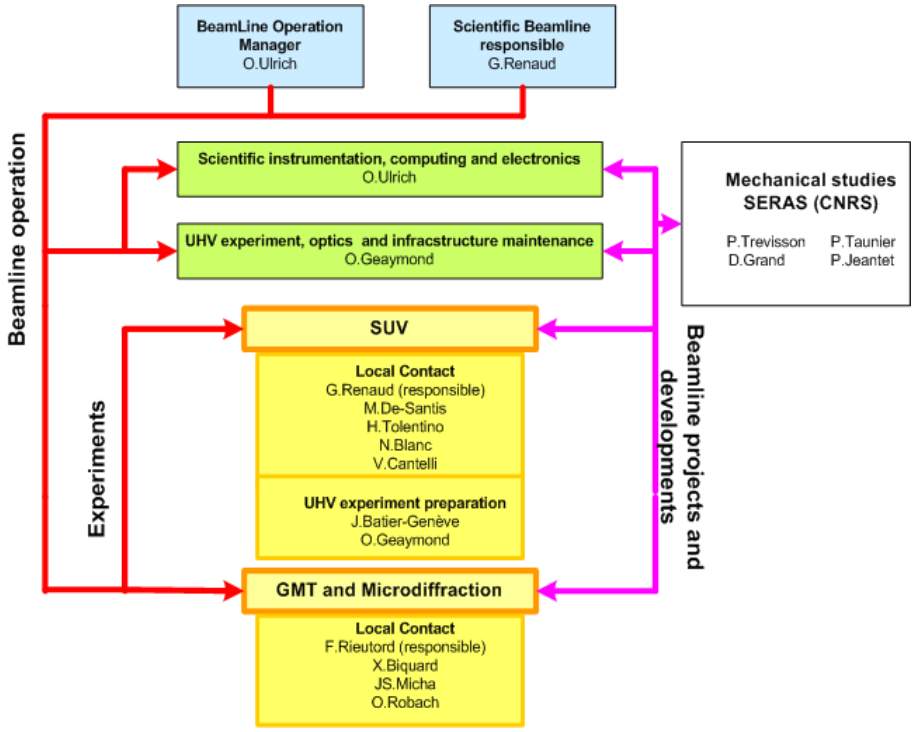

The functions and scientific interest of the beamline staff are briefly described below:

Xavier Biquard CEA-Grenoble, Researcher-Engineer/Local contact on Microdiffraction
- Development of the microdiffraction setup, local contact
- Scientific interest : materials for super-high density data storage or PCRAM

Maurizio De Santis, CNRS INéel/ Researcher/Local contact on INS
- Structure and magnetic properties of ultrathin films and surface alloys.
- Template mediated growth of nanostructures.
- Self-organisation of molecules at the surface.

J.-S. Micha UMR CNRS-CEA-Grenoble, Engineer/Local contact on GMT and Microdiffraction
- Main duty:local contact on GMT and Microdiffraction
- x-ray optics elements optimization: simulation and design of monochromator crystals and optics mirrors
- involvement in development of the microdiffraction setup
- Software developer of LaueTools dedicated to microdiffraction data treatment and analysis.

G. Renaud, CEA-Grenoble, Researcher/Local contact on INS
- *In situ* GIXS/GIXD/GISAXS/GI-MAD/A-GISAXS studies on oxide/metal/semiconductor surfaces growth (non-organized and organized) on metal/oxide/semiconductor surfaces.
- Development of GISAXS.
- Supercooling in metal/semiconductor eutectics. Soon: semiconductor growth (especially nanowires) by UHV-CVD.

F. Rieutord CEA-Grenoble, Researcher
- fundamental studies of technological processes: direct bonding and wafer splitting. Adhesion and wetting at the nanoscale.
- implantation and fracture. Crack development and propagation.
- strain and stress measurements in technological samples (sSOI, interconnects, …)

O. Robach CEA-Grenoble, Researcher/Local contact on Micro-diff and GMT and INS
- development of methods / tools for measuring local strains and microstructure on the micron scale, based on the Laue microdiffraction technique in-depth characterization of the performances of the technique (evaluation of incertitudes) use of the technique to study the characteristic length scale for the excess dislocation density appearing near a grain boundary during plastic deformation
- *in situ* studies of catalysts using surface x-ray diffraction and GISAXS, with an emphasis on the role of gas-solid reactions in activating / deactivating / dispersing the catalyst.

Helio Tolentino, CNRS INéel/ Researcher/Local contact on INS
Surface physics approach to the study of magnetic materials: growth process and structure of ultra-thin films and nanoparticles; interface structure when combining different materials and its impact on the magnetic properties (magnetic anisotropy, spin orientation, exchange coupling and exchange bias).

O.Ulrich CEA-Grenoble INAC, Engineer
- Beamline operation manager, in charge of technical aspects on BM32, including computing control command for the three instruments and detectors.
- Involvement in developing microdiffraction experiment to improve features and performances of data collection.

Beamline Optics

O.Ulrich X.Biquard : **CEA-Grenoble, Institut Nanosciences et Cryogénie, SP2M/NRS**

The beamline optics has been completely refurbished upgraded in 2006 and has two operation modes. A normal mode that delivers a monochromatic (6.5-50keV) 150x250 (VxH) µm2 beam on GMT or INS stations or a pink micro-focus mode (2-30keV) that delivers a 0.5x0.5 µm2 beam on GMT. In this mode, the optics could also deliver a monochromatic beam (10-30keV). The design of the beamline has been performed by BM32 team.

The configuration for the optics is of a classical layout where entrance slits are followed by a 3 optical element group (first mirror, monochromator and second mirror) in charge of X-ray white beam processing, and finally exit slits. To achieve a good harmonic rejection, both mirrors work at variable incidence, therefore adjusting cut-off energy to working energy. Good energy resolution is reached thanks to the first mirror that collimates the beam for the monochromator. The second mirror vertically focuses the beam either on the sample (normal mode) or on a micrometric 2-directions slit system located at the exit of the optical hutch (pink micro-focus mode). For the INS diffractometer, it is necessary to have the beam always at the same height. Therefore, the monochromator crystal gap is adapted to compensate for the height offset given by the variable angle of the mirrors.

The first mirror M1 is made of a monocrystalline 1.3m long Si bar, coated with 500Å Ir exhibiting a 3Å roughness, a slope error of 1.5µrad rms on the full length, and only 1 µrad rms on the 300mm central area. This mirror can be bent up to 5 km radius in order to vertically collimate the divergent beam from our bending magnet onto the first crystal of the monochromator. The cooling system consists in water circulation in copper blades, soaking in liquid InGaAs filling to channels on both side of the Si bar, thus avoiding vibration transmission to the mirror. The maximal allowed thermal power for this mirror is 580W, corresponding to a ring current of 500mA, thus anticipating future ESRF upgrades.

The second mirror M2 is identical to the first, apart from the absence of cooling system and an extended curvature radius ranging up to 2.5km to allow vertical focusing on the micrometric slit.

The monochromator is a double crystal Si(111) type with the whole optical block under vacuum. The rotation stage is equipped with a high resolution encoder to achieve 0.35µrad resolution. It is mounted on a translation stage to follow the beam reflected from the first mirror when the incidence angle is adjusted to select the cut-off energy. The rotation stage carries the first and second crystal assembly.

The first crystal assembly is a 10mm thick Si crystal glued to a copper plate cooled by water circulation. The roll of this plate may be dynamically adjusted by a piezo actuator to achieve automatic stabilisation of horizontal position of the beam against thermal drifts arising from ring current decrease.

The second crystal assembly is the standard Si ribs crystal mounted on an ESRF-CNRS bender type and makes the sagittal focusing. The bender assembly is carried by three rotations (weaklinks): one for the tilt, the second for the yaw to align the bender axis to the beam direction and the third for crystals parallelism. This latter movement will be finely adjusted by a piezo actuator to achieve automatic intensity maximization, thus compensating drifts. Moreover, the bender is carried by two crossed translations: one adjusting the gap between the crystals and the second adjusting the shift between crystals along beam propagation axis.

In pink microbeam mode, the mirrors M1 and M2 are working under a fixed 3mrad incidence angle (cut-off energy > 30keV), the monochromator's crystals are spaced enough to let the beam outgoing from the M1 mirror pass-through the monochromator directly onto mirror M2 and the pink beam is vertically focused onto the micrometric slit. As the main scientific goals are to measure 2D-maps of grain orientation and deformation in thin polycrystalline materials with a lateral resolution of 0.5 µm, we have to take up 2 major challenges: achieve a pink microbeam of size 0.5x0.5µm^2 and have it stabilized to better than 0.2µm.

To make the pink microbeam we are using a classical Kirkpatrick-Baez (KB hereafter) microfocusing device constituted of 2 elliptically bent perpendicular mirrors since it is an achromatic device. The KB mirrors have Pt coating and work under fixed incidence angle of 2.9mrad (cut-off energy > 30keV), the first KB mirror being 300mm long and the second 170mm. The KB works under real object / image condition by demagnifiying the micrometric slit. The demagnification factor is simply the ratio between object distance and image distance. Therefore, the KB is brought as far as possible from the micrometric slit and as close as possible to the sample, leading to demagnification ratio in the vertical plane of 145 and 45 in the horizontal plane. Moreover, we have to limit as much as possible beam spot enlargements coming either from mirror polishing slope errors or from mirror imperfect bending. As a consequence, the slope error of the beamline mirrors M1 and M2 on their central 300mm are below 1µrad, the KB mirror slope errors are lower than 0.2µrad on full length and the shape of the seconf KB mirror is far from rectangular.

For controlling and tuning the optics, specific software have been written, either at low level to support special device controllers, or at high level to have a user friendly and easily adjustable beamline.

Selected publication(s) -	
Grant(s) : CEA-INAC / CEA-LETI / CNRS	Collaboration(s): not relevant here
Patent(s) :	Contact : ulrich@cea.fr

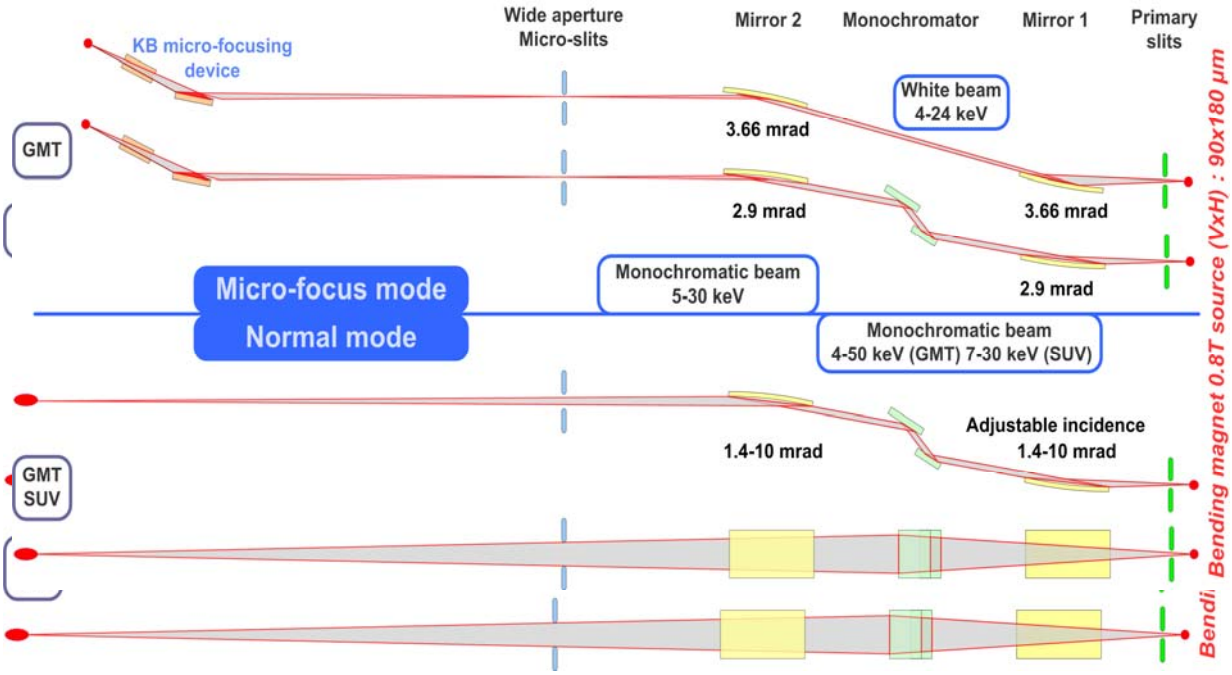

fig 1 : BM32 optics with its 2 operation modes

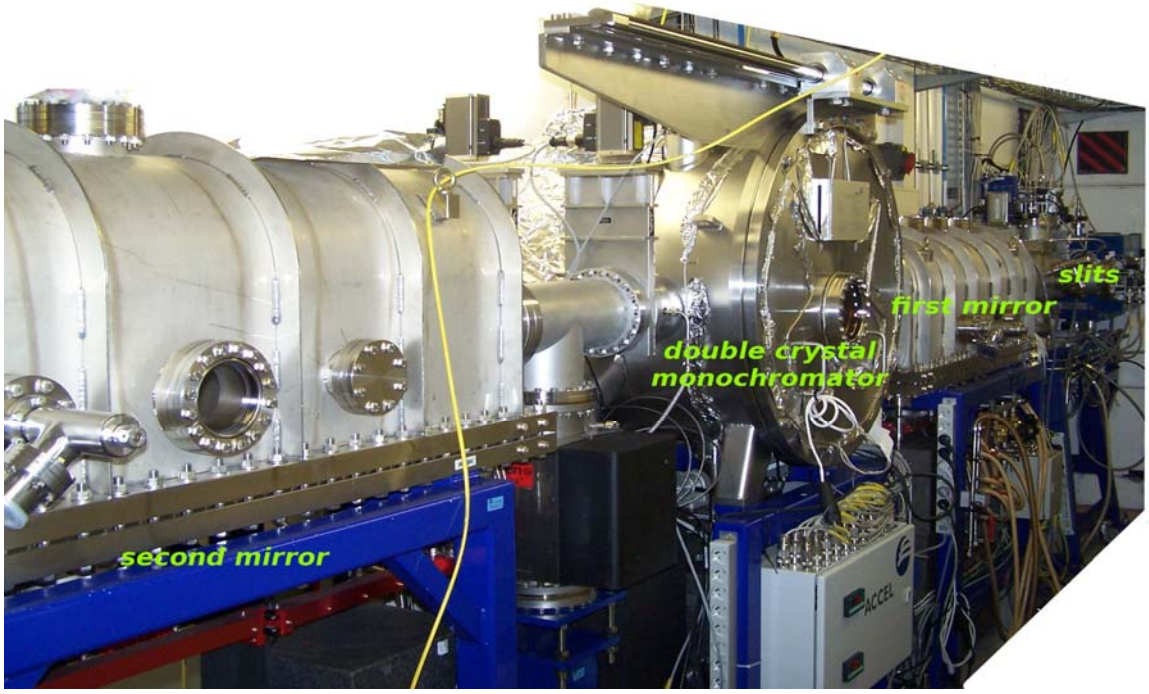

fig 2 : Optics hutch of BM32

Flux enhancement by thermal bump reduction on first monochromator crystal and use of germanium-bonded-on-silicon hybrid crystals.

J.-S. Micha and F. Rieutord

Two ways have been followed to increase the incoming flux on the sample. Efforts have been focused on the monochromator crystals of a Double Crystal Monochromator (DCM) in terms of their surface slope errors and their chemical nature. On the one hand, slope errors originated from thermal load on first crystal have been minimized in the whole illuminated area by optimising the crystal shape by means of finite elements calculations. This design allowed us to reach high transmission without resorting to expensive liquid nitrogen cooling. On the other hand major advantage of Si-based monochromator relies on mature Si crystal manufacturing rather than the corresponding energy resolution. Ge bonded on Si wafer monochromator crystal is being developed in order to multiply the photons flux by three with an acceptable energy resolution for many x-ray diffraction techniques purposes.

The complete refurbishment of the beamline optics hutch has been the opportunity to look for optical elements to get the most of the photons delivered by the ESRF bending magnet source. A reduction of the optical performance with respect to the theoretical incoming flux was observed. According to the quality of the mirrors (roughness and slope errors) major limitations were found to occur at the monochromator level.

First step was to improve photons global transmission of the Si(111) DCM by reducing the thermal bump on the surface of the first crystal. Thermal bump tends to detune some areas of the first crystal with respect to the second crystal. Global DCM flux transmission was modelled as a function of the surface 2D slope errors and was optimized by changing the geometry of the first crystal. A careful design of the first crystal geometry and of the associated heat flux paths allowed us to minimize this effect without resorting to liquid nitrogen cooling, which has high building and running costs and is technically difficult to implement. At each step of the optimisation procedure, slope errors were calculated by finite elements methods (COMSOL). Thermal load due to x-ray photons absorption was applied on the illuminated area. Different

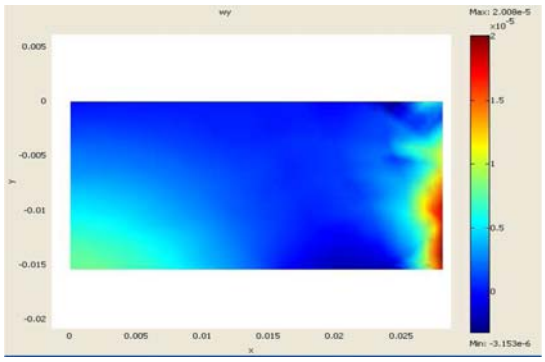

Fig.1: Slope errors calculated on the ¼ first crystal area at 18keV with a ring current of 350mA. (total surface heat power=215W on full area of 56.3X30.4mm²). Most of Slope errors (colorbar in radian) are less than 5 µrad leading to flux transmission of 84% (100% for perfectly flat crystals).

working energies and spatial heat load distributions (slit opening) were considered to find an optimized solution covering the beamline's needs. To anticipate future ESRF upgrades namely the programmed 300mA ring current, we have designed a new first crystal that holds its performance up to 500mA. Simulations have been compared to flux measurements on BM32 at 200mA where heat load is maximum using both traditional (monoblock shape cooled on one face) and optimized crystals. In excellent agreement with simulations, flux has been increased at all energies (8,18 and 27 keV) with the same energy resolution. Flux is doubled at 18keV. This indirect water cooling solution is currently operational on BM32 and BM2 and can be employed at the exit of any 3rd generation bending magnet synchrotron source.

The second development that is carried out stems from the fact that many beamlines (including BM32) use silicon 111 monochromator not because this Bragg line is specially suited but simply because it is the broadest line of silicon crystals. In many experiments, the energy resolution given by such crystals exceeds the need of scattering experiment, resolution being limited by the angular resolution. Hence it would be desirable to increase the bandwidth of the monichromator . Using Germanium crystals instead of silicon gives a factor of 3 increase in flux. Unfortunately, Germanium crystal are very expensive and their mechanical and thermal properties are worse than those of silicon. Our experience in direct bonding has led us to propose to use Ge bonded on silicon hybrid crystal. A thin film of monocrystalline Ge will reflect the X-rays (if its thickness is larger than the extinction length 0.2µm for Ge) while a silicon base will keep the excellent properties of the silicon material. Such material have been processed and tested against line width. Full processing for first and second crystal manufacturing and in-beamline tests remain to be done.

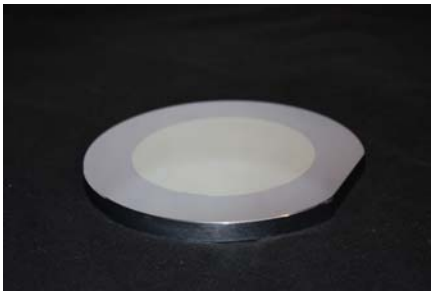

Fig.2 Ge 111 single crystal film bonded on a silicon substrate that can be shaped, machined, cut according to specifications for first or second crystal (rib manufacturing etc..)

Contacts : micha@esrf.fr and francois.rieutord@cea.fr

THE LAUE MICRODIFFRACTION SETUP

X. Biquard, J.-S. Micha, F. Rieutord, O. Robach and O. Ulrich: **CEA-Grenoble, Institut Nanosciences et Cryogénie, SP2M/NRS, 17 rue des Martyrs, 38054 Grenoble Cedex 9**

The applications to micro and nano objects call for intense narrow X-ray beams available at latest generation synchrotron only. The strong demand for structural characterization of objects with ever decreasing sizes has driven the development of new methods to go beyond the average internal structure down to the local structure determination. Probing the local strain, shape (size, orientation) and composition of micro and nano materials are the main objectives of our Laue micro-diffraction setup, this setup being the first in Europe.

To reach its objectives, the Laue microdiffraction setup uses 2 curvature-adjustable KB mirrors to achieve a sub-micron 0.5x0.75 µm2 white beam. This white beam has X-ray energy ranging from 4 keV to continuously adjustable upper energy from 12 to 25 keV. White beam is so intense that collection of a sufficiently intense Laue diagram on any thick grain (>5µm) requires less than 0.5s exposure time (Fig 1).

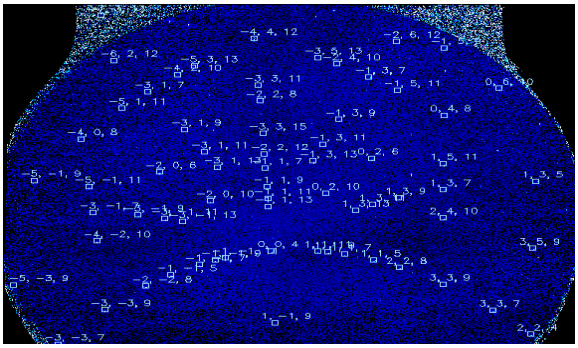

Fig 1: 0.15s recorded Laue diagram of a reference Si(001) wafer. More than 50 Laue diffraction peaks are visible and were indexed.

This sub-micrometer white beam is raster scanned on the sample to perform Laue scattering with sub-micrometer resolution. Laue scattering image are recorded by state-of-the-art large aperture CCD detector. Once indexed, a single Laue scattering diagram fully determines the grain orientation as well as the deviatoric part of the strain tensor (5 out of 6 components). If needed, a micrometric monochromatic beam may be energy-scanned to determine the hydrostatic strain, leading to a fully determined strain tensor. This allows for a grain-by-grain orientation (Fig 2) as well as strain determination with a 2 10^{-4} precision.

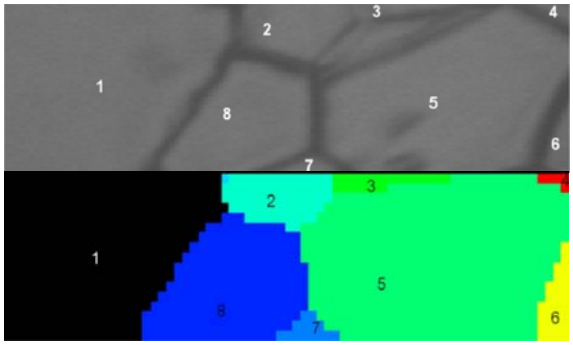

Fig 2: Comparison between our microscope image and grain size and orientation as determine by the white beam raster scan on a UO2 sample. A perfect correlation is clearly visible.

Chronologically, this setup was built along with the beamline refurbishment that started just after precedent BLRP. Given the high technicality and fine tuning necessary to achieve sub-micron white beam, the Laue microdiffraction setup became really operational to external user mid-2007. At that time, it was installed on top of GMT's multi-axis goniometer but we decide to move the setup onto a dedicated support still in used now (Fig 3). Once on this dedicated support, it appeared that vibrations were degrading the overall beam size. A very time-consuming struggle was engaged to find, diagnose and suppress or at least dampen vibration sources: cryogenically assisted pumping on adjacent ID01 beamline was suspended with elastomer sandwiches and the roof primary vacuum pump was anti-vibrated. Finally, we raised the self-resonance frequencies of the setup using reinforcement bars to avoid a very intense 14 Hz vibration frequency due to ESRF's experimental HVAC. This allowed us to achieve an overall 0.5x0.75 µm2 white beam where vibrations account for an estimated 0.25 µm enlarging in each direction.

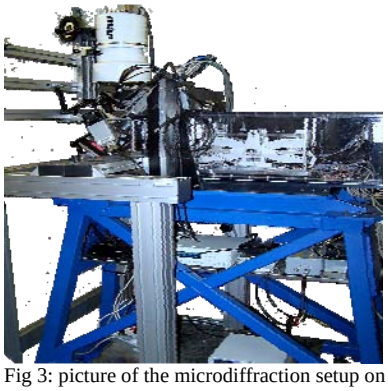

Fig 3: picture of the microdiffraction setup on its dedicated support in blue (cross reinforcement bars are clearly visible). KB mirrors are inside a transparent N2-filled chamber. On the top left, the MAR CCD camera is visible and at 40° our microscope.

The microdiffraction set-up has been fully functional for more than 3 years now and represents approximately 25% of distributed beamtime. Despite drastic spatial constraint, we were able to integrate the necessary specific sample environment for various thematics, namely an oven with temperature ranging from 20 to 400°C for Cu interconnects reliability studies, a precision tensile machine for slip plane studies and a high-precision rotation head for tomography studies

Selected publication(s): not relevant here	
Grant(s): ANR MiDiFaBl	Collaboration(s): not relevant here
Patent(s): not relevant here	Contact: xavier.biquard@cea.fr

The In situ Nanostructures and Surfaces (INS) endstation

G. Renaud, M. De Santis, O. Geaymond, J. Batier-Genève, H. Tolentino, T.U. Schülli **CEA-Grenoble, Institut Nanosciences et Cryogénie, SP2M/NRS and CNRS-Institut Néel MCMF**

The INS station is devoted to studies of surfaces, interfaces and thin films in Ultra High Vacuum, by means of four techniques using hard X-rays: Grazing Incidence X-ray Scattering (GIXS, which here is generic for SXRD, GID, GIXRD etc…), Grazing Incidence Small Angle X-Ray Scattering (GISAXS), Surface Extended X-ray Absorption Spectroscopy (SEXAFS, ReflEXAFS) and X-ray Reflectivity.

The INS instrument consists of a large and well-equipped UHV chamber mounted on a 4-circle diffractometer of z-axis type for X-ray studies, coupled to other UHV chambers located in the X-ray hutch The diffractometer supports the UHV chamber, with allowance for a rotation of the whole chamber defining the incidence angle (α) of the X-ray beam with respect to the vertical sample surface. A goniometric head allows alignment (two perpendicular tilts (χ_1 and χ_2), two translations (X, Z)) of the sample inside vacuum. The rotary motion of the sample is obtained through the rotation of the whole goniometric head thanks to a differentially pumped rotary feedthrough (ω). Two sample surface orientations (parallel and perpendicular) with respect to the X-ray beam polarization are possible. Two circles of the diffractometer are devoted to the two detector rotations defining the Bragg angle projections parallel and perpendicular to the surface (δ and β respectively). The x-ray UHV chamber has large Be windows giving access to large perpendicular momentum transfers (up to 45° input and exit angles). It is equipped with several sources (up to six simultaneously) for in situ epitaxial deposition and with standard UHV preparation and analysis tools (high temperature furnace, Reflection High Energy Electron Diffraction (RHEED), Auger Electron Spectroscopy (AES), Residual Gas Analysis (RGA), Ion Sputtering (IS), quartz micro-balance for calibration of deposition). Simultaneous real-time analysis with x-ray diffraction and RHEED and Auger spectroscopy can be performed during (co)deposition and/or annealing of ultra-thin films.

* The shared beam time with the other station makes it possible to investigate systems that require significant preparation before performing an X-ray experiment (typically the UHV chamber can be available a week before an experiment).
* RHEED, GISAXS, GIXS, XR (and even SEXAFS) experiments on the same sample.
* Co-deposition: deposition of up to 6 materials.
* Better signal to noise performances for samples with large mosaic spreads (~0.1°) because of the large horizontal beam divergence.
* High signal to noise ratio, allowing for example the study of molecules, which would be destroyed by stronger X-ray sources.
* Fast sample introduction system.
* High temperature furnace (up to 2000°C). The temperature of the furnace can be controlled by a computer interface.
* Sample cooling down to -100°C, optional
* The beam energy can be changed easily and continuously. Anomalous scattering is very reliable.

As proposed by the beamline review panel in 2005, in order to obtain a better resolution in GISAXS and GIXD as well as to meet increased safety requirements concerning the working conditions on the instrument INS, a refurbishment of the concerned experimental hutch has been done. The increase of the possible sample-detector distance will permit higher resolution in GISAXS and diffraction. The mounting of bulky 1D and 2D detectors on the diffractometer arm will be possible.

Note that the increase of the possible sample-detector distance will permit higher resolution in GISAXS and diffraction. The mounting of bulky 1D and 2D detectors on the diffractometer arm will be possible.

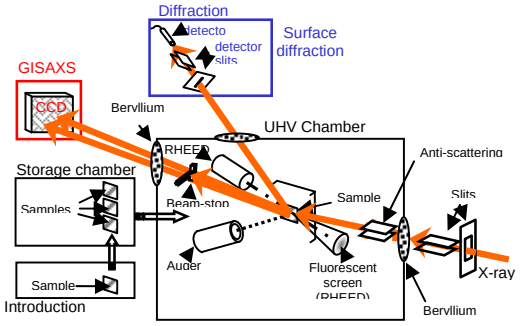

Fig. 1 Sketch of the INS setup

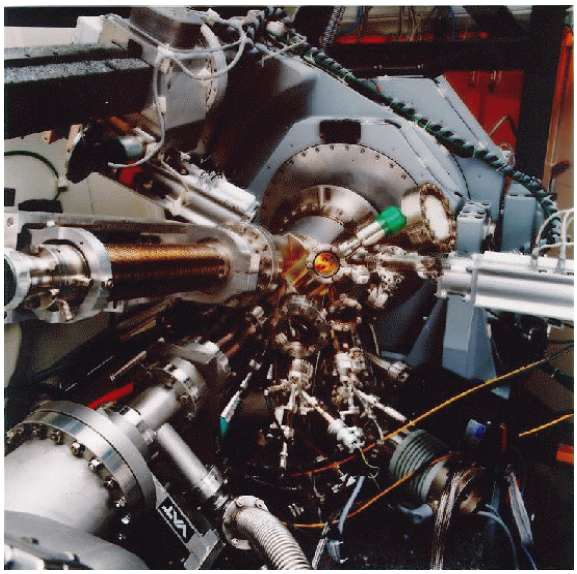

Fig. 2: Photograph of the X-ray station of the INS set-up. The beam comes in through a small Be window (the right hand side) and exits through a large Be exit window.

Multitechnique goniometer (GMT)

F.Rieutord, J.S. Micha **CEA-Grenoble, Institut Nanosciences et Cryogénie, SP2M/NRS and SPrAM/LASSO**

The GMT is a general purpose 2+2 axis surface diffractometer, well suited to most grazing incidence scattering techniques (GIXS,XRR, GISAXS) . It is normally dedicated to samples elaborated ex-situ but it can also accommodate a wide range of sample environments due to the large open space available around the goniometer centre.

.

The multitechnic goniometer (GMT) is a standard 2+2 goniometer devoted to surface scattering studies. It is normally used for surface studies of samples elaborated ex-situ.

As opposed to the UHV setup, the experiments taking place on GMT do not normally request lengthy surface preparations. Being located upstream with respect to the UHV station, it can share the beam and use the beam while the INS setup is preparing its samples. Yet, due to the large volume accessible around its center, the instrument can accommodate a large variety of sample environments, ranging from small enclosures with Kapton windows to a large UHV system with two chambers devoted to in-situ studies of catalytic processes (see figures). The goniometer can also handle vibration filtering tables for liquid surface studies, Helium cryostats, magnets, and a variety of furnaces...

The first microdiffraction experiments were actually run using the goniometer as a support for both focussing and sample movement elements, while the 2D detector was mounted on the detector arm.

The instrument has been used in the last years mainly for the study of buried interfaces e.g. liquid/solid or solid/solid interfaces. We make use of the 20-30keV energy range of our bending magnet to access the interface, crossing one of the phase over its whole length.

The instrument has received little evolutions during the last 4 years. Among them, let us mention

-the build-up of a new system for in-vacuum GISAXS studies. The system includes a front entrance mica window, a sample chamber that can be oriented under vacuum due to the presence of two flexible bellows and a segmented vacuum tube terminated by a mylar window in front of the 2D detector. The beam stop is located and moved under vacuum. All the system was designed to minimize the small angle scattering by the windows and the air environment, hence get a clean signal down to small qs.

- the automatic filter system is now better integrated to the slit systems and being closer to the sample, it accepts a larger solid angle (for use with 1D detector, possibly 2D)
- a Vantec 1D detector can now be installed easily on the goniometer, with the automatic filter system.
- new scintillator crystals (LaCl3) with shorter fluorescence time yet good fluorescence yield were tested. Higher count rates are achievable with these new scintillators that should replace the NaI scintillators when made compatible with the automatic attenuator system.

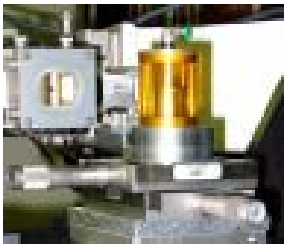

Fig.1 A variety of sample environment: from small Kapton windowed sample enclosure...

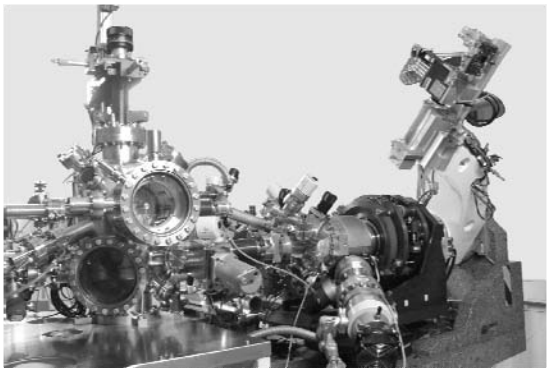

Fig.2 ... to large UHV system for in-situ catalysis studies.

Detectors on BM32

O.Ulrich: **CEA-Grenoble, Institut Nanosciences et Cryogénie, SP2M/NRS**

On BM32 we have a large choice of detectors to cover a wide range of techniques. None of these detectors have been developed by our team. We are using commercially available detectors. For some of them integration and development have been made to include them into our standard control system, which is the ESRF standard. These developments consist in electronics and software, in order to best match the experimental requirements of our 3 instruments.

For the optics, beam monitoring and data normalisation we are using standard silicon diodes with high accuracy electronics that transforms the analogue value into pulses integrated by the counting cards. We are also working on integrating new electronics from Synchrotron Elettra which is a modern device controlled via Ethernet with a high bandwidth up to 1000 samples per second. We aim to use these modules for feedback, and also for beam normalisation on experiments.

On the experiment side we have detectors, from the basic zero dimension detector, to two dimensional CCD detectors.

-0D detector for diffraction :
The standard photomultiplier with NaI scintillator is still used both on the GMT and the INS diffractometer behind slits that defines the analysis direction. Coupled to these detectors we also have automatic filter systems used to avoid detector saturation and to extend the dynamic range of the detection chain.

For experiments that require high energy resolution we have a Rontec Si drift detector. This detector has a typical energy resolution of 250 eV at counting rates up to 400 kcps/s with a 5mm2 detection area. It is mainly used on the microdiffraction experimental setup to monitor the fluorescence signal from the sample, either to build fluorescence maps or simply to locate the sample.

- 1D detector :
A VANTEC-1 sealed gaseous detector which is a parallel plate avalanche counter is mainly used on the INS diffractometer but can be be moved on GMT if needed. It has a 50mm long detection area, a 50µm spatial resolution and high counting rate, up to 10^6 cts/s with a detection efficiency of 45% at 17keV. It is a very good choice for diffraction experiment at energies below 20 keV. Integration of this detector in the existing acquisition framework has been done by the BM32 team. Coupled to this system we also developed a system to automatically control attenuation filters in order to avoid detector saturation.

-2D detectors :
We have four CCD detectors with various input size, pixels number and size, sensitivity, readout speed. Detector choice is done by users and its local contact in order to best match the experiments requirements. During last year we bought 3 CCD detector, firstly to duplicate the main detectors for microdiffraction (QuadRo), secondly to have a faster detector (VHR) and thirdly to replace an old detector (SCX 90-TE). Below we list the main features of each device.

All CCD detectors are fully supported by the standard acquisition system. Some use ESRF software developments, others have required special developments by BM32 team because they are not supported at ESRF or very specific features or control modes are required. On the INS difffractometer the 0D, 1D and 2D detector, can be used at the same time, giving access to many X-ray measurement techniques.

In a very near future we will have a pixel detector that we ordered from ESRF. We aim to use it for diffraction measurements on both diffractometers.

	Input size mm2	Pixel	Pixel size µm2	Readout time no binning s	Readout time binning 2x2 s	Dynamic bits	Dynamic range dB	Specific feature/comments
SCX 90-TE	65x65	1242x1153	52	14.3	-	16	93	Old camera replaced by ImageStar
MAR 165	Φ 165	2048x2048	80	2.5	-	16	77	
QuadRo 4096	Φ 165	4096x4096	40	8.8	2.2	16	78	Off line data correction
VHR	Φ 81	2672x2672	30	1.2/2.4	0.3/0.6	12/16	70	Electronic shutter, Antiblooming x1000, pipeline readout mode, possibility to extend dynamic up to 20 bits
ImageStar	67x67	3056x3056	22	2.5	0.6	16	82	Antiblooming x100

Tab 1 : CCD detectors used on BM32

Selected publication(s) -	
Grant(s) : ANR-MiDiFabl / CEA / CNRS	Collaboration(s): not relevant here
Patent(s) :	Contact : ulrich@esrf.fr

Scientific Research and Highlights

The next following pages present the scientific research on BM32 that is conducted by beamline scientists and external users. Major results from experiments from their collaboration are also shown. The one-page summaries are sorted by instruments (INS, Microdiffraction and GMT).

INS:

- Real-time structural and morphological investigations of size and *In situ* Nanostructures and Surfaces composition effects during CoPt nanoparticle growth

- Structural and order/disorder transitions of annealed supported CoPt nanoalloys

- Nanostructuring surfaces: Deconstruction of the Pt(110)-(1x2) surface by C_{60}

- *In situ* synchrotron radiation studies of the structure and strain of GeMn nanoparticles during their growth

- Organic heterolayers: a dynamic GIXRD study

- Solid state dewetting of Si on SiO_2 by *in situ* GISAXS and GIXD

- Growth and thermal stability of Pd and AuPd nanoparticules grown on a $Al_2O_3/Ni_3Al(111)$ thin film by *in situ* GISAXS

- Growth and structure of Co clusters on alumina on $Ni_3Al(111)$

- *In situ* Grazing-Incidence X-Ray Diffraction Studies of polar MgO film on Au(111)

- Twin and their boundaries during homoepitaxy on Ir(111)

- Structure and magnetism of an ultra-thin [NiO/CoO]/PtCo bilayer with perpendicular exchange bias

- On the growth of chemically ordered MnPt alloy on Pt(001) single-crystal

- Structure and magnetic properties of Mn/Pt(110)-(1×2): A joint x-ray diffraction and theoretical study

- Review article on GISAXS

- *In situ* synchrotron radiation studies of the structure, composition and morphology of nanoparticles during their growth

- Substrate enhanced supercooling in AuSi eutectic droplets

- *In situ* composition and strain of Ge islands on Si(001) during growth by grazing-incidence multiwavelength anomalous diffraction

- *In situ* x-ray investigation of Ge islands on pit patterned Si substrates

- Organized growth of Ge quantum dots on a nano-patterned Si(001) surface obtained by direct wafer bounding followed by chemical etching: An in situ X-ray study

- In-depth atomic structure and composition of the 2×*N* reconstruction of the 1 to 3 monolayer Ge wetting layer on Si(001) by surface x-ray diffraction

- *In situ* synchrotron radiation investigation of catalytic growth of confined silicon nanowires using grazing incidence methods

Microdiffraction

- Crystallographic orientation relationships between UO_2 and U_3O_7

- Laue Microdiffraction for *in-situ* electromigration tracking

- Determination of grain stress in Solid Oxide Fuel Cell by white beam Laue Microdiffraction

- Strain and stress measurements in the vicinity of grains boundaries: study of plastic deformation in multi-crystals using Laue microdiffraction

- In-situ µLaue diffraction on mechanically loaded Cu single crystals

- Development of Laue microdiffraction : estimating the accuracy of the technique : part 1 : relative accuracies between the various strain / orientation components

- Development of Laue microdiffraction : estimating the accuracy of the technique : part 2 : detecting known strain increments

- Development of Laue microdiffraction : a method to obtain the last strain component (lattice expansion), in the white beam mode, using an energy-resolved detector to measure the energy of diffraction peaks

GMT

- *In situ* nanocatalysis: size and catalytic activity of supported gold nanoparticles

- Towards a direct determination of the local atomic displacement field from high resolution x-ray diffraction measurements

- Light ion Implantation in silicon

- Strain in nanowires: assemblies for device integration

- Supported bilayers: Combined specular and diffuse X-ray scattering

- Silicon oxide bonding

Real-time structural and morphological investigations of size and composition effects during CoPt nanoparticle growth

P. Andreazza[1], J. Penuelas[1], C. Andreazza-Vignolle[1], M. De Santis[3], H.C.N. Tolentino[3] and C. Mottet[2], [1] Centre de Recherche sur la Matière Divisée, UMR 6619, CNRS & Université d'Orléans, 1bis rue de la Férollerie, 45071 Orléans Cedex 2, France ; [2] Institut Néel, CNRS & UJF, 25 avenue des Martyrs - BP 166, 38042 Grenoble cedex 9, France ; [3] CINaM, CNRS, Campus de Luminy, 13288 Marseille cedex 9, France

Supported Co-based nanoparticles (NPs) like CoPt exhibit interesting magnetic properties governed by the internal atomic arrangement depending on the combination of size reduction and alloying effects. Besides the size effect, the growth temperature and the composition offer additional degrees of freedom to tune the structure and the magnetic properties. The structure and morphology of 1 to 4 nm size CoPt NPs of equiatomic and Pt-rich composition have been investigated in situ and in real-time under different growth temperatures. The small-angle x-ray scattering measurements have revealed the particle morphology and motion on the surface, while wide-angle scattering results, supported by Monte Carlo simulations, have allowed structure identification. If icosahedra are systematically detected at the first growth stages at RT and at 500°C, the coarsening effect during the growth leads to an icosahedral to truncated octahedral crystalline transition only at 500°C. Meanwhile, the size-dependent evolution of the structure is shifted during the Co_{50} Pt_{50} growth, compared to $Co_{25}Pt_{75}$ NPs.

For most of transition metals, the atomic structure is close-packing based with almost spherical morphology i.e. truncated octahedra (TOh) with face-centered cubic (fcc) or hexagonal compact (hcp) structure. However, ultrasmall particles with icosahedral (Ih) or decahedral (Dh) structures have been commonly observed since the pioneer works of Ino on gold. These non-crystalline structures are composed of distorted tetrahedra connected by twinning planes. At this nanometer size, the internal atomic arrangement could be control by a critical balance between surface and volume contributions to the total energy. Unfortunately, kinetic effect and interface effect with strongly interacting support or matrix have been identified as factors inducing a change of the particle structure and morphology. For this reason, the understanding of fundamental mechanisms passes through the use of UHV conditions, weakly interacting substrates, like a-carbon and low deposition rates.

We used surface sensitive x-ray scattering methods as Grazing Incidence Small-Angle X-ray Scattering (GISAXS) and Grazing Incidence X-ray Diffraction (GIXD) to follow in situ and in real-time the nucleation and growth processes of CoPt NPs. fcc) structures in the 1-4nm size range. The experiment analysis was supported by wide angle scattering calculations using cluster models. Monte Carlo simulations of relaxed CoPt cluster structures (TOh, Dh and Ih) have been performed using a semi-empirical tight-binding potential, to interpret diffraction patterns.

Our results at 500°C show that icosahedral structure dominates at early stage (small particle sizes) of the growth process and fcc structure appears at larger sizes. The GISAXS results concerning the evolution of the shape and cluster density suggest a coalescence process during the early growth stage. Such events can provide sufficient internal morphological disruption to allow the NPs transformation to the minimum energy morphology, i.e. the TOh shapes at larger sizes. The growth mechanism at RT is completely different: the NPs density is higher and the dynamical coalescence is inhibited. After the nucleation stage, the growth at RT corresponds to an atom by atom impingement and the initial Ih structure is preserved without transition towards TOh structures. We show also here that during the growth, not only the size but also the composition of the bimetallic NPs can influence the structural transition. Indeed, at 500°C, by varying the composition from the equi-concentration to a Pt-rich phase ($Co_{25}Pt_{75}$), the Ih-to-TOh NP transition occurs at lower size, resulting of a higher strains effect.

Fig.1: Evolution of the GIXD patterns as a function of deposition time. The inset displays the first scans up to 1.8ML CoPt.

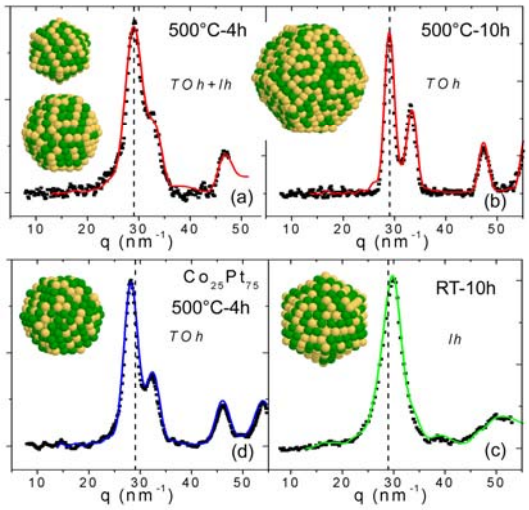

Fig.2: Selected experimental (square) and simulated (line) diffraction patterns of nanoparticlesassembliesduring the growth: at 500°C (a) D=2nm and (b) D=3.2nm; (c) the growth at RT D=2.5nm (d)growth of $Co_{25}Pt_{75}$ at 500°C D=2nm.

Selected publication(s) 1. J. Penuelas, P. Andreazza, C. Andreazza-Vignolle, H.C.N. Tolentino, M. De Santis, C. Mottet, Phys. Rev. Lett. 100, 115502 (2008) and Eur. Phys. J. ST 168, 19 (2009).

Patent(s) :

Contact : pascal.andreazza@univ-orleans.fr

Structural and order/disorder transitions of annealed supported CoPt Nanoalloys

P. Andreazza[1], C. Mottet[2], C. Andreazza-Vignolle[1], J. Penuelas[1], H.C.N. Tolentino[3], M. De Santis[3] and N. Bouet[1] Centre de Recherche sur la Matière Divisée, UMR 6619, CNRS & Université d'Orléans, 1bis rue de la Férollerie, 45071 Orléans Cedex 2, France ; [2] Institut Néel, 25 avenue des Martyrs - BP 166, 38042 Grenoble cedex 9, France ; [3] CINaM, CNRS, Campus de Luminy, 13288 Marseille cedex 9, France

A promising way in the magnetic recording field is to design alloy nanoparticles (NPs) consisting of a combination of a 3d metal with a high spin moment (Fe,Co) and 4d or 5d metals (such as Pd, Rh or Pt) which induces a large orbital magnetic moment (via the strong spin-orbit coupling). As a consequence the magnetic anisotropy is enhanced and the cluster magnetization stabilized against thermal fluctuation. According to the bulk phase diagram, at the equiatomic composition, a tetragonal (fct) $L1_0$ ordered phase can be obtained at low temperature, below the order/disorder temperature, while the face centered cubic (fcc) A1 chemically disordered phase is thermodynamically stable above. Theoretical studies predicted that the critical temperature should decrease with the particles size. We have proposed an in situ x-ray scattering investigation during CoPt nanoparticle annealing in order to get the best description of the size effect on the order/disorder transition.

Contrary to what has been showed by theoretical studies, experimental observations of the transition is difficult because as-synthesized CoPt particles exhibit a chemically disordered structure, i.e. a metastable state according to the theoretical phase diagram, and can be interpreted by a kinetic trapping during their atom-by-atom growth. Therefore a post-synthesis annealing is necessary to provide the needed atom mobility to transform the disordered phase to the ordered equilibrium $L1_0$ one, keeping the temperature below the order/disorder transition temperature of the clusters size. We have provided a quantitative description of the structural and chemical order-disorder phase transitions of 1.5 to 4nm bimetallic CoPt nanoparticles induced by increasing annealing temperatures (300-900K). The combined morphological and structural analysis at nanometer scale is given by an in situ x-ray scattering method at wide and small angles together with the support of Monte Carlo simulations within a semi-empirical tight-binding potential providing a realistic description of the CoPt nanoparticles structure, i.e. crystalline or non-crystalline states, long range order parameter (LRO). If a coalescence process of as-grown icosahedral particles (2nm) induced by annealing is detected at low temperature (<600K), higher temperatures (>700K) are necessary to the formation of decahedral structure by atomic rearrangement, followed by a transition to the fcc morphology. Contrary to what has been suggested in the literature, the investigation of the order/disorder transition at fixed size reveals a bistable state of nanoparticles at 900K with a bimodal distribution of the NPs population corresponding to a coexistence of almost fully chemically ordered and fully disordered particles, as expected by theoretical calculations. It is important to notice that the model structures obtained by the Monte Carlo simulations do not give an homogeneous partially ordered structure (LRO=0.44) which would be in contradiction with the bistability of the order and disordered state. It is rather a transition state with the coexistence of an ordered part and the nucleation of a disordered part inside the same particle.A still remaining question is the competition between the out-of-equilibrium growth conditions and the equilibrium state. It would be worth to check, starting with the ordered distribution of particles, if the NPs becomes disordered by increasing the annealing temperature or ordered by cooling down. Such investigation is still in progress.

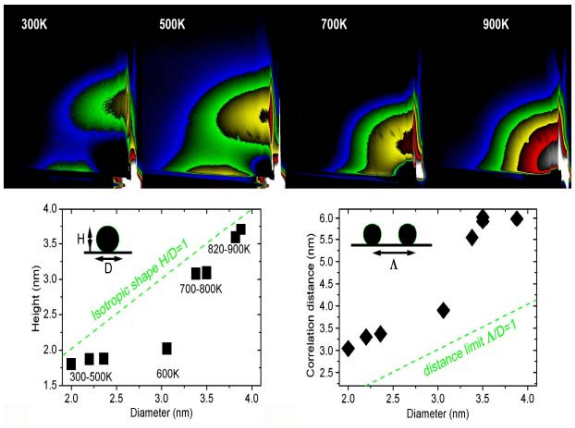

Fig. 1 : GISAXS patterns of annealing CoPt sample at selected temperatures. and Correlation between height H or correlation distance between particles and the diameter D during the temperature evolution (extracted from GISAXS experimental cross sections).

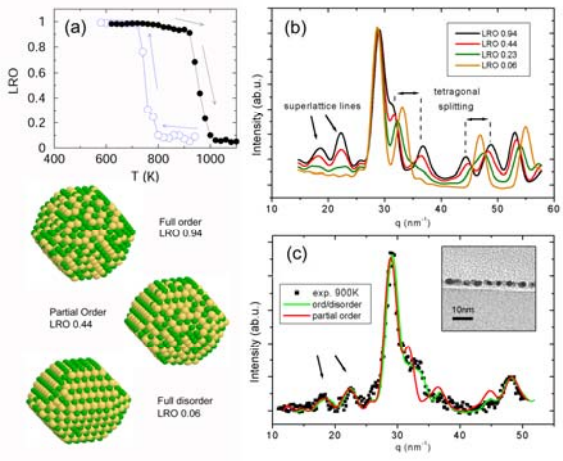

Fig.2: (a) long range order (LRO) parameter of the relaxed 1289 atoms TOh (3nm) particles. The order-disorder transition occurs around 950K in the annealing process (black points) and around 750K in the cooling process (open circles); (b) Calculated GIXD spectra of four different MC relaxed TOh CoPt clusters (1289 atoms) (b) Comparison between 900K-annealed NPs experimental (marks) and calculated (line) diffraction patterns. The simulated patterns correspond to a partial ordered cluster, and a mix of ordered-disordered cluster

Selected publication(s) . P. Andreazza, C. Mottet, C. Andreazza-Vignolle, J. Penuelas, H.C.N. Tolentino, M. De Santis, N. Bouet and R. Felici, Nanoletters, submitted

Patent(s) :

Contact : pascal.andreazza@univ-orleans.fr

Nanostructuring surfaces: Deconstruction of the Pt(110)-(1x2) surface by C_{60}

X. Torrelles,[1] V. Langlais,[2,3] M. De Santis,[3] H. C. N. Tolentino,[3] and Y. Gauthier[3]. **[1]Institut de Ciència de Materials de Barcelona, ICMAB-CSIC, Bellaterra, 08193 Barcelona, Spain. [2]Departament de Fìsica, Universitat Autònoma de Barcelona, Bellaterra, 08193 Barcelona, Spain. [3]Institut Néel, UPR 2940-CNRS, 25 Avenue des Martyrs, Boîte Postale 166, 38042 Grenoble, France. Contact torrelles@icmab.es**

The interaction at the interface between large molecules (LMs) and metallic substrates has attracted considerable interest due to the development of new devices based on organic films and/or functionalized inorganic molecules. When deposited on metal surfaces, C_{60} creates nanoholes. Grazing incidence x-ray diffraction reveals a *c*(4×4) reconstruction induced by C_{60} on Pt(110)-(1×2). While the initial (1x2) missing row is partially deconstructed, under each fullerene we find double atomic vacancy involving two Pt layers. The resulting interface is deeply modified with a 75% Pt occupancy and regularly distributed double vacancy. The orientation of the molecule is compatible with local surface *cm* symmetry with a pentagonal ring almost parallel to the surface while hexagonal rings are almost parallel to the (111) facets of the nanohole.

Two-dimensional molecular ordering is often accompanied by surface restructuring of the two to three topmost atomic layers: such a modified interface may thus be used for both surface molding and surface nanopatterning, with relevant technological applications. The mechanism of molecule's surface anchoring is usually quite complex due to the interplay between intermolecular bonds and molecule substrate interactions involving a large number of adsorption sites. This may result in substrate reconstructions, involving extensive mass transport, which can be accompanied by a structural deformation of the adsorbed molecules. The formation of vacancies at the interface with fullerene was already observed on Pt(111) Pd(110), Ag(110), Ag(111) and Au(110).

We studied the *c*(4×4) reconstruction obtained by depositing a fullerene single layer on the Pt(110)-(1×2) missing row reconstruction, using grazing incidence x-ray diffraction. The substrate was maintained at about 800 K during deposition, and the saturation coverage was determined monitoring one superstructure reflection during the growth. A set of 45 fractional rods and nine crystal truncation rods were measured to optimize the structure (the Figure1 shows a few of them).

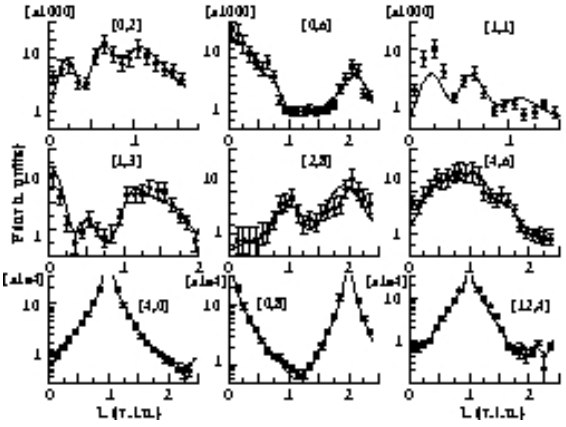

Fig.1. Fractional and Crystal Truncation rods of the C_{60}/Pt(110)-c(2x2) structure. The continuous lines correspond to the best fit model.

The XRD data analysis agrees with a surface substrate ordering where the initial (1x2) missing row is de-reconstructed by partially filling (50%) the missed rows by the effect of the C60 interaction with the substrate (Fig. 2). The resulting surface consists of a Pt top layer with complete rows alternating with half-filled ones, yielding a 75% occupancy with double vacancies alternating with Pt doublets what generates the new c(4x4) surface periodicity. This cell contains a unique bi-atomic Pt-surface hole used to host the C60 molecule and form a regular dense quasi-hexagonal molecular phase.

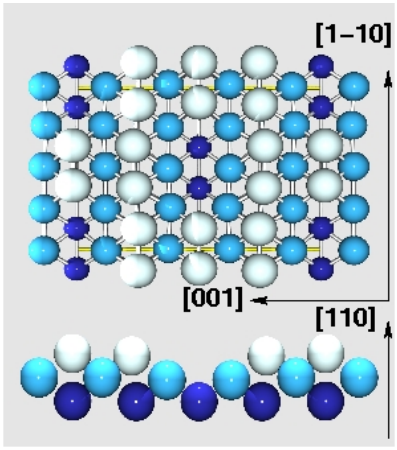

Fig. 1 Pt(110)-c(4×4): top and lateral views of the optimum surface slab ordering showing the geometry and distribution of the nanoholes on the Pt(110) surface. Darker color atoms correspond to deeper surface atoms.

The strong interaction between the C60 molecules with the Pt-substrate is evidenced by the high number of C-Pt bonds participating in the anchoring of the molecules to the substrate. The most stable configuration yields 15 C-Pt bonds with an average bond distance of 2.4 Å which is an indication of charge delocalization from the molecule to the substrate among a rather large contact interface area.

Publications X. Torrelles et al., Phys. Rev. B 81 (2010) 041404(R).

In situ synchrotron radiation studies of the structure and strain of GeMn nanoparticles during their growth

V. Favre-Nicolin[1] , M. Jamet[1] , A. Barski[1] , S. Tardif[2], T. Devillers[1] , C. Porret[1] , M. Rovezzi[3], [1] **CEA-Grenoble, Institut Nanosciences et Cryogénie, SP2M/NRS, Grenoble ; [2] Institut Néel, Grenoble ; [3] ESRF** ***Contact*** ***vincent.favre-nicolin@cea.fr***

Spin injection in semiconductors has been a long-standing issue in the field of spintronics for nearly 10 years. Only at the end of the 90's, electrical spin injection in III-V semiconductors could be demonstrated using spin-Light Emitting Diodes as spin detectors. Although silicon is the key material of microelectronics, spin injection in silicon could be achieved only recently in 2007. For this purpose, we have developed a new ferromagnetic semiconductor (Ge,Mn) that may be suitable for spin injection in silicon. Taking advantage of the in-situ growth facilities at the french INS beamline of the ESRF, we followed the evolution of GeMn layers as a function of the temperature growth and the concentration, exhibiting strong differences in the morphology and strain properties of the GeMn nanocolumns and clusters embedded in the Ge matrix.

We have used low temperature molecular beam epitaxy to grow germanium films doped with manganese. Growth temperatures (between 80°C and 180°C) as well as Mn concentrations (between 1 % and 10 %) were kept low in order to avoid phase separation due to the low solubility of Mn in Ge. Careful structural and chemical analyses showed that (Ge,Mn) films are not diluted magnetic semiconductors. We rather observe high-T_C ferromagnetic self-assembled Mn-rich nanocolumns in the germanium film with magnetic properties strongly dependent on growth parameters. Their diameter is close to 3 nm and they span the entire film thickness (80 nm) as shown in Fig. 1. From magnetic measurements, we could clearly identify four different magnetic phases in Ge1-xMnx films: diluted paramagnetic Mn atoms in the germanium matrix, low-T_C (< 200 K) nanocolumns, high-T_C nanocolumns (> 400 K) and Ge_3Mn_5 clusters. The relative weight of each phase mainly depends on the growth temperature and to a lesser extent to Mn concentration.

To investigate the exact crystalline structure of Mn-rich nanocolumns, and the dependence with the growth parameters, we used both the in-situ (INS) and ex-situ (GMT) instruments of the French CRG beamline BM32 at the ESRF. Layers of GeMn with thicknesses between 1 to 80 nm were synthesized, and then studied using grazing-incidence X-ray scattering. The experimental data comprised both small (GISAXS) and wide angle data, and for some samples repeated after annealing.

These experiments, carried out on a large range of Mn concentration (0.1 – 7%) and temperature (100-150°C, plus annealing) allowed the study of a large range of layers, from the early stages of the nanocolumns formation to the Ge_3Mn_5 clusters and their epitaxial relationship with the Ge matrix. In Fig. 1 are shown large grazing incidence diffraction maps for a sample with nanocolumns and another with clusters – for the latter the complete indexation of all diffraction peaks yielded the epitaxial relationships of the clusters (with their c-axis parallel or perpendicular to the surface) as well as their average strain and distortion from the ideal hexagonal lattice, which can be linked to their magnetic properties.

High-resolution grazing incidence diffraction maps around the Ge Bragg peaks (Fig.3) allowed the determination of the correlations between nanocolumns and of the strain field of the Ge matrix surrounding each column.

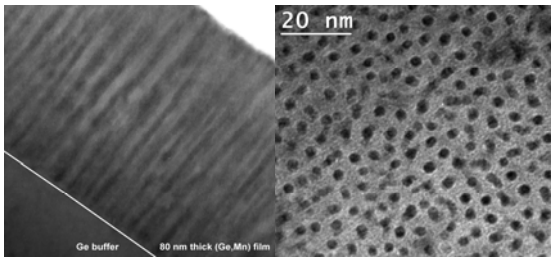

Fig. 1 Transmission Electronic Microscopy (TEM) images of GeMn nanocolumns embedded in Ge. Left: cross-plane view, showing continuous columns within the 80nm layer. Right: plane view showing the distribution of nanocolumns.

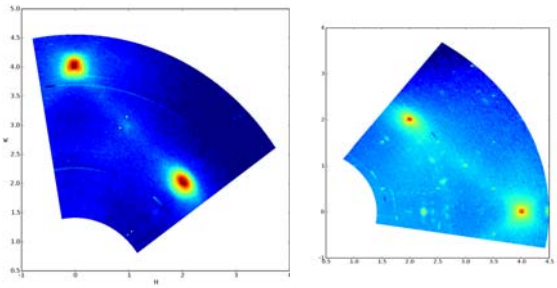

Fig. 2 Left: large grazing-incidence X-ray diffraction map, around the (220) and (040) Ge Bragg peaks, for a sample grown at low temperature (~120°C). Right: similar map, around the (220) and (400) Ge Bragg reflections, after annealing – additional Bragg peaks correspond to Ge3Mn5 magnetic clusters, which are epitaxially aligned.

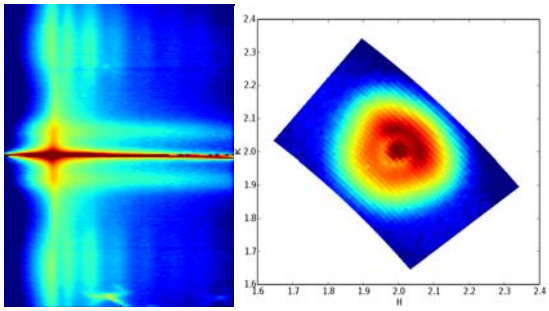

Fig. 3 Left: angular scan around (220). This GISAXS-like information, has two main correlation peaks, the one closest to the Ge Bragg peak (real space distance=40 nm) corresponds to the surface roughness, and the second corresponds to the average distance between nanocolumns (10 nm). Right: grazing incidence diffraction map around the (220) Ge peak, represented in the (HK0) plane: the diffraction presents a correlation ring due to the strained Ge matrix around each nanocolumn.

Selected publication(s)	
Grant(s) : ANR GEMO	Collaboration(s): CEA Grenoble/INAC, CNRS-Institut Néel
Patent(s) :	Contact : vincent.favre-nicolin@cea.fr

Organic heterolayers: a dynamic GIXRD study

M. Oehzelt [a], *G. Koller* [b], *T.U. Schülli* [c], *T. Haber* [d], *R. Resel* [d], *M.G. Ramsey* [b], ***a*** **Institute of Experimental Physics, Johannes-Kepler-University Linz, Altenbergerstraße 69, A-4040 Linz, Austria;** ***b*** **Institute of Physics, Karl-Franzens-University Graz, Universitätsplatz 5, A-8010 Graz, Austria;** ***c*** **CEA-Grenoble, Institut Nanosciences et Cryogénie, SP2M/NRS, 17 rue des Martyrs, 38054 Grenoble Cedex 9, France; Institute of Solid State Physics, Graz University of Technology, Petersgasse 12, A-8010 Graz, Austria. Contact martin.oehzelt@JKU.at**

Organic heterostructures of pentacene (5A) and para-sexiphenyl (6P) are studied with X-ray diffraction methods on a copper single crystal. Initially pentacene molecules are deposited on the metal substrate and exhibit a high degree of order. This organic film is overgrown by a thick 6P layer. The molecules in the second layer are also crystalline and the long molecular axes of the 6P molecules follow the directions of the pentacene substrate molecules. Heating this heterostructure to the sublimation temperature of pentacene, which is lower due to its lower molecular weight compared to 6P, evaporates the pentacene molecules through the 6P layer leaving only the 6P layer while keeping the original orientation of the 6P molecules. A 2D-detector allows to study this evaporation process in-situ and in real-time and can monitor the changes in both organic layers simultaneously. During the evaporation process a higher degree of mosaicity in the 6P layer is observed but the orientation of the 6P layer with respect to the substrate is conserved. After evaporation of the pentacene layer the initial mosaicity is recovered.

Heterostructures of thin molecular layers have received considerable interest as organic devices typically consist of a multiplicity of such layers. The INS end-station at beamline BM32 offered an almost unique possibility to study such heterostructures in a controlled sample environment which in our case means to follow growth/desorption processes in real time in-situ UHV. The z-axis geometry allowed to determine the epitaxial relations between the substrate and the subsequently deposited molecular layers. In the present study single crystalline copper (110) was used as substrate to align the first molecular film uniaxially. On this aligned molecular layer the second molecule was deposited. Azimuthal diffraction scans of the high intensity peaks of both molecular layers determined the molecular orientation to be within a few degrees in the direction of the copper [1-10].

The sequence of layers was chosen in such a way that the molecule with the lower sublimation temperature (5A) was overgrown by a molecular layer with higher sublimation temperature (6P). As the packing and orientation of the crystalline layers is very similar it was possible to detect diffraction peaks of the whole heterostructure on the same ccd-image simultaneously. Figure 1a) shows such a diffraction pattern with peaks of the pentacene (010) oriented film and the peaks of 6P deposited ontop (6P(20-3)). This situation allows to study the evolution of both organic layers simultaneously during heating. The overgrown layer is evaporated first due to its lower sublimation temperature. While the 5A layer is evaporated (Fig. 1 d-f), the 6P rocking curve is increased (see Fig. 1b), but fully recovered after the 5A layer is gone (Fig. 1g-h). Moreover, the orientation of the 6P crystallites is not altered due to the evaporation process. It was thus possible to transfer a 6P(20-3) oriented layer onto Cu(110) whereas if 6P is deposited directly on the clean copper (110) substrate only 6P(62-9) crystallites could be achieved.

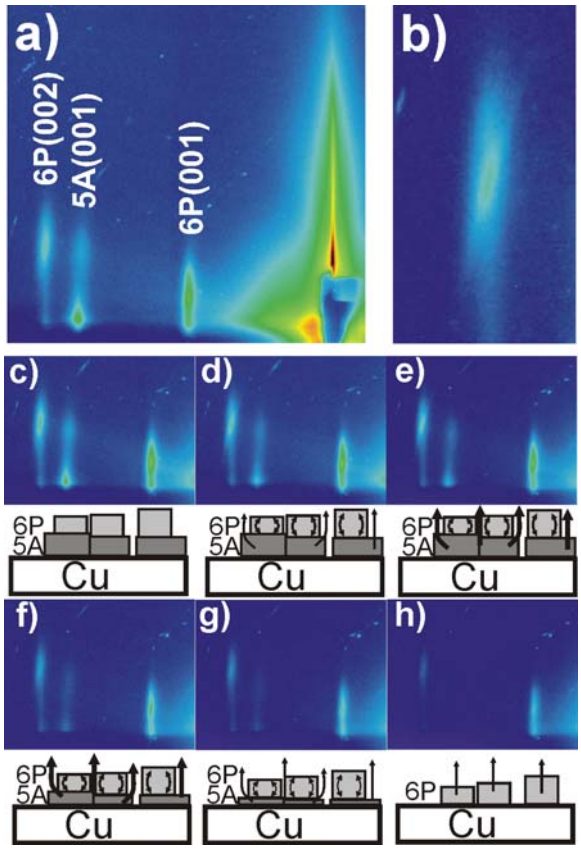

Fig. 1 CCD-image of diffraction peaks of the copper-5A-6P heterostructure. a) depicts the whole image seen on the ccd with the diffuse scattered background and the (00l) diffraction peaks of 5A and 6P. b) a zoom in of the 6P(002) diffraction peak where clearly a streak during evaporation of 5A is observed. c)-h) sequence of diffraction pattern during heating of the hetero-structure with increasing temperature. Schematics below the diffraction pattern are given to illustrate the evaporation process.

Selected publication(s) : (1)M. Oehzelt, *et al.* in prep. (2)Crystal growth of para-sexiphenyl on clean and oxygen reconstructed Cu(110) surfacesM. Koini, et. al. in prep. (3)R. Resel, Surface induced crystallographic order in sexiphenyl thin films J.of Phys. Cond. Matt., 20, p.184009.1-10 (2008) (4)R. Resel, M. Oehzelt, O. Lengyel, T. Haber, T. U. Schülli, A. Thierry, G. Hlawacek, C. Teichert, S. Berkebile, G. Koller, M. G. Ramsey The epitaxial sexiphenyl(001) monolayer on TiO2(110): a grazing incidence x-ray diffraction study Surf. Sci., 600, 4645-9 (2006).(5) M. Oehzelt, G. Koller, J. Ivanco, S. Berkebile, T. Haber, R. Resel, F.P. Netzer, M.G. Ramsey Organic heteroepitaxy: p-sexiphenyl on uniaxially oriented α-sexithiophene Adv. Mat..18,.2466-2470 (2006)

Grant(s) : FWF Austrian Science Funds

Collaboration(s): Linz University, Austria; University of Graz, Austria;TU-Graz, CEA-Grenoble

Patent(s) :

Contact : martin.oehzelt@jku-linz.at; georg.koller@uni-graz.at

Solid state dewetting of Si on SiO_2 by *in situ* GISAXS and GIXD

F. Leroy[1], E. Bussmann[1], F. Cheynis[1], T. Passanante[1], P. Müller[1], J. Eymery[2] . [1]CINaM-CNRS UPR 3118, Campus de Luminy case 913, 13288 Marseille cedex 9. [2] CEA INAC, 17 rue des martyrs, 38054 Grenoble cedex 9. Contact leroy@cinam.univ-mrs.fr

Since a vast variety of technologies rely on solid thin films, a fundamental understanding of the origin of the thermodynamic stability, and failure, of these systems is invaluable. Silicon thin films on silicon dioxide (silicon-on-insulator (SOI)) are essential in microelectronics and a promising material for future nanodevices. SOI are unstable at temperatures T > 800oC typical of annealing required for microelectronics fabrication. The Si dewets from the SiO2 substrate, forming 3D nanocrystals. We measured the morphological evolution and kinetics of the process. More particularly GISAXS and GIXD measurements can provide accurate information on the role of stress in the dewetting kinetics.

Silicon-on-insulator (SOI) substrates are made of a Si(001) single-crystalline thin film on top of an amorphous SiO_2 layer (140 nm) deposited on a wafer of Si. It is expected that an active Si layer as thin as 10 nm will be required in a near future. However this layer is unstable when annealed at high temperature (typically 800°C for SOI system) resulting in agglomerated nanocrystals (Fig. 1). The solid dewetting of SOI thin films represents both a critical process limitation for the fabrication of advanced devices as well as a basic morphological evolution problem.

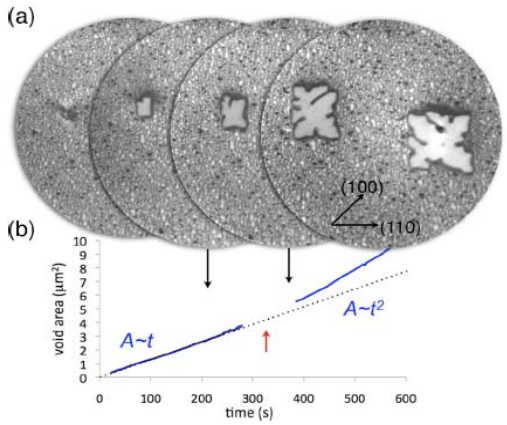

FIG. 1: (a) Darkfield Low Energy Electron Microscopy images showing the dewetting of a 20 nm thick Si film. A square void opens then form fingers at the edges. (b) The dewetted area evolves from A~t to A~t^2.

We have studied in real time by Grazing Incidence Small Angle X-ray Scattering (GISAXS) and Grazing Incidence X-ray Diffraction (GIXD) the morphology and structure of dewetted thin films from the nucleation of voids until the growth of isolated aggregates (see Fig. 1). The key parameters of this solid dewetting transition are: the crystalline orientation, the thickness of the layer, the interfacial stress and the temperature of the process. More particularly it has been proposed that SOI agglomeration is a stress-driven morphological instability caused by a thermal expansion mismatch stress. In order to put in evidence the role of interfacial stress we have used the recently developed strained silicon-on-insulator (sSOI) technology. This technology allows tuning the lattice parameter of the Si adlayer in the range 0 to 1.2% on the same SiO_2 amorphous material.

The structure of the Si/SiO_2 interface has been quantitatively characterized for SOI and sSOI samples by GIXD measuring a set of CTR. For instance fig. 2 a-b shows from CTR (22L) that the strain fields extending into the Si layers for SOI and sSOI are extremely different. Moreover for sSOI samples the Si Bragg peaks are not only shifted compared with bulk Si but also broader

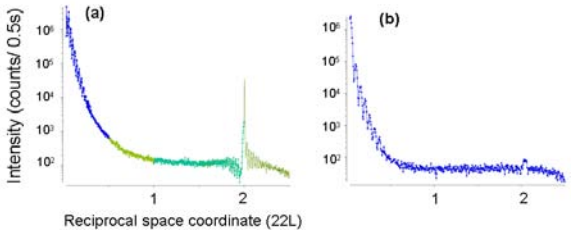

Fig. 2: (22L) scans for (a) unstrained and (b) 0.8%-strained Si thin films. At the reciprocal space coordinate (222), the different deformation fields between unstrained and strained samples is evidenced.

showing that the strain state of the sSOI thin films is not homogeneous (see Fig.3 at the beginning of dewetting).

We have focused our attention on the kinetics of the dewetting process alternating GIXD and GISAXS in order to detect the structural and morphological changes. Figure 3 shows that the dewetting of the strained Si layer gives immediately rise to fully relaxed Si aggregates which are facetted ((113) and (111) facets are predominant) as revealed by GISAXS measurements.

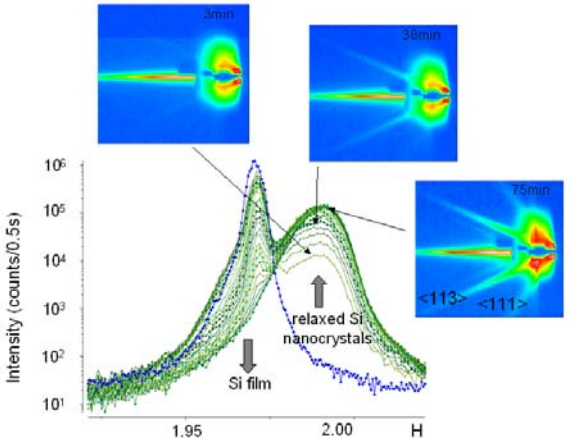

Fig. 3. Overview of the evolution of GISAXS (beam aligned along <110>) and GIXD (scan along (hh0)) as function of time during dewetting of a 1.2%-strained Si film at 950°C. The dewetting starts by the appearance of a bump at (220) corresponding to relaxed Si nanocrystals. Simultaneously, extended strikes arising from <113> and <110> facets appear on the GISAXS patterns. The intensity of this bump from Si nanocrystals increases while the Si film Bragg peak decreases. The time for a complete dewetting is about 1h.

Selected publication(s) E.Bussmann, F.Cheynis, F.Leroy, P.Müller, Material Science and Engineering, to be published (2010).
E.Bussmann, F.Cheynis, F.Leroy, P.Müller, O. Pierre-Louis (submitted to nanoletters)

Grant(s) : ANR-08-NANO-P168-36 « DEFIS »

Collaboration(s): CINaM-CNRS (Marseille, France), CEA INAC (Grenoble, France)

Patent(s) :

Contact : leroy@cinam.univ-mrs.fr

Growth and thermal stability of Pd and AuPd nanoparticules grown on a $Al_2O_3/Ni_3Al(111)$ thin film by *in situ* GISAXS

G. Hamm, G. Sitja, M. Marsault, F. Leroy, C. Henry, G. Renaud, **CINaM-CNRS UPR 3118, Campus de Luminy case 913, 13288 Marseille cedex 9. Contact leroy@cinam.univ-mrs.fr**

Pd and Au/Pd nanoparticules have been grown on an ordered oxide nanotemplate fabricated by thermal oxidation of a $Ni_3Al(111)$ surface. Nanometer size aggregates with a narrow size distribution are obtained giving the opportunity to study their fundamental properties. However for catalysis purposes it is necessary to (i) make sure that the nanoparticules are stable during reaction i.e. at high temperature and in presence of gas and (ii) to know the internal structure and the chemical composition of the nanoparticules in case of bimetallic aggregates. In that purpose, X-ray scattering techniques and especially GISAXS are very appealing. We have studied *in situ* the time evolution of the size, shape, organisation and in some respect composition of Pd and Au/Pd nanoparticules during growth and annealing.

Bimetallic nanoparticles (NPs) supported on oxides often exhibit improved catalytic properties compared to their pure metal counterparts. A thorough understanding of all these performances implies to be able to quantify the importance of each parameter, i.e. size, shape, crystallographic structure and composition in the case of bimetallic NPs. Therefore manufacturing model catalysts of perfectly controlled NPs is an important challenge. In standard growth conditions, a large variety of shape, size and composition of NPs is usually obtained. This precludes any detailed analysis of the catalytic properties

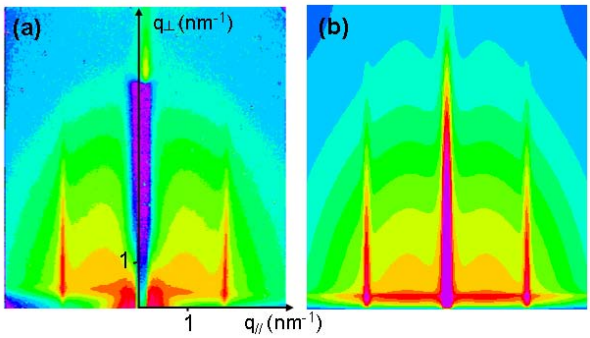

Fig. 1 (a): experimental GISAXS pattern for 0.1 nm Pd/ Al_2O_3. (b) GISAXS simulation obtained from the best fit of size, shape, and spatial order of Pd NPs.

²of the NPs. A very promising way is to use a nanostructured oxide as a template for the organized growth of NPs. In particular it has been shown that Pd and AuPd NPs can be grown on a $Al_2O_3/Ni_3Al(111)$ thin film exhibiting a long-range order and a narrow size distribution (<20%). The NPs grow on the "defects" of a 4.1 nm hexagonal superstructure.

The alumina film is grown *in situ* on a $Ni_3Al(111)$ surface using the INS set-up of the BM32 beamline. Real time GISAXS measurements of the growth of Pd on the alumina film at RT have shown that already at low coverage (0.05 nm) ordered arrays of NPs with a narrow size distribution are obtained. The Pd NPs are organised in a regular hexagonal lattice on the whole sample with two orientational domains rotated by 24°. The best agreement between experiment and simulation (Fig. 1) for instance for 0.1 nm equivalent thickness of Pd deposited at the surface is obtained assuming hemispherical NPs of R=0.95 nm mean radius, ΔR/R=0.25 relative size dispersion and H/R=0.6 aspect ratio. The size and the aspect ratio of the NPs are in agreement with our STM results, keeping in mind that STM measurements on NPs of such size have large uncertainty due to the tip/sample convolution effect. Concerning the lattice, it corresponds to the periodic structure of the underlying reconstructed alumina surface as observed by STM and AFM. From the fit of the full width at half maximum of the narrow scattering rods of the Pd NPs lattice, it is evidenced that the NPs are long-range ordered (200 nm correlation length) on the whole

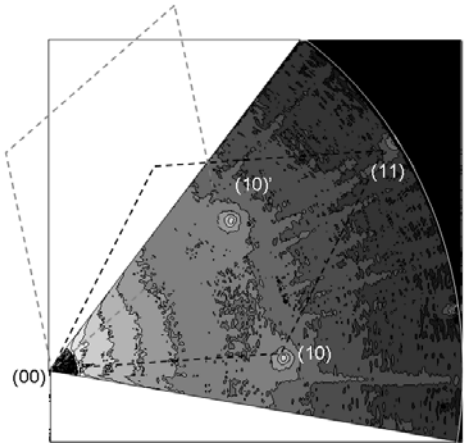

Fig. 2: in-plane map of the reciprocal space extracted from 60 GISAXS patterns. (10) and (10)' "Bragg" spots correspond to the first order diffraction spots of two equivalent Pd NPs lattices rotated by 24°.

sample area. This analysis has been completed by the measurement of a full 3D map of reciprocal space by GISAXS rotating the sample by steps of 1° over a total angular range of 60°. In Fig. 2 is shown a 2D projection of this map in the surface plane. It exhibits clearly the two main spots arising from the two variants of the hexagonal lattice of Pd NPs rotated by 24°.

Currently we are studying the growth and thermal stability of an assembly of AuPd bimetallic NPs on the same ordered surface. The NPs are grown by a sequential deposition process previously developed in CINaM laboratory. First a lattice of Pd NPs is grown on the alumina film, then Au is deposited on the surface. It has been shown by that gold atoms selectively attach on the previously grown Pd NPs (i.e. there is no nucleation of pure gold clusters). We are investigating in real time by *in situ* GISAXS the thermal stability and the evolution of the core/shell structure of the NPs as function of NPs composition.

Selected publication(s) G. Hamm, C. Barth, C. Becker, K. Wandelt, C.R. Henry, *Phys. Rev. Lett. 97* (2006) 126106. G. Hamm, C. Becker, C.R. Henry, *Nanotechnology 17* (2006) 1943 and M. Marsault, G. Hamm, A. Wörz, G. Sitja, C. Barth, C.R. Henry, *Faraday Discussions 138* (2008) 407..M. Marsault, thèse de doctorat de l'Université de la Méditerranée, 2009.

Collaboration(s): CINaM-CNRS (Marseille, France), CEA INAC (Grenoble, France)

Contact : leroy@cinam.univ-mrs.fr

Growth and structure of Co clusters on alumina on $Ni_3Al(111)$

A. Buchsbaum,[1] M. De Santis,[2] H. C. N. Tolentino,[2] M. Schmid,[1] and P. Varga[1]. **[1]Institut für Angewandte Physik, Technische Universität Wien, A-1040 Wien, Austria. [2]Institut Néel, UPR 2940-CNRS, 25 Avenue des Martyrs, Boîte Postale 166, 38042 Grenoble, France. Contact schmid@iap.tuwien.ac.at**

Template-mediated growth of metals has attracted much interest due to the remarkable magnetic and catalytic properties of clusters in the nanometer range. We have grown Co clusters on the ultrathin aluminum oxide on $Ni_3Al(111)$, a template with a 4.1 nm lattice. The structure of this ≈0.5-nm-thick oxide film exhibits holes reaching down to the metal substrate at the corners of the $(\sqrt{67}\times\sqrt{67})R12.2°$ unit cell. Pd atoms trapped in these corner holes create metallic nucleation sites where Co clusters can nucleate and form a well-ordered hexagonal arrangement. We have studied these Co clusters by surface x-ray diffraction to determine their structure. We found a random stacking of close-packed hexagonal planes.

An essential property for technological applications of nanostructures made of magnetic materials is the magnetocrystalline anisotropy energy (MAE), which affects the thermal stability of the collective magnetic moments of nanostructures in the superparamagnetic state. Besides the dependence of the MAE on the material, the size and shape of the clusters are crucial. Many previous investigations show an enhanced MAE and orbital magnetic moment for structures in the subnanometer and nanometer ranges compared to the respective bulk systems due to the lower symmetry of atoms at the surface. For proper investigations and applications of magnetism at the nanoscale, obtaining clusters with well-aligned easy axes and monodisperse size distribution is a key challenge in order to obtain well-defined magnetic properties. A detailed investigation of the morphology and the crystallography is required to understand magnetic properties of nanostructures.

The $(\sqrt{67}\times\sqrt{67})R12.2°$ alumina film was grown by dosing the $Ni_3Al(111)$ substrate with 40 Langmuir of O_2 at 1000 K. Co was deposited on the oxide seeded with 3 Pd atoms per unit cell, trapped in the corner hole.

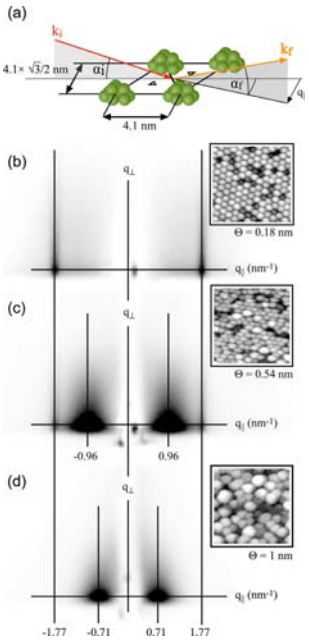

Fig. 1 (a) Sketch of the beam alignment with respect to the cluster arrangement in real space. In situ GISAXS measurements taken at coverage of (b) θ=0.18 nm Co, (c) θ=0.54 nm Co, and (d) θ=1 nm Co, deposited at 470 K (Pd seeded). Insets are STM images (3.1 V/0.1 nA) taken at equal experimental conditions (50-nm wide each).

The growth was monitored by GISAXS, showing a good agreement with STM measured at the TU-Wien (insets of Fig.1). Before coalescence [Fig.1(b)] the two side maxima, found at $q_{//}$ = ±1.77 nm^{-1} in reciprocal space, correspond to the distance of the rows of clusters, which is 4.1×√3/2 nm in real space [the sketch in Fig. 1(a) shows a schematic view of the geometry used for the measurements].

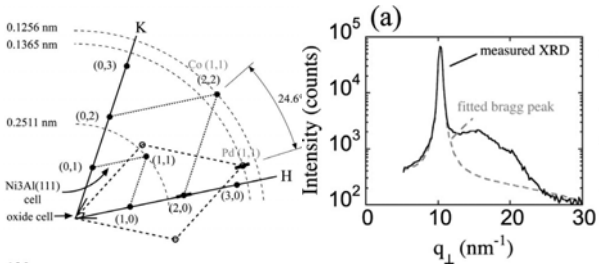

Fig.2. (a) Map of the reciprocal-space projected onto the surface plane, with Miller indices of the $Ni_3Al(111)$ surface cell. The oxide cell and the hexagonal unit cells of Co and Pd clusters grown on the oxide are also shown. (b) (2 0) rod of the $Ni_3Al(111)$ surface [equivalent to the Co (1 0)$_{hex}$ one].

Assuming that the Co clusters do not change their structural properties upon coalescence, as suggested by STM, SXRD was performed at a Co coverage of 2 nm, above coalescence, to ensure a large enough diffracted intensity. The nearest-neighbor distance of bulk Co atoms in a close-packed plane ($d_{Co\text{-}Co}$=0.2507 nm) is almost equal to the nearest-neighbor distance of atoms in the $Ni_3Al(111)$ alloy surface (0.2511). Scanning the scattering vector $\boldsymbol{q}$ parallel to the surface at several values of $q_\perp$, we observed a coincidence of the $Ni_3Al(111)$ CTRs and of the Co clusters rods, telling us that the Co forms close packed hexagonal planes with the same azimuthal orientation as the $Ni_3Al(111)$ surface below the oxide [see the map of the reciprocal space in Fig.2(a), where the reflections are labeled using the surface hexagonal unit cell].

We can now proceed to study the layer stacking of the Co clusters. Figure 2(b) shows a scan along the (1 0)$_{hex}$ Co rod, performed 0.5° off the CTR in azimuth to increase the ratio of the Co signal to the substrate rod. After subtracting the $Ni_3Al(111)$ contribution, a peak at $q_\perp$=15.1 nm^{-1} remains. This peak can be fitted by $I(q) = C/(5/4 + \cos(qd))$, a function that describes the scattering power of close packed planes with random stacking and an interlayer distance d, with d=0.206 nm, the interlayer distance of close-packed Co planes (0.2035 nm for Co hcp).

Publication A. Buchsbaum et al. Phys. Rev. **B** 81 (2010) 115420

In situ Grazing-Incidence X-Ray Diffraction Studies of polar MgO film on Au(111)

S. Benedetti[1], P. Myrach[2], N. Nilius[2], P. Torelli[1], H.J. Freund[2], S. Valeri[1], G. Renaud[3], ***[1]Centro S3, CNR-Istituto di Nanoscienze e Dip. Fisica, Università di Modena e Reggio Emilia, via Campi 213/a, 41125 Modena, Italy ; [2] Fritz-Haber-Institut der Max-Planck-Gesellschaft, Faradayweg 4-6, D-14195 Berlin, Germany ; [3]CEA-Grenoble, Institut Nanosciences et Cryogénie, SP2M/NRS, 17 rue des Martyrs, 38054 Grenoble Cedex 9.***

The (111) surface of rocksalt oxides, unstable in the bulk form because of its intrinsic polarity, can be stabilized on thin oxide films thanks to the metal substrate. Induced morphological deformations, changes in the electronic structure, etc. can determine an unexpected adsorption behaviour and new catalytic properties. We have investigated the growth of thin MgO films on Au(111) by combining Grazing Incidence X-Ray Diffraction (GIXD) and Scanning Tunneling Microscopy (STM), to determine the structure of the film and correlate it with the possible presence of an uncompensated surface polarity.

The MgO films has been prepared *in situ* by deposition on a Au(111) substrate of Mg atoms in O_2 partial pressure. While GIXD has been performed at BM32, STM measurements have been performed at FHI by means of nitrogen-cooled STM. Then a study of the electronic properties has been performed in Modena, together with a check of stoichiometry and contamination, by means of XPS.

By means of the GIXD analysis we have studied the structure of the MgO film. The sharpness of the diffraction peaks allows to separate the Au contribution from the MgO one. The radial scans for increasing oxide thickness show the appearance of an additional peak besides the Au Bragg peak, corresponding to the MgO hexagonal lattice related to its growth in the (111) epitaxy. This conclusion is confirmed also by the STM images, that show a surface covered by triangular islands with a quite homogeneous lateral size of approx. 9 nm, pointing either in the [11̲2] and [112̲] directions (Fig. 2a). The average height of the islands indicates that the main part of the film is a single ML high (where ML means the presence of both Mg and O planes). However islands more than 1 ML high are present, showing a starting second layer or a more 3D profile with a shape more similar to a pyramid. From the position of the MgO Bragg peaks the in-plane lattice parameter has been determined (Fig. 1b). For the (111) component of the film the lattice parameter at 3 ML corresponds already to the bulk value on the (111) face and it does not significantly change with increasing thickness. Furthermore change in the deposition temperature or further annealing does not affect the in plane parameter. For the very low MgO thicknesses, atomic resolution can be achieved on the flattest triangular islands and shows an hexagonal pattern with a lattice parameter of 3 Å, indicating that already for 1 ML high islands the lattice parameter is consistent with a relaxed structure.

Besides the (111) orientation, other peaks are detected in radial scans, as those observed at about h=1.7 (Fig. 1a). They can be explained by the presence of MgO in the (001) orientation. This phase shows a relaxation process, starting from pseudomorphic and moving to a structure more similar to the bulk (Fig. 1b). Again we have detected flat non-triangular islands in STM images after deposition at 500 K (Fig. 2c), where atomic resolution shows that the lattice is square, with a unit cell of 2.9×2.9 $Å^2$. If the deposition temperature is increased to 650K, the sq-MgO peaks disappear and only the hex-MgO peaks remain. This indicates that the most stable phase on the Au(111) surface is the epitaxial MgO(111).

We have measured then the scans along the L direction perpendicular to the surface, that can provide information about the out-of-plane structure of the MgO film. The peak periodicity and position of the MgO film is indicative of an out-of-plane symmetry typical of a fcc or rocksalt structure, while no evidence of a graphite-like structure predicted by theory is present. Additionally domains with a reversed fcc stacking as compared with the Au one are observed. This shows that the film has a bulk-like structure, in spite of the instability. Part of this instability is compensated by a 3D growth and the formation of pyramid, part is healed by H adsorption. However still some islands look very flat and single ML high to indicate the possible presence of an uncompensated polarity.

The study of this system is still running, to combine the information on the morphology, the structure and the electronic properties, to determine whether the islands are polar, to get more details on the structure that can help us to unravel the polarity information, and to find out how these features depend on the kinetic of growth.

Fig. 1 (a) Radial scans along the (h,0, 0.08) direction for MgO films deposited at 500 K of increasing thickness. (b) Hexagonal domain and square domain in-plane lattice parameter.

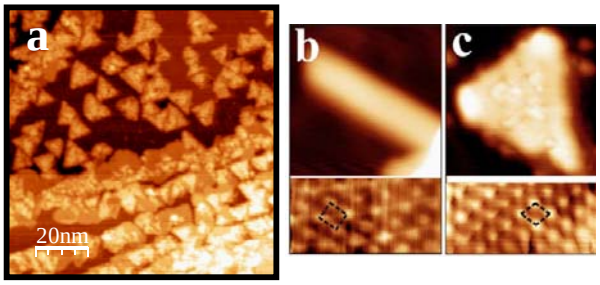

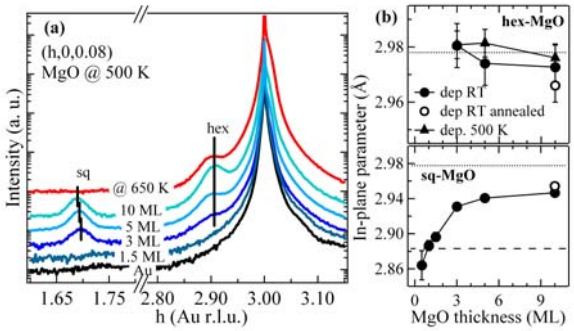

Fig. 2 (a) STM images of 1 ML MgO on Au(111) deposited at 500K (100x100 nm^2). b,c) Details of the sample grown at 500K (9x9 nm^2).

Twin and their boundaries during homoepitaxy on Ir(111)

S. Bleikamp,[1] J. Coraux,[2] O. Robach,[3] G. Renaud,[3] and T. Michely,[1] **[1] II. Physikalisches Institut , Universität zu Köln, 77 Zülpicher Str., 50937 Cologne, Germany – [2] Institut Néel, CNRS-UJF, 25 rue des Martyrs, 38042 Grenoble Cedex 9 – [3] CEA-Grenoble, Institut Nanosciences et Cryogénie, SP2M/NRS, 17 rue des Martyrs, 38054 Grenoble Cedex 9. Contact : johann.coraux@grenoble.cnrs.fr**

Stacking faults and twin boundaries are known to seriously affect the properties of thin films and devices. Magnetic properties, for instance, crucially depend on the stacking sequence, and electrical resistivity is closely linked to the microstructure. Aiming at gaining insight into the structure, formation, and stability of twin crystallites, we have been using Ir(111) homoepitaxy for more than five years. In a homoepitaxial system indeed, no stacking faults and thus twin should be present due to energetics, which allows to explore its kinetics in the pure form, free of the complications imposed by chemical inhomogeneities or epitaxial strain.

The INS end-station was employed to quantitatively characterize the structure of thin, twinned Ir films. For this surface X-ray diffraction (SXRD) was operated in ultra-high vacuum, *in situ* during the growth, as a function of the films thickness and annealing. The measurements were compared to scanning tunneling microscopy (STM) of the surface of the twinned films. Accordingly we developed a deep understanding of the nature and stability of the twins and their boundaries, as well as of the stability of twin structure and twin boundaries.

SXRD was performed for sets of crystal truncation rods (CTRs) for determining the absolute twin fraction in a growing thin Ir film (300 K). A methodology was developed that allowed the refinement of the film structure *via* the simulation of the scattered intensity over full sets of CTRs. We showed that such an approach is not only relevant for ultra-thin films of a few atomic layers which were studied in the past, but also for thicker films. The result of a best fit is shown in fig. 1(a), and the corresponding fraction of twins a as function of the thickness of the thin films in fig. 1(b). A rapid proliferation of twins is observed from 10 atomic layers (monolayers, ML) on, which leads to a fraction of twinned surface in excess of 50 % after 50-60 Ir ML.

In addition to the well-know twins that evolve from stacking faults in the (111) plane, we revealed the formation of twins initiated at {111} side-facets [inclined with respect to (111)]. Such twins were also found at the {111} side-facets of twinned regions. The twins-of-twins and side-twins are detected along reciprocal space directions being perpendicular to the side facets, as shown in fig. 2(a). The nature of the boundaries between the various twins in the thin film was unveiled by combining the surface view from STM and the sub-surface view from SXRD. We found that step edges of height one or two thirds of an atomic step height, which are visible on STM topographs after annealing above 1000 K [fig. 2(c)], result from the sliding of twinned and untwinned crystallites along their {111}/{115} boundary. This is driven by maximization of the contact between the two crystallites. We also found strong evidence that the dissociation of the {111}/{115} [Fig. 2(b)] accounts for the formation of the side-twins and twins-of-twins.

SXRD and STM showed complementary evidences that the annealing of the twinned films proceeds in first *via* the coarsening of the twin boundaries' area, in the range of temperatures between 800 and 1000 K. In this range the side-twins and twins-of-twins, which developed following the dissociation of {111}/{115} boundaries, vanish. Only at much higher temperatures above 1200 K also the twins themselves heal.

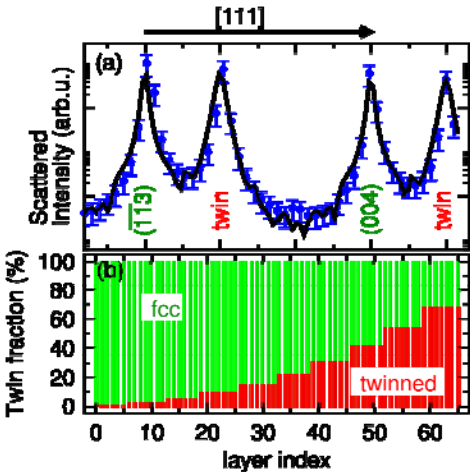

Fig. 1: (a) Scattered intensity along a CTR, perpendicular to (111): Bragg peak from the untwinned and twin regions are seen. Data are shown with dots; the best fit is shown with a solid line. (b) Profile of twin fraction along the film thickness, as refined from a fit of a set of several CTRs such as the one shown in (a).

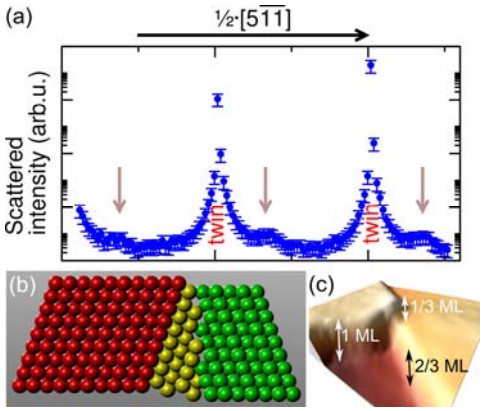

Fig. 2: (a) Scattered intensity along [511], which shows twin peaks and smaller ones (indicated with an arrow) generated by twins-of-twins. (b) Ball-model for the twin boundary between a twin and an untwinned region, comprising a twin-of-twin region (yellow). (c) Three-dimensional STM topograph showing an atomic step height (1 ML), and fractional steps (1/3 and 2/3 ML)

Selected publication(s) S. Bleikamp, J. Coraux, O. Robach, G. Renaud, T. Michely, submitted for publication

Grant(s): Deutsche Forschungsemeinschaft, "Kinetics of stacking faults in thin films"

Collaboration(s) :

Patent(s):

Contact: johann.coraux@grenoble.cnrs.fr

Structure and magnetism of an ultra-thin [NiO/CoO]/PtCo bilayer with perpendicular exchange bias

Maurizio De Santis, Hélio C. N. Tolentino, Jean-MarcTonnerre, Stéphane Grenier, Aline Y. Ramos, Yves Gauthier, Veronique Langlais.
Institut Néel, UPR 2940-CNRS, 25 Avenue des Martyrs, Boîte Postale 166, 38042 Grenoble, France

We have investigated the buried exchange-coupled interface [NiO/CoO]/[PtCo] grown on a Pt(111) single crystal. The magneto-optical Kerr effect reveals a strong coupling at the interface, by an increasing coercivity, and a spin reorientation of the ferromagnetic (FM) layer when ordering occurs in the antiferromagnetic (AFM) layer. The combination of grazing incidence X-ray diffraction (GIXRD), X-ray reflectivity and soft X-ray resonant magnetic scattering (XRMS) yields a comprehensive description of the system.

The exchange bias (EB) effect occurs when an AFM material is placed in contact with a FM one. The interaction at the AFM/FM interface yields an increase of the coercivity and induces an unidirectional anisotropy. The role of the EB effect in devices is to magnetically pin one of the FM layers. The major part of EB studies have been performed with the magnetization parallel to the AFM/FM interface. Studies on systems with perpendicular magnetic anisotropy (PMA) are rather recent and only few address the role of spin configuration at the interface. PMA is recognized as a way for increasing magnetic storage density.

We report here on a combined structural and magnetic study of the [NiO/CoO]/[PtCo] perpendicular exchange bias system. The aim of our investigation is to obtain a fine control of the structure and to reach a comprehension of the exchange coupling mechanism at the interface of AFM/FM systems that are as close as possible to model ones. CoO is an AFM oxide with T_N=293K and a large magnetocrystalline anisotropy. NiO presents a much higher ordering temperature, T_N=523K, and smaller anisotropy. By mixing both oxides, one obtains an AFM material with a high magnetocrystalline anisotropy and with an intermediate Néel temperature.

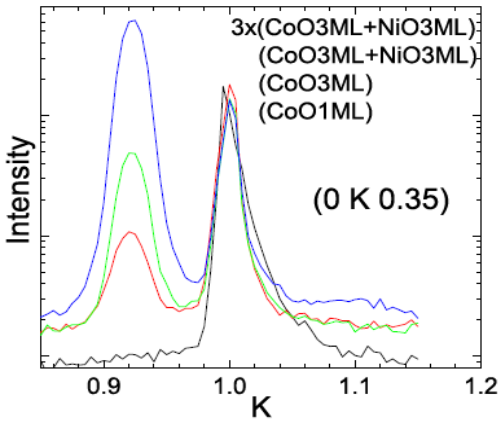

Fig.1: Surface X-ray diffraction pattern during the growth of the NiO/CoO mixed oxide over the PtCo(111) surface alloy.

An epitaxial [NiO(3ML)/CoO(3ML)]x3/PtCo sample was synthesized by sequential electron beam evaporation over a Pt(111) single crystal. 1 ML of Co was deposited onto a clean Pt(111) single crystal, held at 540K to promote the formation of a FM PtCo surface alloy with a strong PMA. The mixed oxide grows in orientational epitaxy on the PtCo(111) surface (Fig.1). The first CoO atomic layer is pseudomorphous on the substrate. After the second oxide layer deposition, the layer relaxes and a bulk-like CoO(111) lattice peak shows up at K = 0.92. The NiO layer grows in coherent epitaxy with the CoO and displays the same in-plane parameter.
Polar magneto-optic Kerr effect (MOKE) was used to study the magnetic properties of our sample (Fig.2). The coercivity H_C presents a maximum of 1.7 kOe at about 320 K, then decreases monotonically to 1.2 kOe at higher temperatures. This is the same coercivity as for the PtCo surface alloy without any capping oxide. For temperatures below 320 K the hysteresis loops shifts. At room temperature, the shift is found to be H_{EB}= -0.6 kOe and characterizes the perpendicular exchange coupling at the interface. The most striking result in this range is that the hysteresis loops becomes less and less squared. This indicates that the easy magnetization axis of the FM layer is no longer perpendicular. The change in the hysteresis loops is related to the reorientation of the Co spins in the FM layer due to exchange coupling with the oxide layer.

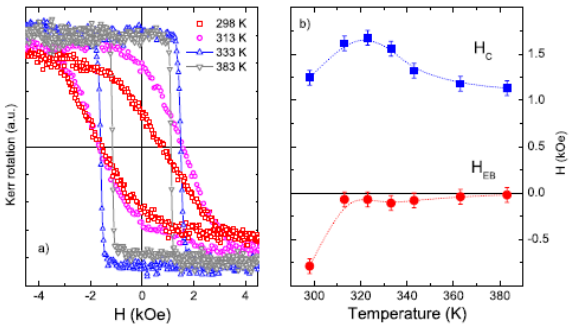

Fig.2: (a) PMOKE hysteresis loops at different temperatures. (b) exchange bias and coercivity dependence on temperature.

The depth dependence of the out-of-plane magnetization across the AFM/FM interface was investigated by soft XRMS. The magnetic profile yields that oxidized Co atoms closest to the interface are ferromagnetically coupled to the PtCo FM layer. The second oxide layer couples antiferromagnetically to this interfacial one.

Selected publication(s) Marcio M. Soares, Maurizio De Santis, Hélio C.N. Tolentino, et al., "On the growth of chemically ordered MnPt alloy on Pt(001)", Surf. Science (2010) submitted
Grant(s) : Marcio M. Soares, RTRA Grant
Contact : helio.tolentino@grenoble.cnrs.fr

On the growth of chemically ordered MnPt alloy on Pt(001) single-crystal

Marcio M. Soares[1], Maurizio De Santis[1], Hélio C. N. Tolentino[1], Aline Y. Ramos[1], Yves Gauthier[1], Xavier Torrelles[2]. **1) Institut Néel, UPR 2940-CNRS, 25 Avenue des Martyrs, Boîte Postale 166, 38042 Grenoble, France ; 2) Institut de Ciència de Materials de Barcelona, ICMAB-CSIC, Bellaterra, 08193 Barcelona, Spain. Contact** helio.tolentino@grenoble.cnrs.fr

MnPt alloy in the tetragonal chemically ordered ($L1_0$) phase is a well-suited antiferromagnetic (AFM) material for device applications. The robustness of the AFM order depends on chemical order and on thickness of the layers. We have shown

that the growth, by alternate thermal deposition in ultra-high vacuum, at room (RT) and elevated (300°C) temperatures yield different ordered structures. At RT, the ultra-thin layer (2.9 nm) is disorded and rough because the Pt growth proceeds through island formation. Subsequent annealing (500°C) smooths the surface but gives rise to a chemically ordered phase with the tetragonal c-axis mainly in the plane of the surface. On the other hand, at 300°C, Pt grows in a layer-by-layer mode, and so does Mn while being kept essentially at the surface with negligible diffusion into bulk. As consequence, by alternating Mn and Pt deposition, an ultra-thin layer (3.2 nm) is formed with the tetragonal c-axis perpendicular to the surface.

The $L1_0$ is formed by alternate atomic plans of Mn and Pt along the tetragonal c-axis. The a and c unit cell parameters of the MnPt alloy are 3.998 Å and 3.669 Å, respectively, i.e., about 2% larger and 7% smaller compared to the Pt lattice constant (3.924 Å). So, the Pt(001) substrate is expected to be a favorable candidate for the growth of the $L1_0$ phase with c-axis perpendicular to the film plane. Grazing incidence X-ray diffraction (GIXRD) was carried out to follow in situ the growth of ultra-thin PtMn layers on Pt(001) at BM32 beamline. The films were grown by alternate electron-beam deposition of Mn and Pt, to favor the perpendicular orientation.

Clean Pt(001) reconstructs to form a closed packed hexagonal monolayer on top of the bulk planes of square symmetry. The hexagonal surface plane is about 20% denser than the original square surface. The rocking scans about the (1.21 0 0.15) position reveal the peaks corresponding to the two equivalent rotated (0.744°) domains of the clean hexagonal reconstruction (Fig.1-a).

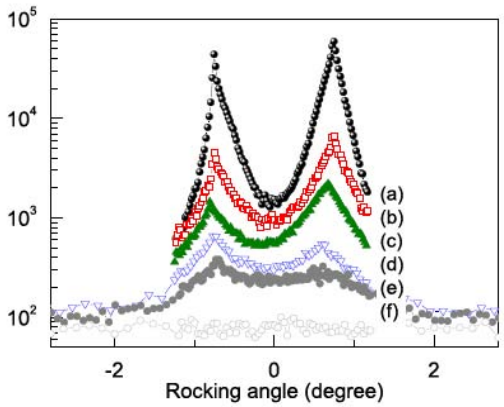

Fig.1: Rocking scans about the (1.211 0 0.15) position showing the two equivalent domains of the hexagonal reconstruction.

After RT deposition of 0.4ML of Mn the reconstruction is significantly attenuated (Fig.1-b). Mn atoms deconstruct more than 80% of the hexagonal layer. Simultaneously, faint c(2x2) peaks have been observed, indicating that Mn atoms react with the excess of Pt atoms to form a partially ordered MnPt-c(2x2) surface alloy.

The deposition of 1.2ML Mn in a fresh substrate yields a first surface layer with about 0.65ML of Mn and 0.35ML of Pt, which is a mixture of (ordered and/or disordered) MnPt alloy and pure Mn atoms, and a second surface layer with essentially the remaining Mn atoms. The deposition of 1ML Pt on top of that Mn/Pt(001) surface indicates an increased roughness. The hexagonal reconstruction was washed out (Fig.1-f). The model that best fits such a surface shows that Pt grows by island formation.

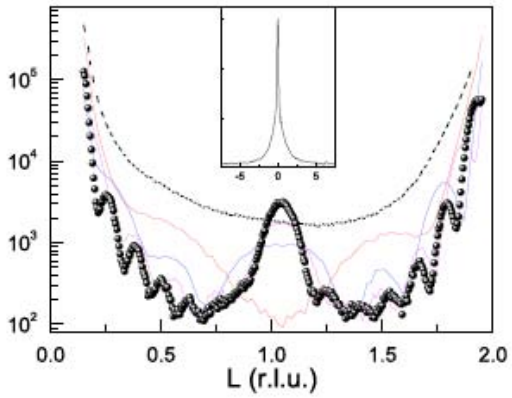

Fig.2: rods at 300°C: clean surface, 2, 4, 6, and 8 (closed circles) MnPt bilayers. Inset: rocking curve at (1 1 1.04) position.

After alternate RT-deposition of a few layers, the resulting ultra-thin PtMn layer is disordered and rough. Subsequent annealing (500°C) smooths the surface but gives rise to a (twinned) chemically ordered phase with the tetragonal c-axis mainly in the plane of the surface. On the other hand, on a substrate at 300°C, Pt grows layer-by-layer, while Mn has negligible diffusion into bulk. As consequence, an ultra-thin layer with the tetragonal c-axis perpendicular to the surface is formed (Fig.2).

Structure and magnetic properties of Mn/Pt(110)-(1×2): A joint x-ray diffraction and theoretical study

M. De Santis[1], Y. Gauthier[1], H. C. N. Tolentino[1], G. Bihlmayer[2], S. Blügel[2] and V. Langlais[1,3]. **1) Institut Néel, UPR 2940-CNRS, 25 Avenue des Martyrs, Boîte Postale 166, 38042 Grenoble, France ; 2) Institut für Festkörperforschung, Forschungszentrum, Jülich, D-52425 Jülich, Germany ; 3) Departament de Fisica, Universitat Autònoma de Barcelona, Bellaterra, 08193 Barcelona, Spain. Contact Maurizio.De-Santis@Grenoble.CNRS.Fr**

Mn shows a large magnetic moment in different metallic environments that motivated extensive studies of thin Mn films on metallic surfaces. We studied the growth of a Mn submonolayer on Pt(110)-(1×2) by surface x-ray diffraction. At room temperature, Mn fills in the empty rows of the clean substrate's missing row structure. Annealing a film of 0.5 ML (or depositing at a substrate temperature of about 570 K) a (2×1) surface alloy forms. It exhibits mixed dense rows where Pt and Mn sites alternate. The top layer is corrugated with Mn going outward. Annealing a 3-ML-thick Mn film, results in a Pt3Mn bulk-like slab. Theoretical calculations were performed, confirming that the (2x1) surface alloy is the low energy state, and showing that Mn atoms form antiferromagnetic chains running in the [001] direction. The ordering within the surface layer switches to ferromagnetic for a 5-ML-thick alloy film. The magnetic moment per Mn atom at the surface is close to 4 μ_B.

Mn is the species that has the largest magnetic moment, 3.64 μ_B, when forming Pt_3M alloys with $L1_2$ phase, where *M* is a 3d transition metal. Deposition of about half a monolayer of Mn onto Cu(100) Ni(100) Cu(110) and Ni(110) results in superstructures with *c*(2×2) symmetry. This is a class of two-dimensional magnetic alloys where Mn atoms occupy substitutional sites in the outermost layer with a checkerboard arrangement. These surface alloys are characterized by a large surface rippling, with Mn atoms shifted outward by 0.2–0.3 Å, which was related to magnetic properties of the surface.

We used surface x-ray diffraction to study the growth and the structure of the PtMn surface alloys obtained by deposition of Mn on Pt(110). This last surface exhibits a (1x2) missing row reconstruction, with a regular distribution of deep troughs. Such a structure is quite attractive to grow atomic chains of magnetic species, separated by metal dense rows.

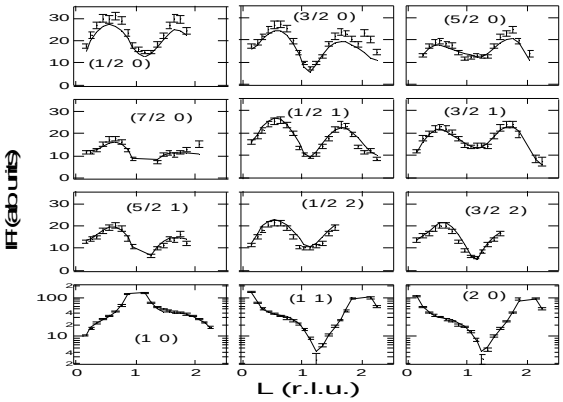

Fig. 1 Experimental structure factors and best fit for the Pt(110)-(2×1)Mn surface alloy obtained by annealing 0.5 ML of Mn deposited on Pt(110)-(1×2)

At room temperature, Mn fills in the empty rows of the substrate structure. For 0.5 ML, a (1x2) PtMn surface alloy is formed, with alternating pure Pt and pure Mn dense rows. Upon annealing, another surface alloy forms with (2×1) symmetry: as in a bulk Pt_3Mn(110) layer, Pt and Mn sites alternate along the dense rows. Fig. 1 shows the structure factors derived from the experiment together with the best fit obtained for the (2×1) surface alloy. Fig. 2 shows a sketch of the surface structure. The top layer of both surface alloys is corrugated, with Mn lying 0.19±0.03 Å and 0.16±0.02 Å above the Pt sites for the (1×2) and (2×1) phases, respectively. These periodicities are at variance with the Mn-Ni and Mn-Cu cases where *c*(2×2) arrangements are found. Annealing a thicker Mn film (3 ML) results in a surface alloy with $L1_2$ phase (similar to bulk Pt_3Mn).

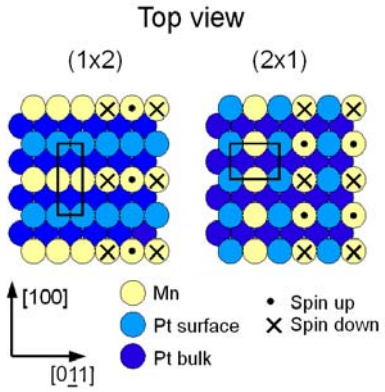

Fig. 2. Models for the Pt(110)-(1×2)Mn surface alloy (left panel) and Pt(110)-(2×1)Mn one (right). The surface unit cell is shown and the magnetic order is sketched with arrows pointing up and down. Note that the AF ordering doubles the surface unit cell.

DFT calculations performed in Julich show that the (1×2) alloy is metastable and forms antiferromagnetic (AF) Mn chains. The stable (2×1) 2-D alloy is also AF, but the coupling switches to ferromagnetic (F) at the surface of a thick Pt_3Mn(110) film albeit with a quite identical surface structure. In this last case we found that the F-ordered surface layer likes to couple AF to a F ordered bulk alloy below. The calculated magnetic moment per surface Mn atom is close to 4 μ_B in all cases. This value, one of the largest ever found in similar metal-Mn surface alloys, is directly related to the surface corrugation and to the Mn volume.

Publication M. De Santis et al. Phys. Rev. **B** 75 (2007) 205432

Review article on GISAXS

Over the last ten years, the local team has developed the technique of GISAXS applied to surfaces and nanostructures, *in situ*, during growth, as well as the quantitative analysis of GISAXS data. This work has been gathered, together with a review of most other (*ex situ*) GISAXS studies until 2008, in a Surface Science Report.

Surface Science Reports 64 (2009) 255–380

Contents lists available at ScienceDirect

Surface Science Reports

journal homepage: www.elsevier.com/locate/surfrep

Probing surface and interface morphology with Grazing Incidence Small Angle X-Ray Scattering

Gilles Renaud [a,*], Rémi Lazzari [b], Frédéric Leroy [c]

[a] Commissariat à l'Energie Atomique, Institut Nanosciences et Cryogénie, Service de Physique des Matériaux et Microstructures, Nanostructures et Rayonnement Synchrotron, 17 Avenue des Martyrs, F-38054 Grenoble, Cedex 9, France

[b] Institut des NanoSciences de Paris, Université Pierre et Marie Curie (Paris 6), CNRS UMR 7588, Campus Boucicaut, 140 Rue de Lourmel, 75015 Paris, France

[c] Centre Interdisciplinaire de Nanoscience de Marseille, CNRS - UPR 3118, Campus de Luminy Case 913, 13288 Marseille Cedex 9, France

ARTICLE INFO

Article history:
Accepted 12 July 2009
editor: G. Thornton

Keywords:
X-ray scattering
Grazing incidence
Synchrotron X-rays
GISAXS
Grazing Incidence Small Angle X-Ray Scattering
Distorted Wave Born Approximation
DWBA
Local Monodispersed Approximation
Decoupling Approximation
Size-Spacing Correlation Approximation
Scaling Approximation
Theory of X-ray scattering
Form factor
Interference function
Assemblies of nanoparticles
In situ
Nano-particles
Nano-structures
Growth modes
Growth laws
Molecular beam epitaxy
Ultra-high-vacuum
Catalysis
Semi-conductors
Metal surfaces
Reconstructions
Self- organized growth
Patterned substrates
Polymers
Metal on oxide surfaces
Quantum dots

ABSTRACT

Nanoscience and nanotechnology are tremendously increasing fields of research that aim at producing, characterizing and understanding nanoobjects and assemblies of nanoobjects. Their new physical or chemical properties, which arise from confinement effects, intimately depend on their morphological properties, *i.e.* their shapes, their sizes and their spatial organization. This calls for dedicated morphological characterization tools, among which is the Grazing Incidence Small Angle X-Ray Scattering (GISAXS). This reciprocal space technique has emerged in the last two decades as a powerful tool that allows investigating in a non-destructive way the morphological properties from one to billions of nanoparticles, either on a surface, or embedded in a matrix, with sizes ranging from 1 nm to several microns. The advantages of the technique are that it is non-destructive; it yields statistical information averaged on a large number of nanoparticles; it allows probing both the surface or deep below it, by changing the incident angle of the X-ray beam; it can be used in very different sample environments, in particular *in situ* in the course of a given process such as growth, annealing, gas exposure; and it may be given chemical sensitivity by use of anomalous scattering.

This report presents a review of the GISAXS technique, from experimental issues to the theories underlying the data analysis, with a wealth of examples. The physical morphological information contained in GISAXS data and its analysis are presented in simple terms, introducing the notions of particle form factor and interference function, together with the different cases encountered according to the size/shape dispersion. The theoretical background of X-ray diffuse scattering under grazing incidence is presented in a general way, and then applied to the particular case of grazing incidence small angle X-ray scattering from assemblies of particles either on a substrate, or buried below it.

Most of the GISAXS measurements published to date are reported, covering the fields of *ex situ* studies of embedded metallic nanoparticles, granular multilayered systems, implanted systems, embedded or stacked or deposited semi-conductor nanostructures, porous materials and copolymer thin films. A special emphasis is brought on *in situ* experiments, performed either in ultra-high vacuum during nanoparticle growth by molecular beam epitaxy, or in gas-reactors during catalytic reactions. This covers a very broad field, from (i) the 3D island (Volmer–Weber) growth of metals on oxides surfaces to (ii) the organized growth of metals on surfaces that are nanopatterned either by surface reconstruction or by underlying dislocation networks or by deposit-induced nanofacetting, to (iii) the *in situ* investigation of the self-organized Stranski–Krastanow hetero-epitaxial growth of semi-conductor quantum dots on semi-conductor surfaces, or (iv) the *in situ* surface nanopatterning by ion bombardment. Many examples are discussed in detail, to illustrate the large diversity of systems and morphologies that can be addressed as well as the different analysis issues and the conclusions of the technique in terms of growth mode.

In situ synchrotron radiation studies of the structure, composition and morphology of nanoparticles during their growth

T.U. Schülli, G. Renaud, M.-I. Richard, **CEA-Grenoble, Institut Nanosciences et Cryogénie, SP2M/NRS, 17 rue des Martyrs, 38054 Grenoble Cedex 9. Contact gilles.renaud@cea.fr**

The physical properties of nanoparticles are intimately linked to their internal structure, shape, size and assembly, which themselves depend on the elaboration conditions. We have developed at the ESRF, on the French "Interface" beamline, a setup that uses the very bright synchrotron X-ray beam to analyze the structural properties of surfaces, interfaces, thin films and nanoparticles *in situ*, during elaboration, annealing or exposition to gases, thus allowing to investigate the laws governing their growth. After a decade devoted to metals and oxides, we have moved to semiconductors, with emphasis on the growth of germanium on silicon, in the form of islands or nanowires.

The endstation consists of a MBE chamber with up to six sources and usual surface science characterization tools, coupled to a diffractometer allowing for grazing incidence X-ray diffraction (GIXD), small angle scattering (GISAXS) and anomalous scattering (GI-MAD), probing respectively the atomic ordering, the shape and size at the nanometer scale and the composition of (nano-)systems.

The growth of Ge on Si(001) is a model system for the Stranski Krastanow growth mode that governs semiconductor (SC) heteroepitaxy: a few deposited layers of Ge form a flat and fully strained "wetting layer", before nucleation of fairly strained pyramids with very grazing ({105}) facets (Fig. 1). These transform into larger domes exposing additional shallower facets (e.g. {113}), before transforming into incoherent islands, relaxed by defects. Our *in situ* X-ray measurements during growth, allow for a wide variation of kinetic conditions, thus bringing some insights on the laws governing the growth. We have shown that, under certain conditions, one equivalent atomic layer is transported from the wetting layer into the domes during the pyramid to dome transition. In addition, the pyramids were found richer in silicon than domes, which explains why domes nucleating on pyramids have a higher Si composition close to their bottom center. We have also shown (Fig. 2) that domes grown on nominal and patterned Si(001) surfaces have very similar composition (Fig. 3), but largely different relaxation; the former being more strained. A combination with simulations allowed determining the complete 3D strain and composition fields inside both kinds of islands. The richer Ge composition at the bottom of organized islands is explained by the flow of Ge inside the pits of the patterned substrate, as evidenced by *in situ* GISAXS measurements. The growth laws have also been investigated during the dome to super dome transition as well as in the super-dome regime, showing self-similar growth.

The *in situ* station is also opened to external users; mostly working in close collaboration with us. Among the many successful results, we may cite the study of shape changes of metal nanoparticles during oxidation and reduction, recently published in Science.

Fig. 1 Typical GISAXS images from Ge pyramids (left) and

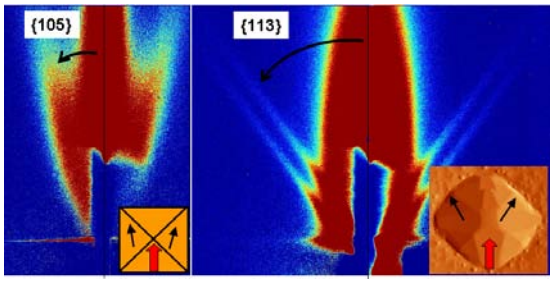

domes (right) on Si(001). The nanoparticle facets yield rods of scattering, which allows indexing the facets.

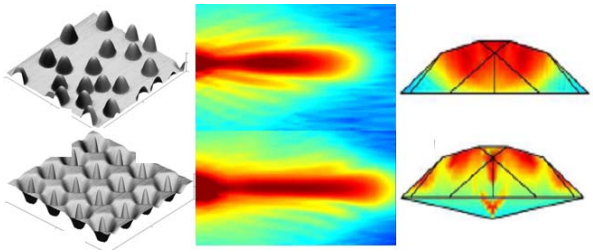

Fig. 2 Left: AFM of Ge domes grown under identical condition on nominal (top) and patterned (bottom) Si(001) surfaces. Middle: Map of the reciprocal space around their (400) Bragg peak. Right: Cross section of the composition profile as deduced by a combined experiment-simulation procedure.

Fig.3: Composition of islands grown on nominal and patterned surfaces as a function of radial position.

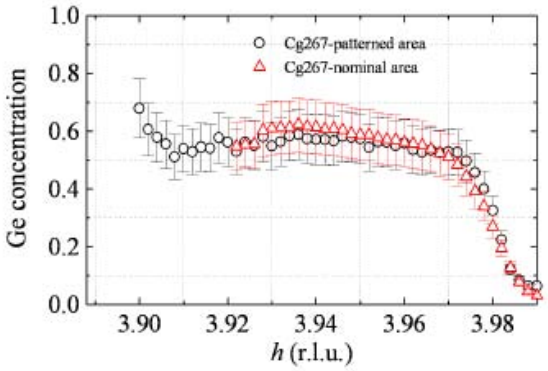

Selected publication(s) G. Renaud et al. Surf. Sci. Rep. **64**, 255-380 (2009), T.U. Schülli, Appl. Phys. Lett. **89** (2006) 143114;T.U. Schülli et al. Phys. Rev. Lett. **102** (2009) 025502; M.-I. Richard, Appl. Phys. Lett. **94** (2009) 013112; P. Nolte et al. Science **321** (2008) 1654

Grant(s) : RTRA 2008, plateformes + nano-caract.

Collaboration(s): Linz University, Austria; Charles University, Prague; ESRF, France; University of Milano, Italy.

Patent(s) :

Contact :gilles.renaud@cea.fr

Substrate enhanced supercooling in AuSi eutectic droplets

R. Daudin, G. Renaud, T.U. Schülli CEA-Grenoble, Institut Nanosciences et Cryogénie, SP2M/NRS

Supercooling in metals i.e. the preservation of a disordered, fluid phase in a metastable state well below the melting point has led to speculations that local atomic structure configurations of dense, symmetric, but non-periodic packing act as the main barrier for crystal nucleation. For liquids in contact with solids, crystalline surfaces induce layering of the adjacent atoms in the liquid and may prevent or lower supercooling. This seed effect is supposed to depend on the local lateral order adopted in the last atomic layers of the liquid in contact with the crystal. Although it has been suggested that there might be a direct coupling between surface induced lateral order and supercooling, no experimental observation of such lateral ordering at interfaces is available. We present evidence for surface and interface induced supercooling of nanometric gold-silicon (AuSi) eutectic droplets laying on a silicon substrate, which stay liquid far below the bulk eutectic solidification temperature (TE=360ºC)

In situ x-ray scattering measurements show that the silicon surface orientation and structure strongly influences the degree of supercooling, its maximum being observed on a gold-induced Si(111)-(6×6) surface reconstruction presenting gold atoms in pentagonal arrangement onto which solidification is observed at 230 ºC**.** Semiconductor (SM) nanowires (NWs), identified as important components for future electronic nanodevices, are produced via the vapour-liquid-solid mechanism in which a supersaturated drop of liquid metal-SC eutectic leads to a catalytic precipitation of the semiconductor. We intensely investigated deposits of Au on Si substrates witch is one of the most used metal-semiconductor eutectic ($Au_{81}Si_{19}$) catalyst for the growth of Si NWs. Seven atomic layers of gold are deposited at room temperature (RT) on an Si(111) substrate witch was previously dioxide (Fig.1).

At RT, the Au film crystalline quality was found to be low but showed a clear preferential epitaxy with identical directions of the two cubic lattices: [110]Au(111)||[110]Si(111). When heating up to 350°C (below the eutectic temperature T_e=363°C) the Au film de-wets to form crystalline islands with a preferential in-plane epitaxy rotated by 19.2° with respect to the aligned epitaxy (i.e. [110]Au(111)||[231]Si(111)). This epitaxial change comes from a difference in thermal expansion between the two materials that lower or increase the mismatch values between Au and Si atoms in coincident sites depending on the involved atomic row. The islands are observed to melt exactly when the temperature is increased to T_e.

From this point we have paid particular attention on the solidification behaviour of these AuSi droplets. *In situ* x-ray scattering measurements show that the silicon surface orientation and structure strongly influences the degree of supercooling (Fig.2). Its minimum is observed on a Si(001) substrate. Depending on thermals treatments, Si(111) substrates present gold-induced either Si(111)-(√3x√3) or Si(111)-(6x6) reconstructions. The maximum degree of supercooling is observed on the latter presenting gold atoms in pentagonal arrangement onto which solidification is observed at 230ºC. *Ab initio* molecular dynamics simulations confirm the possibility of supercooling in a confined $Au_{81}Si_{19}$ alloy, revealing in addition a large proportion of local icosahedral order with a five-fold local ordering similar to that of the reconstructed surface. This reveals that pentagonal atomic arrangements of Au atoms at this interface favour a lateral-ordering stabilization process of the liquid phase (Fig. 3).

This interface-enhanced stabilization of the liquid state proves the importance of solid–liquid interaction on the structure of the adjacent liquid layers as well as for the stability of liquids under confined conditions.

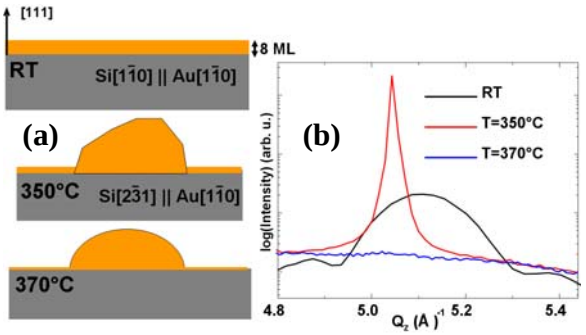

Fig.1: Growth of Au-Si eutectic catalysts (a), the black curve in (b) shows size oscillations corresponding to its thickness. Annealing at 350°C leads to islands (red curve in (b)). At 370°C the island transforms into a $Au_{82}Si_{18}$ liquid droplet.

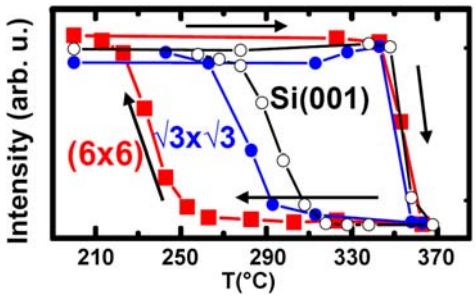

Fig. 2: Hysteresis loops of the integrated intensity of the Au(220) Bragg peak during the solid-liquid-solid transition on Si(001) (black open circles), on a Si(111)-(√3×√3)R30° reconstruction (blue disks) and on a Si(111)-(6×6) reconstruction (red squares).

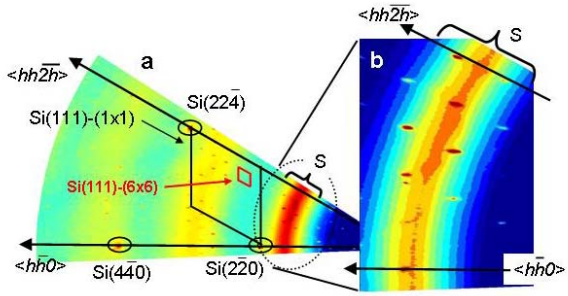

Fig. 3: (a): Reciprocal space map of the liquid in its supercooled state on a (6×6) reconstructed Si(111) surface
(b): First order maximum of the liquid structure factor in the vicinity of strong (6×6) reconstruction peaks.

Selected publication(s) T.U. Schülli, R. Daudin, G. Renaud et al., Nature (2010) accepted.	
Grant(s) : RTRA 2008, plateformes + nano-caract.	Collaboration(s): A. Pasturel, CNRS-SIMAP

In situ composition and strain of Ge islands on Si(001) during growth by grazing-incidence multiwavelength anomalous diffraction

M.-I. Richard, T.U. Schülli, G. Renaud, V. Favre-Nicolin, **CEA-Grenoble, Institut Nanosciences et Cryogénie, SP2M/NRS, 17 rue des Martyrs, 38054 Grenoble Cedex 9. Contact gilles.renaud@cea.fr**

Grazing-incidence multiwavelength anomalous diffraction is employed *in situ*, during growth, to quantitatively determine the average Ge composition of Ge/Si(001) islands, coherent pyramids and domes and incoherent superdomes at different growth temperatures and for different Ge fluxes. The average Ge composition of the different islands slightly evolves during growth suggesting that the composition is strongly correlated to surface morphology.

Growth of semiconductor islands has been studied in great detail on a variety of heteroepitaxial systems. During growth, the deposited material mixes with the substrate material, leading to the formation of alloyed nanocrystals. Intermixing leads to a reduction of misfit strain between epilayer and substrate. The mechanisms leading to intermixing and their dependence on the growth conditions have been thoroughly studied in recent years, especially for the SiGe/Si model system. Pure bulk diffusion (i.e. atomic motion events in regions that are far from the surface) can be considered as practically absent due to its high potential barriers. Sub-surface processes can be relevant as the strain stored during the growth of Ge on Si substrates could significantly increase the atomic mobility in the sub-surface region. The general picture emerging from these studies is that surface diffusion (i.e. migration of Si and Ge adatoms at the surface) must be regarded as the most active process as diffusion events are faster than bulk and sub-surface processes.

The samples studied here were grown by molecular beam epitaxy (MBE) in the dedicated ultra-high vacuum chamber on the BM32 synchrotron beamline. Germanium was deposited with a ~0.0048 ML/s growth rate. Height Ge monolayers (MLs) were deposited monolayer after monolayer at two growth temperatures, 500°C and 650°C, respectively. After growth, the surface morphology of the grown samples was investigated by means of atomic force microscopy (AFM) in tapping mode. The AFM analysis (Figure 1) of the grown samples reveals the coexistence of pyramids (Ps), domes (Ds) and superdomes (SDs) at the end of the growth.

During growth, the islands were characterized by grazing incidence x-ray diffraction measurements which were performed mostly along the <h0l>, h being variable and l being small: l=0.04 with finer measurements in the vicinity of the Si(400) and Ge(400) Bragg peaks (Fig. 2). These radial scans, which are sensitive to the strain relaxation of the islands, were recorded *in situ* for each added monolayer from the very first stages up to the nucleation of dislocated islands at T=500°C (Fig. 2a) and T=650°C (Fig. 2b). First, small pyramids were formed. Then, the introduction of dislocations led to a more complete relaxation: coherent islands such as domes or barns are much more strained by the Si substrate. All the peaks have been indexed by the letters P, D and SD in Fig. 2. Their indexation is consistent with the AFM images at the end of the growth and also with finite element simulations. Further analysis was made possible by distinguishing the Ge and Si contributions during the growth process, using grazing-incidence multiwavelength anomalous diffraction (GI-MAD). This allows to determine how the Ge composition evolves inside pyramids, domes and superdomes during their growth. The Ge composition is given by the percentage in Fig. 2. The average Ge composition inside pyramids may be underestimated by GI-MAD results as expanded regions of the Si substrate due to island growth can possibly contribute in the scattering regions of strained pyramids. A correlation between surface morphology and composition has been observed leading to less intermixing inside dislocated superdomes. During growth, the average Ge content of the different island shapes slightly evolves.

In conclusion, we have presented a technique to quantitatively determine the average composition inside different scattering regions of self-assembled nano-islands during their in situ growth.

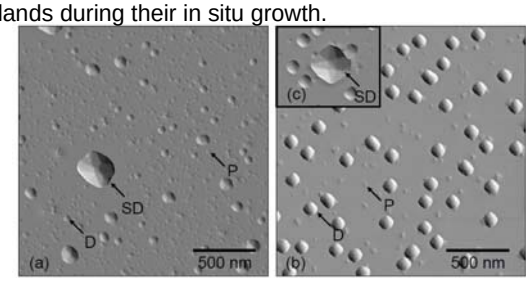

Fig. 1 AFM images of samples grown (a) at 500°C and (b) 650°C. (c) The insert in Fig. 1b shows a 200 nm wide superdome observed on the sample grown at 650°C.

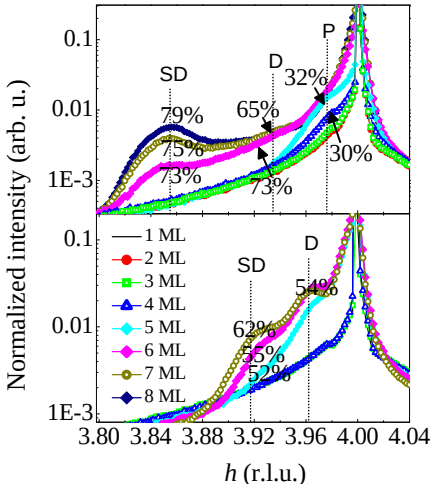

Fig. 2 Radial scans around the (400) Si Bragg reflection at an energy of 11.043 keV for samples grown with growth interruptions in-between deposited monolayers with a slow growth rate (a) at T=500°C and (b) at T=650°C. The numbers correspond to the Ge content associated to the different reciprocal space units, h.

Selected publication(s) M.-I. Richard, T.U. Schülli, G. Renaud, V. Favre-Nicolin, G. Bauer, to be submitted	
Grant(s) :	Collaboration(s): Linz University, Austria
Patent(s) :	Contact : gilles.renaud@cea.fr

In situ x-ray investigation of Ge islands on pit patterned Si substrates

M.-I. Richard, T.U. Schülli, G. Renaud, **CEA-Grenoble, Institut Nanosciences et Cryogénie, SP2M/NRS, 17 rue des Martyrs, 38054 Grenoble Cedex 9. Contact gilles.renaud@cea.fr**

A challenge for the development of nano-electronics is to elaborate semiconductor quantum dots (QDs) that are homogeneous in shape, size, strain and composition, thus resulting in well-defined electronic and optical properties. This is obtained by *e.g.* the growth of Ge islands on lithographically prepatterned Si(001) substrates in the form of ordered pits. These ordered Ge islands are investigated *in situ* during growth by a combination of Grazing Incidence Small Angle X-ray Scattering (GISAXS) and X-ray Diffraction (GIXD) measurements. These provide the organization of the Ge QDs, their strain, size and shape.

The growth of ordered Ge islands on lithographically prepatterned Si(001) substrates has been intensively studied by *ex situ* techniques like AFM (for instance Ref. [1]), STM and *ex situ* x-rays. As these techniques do not allow to determine the chemical composition and the variation of relaxation prior to and during island formation, *in situ* x-ray scattering during growth appears to be very well adapted and capital to understand and investigate the whole dynamic growth process. To answer to these questions, two x-ray techniques, GISAXS and GIXD were combined to follow the *in situ* growth of ordered Ge islands on a Si(001) prepatterned substrate.

The pit patterns of the substrate are two dimensionnally ordered with a periodicity of ~400nm. After an *ex situ* chemical cleaning process, including a final HF dip, and an *in situ* thermal treatment at ~725°C under UHV conditions, a 60-nm-thick Si buffer layer was grown on the Si substrate while ramping the substrate temperature from 420°C to 650°C. This growth procedure eliminates the surface roughness. The surface quality was characterized with GIXD and reflection of high energy electron diffraction (RHEED), showing a Si 2x1 reconstructed surface. Then, 7 monolayers (ML) of Ge were deposited at 650°C by molecular beam epitaxy.

Figure 1 summarizes the growth process. During the very first stages of Ge growth (θ < 4ML: growth of the pseudomorphic wetting layer), the preliminary facets of the Si substrate are energetically unfavourable, and the pit facets break up into a rather complex pattern of {10n} and {11m} facets with n>7 and m>11. With increasing deposit, the angles of the facetted pits relative to the (001) plane decrease. The variation of the sidewalls inclination shows that Ge atoms preferentially fill the etched pits. Between 4 and 5 deposited ML, diffuse scattering appears around the Si(220) Bragg peak revealing the nucleation of 3D islands. These results show that GIXD is very sensitive to the onset of islands nucleation by detecting the very first stages of relaxation of the crystal lattice. At 5 ML, rods of scattering by {105}-type facets appear in the GISAXS image revealing the formation of pyramids. After 5ML, intense periodic rods arising from the ordered Ge QDs are evidenced by GISAXS and an increase of the relaxation state is observed by GIXD. Then, after a deposit of 6ML, {113} and {15 3 23} facets are found. There is also an increase of the diffuse scattering around *h*=2 which broadens the Si Bragg peak. This is linked to the formation of large domes of mixed composition, Ge_xSi_{1-x}, which strongly distort the Si substrate below them, leading to the Si substrate deformation signal. At this pyramid to dome transition, an increase of the Ge content (from 40 to 50%) inside the islands is observed by anomalous GIXD. At the end of the growth (*i.e*: after a deposit of 7 ML of Ge), no superdomes are formed. As previously observed [2], larger coherent islands can be grown on the patterned substrates as compared to island growth on at substrates.

A possible explanation of the localization of islands at the pit bottom is the asymmetrical migration of adatoms over steps of the sidewalls of patterned pits. Provided that the sidewalls of patterned structures are composed of steps and the activation barrier for adatoms migrating downwards over step is smaller than upwards, a net flux of adatoms at the sidewalls can be formed [2].

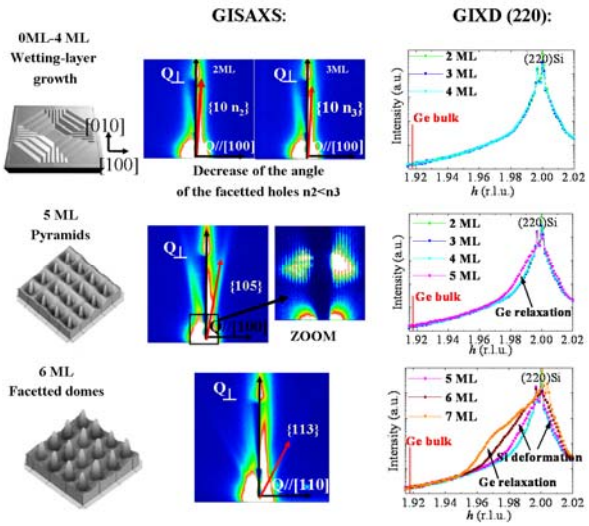

Fig. 1 Summary of the growth. The left part of the figure shows drawings of the sample. In the middle, GISAXS images can be observed along the <100> and <110> azimuths. The right part of the figure shows GIXD scans recorded during the growth.

In conclusion, the combination of GISAXS and GIXD provides detailed results on the evolution of the shape, the strain and the degree of atomic ordering of Ge islands during the whole growth process. It is demonstrated to be a useful, destruction-free tool to understand and control the self-organized growth of nanostructures.

Selected publication(s) [1] G. Chen, et al., Cond. Mat. 0602175 (2006) ; [2] Z. Zhong, et al., Physica E 23, 243-347 (2004).

Grant(s) :

Collaboration(s): Linz University, Austria

Patent(s) : style Cartouche

Contact : gilles.renaud@cea.fr

Organized growth of Ge quantum dots on a nano-patterned Si(001) surface obtained by direct wafer bounding followed by chemical etching: An in situ X-ray study

M.-I. Richard, G. Renaud, T.U. Schülli, A. Pascale, J. Eymery, **CEA-Grenoble, Institut Nanosciences et Cryogénie, SP2M/NRS, 17 rue des Martyrs, 38054 Grenoble Cedex 9.** *A. Bavard, F. Fournel,* **CEA-Leti, 17 rue des Martyrs, 38054 Grenoble Cedex 9. Contact gilles.renaud@cea.fr**

The simultaneous control of the localization, density and size uniformity of epitaxial nanostructures is a key parameter for future nanoelectronics devices. To fulfil these requirements, Si(001) substrates with a periodic nanometre scale patterning have been developed using wafer bounding and preferential chemical etching techniques. The combination of Grazing Incidence Small Angle X-ray Scattering (GISAXS), X-ray Diffraction (GIXD) and Anomalous Scattering performed *in situ*, during growth in an Ultra High Vacuum chamber, allows for the characterization of the Ge QDs regarding their shape and organization (GISAXS) as well as their strain and composition (GIXD).

The Si template is obtained by combining the Smart Cut®[1] technology [1], wafer bounding and chemical etching of the surface. As the dislocation network is at the interface of the two bonded wafers it is necessary to perform a preferential etching to transfer the dislocation network symmetry (and period) to the surface [2]. The samples studied presented a square 20nm surface-patterning of periodic mesa separated 3 to 4 nm deep trenches.

After a chemical cleaning process, including a final HF dip, and thermal treatment in UHV at ~650°C, a 2.5-nm-thick Si buffer layer was first grown on the surface at 650°C. The surface quality was characterized with GIXD and reflection of high energy electron diffraction (RHEED). GIXD allowed determining whether the Si bonded layer is removed by the chemical etching. For an increase of the etching time (depth), the disappearance of Bragg peak of the bounded layer and of the diffraction satellites by the dislocation network proves that the bonded layer is completely removed. This leaves a perfectly patterned Si(001) surface, which, however, is still periodically strain modulated.

Six monolayers (ML) of Ge were then deposited at 500°C by molecular beam epitaxy. The deposition was followed *in situ* by X-rays, monolayer by monolayer. GISAXS measurements provide the detailed evolution of the morphology such as the faceted pits and shape of the grown QDs and allow characterizing the degree of ordering between islands, at the nm to µm scale [3]. GIXD adds information on the island nucleation after the beginning of lattice relaxation and the evolution of the in-plane size, epitaxial orientation and strain of the Ge QDs during growth. In addition, for each added ML, the Ge content inside the islands was determined using the grazing incidence MAD (Multiwavelength Anomalous Diffraction) [4] method.

The 20 nm surface-patterning was not homogeneous over the whole surface. Scanning Electron Microscopy and Atomic Force Microscopy show that the patterned areas are localized on stripes with a width of typically 300nm (see Fig. 1). Two contributions are then found by X-rays one induced by the organized growth of Ge nanoparticles on the stripes and one corresponding to growth on a standard, non-patterned Si(001) surface. Nevertheless, the organization of Ge QDs on the well-etched parts of the surface is confirmed by GISAXS, as intense periodic rods arising from the ordered Ge QDs are evidenced by (anomalous) GISAXS (see Fig 2). The form factor of the mesa (trench depth, residual roughness, facets…) is found to have a strong influence on the quantum dots shape and position, and especially to define the dots registry with the underlying substrate. In these samples, it appears that the trenches depth acts as an effective diffusion barrier to prevent large islands coalescence and intermixing between the dots and the substrate.

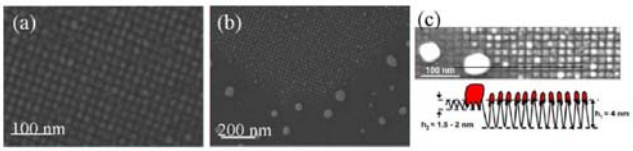

Fig. 1 (a)-(b)-(c) SEM images obtained after the growth of 6 ML of Ge at 500°C on the 20 nm twisted substrate and schematic drawing of the surface

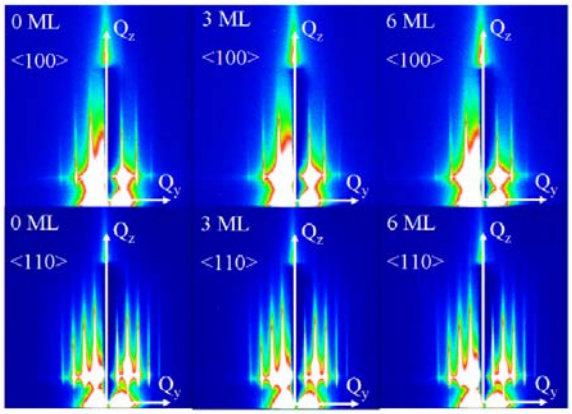

Fig. 2 GISAXS intensity maps along the <100> and <110> azimuths obtained at a growth temperature of 773 K for the 50 nm patterned template. The numbers denote the Ge thickness in ML.

This study gives a clear indication of the potential of this new substrate for the self-organization of nanostructures. It demonstrates that Ge islands are organized on well etched surfaces and that grazing incident X-rays scattering is a useful, destruction-free tool to understand and control the organized growth of nanostructures on substrates that are patterned at the nanometer scale.

References: [1] M. Bruel, Electron. Lett. 31, 1201 (1995) [2]. F. Leroy, J. Eymery, P. Gentile, and F. Fournel, Surf. Sci. 545, 211-219 (2003) [3] G. Renaud et al, Science 300, 1416 (2003).[4] A. Letoublon, V. Fabre-Nicolin, H. Renevier, et al, Phys. Rev. Lett. 92, 186101 (2004)

[1] Trade Mark of Soitec S.A.

In-depth atomic structure and composition of the 2×*N* reconstruction of the 1 to 3 monolayer Ge wetting layer on Si(001) by surface x-ray diffraction

T. Zhou, J. Issartel, G. Renaud, C. Revenant, T.U. Schülli, **CEA-Grenoble, Institut Nanosciences et Cryogénie, SP2M/NRS, 17 rue des Martyrs, 38054 Grenoble Cedex 9.**

The Ge/Si(001) islands have been extensively studied because of their novel electronic and optical properties related to quantum confinement. Apart from its relevance to applications, the heteroepitaxy of Ge on Si has become a prototype system for the investigation of the Stranski-Krastanow growth mode. Island nucleation, ripening, facet evolution, and alloying of islands have been studied in great detail. Many of the underlying mechanisms are now reasonably understood. Despite the fact that the growth of the Ge islands is intimately linked to the structure and composition of the wetting layer (WL), less attention has been devoted to its properties. The nucleation process of the islands on the WL cannot just be described by the capture of newly deposited Ge atoms, since it also involves a diffusive interaction with the SiGe WL. At elevated growth temperatures around 600°C, a substantial amount of material is transferred from the WL to the islands during the initial stages of island formation. Thus, a quantitative determination of the WL composition profile is essential for a detailed understanding of island formation and intermixing.

The atomic structure of the 2×*N* reconstruction of the Ge/Si(001) wetting layer was investigated by *in situ* surface x-ray diffraction (Fig. 1). Ge was deposited by Molecular Beam Epitaxy in ultrahigh vacuum at 670°C. The *N* periodicity of the reconstruction decreases from 11.5 to 8 as the Ge deposition increases from 1 to 3 monolayers (ML). The best fit structure (Fig. 2) clearly indicates the presence of asymmetric dimers with a dimer bond length in the range of 2.50-2.60 Å and a buckling angle in the range of 9.4-15.6° depending on the Ge coverage. The obtained dimer bond lengths correspond to those calculated for alternating asymmetric dimers. In addition, intermixing down to the sixth (resp. eighth) layer has been found for the 2 (resp. 3) Ge ML coverage. For a 2 Ge ML coverage, the atomic structure and the Ge occupation probability for the 2×9 reconstruction have been determined (Fig. 3). Moreover, experimental evidence for the site selectivity of Si-Ge intermixing is provided.

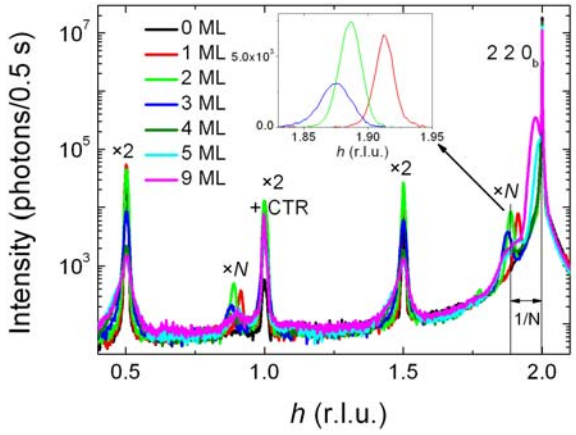

Fig. 1 Measured intensity (logarithmic units) on BM32 during radial scans along the (hh0)b direction for clean Si and different deposited Ge ML indicated in the graph. The separation between the ×N rod and the (220)b peak, for example, is equal to 1/N. Note that the ×N reconstruction peaks are much wider and less intense than those of the ×2 reconstruction. Inset: Background-subtracted ×N rods for 1, 2, and 3 Ge ML

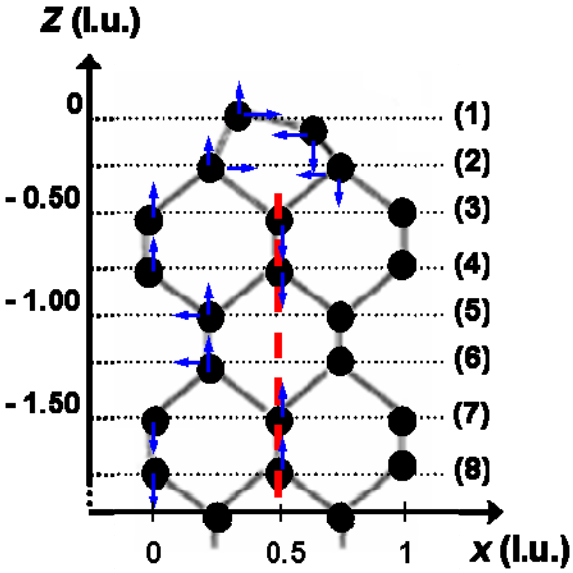

Fig. 2 . Schematic diagram of the atomic position in the eight layers included in the calculations. The arrows indicate the atomic displacements from their bulk positions (not to scale). The dashed line represents the symmetry axis

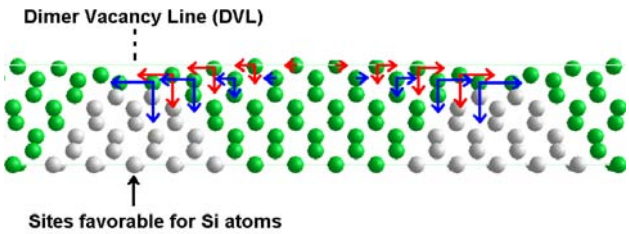

Fig. 3 . Schematic of the atomic structure of the 2×9 reconstruction. The red (resp. blue) arrows indicate the displacements of the atoms in the layer (1) (resp. [2]). Lattice sites which are under tensile strain and thus richer in Ge atoms are marked with green disks. Sites under compression and thus richer in Si atoms are marked with white/grey disks.

Selected publication(s) T. Zhou, J. Issartel, G. Renaud, C. Revenant, T.U. Schülli et al., to be submitted to Phys. Rev. B	
Grant(s) :	Collaboration(s):
Patent(s) :	Contact : gilles.renaud@cea.fr

In situ synchrotron radiation investigation of catalytic growth of confined silicon nanowires using grazing incidence methods

D. Buttard, T. David, T.U. Schülli**, P. Gentile, F. Oehler* **CEA-Grenoble, Institut Nanosciences et Cryogénie, SP2M/SINAPS, 17 rue des Martyrs, 38054 Grenoble Cedex 9. Contact denis.buttard@cea.fr, *also at University J. Fourier-Grenoble, ** CEA-Grenoble/INAC/SP2M/NRS**

In many physics fields today, there is a growing need for smaller and smaller structures. One may think of microelectronics but biology, optics, or even mechanics are hardly outdone. Nanowires (NWs) grown by Vapor-Liquid-Solid (VLS) process are of excellent crystalline quality and offer many possible applications. Silicon as a candidate for NWs is extremely well-known as a bulk material. The first obvious use would be in microelectronics but these nanowires could also be extremely interesting in the field of sensors or in high efficiency photovoltaic. In order to use these basic structures, we need to understand their structural properties.

Confined growth of catalytic silicon nanowires (SiNW) have been elaborated and investigated. The aim of these studies is to investigate the morpholgy of the nanoporous alumina template as well as the morphology of SiNW.

We have performed GISAXS observations of nanoporous alumina (Fig. 1). GISAXS image reveal periodic scattering coming from a hexagonal distribution of cylindrical pores. From a cross section (right), we measure the distance between two adjacent pores (inter fringe) and the size of the domain (width of one peak). We can also estimate the pore diameter with the form factor which envelops this function. Typically, we estimate the following values: pore diameter ≈ 80 nm, cell size ≈ 93nm, and domain size ≈ 2.5µm. The influence of the temperature has also been investigated and an amorphous/crystalline transition of alumina has been measured around T = 840°C.

The SiNW investigation was then undertaken. As the specific surface of nanowires is very high, surface effects are very important and the study under INS conditions is essential. Our *in-situ* measurements using Grazing Incidence X ray Diffraction (GIXD) on SiNW on a silicon substrate reveal that SiNW are in epitaxy with the silicon substrate (Fig. 2). On this map, we also see six scattering rods produced by vertical facets, providing evidence of hexagonal cross-section of wires. Sometimes wires have been found with a dodecagonal cross-section. The vertical structure of these facets has been investigated by Grazing Incidence Small Angle X ray Scattering (GISAXS) (Fig. 3). Our measurements evidence the presence of an additional complex saw-tooth faceting on the principal hexagonal facets. We observe several tilted rods on the left and right of the image produced by supplementary facets on the principal facets. This saw-tooth faceting appears with alternating upward and downward orientations on each side of the nanowires, showing the trigonal symmetry of Si nanowires.

Recently we have investigated an assembly of SiNW with a constant diameter (Fig. 4). From GISAXS measurements, we observe periodic interferences fringes produced by the cylindrical wires. From the analysis of these oscillations we measure morphological parameters of the wires (diameter…).

These studies are crucial to improve the knowledge of silicon nanowires and their interactions with the nanochannels of alumina template during the growth. Particularly it will be necessary to investigate the influence of catalyst, temperature, diameter… Others experiments will be useful in a next future.

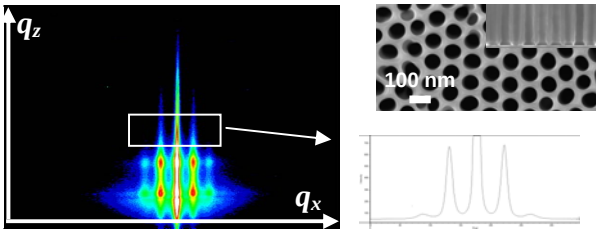

Fig. 1 Typical GISAXS image from Nanoporous alumina with hexagonal cell. The periodic scattering is related to the cell size.

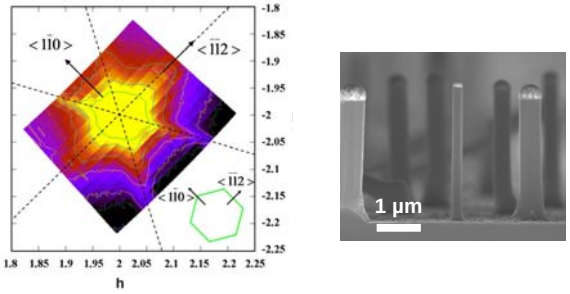

Fig. 2 GIXD map around $(2\bar{2}0)$ peak of Si from epitaxial wires. The six scattering rods evidence the hexagonal section of SiNW

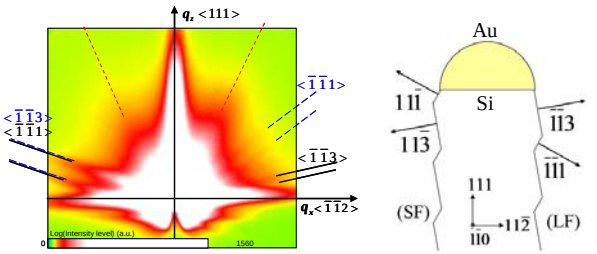

Fig. 3 GISAXS image from SiNW with complex fine saw tooth faceting with the trigonal geometry (schematically shown on right).

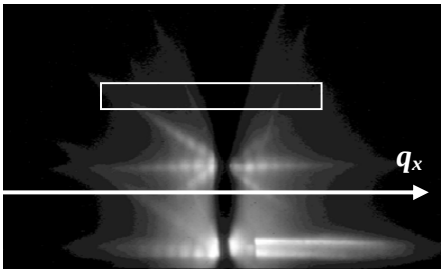

Fig. 4 GISAXS image from an assembly of SiNW with monodisperse diameter (D = 100 nm). The constant diameter leads to the visible periodic oscillations.

Selected publication(s) T. David, et al., Surface Science **602** 2675 (2008); D. Buttard et al., Phys. stat. sol. (a) **205**, 1606 (2008); D. Buttard, et al. Phys. Stat. Sol. (a), RRL **3** 19 (2009).	
Grant(s) : Technical platforms (PTA,…)	Collaboration(s): LTM CNRS (France), Institut Néel CNRS, (France), ESRF (France)
Patent(s) : D. Buttard, 06/01924 (INPI) PCT/FR2007/000211 (PCT	Contact : denis.buttard@cea.fr

Crystallographic orientation relationships between UO_2 and U_3O_7

H. Palancher[(1)], J.-S. Micha[(2)], A. Richard[(1)], L. Desgranges[(1)], Ph. Goudeau[(3)]

Laue micro-diffraction has been shown to be an extremely well suited technique for characterizing the strains at the UO_2 sample surfaces (single or polycristal). After having analyzed the case of oxidation (which is detailed in the following), a large range of studies concerning the influence of heavy ion implantation has been undertaken. Analysis of the results is undergoing. However the lack of depth resolution of Laue diffraction appears in this field as a limitation since the depth of the strained layer is difficult to determine. To overcome this issue, first tests to implement the DAXM (differential aperture X-ray microscopy) technique on BM32 will be performed.

The oxidation of uranium dioxide is a key process involved at least in two important steps of nuclear industry: fuel fabrication and safety of spent fuel dry storage. Oxidation induces cracking and spalling of the initial UO_2 material, which allows the recycling of fresh defective fuel, but which might also lead to rod cracking in case of defective fuel in dry storage conditions.

It has been shown that during the first stage of the oxidation in the air at 300°C, a U_3O_7 (tetragonal, a=b=5.38Å c= 5.55Å) thin layer grows on the surface of a UO_2 (cubic, a=5.47Å) sample. In literature orientation relationships between UO_2 and the oxidised layer have already been proposed but the existence of topotaxy at the UO_2-U_3O_7 interface, at which cracking occurs, still needs to be determined.

For that purpose, a (111) UO_2 single crystal has been oxidised in the air during 1.5 hours thus leading to the growth of an about 100nm thick U_3O_7 layer. High resolution laboratory XRD investigations failed in elucidating the orientation relationships between UO_2 and U_3O_7 mainly because of the broad U_3O_7 peaks.

To overcome this difficulty, the oxidised surface has been mapped using µ-XRD in Laue mode on BM32 at the ESRF. X-ray beam size on the sample was 2×1µm² (H×V) and the full energy spectrum was used (5-28keV) to probe both the oxidised layer and the substrate. Fig. 1 shows a typical XRD image collected on that sample and compares it to a strain free UO_2 single crystal. The shape of the Bragg spot, initially round on the UO_2 reference, became elongated along three different directions. The collected image can thus be considered as the sum of two contributions, the first coming from the unstrained UO_2 (central round part of the Bragg spot) and the second of the oxidised layer (elongations).

At a first step, the orientation of the UO_2 unstrained substrate was determined and each peak indexed. To reach that goal only the central part of each Bragg peak (i.e. the unstrained one) was considered. These calculations confirmed the (111) orientation of the substrate.

At a second step, it has been tried to simulate the measured peak elongation using a strained UO_2 structure having the appropriate orientation. The Laue tool software package has been used [18]. Calculations showed that to reproduce accurately the shape of the elongations and their intensities, one had to introduce strains of 3% along three different directions: (100), (010), (001).

The measured distortion is thus consistent with the presence in the oxidised layer of the U_3O_7 crystalline structure, whose c/a ratio is reported to be 1.03. Since the c axis of U_3O_7 remains aligned with either (100) or (010) or (001) axis of the UO_2 substrate, the topotactic growth of U_3O_7 on UO_2 is demonstrated. Whereas the size of the X-ray beam and thus the probed volume in the oxidised layer are rather small, U_3O_7 grain size is clearly below 1µm². Interpretation of this data is thus in favour of the presence of U_3O_7 domains at the surface of the UO_2 substrate.

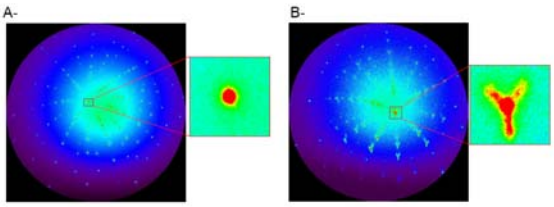

Fig. 1 Comparison of the µ-XRD Laue images collected on a strain free (A-) and on an oxidised (B-) UO2 single crystal

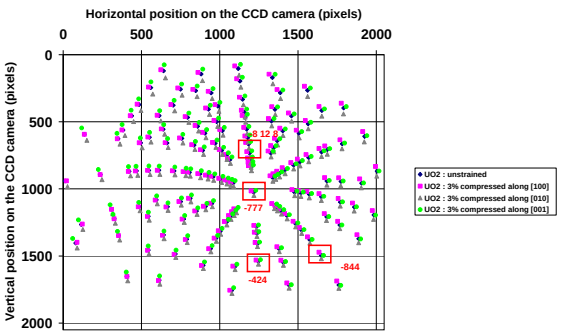

Fig. 2 Analysis of the strains in the UO2 oxidized single crystal using Lauetools.

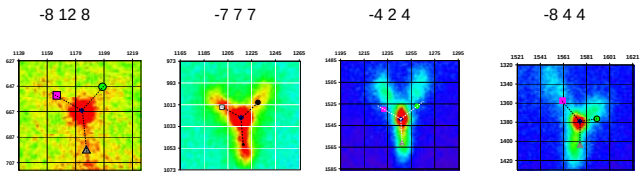

Fig. 3 Comparison simulation/measurement on 4 different Bragg peaks.

Addresses: (1) CEA, DEN, DEC, Cadarache (2) DSM / INAC / SPrAM / LASSO (3) DSM / INAC / SPrAM / LASSO (2) PHYMAT CNRS Poitiers

L.Desgranges et al., accepted in J. Nucl. Mater.

Contact : ***herve.palancher@cea.fr***

Laue Microdiffraction for *in-situ* electromigration tracking

P. Bleuet[(1)], P. Gergaud[(1)], P. Lamontagne[(2)]

Laue microdiffraction has been performed on polycrystalline Cu interconnects under electrical current load. Technological issues at the micrometer scale can be addressed by in situ x-ray experiments that help for clarifying the fundamental mechanisms involved in applied devices.

Electromigration (EM) happens in copper interconnects and is a major reliability concern for integrated circuits. This physical process is a mass transport driven by an

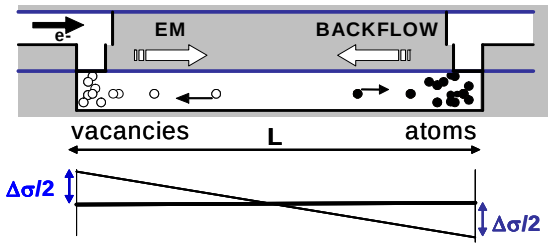

Fig 1. Schematic view of the stress gradient along the line

electrical field and activated by temperature. In confined interconnects (see Fig.1), the EM mass flux induces mechanical stress backflow. The copper accumulation at the anode induces a local compressive stress of the line while the copper is in a tensile state at the other extremity

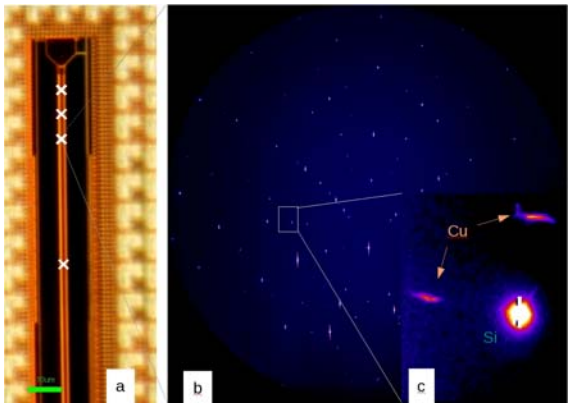

Fig 2: Cu interconnects 100nm wide in between two thick Cu lines probed at different locations (b) Laue Pattern collected featuring mainly Si substrate peaks (c) Laue peaks from Cu and Si

because of a lack of atoms. Therefore, a stress gradient $\Delta\sigma$ is expected along the line length in the steady state. Various models propose the variation of the stress along the line (linear, non linear). Correlation between the stress amplitude spatial distribution and voids onset is still unclear.

The copper critical product has been calculated and the possible links between EM performances and interconnect length determined as well as its dependence on copper mechanical environment. In this context, a study has been lead that aimed at following up the electromigration process while collecting Laue diffraction images, with the goal to track and monitor the evolution of grain behavior. Sample was then not prepared specifically for this x-ray experiment but kept its usual packaging.

Preliminary results obtained in very narrow copper lines deposited on Silicon substrate are presented here (100nm wide, 45 micrometers long and 220nm thick). Earlier, in 2007, full strain tensor was successfully determined on a Cu grain smaller than 1 micrometer cube [1]. But this time, due to the technological needs, measuring and analysing the Laue pattern of a Cu grain 100 times smaller was very challenging for the current Microdiffraction setup. To our knowledge, Laue diffraction has never been reported on such small lines.

To speed up the electromigration process, the sample was heated at 350°C using a furnace. The current in the line was set to a constant value, and resistance measured all along the test. Very weak Cu peaks could be isolated from high saturated and streaked Si substrate, and next indexed; their evolution has been tracked as shown on figure 2. In particular, we could observe a “rigid body” transformation of the diffraction pattern during the electromigration test: peaks are shifting all with the same amount and in the same direction, as illustrated on figure 8 with 3 reflections (non saturated Si peaks are not moving). It can also be seen that the peak shift is

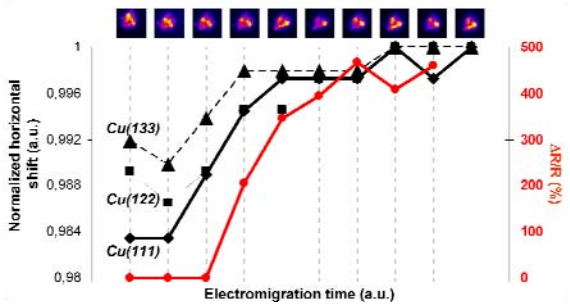

Fig 3. Evolution of diffraction spots during electromigration test. The red curve shows the normalized resistance while black curves (diamond, square, triangle) show the horizontal shift of the (111), (122) and (133) reflections, respectively. Cu(111) reflections can be seen at the top of the figure.

correlated with the resistance evolution of the line, *i.e.* with the apparition of potential voids. This behavior demonstrates that the grains are rotating on themselves during the electromigration test [2]. This observation, though not understood so far, is in agreement with other works already published and appears to be typical of small copper lines.

Upgrade of the KB mirrors and new fast antiblooming CCD cameras will help considerably this study by allowing to scan more line regions and collecting stronger signal from Cu grains, and consequently facilitating the analysis and the interpretation of the data.

Addresses : (1) LETI-MINATEC, Grenoble
(2) ST-Microelectronics, Crolles, France

Reference: [1] O. Sicardy et al, ESRF highlights (2007) [2] P. Bleuet et al, AIP Conf. Proc. 1173, 181 (2009)
Contact : pierre.bleuet@cea.fr

Determination of grain stress in Solid Oxide Fuel Cell by white beam Laue Microdiffraction

J. Villanova[(1)], O. Sicardy[(1)], R. Fortunier[(2)], P. Bleuet[(3)] and J.-S. Micha[(3)]

Local stress measurements were made on the electrolyte layer of Solid Oxide Fuel Cells (SOFC) by X-ray Laue microdiffraction. High accuracy stress determination at the (sub-) micrometer scale were compared to macroscopic measurements which had revealed stress gradient inside the layer. Control of residual stress after manufacturing and stress induced by cell operation is of crucial importance to improve cell efficiency and durability.

Solid Oxide Fuel Cell (SOFC) is a high-performance electrochemical device for energy conversion. A single cell is composed of 5 layers made of different ceramic materials: anode support, anode functional layer, electrolyte, cathode functional layer and cathode. The mechanical integrity of the cell is a major issue during its lifetime, especially for the electrolyte layer. Damage of the cells is mainly due to the high operating temperature, the "redox" behaviour of the anode and the brittleness of the involved materials. Since residual stresses are known to play a significant role in the damage evolution, it is important to determine them.

Laue Patterns have been recorded on BM32 and have corresponded to several grains for which the full strain tensors have been determined. White beam Laue patterns are sensitive to 5 over 6 strain (symmetric) tensor elements. Last elements are obtained by scanning with a monochromator the energy corresponding to at least one Bragg's reflection. The combination of white and monochromatic beam diffractions that must be taken at the same place on the sample is particularly challenging from the experimental point of view but also from the data analysis point of view in case of spatial variation of strain in the sample.

In addition to positioning challenges, the accuracy on strain determination depends directly on the accuracy on the diffraction angles measurements. Hence, detector plane position with respect to x-ray impact on sample surface and pixel locating of Laue spots on camera need the highest care.

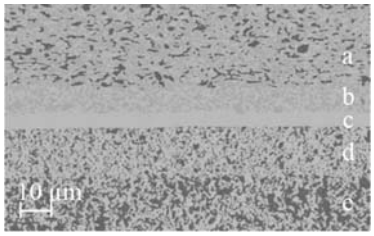

Scanning Electron Micrograph of the cell section after manufacturing. (a) Anode-support: NiO + YSZ (Yttria-Stabilized Zirconia), (b) Anode Functional Layer: NiO + YSZ, (c) Electrolyte: YSZ, (d) Cathode Functional Layer: LSM (Sr-doped Lanthanum Manganite) + YSZ, (e) Cathode: LSM.

First, calibration has been performed by using the Laue pattern of a reference sample, e.g. a <001> stress free Si single crystal. The deviatoric strain tensor values were found lower than 10^{-4}. Second, since the electrolyte and the anode are polycrystalline materials, the recorded CCD images contain bright spots due to diffraction by well crystallized electrolyte grains and numerous tiny spots coming from the AFL grains (The high energy photons of the white beam crosses the electrolyte and reaches the AFL). A threshold image processing has been applied to eliminate these small peaks. A reliable methodology was set up to find the orientation of different grains in the CCD images. In each image, at least three grains have been identified (Fig.5). Since the scanning step was 1µm and the electrolyte grain size was around 5µm, each grain appears on several consecutive CCD images. Each grain probed at different locations was found to have the same orientation corresponding to the absence of internal micro-misorientation in grain. Analysis over the entire area confirms that the electrolyte is a non-textured material. The obtained stress tensors are consistent with global measurements i.e. grains are under strong compression state. For example, the stress tensor of a <-1 -3 5> oriented grain (along sample z axis) has been determined by combining of white and monochromatic measuren xpressed in the sampl

$$\begin{pmatrix} -986 & -35 & 30 \\ -35 & -878 & 25 \\ 30 & 25 & -209 \end{pmatrix}$$

This preliminary study has been made on two targeted measurement points where four different stress tensors corresponding to four different grains have been calculated, showing that the stress state is not the same for each one. Additional measurements have been carried out to get more details on strain heterogeneities from grain to grain.

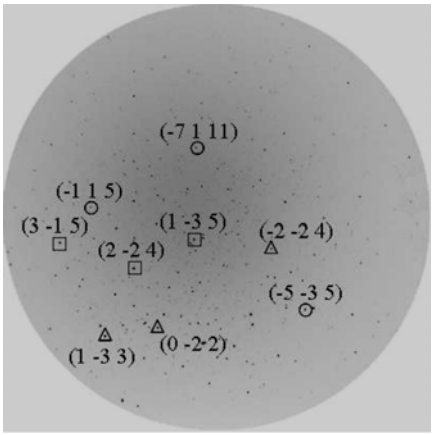

Laue pattern of a point scanned on electrolyte in white beam mode: open squares (resp. triangles and circles) represent reflexions indexed for the grain n°1 (resp. 2 and 3).

CEA-Grenoble (1) DRT/LITEN (3) DSM / INAC (2) Ecole Mines St-Etienne

J. Villanova et al Nucl. Instr. Meth.B, 268 (2010) 282

Grant : ANR MiDiFabl, *Contact : micha@esrf.fr*

Development of Laue microdiffraction : estimating the accuracy of the technique : part 2 : detecting known strain increments

O. Robach[(1)], J.-S. Micha[(2)], C. Le Bourlot[(3)], D. Faurie[(3)], R. Chiron[(3)], O. Castelnau[(3)]

Laue microdiffraction provides 2D maps of crystalline orientation and deviatoric strain in polycrystalline materials. The capability of the technique to detect small known strain increments was tested by performing an in situ tensile test on a W polycrystal. This test is representative of the differential accuracy on strain in conditions as close as possible to realistic ones, where the uncertainties are related not only to the extraction of the strain tensor from a Laue pattern, but also to the repositioning of the microbeam with respect to the grain of interest, from one tensile state to the next.

As mentioned in part 1, analyzing local elastic strain with Laue microdiffraction requires precautions. "Elastic strain" here is obtained from the lattice parameters α, β, γ, b/a and c/a, "diffraction-averaged" over the illuminated portion of the grain of interest, i.e. space-averaged with a weighting by local crystalline order. The input ingredients for this analysis are the center-of-mass positions of the Laue spots produced by the grain.

Any perturbation in the evaluation of the spots center-of-mass directly impacts the strain measurement. Irregular spot shapes linked to intra-grain distributions of orientation and strain associated with plastic defects are the most frequent cause of inaccuracy. Sorting the spots to remove the irregular ones is a crucial step in the image analysis.

Extending elastic strain measurements to grains producing irregular spot shapes is therefore strongly desirable, to extend the applicability of the technique to materials with large amounts of plastic deformation.

Before this, the strain accuracy of the newly installed Laue microdiffraction setup needed to be checked in a case with simple spot shapes.

Fig. 1 shows a sketch of the tensile test machine that was used, with the dog-bone W sample, and a typical Laue pattern. Note that very perfect grains (sharp spots) coexist with plastically deformed grains. The data may therefore also be used later for testing methods of strain analysis for more complex peak shapes.

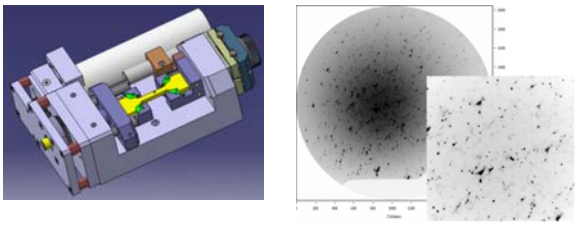

Fig. 1. Left : tensile machine, with the dog-bone sample (length = 7 cm). Right : a typical "multi-grain" Laue pattern.

Tungsten was chosen for its large yield stress (above 500 MPa) and its reputation of elastic isotropy, i.e. an increment of the macroscopically applied elastic stress will cause an equal increment of the local elastic stress inside each grain. Here the traction is along x, and the expected deviatoric strain increment is exx = 2.1e-4 and eyy=ezz=-1.0e-4 for a stress increment of 100 MPa. (eyz = exz = exy = 0).

Fig. 2 shows a map of grain orientation, taken at a load of 5 MPa. Grain size varies between 1 and 5 microns. The corresponding sequence of Laue images was repeated for successive elastic loading steps of 100, 200, 300, 400, 500 and 5 MPa. Maps were recorded with three different sample-detector distances to test several compromises between the number of spots and the x,y accuracy on each spot. The 5 and 500 MPa situations were investigated using both white and monochromatic beam in another experiment, to check the detectability of a small increment of lattice expansion.

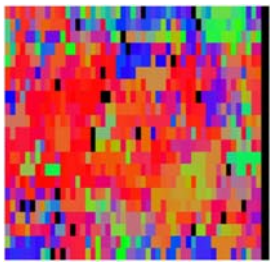

Fig. 2. : 50x50 microns orientation map (step 1x2 microns) at a load of 5 MPa. The color indicates which <HKL> is parallel to z : blue : [111], red [001], green [110]. Many grains diffract at each position in the map, only the grain giving the most intense Laue spot is shown here.

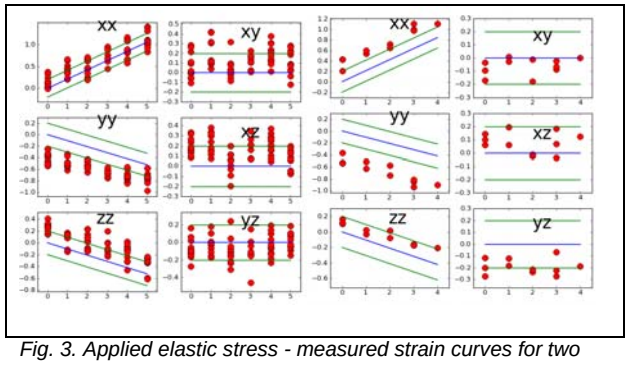

Fig. 3. Applied elastic stress - measured strain curves for two grains. The expected strain is shown as a blue line, with green lines at +/- 2e-4. Vertical shift between experimental data and expected strain is due to residual stress. There are several points for each stress corresponding to various measurement points on the grain. Left : 5 to 500 MPa, grain of 5 microns diameter. Right : 5 to 400 MPa, grain of 1.5 micron diameter.

Addresses : CEA-Grenoble, 17, rue des Martyrs, 38054 Grenoble cedex 9, (1) DSM / INAC / SP2M / NRS, (2) DSM / INAC / SPrAM / LASSO, (3) LPMTM-CNRS, Université Paris 13, av JB. Clément, 93430 Villetaneuse
Grant : ANR MiDiFabI, *Contact : odile.robach@cea.fr*

Strain and stress measurements in the vicinity of grains boundaries: study of plastic deformation in multi-crystals using Laue microdiffraction

G.Daveau[(1)], B.Devincre[(1)], T.Hoc[(2)], O.Robach[(3)]

In order to extend a dislocation density based model for fcc single crystal to the case of the poly-crystal, we have used Laue microdiffraction to measure plasticity mechanisms in copper samples. Two bi-crystals and one tri-crystal were deformed under compression. Crystal rotations, and deviatoric strain and stress evolution were measured during this deformation, using the microdiffraction setup on BM32. The results of the experiment will next serve as an input for the numerical simulations (dislocation dynamics and finite element method).

Laue microdiffraction gives the possibility to measure crystal rotation and strain evolution on poly-crystals. Mechanical fields induced by plastic deformation on multi-crystals were thus measured with this technique. Three copper samples (two bi-crystals and one tri-crystal) were deformed with compression. Laue microdiffraction measurements were made at several steps of compression, in order to look at the grain boundary influence on mechanical fields during deformation.

The samples were cut to form small parallelepipeds with millimeter dimensions. Attention was paid to the good perpendicularity of each face with the contiguous faces, in order to perfectly obtain an axial compression. Nano-indents were made on the samples surface to allow macroscopic deformation measurements (made by image correlation) and to serve as reference points for the Laue beam repositioning on each measurement step.
Only small macroscopic strains (<3%) were induced on the sample. Indeed, a relatively low dislocation density is needed to allow comparison with dislocation dynamics simulation and to clearly observe the grain boundary influence on dislocations comportment.Two kind of Laue microdiffraction maps were made on each sample: a large map (~500*500 µm², 5000 points) to see long range effect of the grain boundary, and a small map (~250*250µm², 2500 points) to catch the strong gradients close to the grain boundary.

The local rotations induced by deformation were revealed. The perfect beam repositioning between two steps of measurements allowed obtaining maps of difference of orientation between these two steps (figure1: tri-crystal case). Only very small rotations were induced by the macroscopic strain.
The local strain and stress fields were measured. The deviatoric strain was obtained with white beam measurement. The deviatoric stress tensor was then calculated using the copper stiffness modulus. The compression was made along the sample x-axis. The stress components are quite impacted by the proximity of the grain boundary, even before the compression. Indeed, a stress concentration can be observed (figure 2).

The difference map of the xx stress component (along the compression axis) is shown on figure 3. This map was obtained by subtracting the stress component in initial state to the same stress component in deformed state. This change appears to be higher in the grain boundary vicinity than in the grain core. This stress concentration could be due to dislocation storage near the grain boundary, as a consequence of the macroscopic deformation.
The stress concentration measured will now be used as an input for multi-scale modelization, based on dislocation dynamics and finite element method.

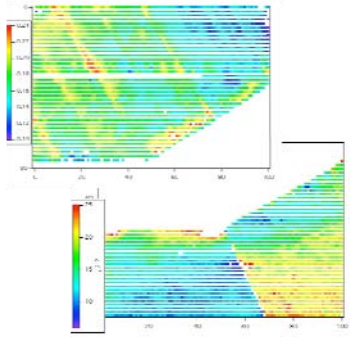

Fig. 1. Local crystallographic rotations induced by the macroscopic deformation on the tri-crystal sample. Color scale = angle of quaternion : top map : 0.1-0.24°, bottom map : 0-0.025. Macroscopic strain: 22 MPa.

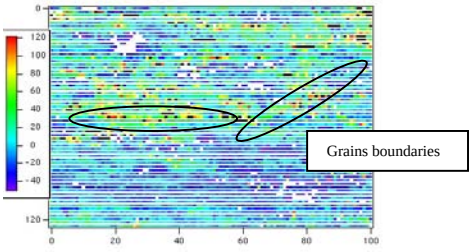

Fig. 2. Initial map (before loading) of the deviatoric stress along the compression axis in the tri-crystal sample. An area of small stress concentration is already seen in the vicinity of the two grain boundaries. Color scale : -40 to 120 MPa.

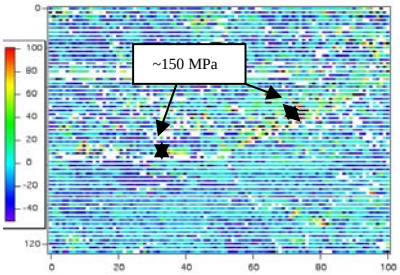

Fig. 3. Evolution of the deviatoric stress component along the compression axis during deformation. Stress localization close to the grain boundaries is revealed. Color scale : -40 to 100 MPa. Macroscopic strain applicated: 22 MPa.

Addresses: (1) CNRS-ONERA, Châtillon, France (2) EC-Lyon Ecully & ECP Châtenay-Malabry, France (3) CEA-Grenoble/INAC

Contact : gael.daveau@onera.fr

In-situ µLaue diffraction on mechanically loaded Cu single crystals

C. Kirchlechner[1], G. Dehm[1], J.S. Micha[2], O. Ulrich[2] and J. Keckes[1] [1]**Austrian Academy of Sciences and Universtiy of Leoben, Austria** [2]**CEA and ESRF, Grenoble, France**

The mechanical response of micron and submicron-sized materials is dominated by a strong size effect for which the underlying strengthening mechanisms are not yet understood. We have implemented a micro-mechanical test setup at the French BM32 beamline enabling to monitor the deformation behavior of small volumes using µLaue diffraction. The first diffraction experiments coupled with tension, compression and bending indicated a presence of complex dislocation structures depending on the sample geometry and the test type. In future, it is planned to perform in-situ mechanical tests on micron-sized poly-crystals and to correlate the initial grain and dislocation structures with the stress-strain response.

Several efforts have been made during the past years to characterize the mechanical response of small scale specimens. Even though the mechanical loading and sample preparation were enhanced dramatically, the structural investigation of deformed volumes is still limited due to the lack of appropriate characterization methods. Besides post mortem transmission electron microscopy (TEM) and electron backscatter diffraction (EBSD) which both have essential drawbacks (for instance sample preparation), µLaue diffraction provides some unique statistical information of deformed volumes with a typical spatial resolution in the micrometer regime.

In order to perform in-situ µLaue diffraction at BM32 beamline, a micro-testing system based on piezo drives and a commercial load cell provided by Kammrath and Weiß was installed. Loading is performed in displacement controlled closed loop with a accuracy in force of 10µN. Sample alignment is carried out by piezo stages and assisted by optical microscope and a fluorescence detector system. Based on this approach, load displacement curves (Fig.1) and diffraction patterns can be recorded simultaneously during *tensile, compression and bending experiments*. The samples are produced using a focused ion beam workstation and / or lithographic methods.

First in situ experiments revealed a very homogenous deformation of tensile samples with the activation of an unpredicted slip system at the beginning of plastic flow. Thereby, the pile up of dislocations leads to an increase of the diffraction peak widths in the direction expected for the unpredicted (1-11)[011] system (Fig. 2b) having the fourth highest Schmid factor. After reaching the stress plateau, the streaking axes instantly changes and upon further straining, the pile up of dislocations on the unpredicted system decreases. After approximately 22% engineering strain the diffraction peak width is slightly increased compared to the undeformed peak. In contrast, compressions samples do not only start to deform on an unpredicted system, but also indicate the storage of dislocations on several slip systems and the formation of subgrains with split Laue reflexes (Fig. 2d) at higher strains.

The in-situ tests are fully consistent with our former studies [1]. In the future micro tension, compression and bending tests are planned in order get a deeper insight in the nature of plasticity.

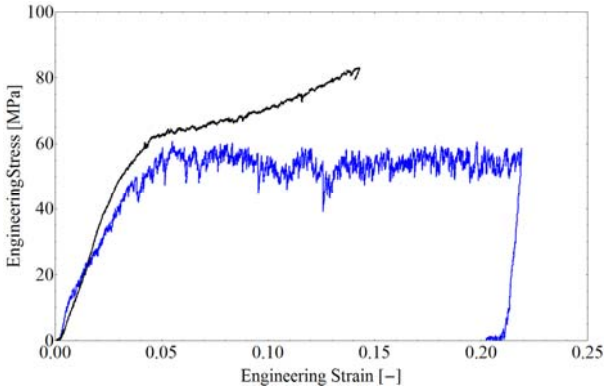

Fig. 1 The black and blue curves represent typical stress strain curves of a Cu micropillar and a Cu tensile sample respectively, both oriented for single slip

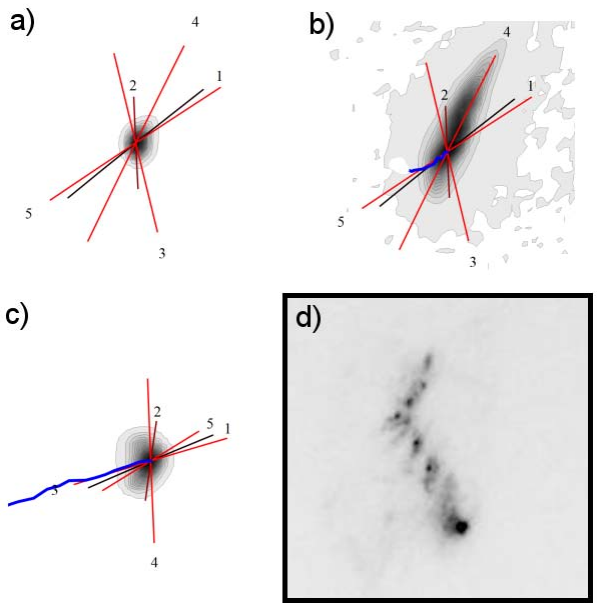

Fig. 2 Laue (024) reflection in a, b and c recorded during a tensile experiment. The lines represent projections of possible streaking axes caused by the storage of excess dislocations. The number gives the rank of the slip system (sorted by Schmid factors, 1 = highest). The peak movement during the deformation is indicated by the blue path: a) initial Laue spot b) recorded shortly before reaching the stress plateau and c) after loading to 22% strain. In d, Laue (111) reflection of a compression sample after 15% strain is presented. Satellite peaks indicate the formation of dislocation sub-structures.

Selected publication(s) : [1] Kirchlechner et al, submitted to Phil Mag Letters	
Grant(s) :	Collaboration(s): Erich Schmid Institut, Austrian Academy of Sciences and University of Leoben, 8700 Leoben, Austria
Patent(s) :	Contact : christoph.kirchlechner@stud.unileoben.ac.at

Development of Laue microdiffraction : estimating the accuracy of the technique : part 1 : relative accuracies between the various strain / orientation components

O. Robach[(1)], J.-S. Micha[(2)], C. Le Bourlot[(3)], D. Faurie[(3)], R. Chiron[(3)], O. Castelnau[(3)]

Laue microdiffraction provides 2D grain-by-grain maps of crystalline orientation and deviatoric strain. For each point inside a given grain, the HKL's of N indexed spots and their x,y positions on the detector are used to fit 8 of the 9 components of the matrix giving the coordinates of the a*, b*, c* vectors in the detector frame. In fact, four indexed peaks are sufficient [ref. 1] to obtain the matrix through an analytical formula. We perform statistics on 4-peaks determinations to highlight the relative accuracies between the various strain and orientation components.

Laue microdiffraction uses a white (5-30 keV) microbeam to obtain 2D maps of orientation and deviatoric strain on the near-surface region of polycrystals. At each beam position on the sample, every illuminated grain produces a Laue pattern, on a 2D detector placed around 2θ=90°, without any sample rotation. For each grain, the Laue spots center-positions are analyzed to retrieve a strained orientation matrix, which is then decomposed into local grain orientation and deviatoric strain.

In practice, the strain map obtained from an automated analysis of a series of detector images usually needs to be strongly filtered, to retain only the points where accuracy on strain is acceptable. The x,y pixel deviation on the detector between theoretical and experimental spot positions, averaged over the N spots of the pattern, needs to be typically around 0.2-0.25 for good accuracy.

This average pixel deviation is however not sufficient to get a feeling about what governs the incertitude on each of the 8 parameters taken individually.

Here we examine the relative accuracy of the various strain and orientation components. We consider all the quadruplets of peaks that can be formed from the set of N indexed peaks, and examine how the matrix varies from one quadruplet to the other. Histograms of the distributions of the various parameters are then plotted, whose shape and width allow to gain confidence on which parameter is more reliable and which is less.

Fig. 1 shows the histogram of the 6 deviatoric strain components xx, yy, zz, yz, xz, xy, for a well crystallized micrometer-sized W grain, in the xyz frame attached to the sample. The relative widths of the distributions indicate that uncertainty on the xz and yz strains is about two times larger than on the xx, yy, zz and xy strains. This behavior is independent on grain orientation. It is an instrumental effect, part of which probably comes from the limited cone that is explored in reciprocal space around the sample surface normal. Note that xx+yy+zz = 0 i.e. there are only 5 independent variables. On the "tetragonalization" terms xx-zz, yy-zz, or xx-yy the width is of the same order as on the yz and xz terms.

Fig. 2 shows the corresponding histograms for the 6 orientation components. Here we describe the orientation variations between the different quadruplets-solutions with 6 parameters instead of 3, to avoid the arbitrary privileging of a* over b* and c* that is introduced when converting the strained matrix into a pure rotation matrix. The orientation parameters are the dx and dy components of the [HKL] axis oriented along z for the reference matrix, then the dx, dz of [HKL]y and dy,dz of [HKL]x. This allows to take into account all the variations of orientation of b* and c*, whether they come from orientation or from strain.

The best accuracy is obtained on the orientation of [HKL]z. The accuracy on the rotation around z of [HKL]x and [HKL]y is about 3 times worse, and the accuracy on the z component of [HKL]x and [HKL]y about 10 times worse. This is again independent of grain orientation.

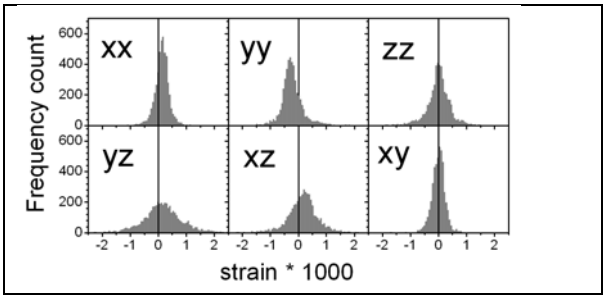

Fig. 1. Histograms of the 6 deviatoric strain components for a well crystallized W grain (z perpendicular to the sample surface, y at 40° from incident beam). The statistics is from 4827 "good" quadruplets selected from 30 indexed peaks (minimum angle between qi and qj = 11.5° = minimum angle between qi and qj,qk plane, where q is the diffraction vector).

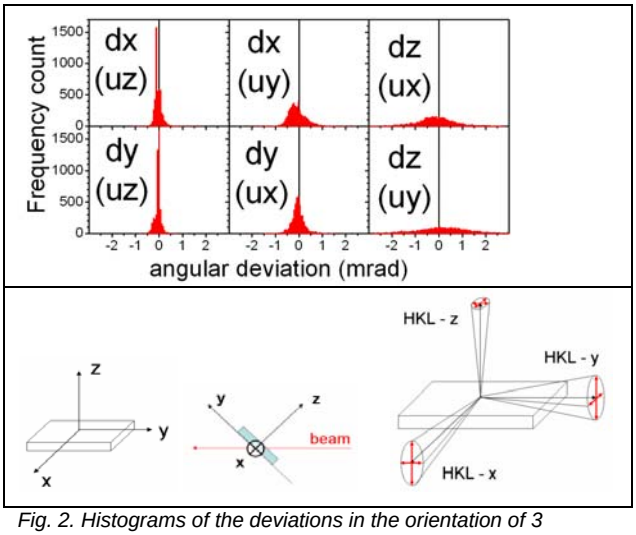

Fig. 2. Histograms of the deviations in the orientation of 3 reference [HKL] vectors, that point along x, y and z respectively in the reference orientation, for the grain of Fig. 1.

Addresses : CEA-Grenoble/ INAC (1) SP2M (2) SPrAM (3) LPMTM-CNRS, Université Paris 13, av JB. Clément, 93430 Villetaneuse
Ref. 1 : J-S Chung, G.E. Ice, J. Appl. Phys., 86 (1999) 5249
Grant : ANR MiDiFabI, Contact : odile.robach@cea.fr

Development of Laue microdiffraction : a method to obtain the last strain component (lattice expansion), in the white beam mode, using an energy-resolved detector to measure the energy of diffraction peaks

O. Robach[(1)], P. Gergaud[(2)], J.-S. Micha[(3)]

To enhance the capabilities of the micro-Laue technique, a method was developed to simplify the measurement of the sixth component of the strain tensor. The principle is to measure in the white beam mode both 1) the Laue pattern of a grain using a 2D detector and 2) the energy of one of the "side" diffracted beams of this grain (i.e. a beam not intercepted by the 2D detector) using an energy-resolved point detector. This allows to access simultaneously 1) the theoretical peak energy for zero lattice expansion, $E_{theor}(HKL)$, which quickly varies with both orientation and deviatoric strain of the unit cell, and 2) the experimental peak energy, E_{exp}. This leads to an improved accuracy on $\Delta a / a = - (E_{exp}-E_{theor})/E_{theor}$.

Laue microdiffraction uses a white (5-30 keV) microbeam to obtain 2D maps of orientation and deviatoric strain on the near-surface region of polycrystals. At each beam position on the sample, every illuminated grain produces a Laue pattern, on a 2D detector placed around 2θ=90°, without any sample rotation. For each grain, the Laue spots center-positions are analyzed to retrieve 8 of the 9 components of the matrix giving the coordinates of the **a***, **b***, **c*** vectors in the detector frame. These coordinates are then decomposed into local grain orientation and deviatoric strain. What misses in the matrix is the lattice expansion "a". Indeed, the diffracted beam direction (unit vector uf) is derived from the incident beam direction (unit vector ui) and the diffraction vector direction (unit vector uq = q / ||q|| where **q** = H**a***+K**b***+L**c***) by :

$$\mathbf{u_f} = \mathbf{u_i} + 2\sin\theta\ \mathbf{u_q}$$

i.e. it is independent of the length of **q**. An expansion Δa of the unit cell only changes the wavelength λHKL that is extracted from the incident spectrum, without changing the diffracted beam direction.

Once the 8 components of the matrix are known, obtaining the lattice expansion is "only" a matter of measuring the energy of one of the diffraction peaks. The standard method is to monochromatize the incident microbeam, and scan its energy around the theoretical peak energy for a given HKL spot, to locate the energy giving a maximum of diffracted intensity.

The most difficult task in this method is to ensure that the Laue pattern and the experimental energy are measured in the same conditions of beam size, experimental geometry and beam position with respect to the grain of interest. The re-positioning between white and monochromatic modes is particularly crucial for plastified grains, with fast intra-grain spatial variations of orientation. As a result, the 9nth component is usually measured only on a few points of the sample, without real mapping.
Based on the idea developed by Pyzalla on ID15 for energy-resolved fixed-angle high-energy powder diffraction [1] we developed a method to measure the energy of Laue peaks while remaining in the white beam mode, using an energy-resolved point detector. The main advantage is to ensure that $E_{theor}(HKL)$ (which is derived from the Laue pattern) and $E_{exp}(HKL)$ (which is derived from the HKL peak's energy spectrum) are measured exactly in the same conditions.

The peak energy spectra are measured using a Rontec XFlash lightweight Si-drift detector mounted on two translation tables, to collect the "side" Laue peaks, whose positions are predicted using the "top" Laue pattern measured with the 2D detector (Fig. 1).

To reach the desired accuracy on peak energy, frequent recalibration of the detector's energy-channel relation is performed using fluorescence standards. Measured energies are also corrected for the variations of E(ch) with the detector's total intensity. Fig. 2 shows the comparison between the two methods for the test-case measurement of lattice expansion of a Ge(111) single crystal, using several peaks. The measurements for the same comparison on micron-sized Cu grains are currently under analysis. On the Ge the two methods appear to have comparable accuracies around +/- 2e-4 on Δa/a, for peaks with E > 10 keV.

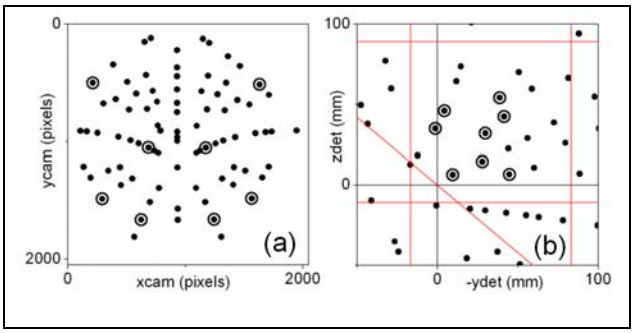

Fig. 1 "top" (a) and "side"(b) Laue patterns for a Ge (111) single crystal. (a) 2D detector 165 mm diameter at 72 mm. (b) 100x100 mm² accessible range for 0D detector at 119 mm. The 40° line marks the projection of the sample surface. Bigger circles indicate peaks whose measured energy is given in Fig.3.

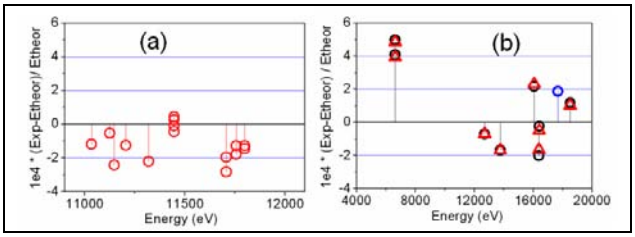

Fig. 2 Comparison of measured lattice expansion -Δa/a by the two methods for a Ge(111) single crystal. (a) : monochromatic-beam method, (b) : white-beam method

Addresses : CEA-Grenoble, 17, rue des Martyrs, 38054 Grenoble cedex 9, (1) DSM / INAC / SP2M / NRS, (2) LETI, MINATEC (3) DSM / INAC / SPrAM / LASSO

Ref. 1 : A. Pyzalla, J. Nondestructive Evaluation, 19 (2000) 21-31
Grant : ANR MiDiFabI, Contact : odile.robach@cea.fr

In situ nanocatalysis: size and catalytic activity of supported gold nanoparticles

M.-C. Saint-Lager, I. Laoufi, S. Garaudée, P. Dolle, R. Lazzari, J. Jupille, O. Robach

Nanocatalysis is a very active research field with the aim of controlling chemical reactions by catalyst engineering at the nanometer scale. This implies to be able to follow dynamic processes occurring at temperature and pressure of reaction conditions. Our group has developed a new setup which allows to elaborate model catalyst in UHV environment and then to follow their modifications during catalytic reaction by X-ray measurements on the GMT diffractometer on BM32. Grazing Incidence X-ray Diffraction (GIXD) and Grazing Incidence Small Angle X-ray Scattering (GISAXS), which provide the particle size, shape and structure, can be simultaneously performed together with activity measurements by mass spectrometry. Since it was found that gold, usually known to be inert, can become a very good catalyst for carbon monoxide oxidation even at room temperature, it is therefore the subject of many studies in order to understand such amazing properties.

The catalytic properties of gold supported on oxide are clearly associated with particles size, in the nanometer range [M. Haruta *et al.*, J. Catal. **115**, 301(1989)]. However, the relationship between the size and the activity is still debated and is a key issue for the understanding of the catalytic properties. Indeed, a maximum of activity was observed for nanoparticles (NPs) of ca. 2.5 to 3 nm for gold clusters on TiO_2, [M. Valden *et al.*, *Science* **281**, 1647(1998)]. As it corresponds to two atoms thick clusters it was attributed to synergetic effect of the two first gold atoms layers at the interface perimeter with the oxide substrate. But other authors claimed that the activity is proportional to the number of atoms at the NPs corners and they pointed out a dominant role of the low-coordinated sites on the activity [N. Lopez *et al.*, J. Catal. **225**, 86 (2004)].

We studied gold NPs deposited on TiO_2(110) by GIXD and GISAXS thanks to our new setup (Fig.1). The aim is to establish a link between the structure, the morphology of the particles and their reactivity in the frame of the CO oxidation.

Figure 2 illustrates the evolution of GISAXS patterns as a function of the gold deposit thickness and the sample gaseous environment. The thickest deposits (> 0.2 nm), giving NPs with larger diameter *d* are stable, whereas the NPs size increases for the thinnest ones. In step 2, at 473K, in presence of 20 mbar of argon or oxygen, a similar change is observed indicating an effect of the temperature. During step 3, a new sintering occurs only for sample B which is exposed to the reactive mixture O_2+CO. At the same time, mass spectrometry shows that CO is converted into CO_2. Thus this new sintering is probably due to a local heating induced by the exothermic CO oxidation. This result is particularly interesting since it indicates that the NPs measured by GISAXS are really those which react.

The geometrical parameters are deduced using a truncated sphere for modelling the NPs shape. As the catalytic activity is recorded at the same time, a direct correlation between NPs size and activity is then obtained. The activity presents a maximum for d=2.3 nm. Above the maximum, it follows a power law of *d* indicating that the active sites are the low-coordinated atoms on the edges and corners. Below the maximum, the NPs shape is flatter. This makes very unlikely that active sites are on the NPs perimeter or for 2D clusters. The 3D character of the active NPs is confirmed by the intensity profiles such as Fig. 3. It exhibits two peaks corresponding to the signal of the two sequences ABC and ACB of the gold fcc stacking along the (111) direction, which means at least 3 atomic planes.

This work tends to prove that the remarkable catalytic properties of supported gold nanoparticles are pure golden route and originate from low-coordinated sites, mainly edges, of the gold NPs.

Addresses :
(1) Institut Néel CNRS, Grenoble
(2) Institut des Nanosciences de Paris
(3) CEA-Grenoble/ INAC

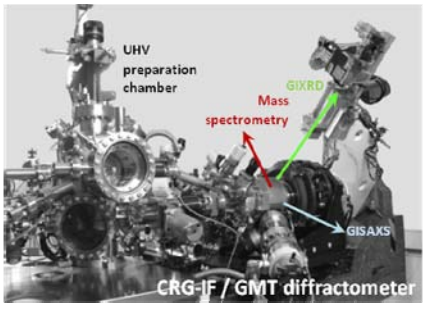

Fig. 1: setup on the GMT diffractometer with the two main parts: the UHV preparation chamber and the X-ray reaction chamber for GIXD, GISAXS and reactivity measurement.

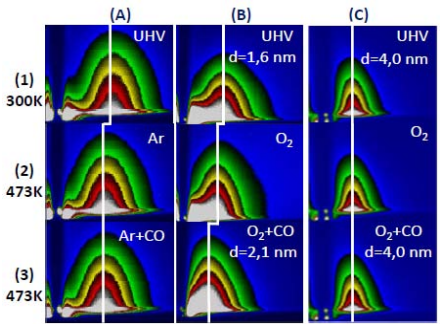

Fig. 2: GISAXS patterns of 0.05nm-thick gold deposit (A and B), 0.25 nm-thick (C) (1) in UHV 300K, then at 473K (2) under 20 mbar argon (A), 20 mbar oxygen (B) and (C), and (3) after adding 0.2mbar of CO.

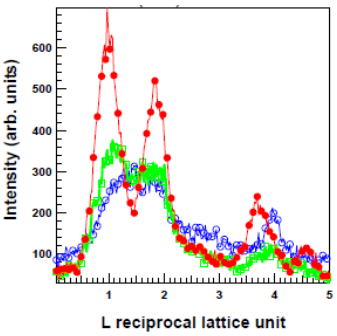

Fig. 3: Diffraction profile along the $(02)_{Au}$ rod : blue, in UHV at 300K, green: in 20 mbar of oxygen at 473K and red, after adding 0.2 mbar of CO.

Selected publications: M.-C. Saint-Lager *et al.*, *Rev. Sci. Instrum.* **78**, 83902 (2007) ; M.-C. Saint-Lager *et al.*, Gold Bull. **42**, 159 (2008)

Collaboration(s): INSP-Paris

Contact : marie-claire.saint-lager@grenoble.cnrs.fr

Towards a direct determination of the local atomic displacement field from high resolution x-ray diffraction measurements

A.A. Minkevich, M. Gailhanou, M. Eberlein, A. Loubens, S. Escoubas, V. Chamard and O. Thomas

Reciprocal space maps (RSM) of silicon on insulator (SOI) periodic lines are obtained using high resolution x-ray diffraction. RSMs can be used to determine indirectly the displacement field by comparing the experimental intensity map to that using model-dependent finite elements and prior knowledge of the object shape. The displacement field even in highly inhomogeneously strained lines is obtained by addition of constraints to an iterative phase retrieval algorithm. These constraints include direct space density uniformity and also constraints to the sign and derivatives of the different components of the displacement field.

Elastic strains play an important role in modifying physical properties such as the mobility of charge carriers in semiconductors. Strain engineering of the properties of silicon devices is now currently being considered as a way to improve electrical performances. It is, however, a real challenge to measure strain fields in such object. High resolution reciprocal space map (RSM) can be carried out in a non destructive way on samples containing devices or small objects in their (or very close) working and packaging conditions. 2D scattering intensities recorded near a bragg's reflection is actually sensitive to elastic strain that is generated at the epitaxial interface between two materials with different lattice parameter and due to the geometrical confinement.

Silicon on insulator (SOI) periodic arrays of lines are then interesting systems for the study of two-dimensional strain fields at the nanometer scale as well as objects of technological interest for semiconductor device fabrication. In this study, a 100nm SOI (001) was prepared on 200 nm SiO2 buried oxide (BOX). SOI and SI wafer were rotated by 45° prior to bonding. A 160 nm silicon nitride capping layer was deposited at the top.

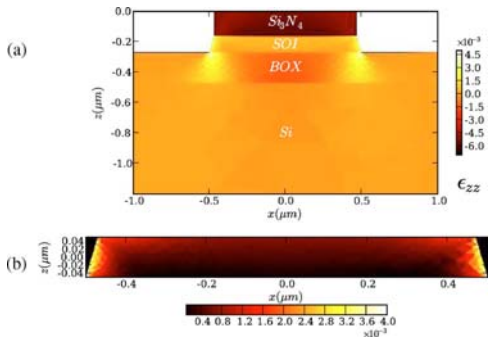

Fig 1:(a) Cross section showing the structure and the ε_{zz} strain field component. (b) Magnification and scale are adjusted for the SOI crystal; z is parallel to the (001) direction and x is parallel to (100).

Calculations of the displacement field in the lines by finite element (FE) modeling were first carried out. The shape was taken from a scanning electron microscopy cross section and the calculation was performed under plane strain conditions. Periodic boundary conditions were applied and the residual stress in the nitride cap was introduced via thermal loading. The only free parameter in this modeling is then the residual stress σ_0 in the nitride film. The displacement field obtained in this way has been used to calculate the diffracted intensity in the framework of the kinematical approximation. The best agreement has been found for σ_0=1.5 GPa for RSM in the vicinity of (004) reflection where only z-displacement is involved (see Fig 2) and (206) (both z and x-displacements). Highest displacement - e_{zz} strain (3.5 10^{-3}) and nearly 0.5° lattice rotation - is located at the edges of the lines (Fig 1b) which contributes predominantly to the two outer lobes and to the scattering intensity extension along q_z.

An other method relying on an iterative phase retrieval is not as model-dependent as the former method based on finite elements and knowledge of shape. This method is a standard direct inversion algorithm with additional constraints on spatial phase variations and on crystal density uniformity.

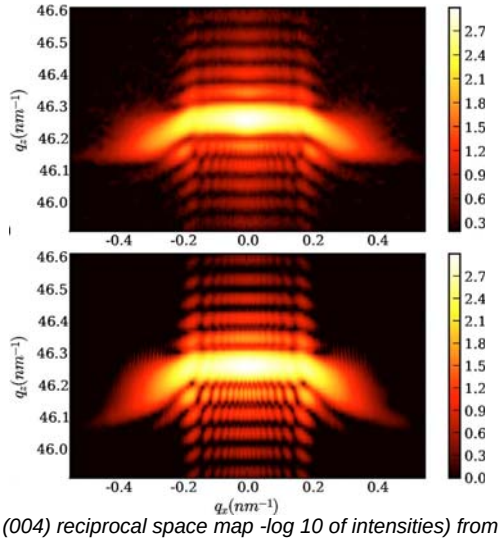

Fig 2: (004) reciprocal space map -log 10 of intensities) from SOI 1 µm lines. (b) Experimental: resolution is 10−3 nm−1. (c) Calculated: shape and displacement field determined using finite element calculations are considered

Space variation constraints allows the iterative procedure to converge: at each step phase differences between two neighbouring sampling points are limited by some magnitude parameters. It has been demonstrated that these parameters do not need to be accurate but can be easily estimated or found simply by a trial and error procedure.

Address: Institut Matériaux Microélectronique Nanoscience de Provence (IM2NP) Université P. Cézanne, Marseille, France

References : M. Gailhanou et al. Appl. Phys. Lett. ***90****, 111914 (2007). A. A. Minkevich et al.Phys. Rev.* ***B*** *76, 104106 (2007). M.Eberlein et al. Phys. Stat. Sol. (a)* ***204****, No. 8, 2542 (2007)*

Contact : ***olivier.thomas@univ-cezanne.f***

Light ion Implantation in silicon

F. Rieutord, JS Micha, JD Penot , F. Mazen

The effect of light ion implantation in silicon has been studied using high resolution X-ray scattering. We could measure the strain induced by implantation and the evolution of implanted species upon annealing.

The implantation of light ions (H, He) in a silicon matrix has been studied because it has many technological applications. Hydrogen is a dopant passivating species and ion implantation is used in a series of technological process to create defects at a controlled depth beneath a surface. This weakening effect may even eventually enable the splitting of the material, which can be used to transfer a thin layer of material to a substrate in technologies like the SmartCut™ technology.
The first step to be studied is the as-implanted material. We have studied the implant of silicon as a function of different parameters as for example the implantation dose. A typical reflection profile along the 00l rod around the 004 Bragg line is shown Fig.1.

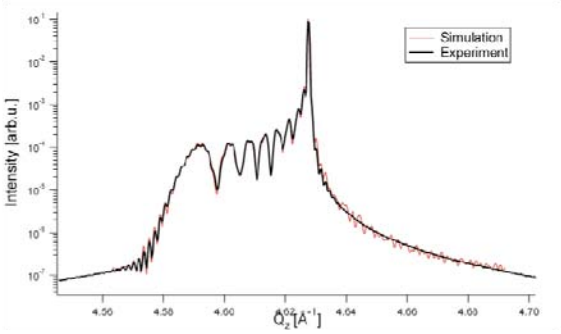

Fig.1: Intensity profile along the 00l Bragg line rod. .

The intensity shows several fringe systems associated with different periods. All extra intensity is located on the low-q side of the Bragg peak as the implantation produces an expansion of the lattice only. The data can be interpreted using two parameter profiles: a lattice parameter profile that shows an expansion on a certain width at a certain depth below the surface and a Debye-Waller profile that describes the lattice plane reflection coefficient associated to implantation damage.
These parameters are accessible rather independently: the lattice parameter expansion is given by the q-range over which extra intensity is visible. The periods of the fringe are related to the width of the expanded area in the material. As the strain profile tends to get narrower for higher strain value, the fringe spacing is not constant and increases with decreasing q. Superimposed to these fringes are narrower fringes associated to the distance between the strained zone and the surface. Accounting for the exact position of these fringes allows separation of different symmetrical solutions for the profiles. Finally the intensity of the fringes is a function of the Debye Waller factor profile. A fair account of the profile is generally obtained assuming the rms displacement of the DWF is proportional to the strain.

We extracted the strain profile for different implant conditions. Fig.2 shows the dependence of the max strain as a function of dose. The observations are in good agreement with ab-initio calculations for doses below 1.5 10^{16}H/cm^2. It is surprising to observe a faster than linear dependence for the strain-dose relation at higher doses.

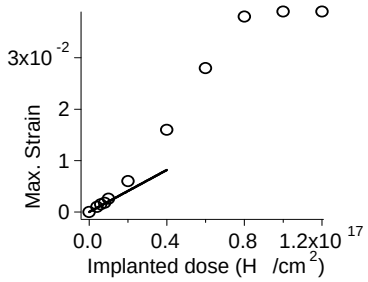

Fig.2 Dependence of maximum strain as a function of dose. Note the three regimes: a linear dependence at small doses, followed by a rapid rise in strain at higher doses and a saturation at very high doses

A second study can be performed upon annealing of such system. It is found that the average lattice distortion disappears rapidly while diffuse scattering components appear that are visible around many Bragg lines of the reciprocal space. This is associated to the formation of micro-cavities (platelets) that produce scattering at small angles and around Bragg peaks. We have used this diffuse scattering signal to monitor the growth of these pressurized platelets as a function of annealing time.

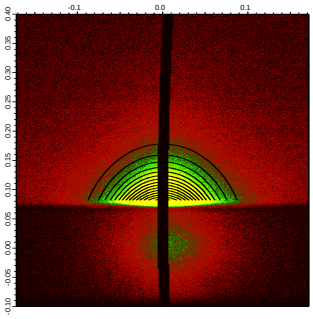

Fig.3 RSM (q_r,q_z) around the 220 Bragg reflection of silicon. The extent of the signal gives the lateral and vertical sizes of the cavities

The diameter size obtained for the platelets is in good agreement with measurements obtained by other techniques e.g. transmission electron microscopy. The advantage of X-ray techniques is that they can be performed in-situ, with little or no sample preparation. We plan to improve the description of the scattering by these objects in order to be able to extract more details about the strain field around a cavity

Selected publications L. Capello, F. Rieutord, A. Tauzin, et al J. Appl. Phys.,102, 026106, (2007).; N. Sousbie, et al. J. Appl. Phys., **99**, 103509, (2006).

Contact : francois.rieutord@cea.fr

Collaboration(s) : CEA-LETI, SOITEC Group

Strain in nanowires: assemblies for device integration

J. Eymery[(1)], V. Favre-Nicolin[(1,2)], F. Mastropietro[(1,3)],S. Baudot[(1,4)], R. Koester[(1)], F. Rieutord[(1)], F. Andrieu[(4)]

Grazing incidence methods have been applied to measure the strain and shape of several semiconductor nanowire heterostructures. These results open the way to the quantification of the nanowire elastic relaxations and to the investigation of more complex systems including radial and longitudinal growths coupling strain relaxation and chemical mixing.

One-dimensional nanowires (NWs) have been often presented as promising materials for future nanodevices owing to their small dimensions and novel properties. After ten years of growth experiments, it is now possible with the help of X-ray to draw some preliminary conclusions about the structural requirements necessary for demanding devices. For applications like field effect transistors [1], the properties of individual (and identical) NWs must be mastered, whereas in other applications, device operation depends on the characteristics of a number of NWs in parallel and therefore on the distribution width of the assembly. Most of these applications require controlling the strain in *heterostructures* to tune the physical properties or just to avoid dislocation nucleation. Moreover, the NW integration in devices may significantly affect the active region even for "homogeneous" wires.

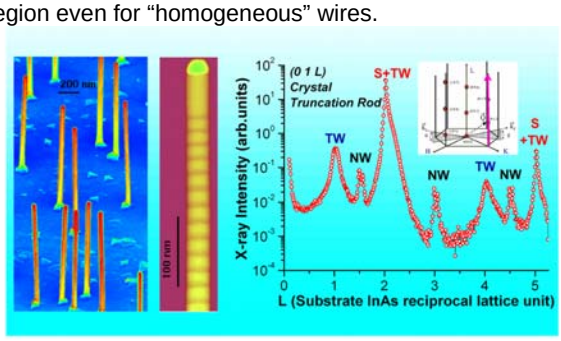

Fig. 1 (Left) scanning electron microscopy images of an assembly of InAs/InP longitudinal nanowires grown on InAs $(111)_B$ substrates. (Right) Measurement of the (0 1 L) crystal truncation rod and indexation of the different contributions [1,2].

Quantitative structural information about epitaxial arrays of VLS-NWs has been reported for a InAs/InP longitudinal [2] and core-shell [3] heterostructure grown on InAs $(111)_B$ substrate (collaboration with Lund University). Grazing incidence X-ray diffraction allows the separation of the nanowire contribution from the substrate overgrowth (see Fig. 1 for crystal truncation rod measurements in grazing incidence) and gives averaged information about crystallographic phases, epitaxial relationships with orientation distribution, and strain. Wrap gate InAs NWs have been also studied after HfO_2 dielectric coating and Cr metallic deposition necessary for transistor integration (see Fig. 2, left). X-ray diffraction allows determining the strain tensor and shows a longitudinal contraction increasing with HfO_2 and Cr depositions. The measurement of grazing incidence X-ray scattering [2,3] for different azimuths with respect to the nanowire edges has shown the signature of the initial hexagonal shape and of the coating thicknesses of the wires (see Fig. 2, right). More recently we studied by truncation rod analysis (unpublished results), InAs and InP nanowires having a controlled alternance of Wurtzite and Zinc-Blende domains along the growth direction and also InP/InAs/InSb heterostructures by anomalous measurements at both As and Sb absorption edges (11.8 and 30.5 keV) to estimate the InAs interdiffusion inside the wires. In the future, such experiments will be very interesting to deconvolve the structural and chemical part of the strain relaxation occurring in nanowire heterostructures.

Using conventional GIXRD, we analyzed quite extensively the mechanical relaxations of etched strained Silicon On Insulator (sSOI) lines used in transistor technology (CEA Leti) [4]. The strain of the initial 2D layer is conserved along the longer (*i.e.* the transport) direction. Along the small direction, a large relaxation is observed especially for the smaller widths (< 100 nm). This relaxation is almost complete for thicker samples (70 nm), whereas it is much more limited for thinner ones (10 nm). As shown by transport measurements, the tuning of the sSOI initial *biaxial* stress into *uniaxial* stress along the transport direction represent a great advantage for nMOS devices in terms of mobility.

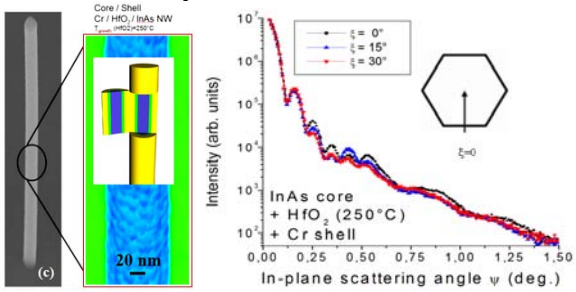

Fig. 2 (Left) scanning electron microscopy images of a core/shell structure, (right) scattering at small angle of incidence.

The versatility of this approach has been also applied to self-organized GaN wires grown in our laboratory [5] to get their epitaxial relationships and disorientations. Finally, such GI experiments performed on assemblies have also given very strong supports to select single wires studied in other ESRF beamlines with coherent imaging techniques [6,7] to gain insights into the *shape* of the objects [6], but also into the *strain* distribution inside a single object [7].

Addresses: (1) CEA-INAC-SP2M, 17 rue des Martyrs, Grenoble, France, (2) Université Joseph Fourier, Grenoble (3) ESRF, Grenoble,(4) CEA-LETI-MINATEC.

[1] C. Thelander et al., MaterialsToday **9** (10) 28 (2006).
[2] J. Eymery et al., NanoLetters **7** (9) 2596 (2007).
[3] J. Eymery et al., Appl. Phys. Lett. **94,** 131911 (2009).
[4] S. Baudot et al., J. of Appl. Phys. **105**, 114302 (2009).
[5] R. Koester et al., Nanotechnology **21**, 015602 (2010).
[6] V. Favre-Nicolin et al., Phys. Rev. B **79**, 195401 (2009).
[7] V. Favre-Nicolin et al., New J. of Phys. **12**, 035013 (2010).

Supported bilayers: Combined specular and diffuse X-ray scattering

T.Charitat[(1)], J. Daillant[(2)], G. Fragneto[(3)], L. Malaquin[(1,2)], J.-S. Micha[(4)]

A method is proposed for the analysis of specular and off-specular reflectivity from supported lipid bilayers. Both thermal fluctuations and the "static" roughness induced by the substrate are carefully taken into account. Examples from supported bilayers and more complex systems comprising a bilayer adsorbed or grafted on the substrate and another "floating" bilayer are given. The combined analysis of specular and off-specular reflectivity allows the precise determination of the structure of adsorbed and floating bilayers, their tension, bending rigidity and interaction potentials. We show that this new method gives a unique opportunity to investigate phenomena like protrusion modes of adsorbed bilayers and opens the way to the investigation of more complex systems including different kinds of lipids, cholesterol or peptides.

There is a great interest in determining the elastic properties and interactions between membranes at the microscopic scale. One attractive way to do it is to investigate thermal fluctuations of supported bilayers. When obtained by vesicle fusion, it is likely that some defects will remain, but almost defect-free samples can be obtained by using the Langmuir-Blodgett (LB) technique. In a set of experiments, we have developed combined specular and off-specular X ray reflectivity on supported membranes (see Fig. 1). We consider adsorbed bilayers where the spacer is either a first lipid bilayer adsorbed on the substrate (double bilayers) or a mixed octadecyltrichlorosilane (OTS) layer-lipid monolayer (OTS bilayers), where the OTS layer is chemically grafted on the substrate. A first study of such floating bilayers, mainly limited to the investigation of their structural and elastic properties has been first published [1] and further extended to the determination of the interaction potential. We then developed the underlying theory leading to the full determination of structural and elastic properties of bilayer membranes and their interaction potentials [2]..

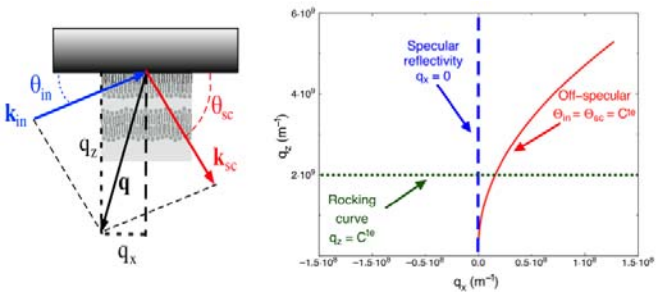

Fig. 1 (Left) schematic view of the experimental setup for specular and off-specular reflectivity and (Right) Fourier space trajectories in specular and off-specular reflectivity experiment. The grazing angle of incidence is θ_{in}. θ_{sc} is the angle of scattered x-rays in the plane of incidence (Y normal to it).

We extended to more complex samples, in particular double bilayers, a first analysis of the height-height correlation functions of correlated interfaces by Swain et al. We show in particular that only a joint analysis of the specular and off-specular reflectivities allows a full characterization of the system. Specular reflectivity is more sensitive to the adsorbed bilayer whereas off-specular scattering is more sensitive to the floating bilayer. It consists in the systematic convolution of the substrate height-height correlations with susceptibility functions in order to appropriately propagate the correlations, and also takes into account thermal fluctuations. We then perform an efficient numerical integration to obtain scattering cross-sections and intensities, taking precisely into account resolution functions.

By performing simultaneous analysis of specular and off-specular datas (see Fig. 2), we characterize both structure and parameters of the fluctuation spectrum: tension, rigidity and interaction potentials. By studying single supported bilayers, we measure for the first time the effective microscopic tension related to protrusions inside the membrane (about 80 mN/m). Long range fluctuations are determined by moving the membrane away from the substrate by the addition of an adsorbed membrane. Therefore we precisely measure the interaction potential between neutral membranes in a state of equilibrium. Non equilibrium fluctuations are studied by applying an electric field. We directly show that the field induces a negative electrostatic tension on the order of 1 mN/m and a positive rigidity of about 100 k_BT. We finally begin the study of more complex interactions by analysing the signal of charged membranes by X-ray and neutron reflectivity..

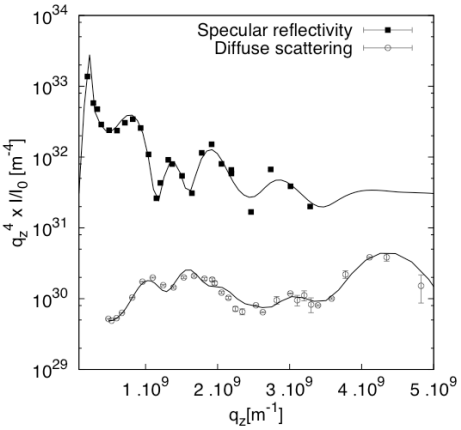

Fig. 2 Specular reflectivity and diffuse scattering from a double bilayer at 49°C. q_z^4 I/I_0 as a function of q_z. The maxima in the specular intensity correspond to minima in the diffuse scattering at low q_z.

This method is quite general and could be applied to similar problems like wetting films, polymer thin films or synthetic multilayers.

Addresses : (1) Institut Charles Sadron, Université de Strasbourg, CNRS UPR 22, 23 Rue du Loess, BP 84047 67034 Strasbourg cedex 2, France

[1]. J. Daillant et al *The Proceding of the National Academy of Sciences USA*, 2005, 102, 11639-11644.
[2] L. Malaquin, T. Charitat, J. Daillant, to appear in *Euopean Journal of Physic E*, DOI: 10.1140/epje/i2010-10578-

Silicon oxide bonding

F. Rieutord[(1)], H. Moriceau[(2)], C. Ventosa[(2)], S. Vincent[(2)], L. Libralesso[(2)]

We describe here some results of our research about the mechanisms of interface closure for silicon oxide to silicon oxide bonding. High energy X-ray reflection on the bonding interface allows a description of the mechanisms at play during the interface sealing obtained through thermal annealing. A detailed balance of interfacial materials is available through the study of the evolutions of the different component parameters of the interface.

Material direct bonding (also called wafer bonding, direct bonding, molecular bonding) is an attractive technique for assembling two materials and build heterostructures. It has the advantage of requiring a low thermal budget and of being applicable to a wide class of material, irrespective of their structure or physical properties. This technique is widely used in micro-electronics e.g. for mass production of advanced Silicon-On-Insulator substrates. In this case, a key step is the assembling of oxide-covered silicon wafers. We have studied the mechanism of interface sealing using high-energy X-ray reflection. The study of such buried interfaces at the nanometer scale is difficult as the interface is buried between thick materials that prevent access to standard surface probes (electrons, AFM probes, light, standard X-rays). We have used X-ray interface reflection (i.e. where the beam enters the side of the top material) to do so. The geometry is shown below:

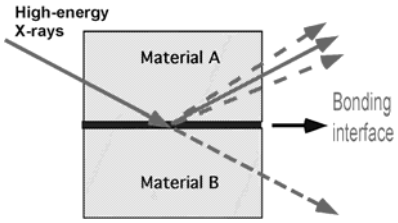

Fig.1: Geometry of solid/solid interface reflection experiments.

This geometry has a major advantage of getting rid of the strong outer surface contributions. Hence it can be very sensitive to the minute density gradients present for example between silicon and silicon dioxide. In addition, no total reflection effects are present in most cases and simple kinematical modeling of the profiles is suitable. At last, when the profile is symmetrical, direct inversion of reflectivity curves is possible.

We have used the technique to study the so-called silicon to silicon oxide hydrophilic bonding case, which is the standard for SOI manufacturing. The bonding is termed hydrophilic as the clean oxide covered silicon surfaces are hydrophilic and covered with water monolayers. This water is trapped at the interface on bonding. This is visible from X-rays comparing the interface densities of hydrophilic and hydrophobic bonding. Thermal treatment is then applied to the assembly to strengthen the interface. We studied the evolution along this annealing step.

The main steps that have been identified using X-rays are the following:

a sealing step that occurs around 200°C. The contacting asperities tend to spread and the interfacial density rises. The bonding energy strongly increases as covalent bonds form.

a water removal step. This step proceeds differently whether native or thermal oxide are involved:

- When native oxides are present, water can reach the silicon easily and react to produce hydrogen right after 200°C. This hydrogen may dissolve in the oxide or create interface defects.
- When thermal oxides are present, water remains confined in wide pockets at the interface. At higher temperature, this interface water will solubilize in the oxide and eventually oxidize silicon at elevated temperatures only.

This scenario has been mainly established from the evolution with temperature of the density profiles. Interface widths and densities could be followed together with the oxide thicknesses. The detailed quantitative measurements of interface and oxide changes allowed detailed balances of material to be made.

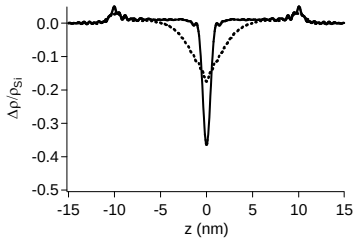

Fig.2 Thermal evolution of a symmetrical thermal oxide (10nm) to thermal oxide (10nm) SiO2//SiO2 bonding from room temperature (solid line) to 400°C (dashed line). The profiles show the interface closure (increase of density at z=0), water removal (surface area of the interface dip is larger at 400°C) and absence of oxide growth (the silicon/silicon oxide position stays constant). The profiles were directly inverted from the reflection curves.

Addresses : CEA-Grenoble (1)/ INAC (2)/ LETI-MINATEC

Selected publication(s) S. Vincent, I. Radu, D. Landru, F. Letertre, and F. Rieutord, Appl. Phys. Lett., **94**, 101914, (2009); S. Vincent et al, J.Appl. Phys. accept. (2010);C. Ventosa, F. Rieutord, L. Libralesso, et al., J.of the Electrochemical Soc., **156**, H818, 2009; C. Ventosa et al. Electronic and Solid State Letters, **12**, pp. H373, (2009); C. Ventosa, F. Rieutord et al. ECS Transactions, vol. **16**, 361-368 (2008); C. Ventosa, F. Rieutord, F. Fournel et al. J. Appl. Phys., **104**, 123524 (2008).

Grant(s) : Industry

Collaboration(s) : CEA-LETI, SOITEC Group

Patent(s) :

Contact : francois.rieutord@cea.fr

Scientific perspectives and development of the beamline

Several projects of upgrade and development are presented in this part. Since the last optics refurbishment occurred in 2006, they concern only the three experimental station of the beamline. For the microdiffraction setup, experimental improvements are foreseen by using new state-of-the-art achromatic focusing KB mirrors and by recording fast and reliable full strain tensor by means of an auxiliary energy–resolved detector. INS station will start its scientific investigations of the the various fundamental growth processes on surfaces from the very soon completion of the UHV-CVD installation coupled to current INS chamber. Moreover, in the frame of the SMOKE project, magnetic informations will enlarge the INS characterization panel. Finally GMT is planning to answer growing demands of technology and applied science by upgrading its instruments and enhancing its data and analysis throughput.

Microdiffraction

- Ongoing development of Laue microdiffraction : wire-scanning technique to gain spatial resolution along the incident beam

- New Fixed-Shaped KB Mirrors for the Microdiffraction Setup

INS

- Foreseen research with the INS instrument; Following the CVD growth of nanowires in situ with synchrotron X-rays

- Magneto-Optical and Structural properties of Surfaces and Interfaces studied *in situ* on complex nanostructures

GMT

- Foreseen research directions using GMT

Ongoing development of Laue microdiffraction : wire-scanning technique to gain spatial resolution along the incident beam

O. Ulrich[(1)], J.-S. Micha[(2)], X. Biquard[(1)], F. Rieutord[(1)], O. Robach[(1)], H. Palancher[(3)]

In its basic version, Laue microdiffraction provides 2D maps of crystalline orientation and deviatoric strain near the surface of a polycrystal. The probe volume is of submicrometer dimensions perpendicular to the x-ray beam, but is much bigger along the x-ray beam. A system is being built to precisely translate a thin absorbing wire close to the surface, following the method developed by GE Ice et al. at APS [Ref. 1]. Using the wire as a mask for the diffracted beams should allow in a first stage to locate the grains center-of-mass along the beam, and in a second stage, more involved, to gain depth resolution on intra-grain variations of lattice strain and orientation. The first tests of this system are scheduled in April 2010.

In basic Laue microdiffraction, lateral resolution parallel to the sample surface is high due to the submicrometer size of the beam, but there is no spatial resolution along the beam : the diffraction pattern contains the contributions from all the grains along the beam path.

Probe depth inside a Laue pattern is a spot-dependent quantity, as each HKL spot filters a different energy from the incident beam. It is given by the material- and energy-dependent x-ray attenuation length, possibly reduced by the grain size along the beam. It can vary from a microns up to millimeters (e.g. for a 30 keV spot in a Si single crystal). The situation is even more complex for spots containing harmonics (e.g. (002) at E_0, (004) at $2E_0$), which combine several probe depths.

3D spatial resolution is desirable. In materials with small grains, chosing which grain to display at each x,y position in a 2D map is always a problem. A 3D resolution will allow to sort the simultaneously illuminated grains according to their depth below the surface. In materials with bigger grains showing intra-grain strain or orientation distribution, a 3D resolution will allow to measure the gradient along the beam of the strain/orientation matrix. This will allow for example to distinguish the part of spot elongation that is representative of the volume of the material, from the part due to surface effects. This is important to later convert spot-width into density of defects.

The system under construction will operate using the "Differential Aperture X-Ray Microscopy" method shown on Figure 1.

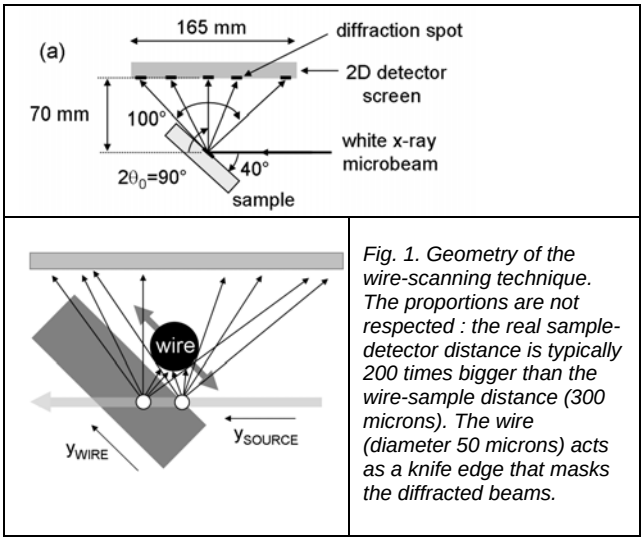

Fig. 1. Geometry of the wire-scanning technique. The proportions are not respected : the real sample-detector distance is typically 200 times bigger than the wire-sample distance (300 microns). The wire (diameter 50 microns) acts as a knife edge that masks the diffracted beams.

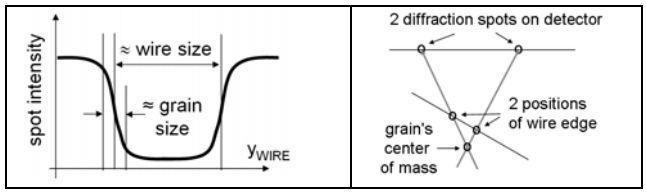

The method relies on the accurate (few 0.1 micron) positionning of the wire in y and z above the surface, and on the large ratio (dsd / dsw) between the sample-detector distance and the sample-wire distance. The wire is used as a "differential mask", i.e. the information is in the difference images obtained by subtracting the image at ywire0 from the image at ywire0 + dy.

In materials with small grains, the locating of a grain's center of mass is done by triangulation. For a given spot, the average position of the spot on the detector, and the y position of the wire to cut half of the spot intensity are used to trace the diffracted ray. This ray-tracing is particularly precise close to the sample, thanks to the large distance ratio dsd/dsw. Repeating the process for several spots belonging to the grain's Laue pattern, allows to locate the grain from the "point" of crossing of the rays (which is a triangle for 3 rays).
In a big grain with a strain / orientation distribution, the problem is to reconstruct, from the series of difference images, the Laue pattern produced by a slice located at a certain distance ysource below the surface. This in order to later analyze this pattern in terms of strain and orientation. On a given difference image where a fraction of spot N is visible (i.e. taken at a ywire where the wire partially masks this spot), ray tracing using the position of the spot, and crossing with the (known) incident beam, will allow to locate the source of the (partial) spot. The list of N spot-positions for a given slice will therefore combine spot-positions from N difference images.

The choice for the step of the wire displacement will compromise between depth resolution and intensity of difference images. Wire alignment will use both the optical microscope and the incident beam. The stability of the beam / sample / wire assembly needs to be established, in particular concerning beam intensity. A specific analysis software needs to be developed. A refined method for the calibration of the experimental geometry will also be needed, to precisely locate the sample surface along the beam.

Addresses : (1,2) CEA-Grenoble, 17, rue des Martyrs, 38054 Grenoble cedex 9, (1) DSM / INAC / SP2M / NRS, (2) DSM / INAC / SPrAM / LASSO, (3) CEA-Cadarache, DEC/SESC/LLCC, 13108 Saint-Paul lez Durance
*Ref. 1 : G.E. Ice, B.C. Larson, Adv. Eng. Mat. **2** (2000) 643*
Grant : ANR MiDiFabl, Contact : odile.robach@cea.fr

New Fixed-Shaped KB Mirrors for the Microdiffraction Setup

X. Biquard, J.-S. Micha, F. Rieutord, O. Robach and O. Ulrich: **CEA-Grenoble, Institut Nanosciences et Cryogénie, SP2M/NRS, 17 rue des Martyrs, 38054 Grenoble Cedex 9**

After 3 years of satisfactory functioning of the microdiffraction setup, we decided to upgrade our setup. The aim of this upgrade is to provide a simultaneously smaller and more intense white beam to follow global miniaturization and limit raster scan acquisition time. To achieve both goals, we decided to move to KB mirrors of fixed shape and focal length. These 150 and 300 mm long KB mirrors will exhibit state-of-the-art characteristics: slope error smaller than 0.25 µrad rms, average rugosity of 2 Å rms as well as a shape error of 2 nm rms. JTEC has won the corresponding call for tenders and both KB mirrors are expected for delivery in September.

The main drawback of the present adjustable curvature KB mirrors is that mechanical bending induces rising slope errors when moving away from the center of mirror: illuminated length had to be limited to 1/3rd of total mirror length. An illuminated length that will be increased to 85% of total mirror length thanks to fixed shape mirrors would lead to an increase of a factor of 6 in total flux. Without mechanical bending, KB mirrors are more compact: they will be moved downstream and demagnification will be higher. Combined with a better shape, this leads to an expected beam size 1.6 times smaller in each direction than presently.

Overall – not taking into account vibration enlarging - we expect a white beam size of 175*380 nm2 with a 6 times more intensity leading to an overall 15 times higher photon density.

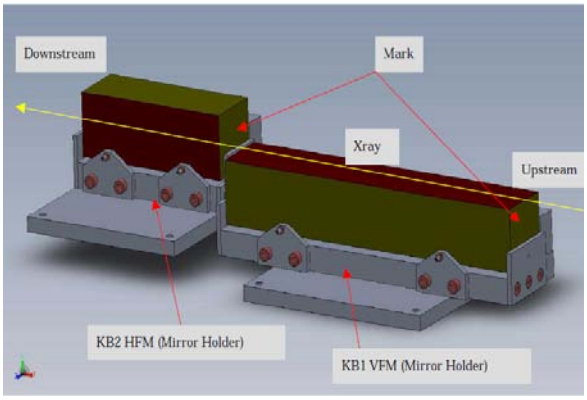

Fig 1: 3D view of our future KB mirrors. The absence of mechanical bending mechanism leads to a maximal compacity of the holder as is clearly visible here.

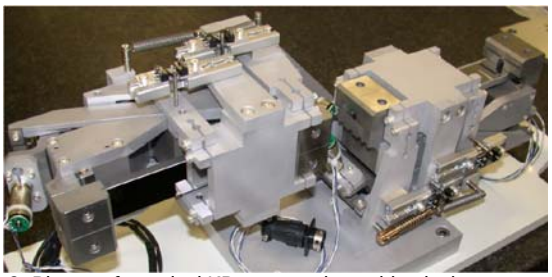

Fig 2: Picture of a typical KB system almost identical to current Pt-coated mirrors are clamped to allow their bending by clearly visible stepper motors. Call-back springs are for tilt rotation.

We are presently designing the mechanical structure that will adjust the positions (tilt, yaw, roll and distance) of mirrors relative to the X-ray beam and the sample. Our XYZ combination of high-precision linear stage for the sample as well as our optical microscope being fully satisfactory, we will re-use them in our future setup with new KB mirrors. Concerning beam size enlarging by vibrations, we believe that the better compacity of fixed-shape KB mirror will help us dampen vibrations by raising self-resonance frequencies of the setup (ESRF's biggest vibration contributors are below 30 Hz) and we are evaluating the use of a vibration isolation table.

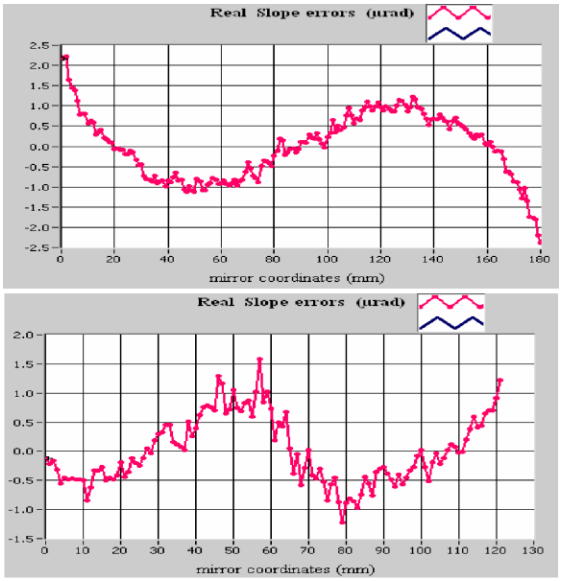

Fig 3: Slope error measurements with the Long Trace Profiler of current KB mirrors (upper graph=first horizontal 300mm long and lower graph=second vertical 170mm long). Illuminated lengths are 100 mm at centre on first and 50 mm at -30 mm on second

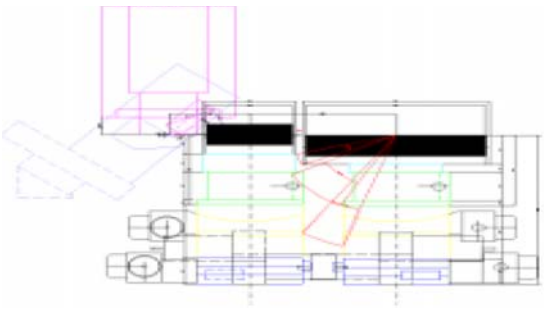

Fig 4: foreseen implantation of the new microdiffraction setup

Grant(s): ANR MiDiFaBl

Contact: xavier.biquard@cea.fr

Foreseen research with the INS instrument; Following the CVD growth of nanowires in situ with synchrotron X-rays

The 2005 beamline review committee followed our suggestion for the midterm of the installation of a UHV-CVD system in order to expand the capabilities to different growth systems. We have thus installed a UHV-compatible CVD gas injection system for a variety of process gases that will allow a quick change from UHV growth (e.g. during surface preparation and metal catalyst deposition) to CVD growth (wire/heterostructures growth).

Indeed, a major challenge for the coming years is the investigation of the growth of semiconductor nanowires. We will address the questions of the catalytic eutectic Vapor-Liquid-Solid growth process, the relation between the composition/shape/structure of the metal-semiconductor catalyst and the growth and structural properties (strain shape, facets, composition) of the nanowires, the intermixing and the strain at the nanowire/substrate and nanowire/droplet interfaces; the question of the dilution of the metal into the nanowire; the effect of choice of reactant and feeding gas on growth speed; the effect of kinetic parameters on the composition/strain at Ge/Si interfaces in nanowire hetero-structures; the different growth regimes, axial or radial; the localization of the nanowires and their organization on patterned substrates…

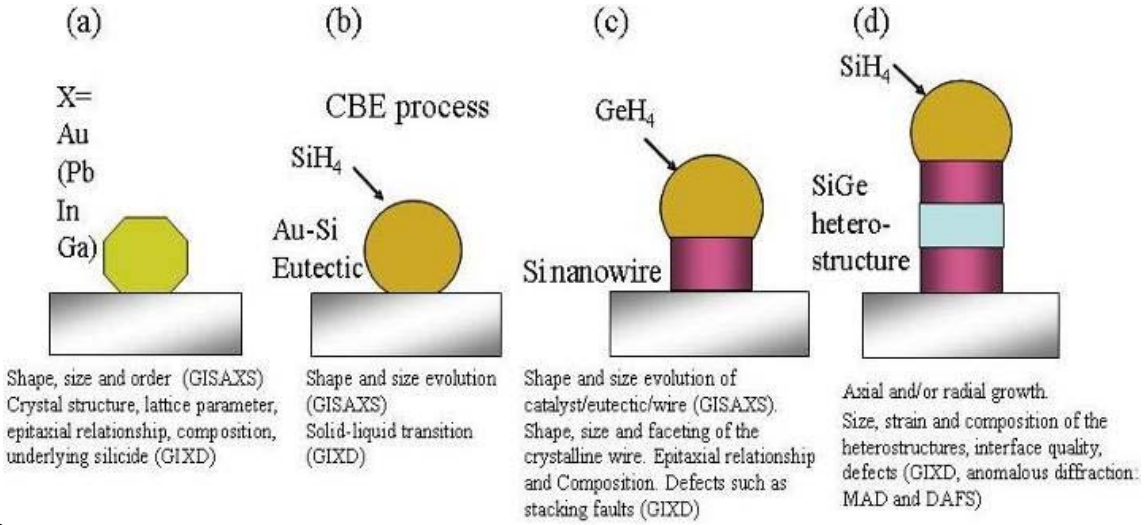

Overview of the accessible parameters via in situ x-ray scattering during different stages of the catalytic growth of SiGe nanowires on Si(111). (a): deposition of the Metallic catalyst. (b) Exposure to Silane (SiH4), causes to the catalyst to crack the molecules, release the hydrogen and form a liquid phase eutectic. (c): After saturation of the eutectic, Si nucleates on the Si-surface and forms a Si-wire. (d) Alternative exposure to SiH_4 and GeH_4 causes the growth of a heterostructure inside the wire.

This extension to the current instrument allowing for MBE and CVD growth whilst applying x-ray scattering methods on a powerful synchrotron source will be the only of its kind in Europe and, to our knowledge, worldwide. The figure below schematically shows the different steps of the wire fabrication and the various parameters accessible by *in situ* x-ray scattering during the growth for the example of SiGe-wires based on MBE-grown Au-catalysts and silane/germane as process gases. The establishment of this method will certainly also lead to an extension of the complexity of the investigated wire systems. Heterostructures of group IV semiconductors and, in a later stage of the project, semiconductors of III-V nitride type will be in the focus of interest. Nevertheless, during the first year of the project, the extension of the current equipment by a UHV-CVD gas injection system has to be realized. With the installation of the UHV-CVD equipment, the CBE-Vapour liquid solid (VLS) transition will be investigated in detail. Here, x-ray diffraction definitely offers a tool yielding unequaled information about details and kinetics of this process. These range from extreme sensitivity to the solid-liquid transition up to stages of solidification and epitaxial relationship. Diffraction yields the possibility to follow in detail the formation of eutectics, and thus our instrument will be ideally suited to search for alternative catalysts for the VLS process.

Gas source deposition in porous structures

Recent efforts have shown that a growth of vertical Si nanowires is also possible on Si(001)by UHV-CVD and the use of a guiding Matrix of porous alumina and gold catalysts. This promises to allow a combination with conventional microelectronics. Our

collaborators from the CEA and MINATEC Labs also succeeded in the growth of such structures recently. However not all pores are filled so far and little is known about the
crystallisation and growth process of the wires inside the pores, as well as the Au catalysts at the Si-surface. In situ X-ray experiments are currently performed on the alumina templates of these structures. To permit in situ growth, the presence of a gas injection system on a synchrotron beamline is required.

Gas source deposition beyond nanowires

With the UVH-CVD injection we aim to contribute with a unique tool to the fundamental understanding of
catalytic semiconductor wire growth, notably atomistic details of the VLS process. A part from these short and mid-term goals, the injection system will have four injection lines and thus allow for an extension of the deposited elements. It is self-evident that fundamental knowledge on CVD processes are of high technological interst, as most of the semiconductor devices originate from this technology. Furthermore, materials as SiC on Si or Diamond are only obtainable by Gas source deposition. The CEA LETI and the CNRS in Grenoble are very competitive in this field. Both materials still suffer from poor crystalline quality and a high density of defects. SiC as a promising semiconductor has partially been abandoned due to the high amount of defects. X-rays are an ideal (the only) tool to detect and quantify the formation of defects during growth and thus open a way to analyze and to understand these crucial problems of crystal synthesis.

The implementation a gas distribution system was the first technical step of this projet, now completed, thanks to a financial support by the Grenoble “Nanoscience Fundation, Nanosciences aux limites de la nanoélectronique “. It consisted in an extension of the previous INS hutch, and in the integration of a gas injection system provided by the company VEGATEC to combine solid source and gas source MBE.

Marked in red are the parts already present on site: extraction, primary vacuum, CBE injector. The connection of the primary pump to the extraction as well as the N_2 flux at the exit of the primary pump has to be realized by the supplier of the gas cabinet, as well as the connection of the gas cabinet to the extraction (present on the ceiling of the experimental hutch).

Sketch of the gas injection system with a technical representation of one of the four equivalent gas-distribution lines.

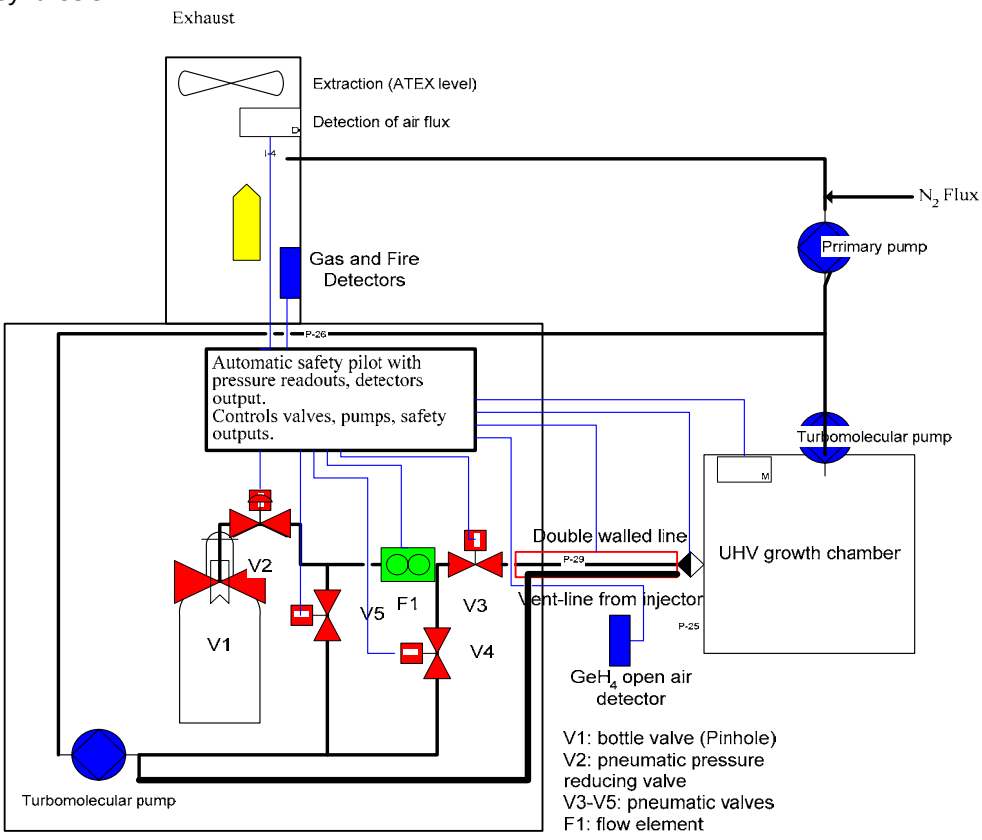

Magneto-Optical and Structural properties of Surfaces and Interfaces studied *in situ* on complex nanostructures

One of the main envisaged development at BM32 beamline consists in a magneto-optical Kerr effect (MOKE) set-up coupled to the INS chamber. Our aim is to make available at the beamline an instrument for measuring *in situ* the magnetic properties of the ultra-thin films, surfaces, interfaces and nanomaterials that are deposited and characterized using the INS chamber. We intend to study novel magnetic materials starting with well-defined surfaces prepared by electron beam epitaxy with an *in situ* control of the structure and morphology by grazing incidence X-ray diffraction (GIXRD) and small angle scattering (GISAXS).

The experimental hutch (Fig.1) has been recently refurbished. This created the conditions in terms of security and space for improving the instrumentation and for the implementation of the UHV CVD (Chemical Vapor Deposition) apparatus and of a MOKE set-up for magnetic characterization.

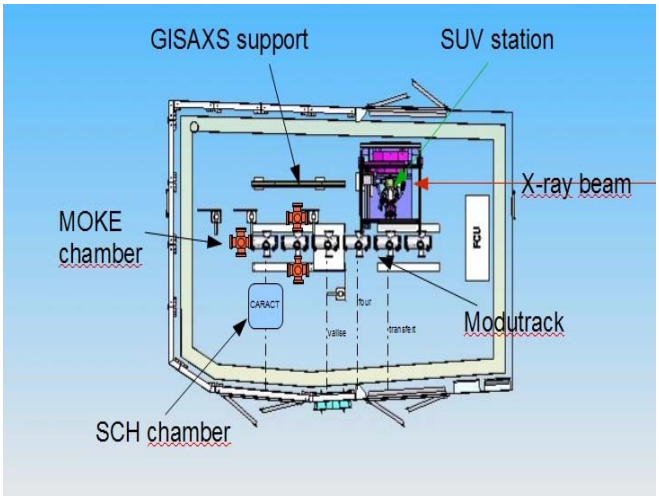

Figure 1: Overview of the new experimental hutch, displaying the INS station connected to the Modutrack system and the characterisation chamber. The three possible positions for the MOKE set-up (in orange) are indicated.

Description and expected characteristics

The magnetic behaviour of ultra-thin films and nanoparticle alloys is closely related to their chemical compositional, structural and morphological aspects as well as to their interacting environment. Many different techniques may be applied to probe the magnetic properties correlated to these aspects. Among them, the magneto-optical Kerr effect (MOKE) is a well-established technique to study magnetism of ultra-thin ferromagnetic films[2]. Its sub-monolayer sensitivity has been verified in many situations[3]. It has recently been successfully applied to study topological changes of Co on Pd surfaces[4], the thermal evolution of magnetic anisotropy of Fe nanoparticles[5] and in the case of a dense CoFe nanoparticles ensemble presenting a superferromagnetic state[6]. Maybe the most important advantage of the MOKE technique compared to other ones, like SQUID or VSM techniques, is the simplicity of implementation and flexibility of the sample environment. Such an apparatus may be easily coupled to a Surface Science set-up in order to follow, in an UHV environment, the magnetic properties at the different stages of growth[7].

The MOKE macroscopic description is based on the analysis of the dielectric properties of a magnetized medium. The polar and longitudinal Kerr effects are characterized by a complex rotation of the plane of polarization of the linearly polarized incident light upon reflection from the surface of a ferromagnetic material. The rotation is directly related to the magnetization of the material within the probed region of the light. Because light penetrates more than 20 nm into metals, the MOKE technique derives its surface sensitivity, in fact, from the limited thickness of the deposited magnetic nanostructures.

The MOKE apparatus requirements have to cope with polar and longitudinal geometry in a ultra-high vacuum environment. Sample holder has to be mounted in a manipulator with XYZθ moving parts and laser light must reach the sample through sapphire windows. The sample temperature must be controlled between 5K to 450K and the magnetic field limit should be close to 1 Tesla, with a uniformity of about 1% within a sample of about 6 to 8 mm in diameter. This apparatus should be

---

2 S.B. Bader, J. Magn. Magn. Mater. **100**, 440 (1991)
3 Z.Q. Qiu and S.B. Bader, J. Magn. Magn. Mater. **200**, 664 (1999)
4 M.Przybylski et al., Phys. Rev. B **73**, 085403 (2006)
5 J.H. Lai et al. J. Magn. Magn. Mater. **310**, e803 (2007) ;
6 S. Bedanta et al. Phys.Rev. Lett. **98**, 176601 (2007)
7 Z.Q. Qiu and S.B. Bader, Rev. Sci. Instrum. **71**, 1243 (2000) ; Boukari et al., Vacuum **52**, 327 (1999)

coupled to the main chambers by easily transfer facilities. The total cost of this set-up is estimated to be around 350 k€. A demand for financial support has been sent to a funding agency.

One of the originalities of our INS station at ESRF is to combine surface preparation and electron beam deposition facilities to produce novel systems (thin films and nanoparticles) with the *in situ* and real time study of their structure and morphology. We are proposing here a step further, with an instrumental development for *in situ* magnetic characterization of the samples by magneto-optical Kerr effect (MOKE) technique.

Scientific proposals related to magnetism

The research domains that will benefit from this development are related to nanomagnetism and spintronics. Materials with high magnetic anisotropy for recording media, the exchange coupling at the interface of ferromagnetic and antiferromagnetic materials, the use of self-organized systems to create a two-dimensional array of dots or wires, ordered bimetallic nanoparticles with high magnetic anisotropy, are examples of interesting systems where the atomic arrangement and the morphology play a key role in the magnetic properties. Magnetization measurements at different stages of the growing process leads to the optimization of the properties and to a better understanding of the relation with structure and morphology.

Among recent proposed experiments to the French CRG committee that would have benefited from a simultaneous magnetic characterisation, we can mention :

- Chemical ordering processes in nanometer-sized FePt nanoparticles prepared by a chemical route;

Resp. Michael Delalande (**CEA, Grenoble**);

- Investigations of the first growth stages of GeMn on Ge(001),

Resp. André Barski, Mathieu Jamet (**CEA, Grenoble**);

- Size dependence of shape and ordering in growing L10 FePt nanostructures,

Resp. Mireille Maret (**UJF, Grenoble**);

- Growth and structure properties of ultrathin MnPt layers on Pt(100),
- First stages of Fe growth on Pt(100)-hex reconstruction: seeking for chemically ordered FePt nanostructures
- Structure of cobalt oxide on Pt(111) and of interface by capping with Pt.

Resp. Maurizio De Santis (**CNRS, Grenoble**)

- Growth of ultrathin FePt/MnPt exchanged-coupled bilayers on Pt(100),
- Exchange coupled CoO / FePt ultra-thin films grown on Pt(001).

Resp. Hélio Tolentino (**CNRS, Grenoble**)

- Structure determination of thin chemically ordered antiferromagnetic films by SXRD: c(2x2)NiMn/Cu(001) Resp.: Carsten TIEG, Holger MEYERHEIM (**MPI, Germany**), M. De Santis (**CNRS, Grenoble**)
- Structural transition of core-shell and alloyed bimetallic Co-based nanoparticles,
- Coalescence versus size-dependant ordering transition of CoxPt1-x nanoparticles

Resp. Pascal Andreazza (**CNRS, Univ. Orleans**)

- Highly ordered Pd, Fe and Co clusters on alumina on Ni3Al(111).

Resp. : Andreas Buchsbaum (**Univ. Wien, Austria**), Maurizio De Santis (**CNRS, Grenoble**)

- Correlation between structural properties and magnetic behaviours of Fe1-xCox thin films grown on
Rh(001) and Pd(001) surfaces.

Resp. Marek Przybylski (**MPI, Germany**), Hélio Tolentino (**CNRS, Grenoble**)

- Fabrication of magnetic arrays through the use of molecular templates,
- Growth and structural study of magnetic array into molecule template.

Resp. Véronique Langlais, Maurizio De Santis (**CNRS, Grenoble**)

The MOKE instrumental development will be conducted by the BM32 staff and led scientifically by the CNRS team (Hélio Tolentino and Maurizio De Santis).

Foreseen research directions using GMT

Being a general purpose diffractometer, the research areas covered by the multechnique goniometer are by essence very diverse. Based on the trends observed during the last four years, we give here a few lines along which the instrument may develop. This will include high energy studies of buried interfaces and thin films and better techniques . An important source of experiments will come from technological materials, from micro-electronics related subject area to new energy technologies.

The multitechnique goniometer has been extensively used for a variety of scattering studies, mainly concentrated on the interfaces studies. Due to the high flux available at high energy on our beamline (especially compared to national synchrotron beamlines), we tried to develop specifically experiments requiring this type of energy range.

Not surprising, studies of liquid/solid interfaces or solid/solid interfaces (bonding) represent a significant part of GMT activity. This development will be continued, as the possibility for medium to high energy X-rays to penetrate fair lengths of materials, is clearly an asset of X-ray techniques over other structure determination techniques (e.g. electron based). The ability to study in-situ materials, in operando with no or little sample preparation is specially important for technological samples which have to be characterized as close as possible from their conditions of use. When strain and stress measurements are concerned, this remark is even more important. Strain depends on boundary conditions which must not be changed by sample preparation. Soft condensed matter processes or electrochemical processes involving liquids at electrodes are also difficult to study using other techniques.

The demand to characterize thin deposits of material is very strong, especially from our colleagues from applied research.

Polycrystalline thin films are a very important class of materials that we do not handle well at the moment. Being thin, we tend to study them under grazing incidence but the long resulting footprint causes resolution problems. We use Sollers slits or analyser crystals in front of the detector to cope for this, but we are then usually limited to point detection measurements which is a rather inefficient way of collecting photons. For this kind of sample producing a weak scattering distributed along scattering cones in large solid angles, 2D detection would clearly be advantageous, not the mention the possibility then to measure textures, an often important searched data.

The availability of new 2D detectors on the beamline (specially pixel detector) should foster the development of new techniques for polycrystalline thin film studies. Strategies to maintain angular resolution (e.g. beam microfocussing to limit footprint length, knife edge above sample...) will have to be developed.

This type of studies using monochromatic beam would complement very well the local measurements performed using the Laue microdiffraction setup.

Reciprocal space maps using these 2D detectors will also be carried out (e.g. on implanted samples) should also be developed to perform the so-called 3D scattering. We anticipate that significant software development will be needed to tackle the large amount of data produced by this type of studies.

The goniometer is also rather old and several parts of it could be improved. For example, an increased stiffness of the goniometer head would be desirable, together with sample changer capabilities in order to better automate some experiments. The horizontal sample geometry could be improved (access to higher angle) if extra movement stages were present.

The high demand for scattering studies on technological samples, together with the mid-term need for renewed instruments may call for the building of a new CRG beamline dedicated to these new technology materials and to the techniques covered at the moment by the GMT goniometer. This would extend the amount of beamtime and reduce the pressure on the in-situ station (INS) and and Microdiffraction instruments.

Conclusions

The “Interface” beamline has been operated smoothly for the last years, thanks to its new optics dating from 2006 and its three complementary instruments. Since the last BLRP, a new instrument has been developed, dedicated to microdiffraction experiments. After a commissioning and development period, this instrument is becoming mature, and the first scientific papers are being published. In parallel, different CCD detectors have been acquired thanks to external funding, and a Maxipix pixel detector will complement them before the end of 2010. These will improve the microdiffraction measurements on the one hand, and allow speeding up some of the other measurements on the other hand.

A significant development is desired in the coming years on the INS end station, by implementing in situ SMOKE measurements. This, however, requires the project to be accepted by the French funding agencies.

The two original diffractometers, GMT and INS, are now 17 years old, and display some signs of weaknesses. In the midterm, it would be desirable to replace these two diffractometers, which will require significant additional funding that will have to be looked for actively in the near future. Last but not least, some of the scientists with local contact duties on the instruments were already here at the start of the beamline project, some twenty years ago, and might think of moving toward other activities, which claims for the permanent hiring of younger people.

Acknowledgements

Many people from many different laboratories have been involved at one time or another in the project. We would like to acknowledge all of them here. In addition to our home institutions (CEA & CNRS), we would like to acknowledge funding supports from the Agence Nationale de la Recherche - PNano program (MiDiFabl project) and from the RTB (Basic Technological Research) research program. We also deeply acknowledge the efficient help of the ESRF CRG officer, Axel Kaprolat, the secretaries, Murielle Rigolet, Marion Glueckert and Valerie Clément and the ESRF CRG technician, Eric Dettona, as well as all the staff of the ESRF.

Annexes

Annex 1

Statistics on the ESRF and CRG beamtime use at BM32

The following statistics cover the period 2006-2010 of operation of BM32 beamline. As a CRG beamline, two selection committees hereafter called ESRF and CRG committee allocate beamtime to european and french users (resp. one third and two thirds). Three instruments share the beamtime: INS, µdiff and GMT (the two latter are hosted in the same experimental hutch and have often common users).

Beamtime overbooking: 240 shifts (resp. 120 shifts) are allocated by a single CRG committee (resp. several ESRF committees) per full operational year. Over the 4 years period the mean overbooking ratio (requested/allocated number of shifts ratio) is about 3.5 for ESRF beamtime and 2.25 for CRG beamtime.

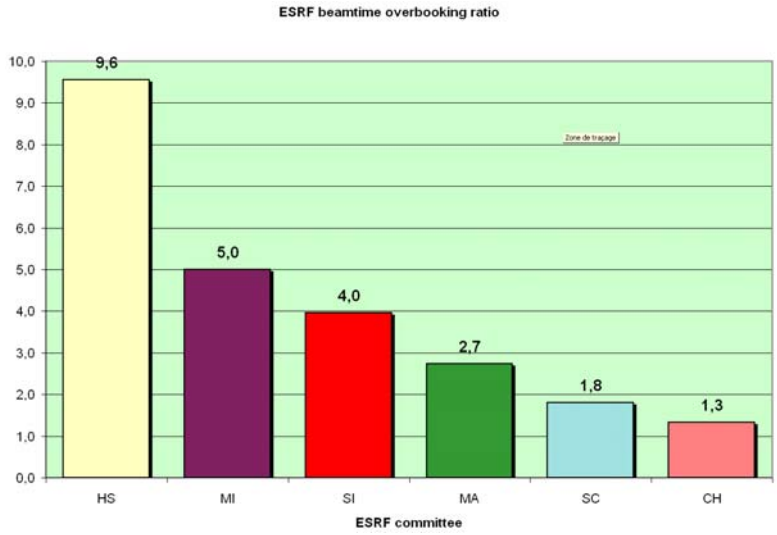

Fig 1 : Overbooking ratio (requested/allocated shifts) of ESRF beamtime (2006-2010) distributed by ESRF committee..

Scientific Fields and Committees: BM32 has been originally dedicated to interface and surface studies. The distribution of allocated ESRF beamtime by ESRF committee is representative of the scientific fields covered by the beamline with its three instruments, even for the CRG beamtime (Fig 2). One experiment over two is devoted to surface and interface studies (SI ESRF committee), among them a large majority are carried out on the INS instrument. One experiment over four concerns applied materials science (MA ESRF committee). Most of these experiments are performed with the Microdiffraction setup. The versatility of the GMT instrument is refleced by the remaining committees mainly SC committee and some MA and Si experiments.

The instruments distribution of requested and allocated beamtime on CRG beamtime in figures 3 and 4 illustrates how the beamtime is shared among the instruments. The demand and offer (respectively requested and allocated number of shifts) is rather constant (overbooking ratio slightly above 2): the first half of the beamline activities is devoted to the INS instrument and the other half is divided between µdiff and GMT instruments. Due to the development of the µdiff setup – operational since 2006 – a growing demand has been satisfied by the ESRF and CRG committees. Many IHR shifts were also devoted to the development of this new technique. µdiff experiments use currently about 25% of the beamtime on BM32.

Users Countries and Laboratories: Figure 5 and 6 present the panel of countries and laboratories from which the main proposer of the experiment originates. The distribution retrieved from main proposer data or all users data are quite the same. If obviously the very most of the users of BM32 are french through the CRG committee, more than one user over two are french through the ESRF committees. French main proposers come mainly from Grenoble and specifically from the two institutes CEA-INAC and CNRS-Grenoble to which the BM32 staff belong. Strong interest in the applied materials field explains the important number of experiments from outside experts and recurrent users coming from Austria (Leoben university) Marseille (I2MNP Laboratory) and CEA-LETI in Grenoble.

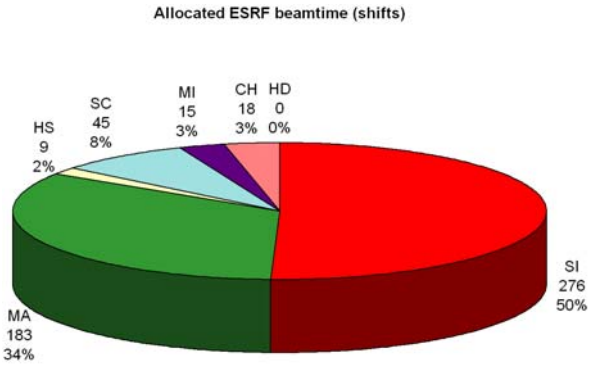

Fig 2 : Distribution of allocated ESRF beamtime shifts (2006-2010).

Publications: More than 80 publications have been published from experiments performed at BM32 for 4 years (Figure 7). It

corresponds then to a steady rate of 20 publications per year. On the INS instrument, half of the experiments are initiated by outside users, collaborations with beamline scientists are often needed to manage demanding experiments whose success is not always warranted. Due to the youth of the microdiffraction setup and its early opening to users, only 3 publications driven by outside users are related to standard but original use of this new technique. Concerning the GMT instrument, due to its versatility, experiments are usually simpler than on INS from the experimental point of view: sample environment is generally managed by users that may handle experiments with less assistance. The number of publications from outside users is therefore larger than that of beamline scientists. Since applied material experiments aims at characterizing materials from real-life and technological issues, data analysis and interpretation are straightforward and clear results from the X-ray experiments specifically are less numerous.

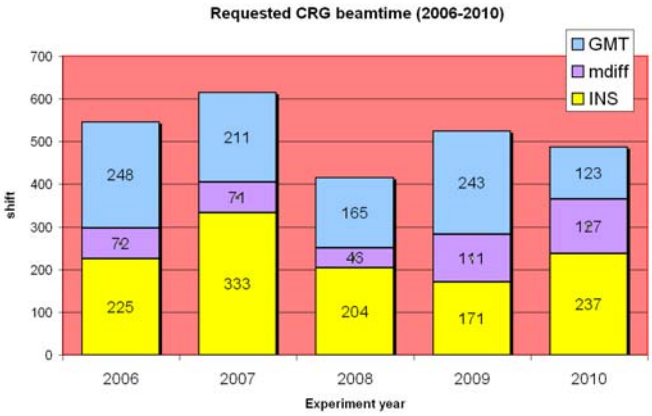

Fig 3 : Distribution of requested CRG beamtime (2006-2010) by BM32 instruments

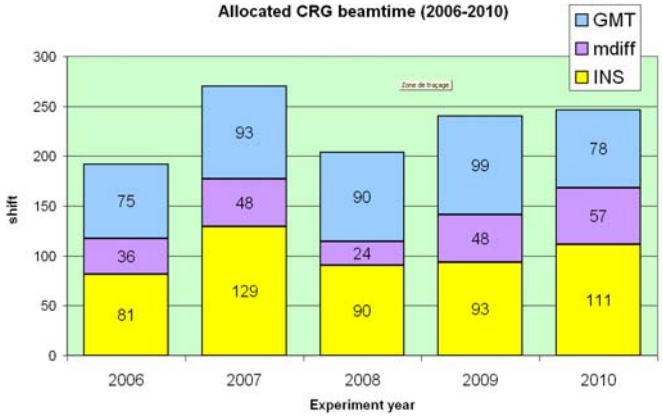

Fig 4 : Distribution of allocated CRG beamtime (2006-2010) by BM32 instruments

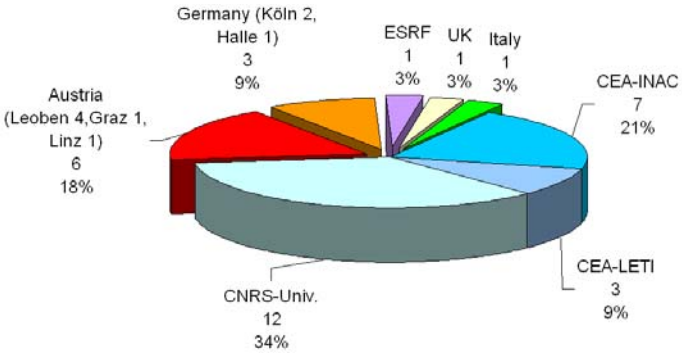

Fig 5 : Main proposer Country Distribution for allocated ESRF experiments (experiment years 2006-2010).

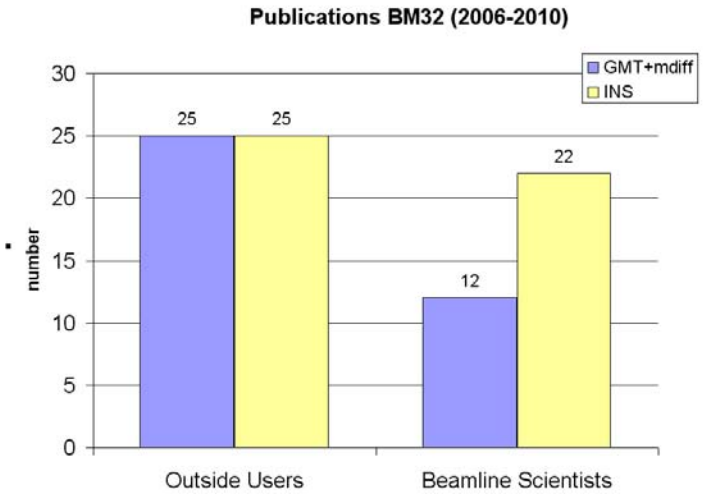

Fig 7 : Number of publications on topics that have been initiated by outside users or beamline scientists (2006-2010)

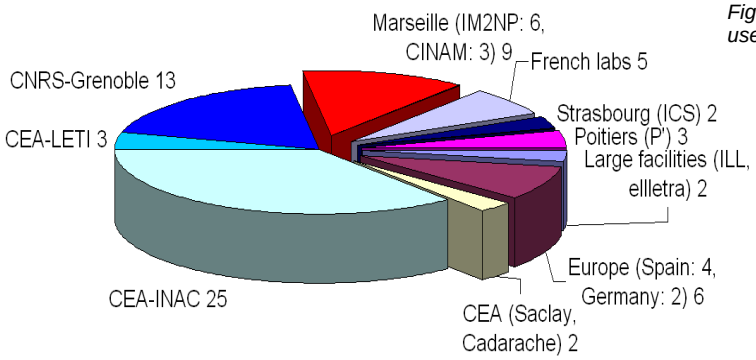

Fig 6 : Main proposer Laboratory distribution for allocated CRG experiments (2006-2010).

Annex 2

Scientific Productions (2006-2010)

In bracket before title, the 2-year impact factor. In parentheses before title, times cited

Microdiffraction (mdiff)

[1.00] " *Determination of global residual stresses in SOFC by X-ray diffraction*"
J. VILLANOVA, O. SICARDY, R. FORTUNIER, J.-S. MICHA, P. BLEUET
Nucl. Instr. Meth. **B**, **268** (2010) 282

[1.38] « *Dislocation storage in single slip oriented Cu micro-tensile sample: New insights by X-ray microdiffraction* »
C. KIRCHLECHNER et al
To appear in Philosophical Magazine, special Issue: Nano-mechanical testing in materials research and development

[1.50] " *Influence on the U_3O_7 domain structure on cracking during the oxidation of UO_2*"
L. DESGRANGES et al,
accepted in J. Nuclear Mat.

« *Towards synchrotron-based nanocharacterization* »
P. BLEUET, L. ARNAUD, X. BIQUARD, P. CLOETENS, L. DOYEN, P. GERGAUD, P. LAMONTAGNE, M. LAVAYSSIÈRE, J.-S. MICHA, O. RENAULT, F. RIEUTORD, J. SUSINI, O. ULRICH
AIP Conf. Proc. 1173, 181 (2009)

In situ Nanostructures and Surfaces (INS)

2010

[31.4]"*Substrate-enhanced supercooling in AuSi eutectic droplets*"
T.-U. SCHÜLLI, R. DAUDIN, G. RENAUD, A. VAYSSET, O. GEAYMOND, A. PASTUREL
Nature, in print, April 2010

[3.32]«Highly ordered growth of Fe and Co clusters on alumina on Ni3Al(111)»;
A. BUCHSBAUM, M. DE SANTIS, H.C.N. TOLENTINO, M. SCHMID, P. VARGA;
Phys. Rev. B **81** (2010) 015011

[3.32]"Nanostructuring surfaces: Deconstruction of the Pt(110)-(1 X 2) surface by C-60";
X. TORRELLES, V. LANGLAIS, M. DE SANTIS, H.C.N. TOLENTINO, Y. GAUTHIER;
Phys. Rev. **B 81** (2010) 041404(R)

[3.44]«*Growth, structure and magnetic properties of FePt nanostructures on NaCl(001) and MgO(001)*»;
LISCIO, F., MAKAROV, D., MARET, M., DOISNEAU-COTTIGNIES, B., ROUSSEL, H., ALBRECHT, M.;
Nanotechnology **21** (2010) 065602

2009

(1) [12.8] "*Probing surface and interface morphology with Grazing Incidence Small Angle X-Ray Scattering* "
G. RENAUD, R. LAZZARI AND F. LEROY,
Surf. Sci. Rep. **64**, 255-380 (2009)

(6)[7.18] "*Enhanced Relaxation and Intermixing in Ge Islands Grown on Pit-Patterned Si(001) Substrates* "
T. U. SCHÜLLI, G. VASTOLA, M.-I. RICHARD, A. MALACHIAS, G. RENAUD, F. UHLIK, F. MONTALENTI, G. CHEN, L. MIGLIO, F. SCHÄFFLER, G. BAUER,
Phys. Rev. Lett. **102**, 025502 (2009)

[3.73] "*Multiple scattering effects in strain and composition analysis of nanoislands by grazing incidence x-rays.*"
M.-I. RICHARD, V. FAVRE-NICOLIN, G. RENAUD, T. SCHÜLLI, C. PRIESTER, Z. ZHONG, AND T.-H. METZGER
Appl. Phys. Lett. **94**, 013112 (2009)

(1) [3.32] „*In situ x-ray scattering study on the evolution of Ge island morphology and relaxation for low growth rate: advanced transition to superdomes*
M.-I. RICHARD, T. U. SCHÜLLI, G. RENAUD, E. WINTERSBERGER, G. CHEN, G. BAUER, V. HOLY,
Phys. Rev. **B 80**, 045313 (2009)

[3.32] "*Defect-pinned nucleation, growth and dynamic coalescence of Ag islands on MgO(001): An in situ grazing-incidence small-angle x-ray scattering study*"
C. REVENANT, G. RENAUD, R. LAZZARI AND J. JUPILLE,
Phys. Rev. B **79**, 235424 (2009)

(3)[3.32] «Adhesion of growing nanoparticles at a glance: Surface differential reflectivity spectroscopy and grazing incidence small angle x-ray scattering »
R. LAZZARI, G. RENAUD, C. REVENANT, J. JUPILLE, AND Y. BORENSZTEIN,
Phys. Rev. B **79**, 125428 (2009)

[0.69] "*Structural properties of Ge/Si(001) nano-islands by diffraction anomalous fine structure and multiwavelength anomalous diffraction* "
M.-I. RICHARD, N.A. KATCH, M.G. PROIETTI, H. RENEVIER, V. FAVRE-NICOLIN, Z. ZHONG, G. CHEN, M. STOFFEL, O. SCHMIDT, G. RENAUD, T.U. SCHÜLLI, AND G. BAUER,
Eur. Phys. J. Special Topics **167**, 3 (2009)

[0.69] "*Real-time icosahedral to fcc structure transition during CoPt nanoparticles formation*",
PENUELAS J, ANDREAZZA P, ANDREAZZA-VIGNOLLE C, MOTTET C, DE SANTIS M, TOLENTINO HCN.
European Physical Journal -SPECIAL TOPICS Volume: **167** Pages: 19-25, Feb. 2009

[0.51] *"Structure, morphology and magnetism of an ultra-thin [NiO/CoO]/PtCo bilayer with perpendicular exchange bias "*,
H. C. N. TOLENTINO, M. De SANTIS, J.-M. TONNERRE, A. Y. RAMOS, V. LANGLAIS, S. GRENIER, A. BAILLY
Brazilian Journal of Physics, vol. **39**, 150 (2009)

2008

(22) [28,1] *"Shape Changes of Supported Rh Nanoparticles During Oxidation and Reduction Cycles"*,
P. NOLTE, A. STIERLE, N. Y. JIN-PHILLIPP, N. KASPER, T. U. SCHULLI, H. DOSCH,
Science **321**, 1654 (2008)

(6) [7,18] *"Depth Magnetization Profile of a Perpendicular Exchange Coupled System by Soft X-ray Resonant Magnetic Reflectivity",*
J. M. TONNERRE, M. DE SANTIS, S. GRENIER, H.C.N. TOLENTINO, V. LANGLAIS, E. BONTEMPI, M. GARCIA-FERNANDEZ, AND U. STAUB
Phys. Rev. Lett. **100**, 157202 (2008)

(4) [7,18] "*Controlling structure and morphology of CoPt nanoparticles through dynamical or static coalescence effects",*
J. PENUELAS, P. ANDREAZZA, C. ANDREAZZA-VIGNOLLE, H.C.N. TOLENTINO, M. DE SANTIS, AND C. MOTTET
Phys. Rev. Lett. **100**, 115502 (2008)

[3.32*] «Structure and morphology of thin MgO films on Mo(001) «*
S. BENEDETTI, P. TORELLI, S. VALERI, H.M. BENIA, N. NILIUS, G. RENAUD
Phys. Rev. B **78**, 195411 (2008)

(5) [3.32] *"Kink ordering and organized growth of Co clusters on a stepped Au(111) surface: A combined GISAXS, GIXD and STM study"*
F. LEROY, G. RENAUD, A. LÉTOUBLON, A. ROHART, Y. GIRARD, V. REPAIN, S. ROUSSET, A. COATTI, Y. GARREAU
Phys. Rev. B **77**, 045430 (2008)

(4)[3.32] *"Growth of Co on Au(111) studied by multiwavelength anomalous grazing-incidence small-angle x-ray scattering: From ordered nanostructures to percolated thin films and nanopillars"*
F. LEROY, G. RENAUD, A. LETOUBLON, R. LAZZARI,
Phys. Rev. B **77**, 235429 (2008)

(6) [3.32] *"Self-organized growth of Ni clusters on a cobalt-oxide thin film induced by a buried misfit dislocation network"*
P. TORELLI, E.A. SOARES, G. RENAUD, L. GRAGNANIELLO, S. VALERI, X. GUO AND P. LUCHES,
Phys. Rev. B **77**, 081409(R) (2008)

(1) [1.73] *"Coalescence of domes and superdomes at a low growth rate or during annealing: Towards the formation of flat-top superdomes"*

M.-I. RICHARD, G. CHEN, T.U. SCHÜLLI, G. RENAUD, G. BAUER,
Surf Sci. **602**, 2157 (2008)

(2) [1.73] *"Structural investigation of silicon nanowires using GIXD and GISAXS: Evidence of complex saw-tooth faceting"*
T. DAVID, D. BUTTARD, T. SCHÜLLI, F. DALLHUIN, P. GENTILE
Surf. Sci **602**, 2675 (2008)

(1) [1.58] *"Real time investigation of the growth ofsilicon carbide nanocrystals on Si(100) using synchrotron X-ray diffraction"*
S. MILITA, M. DE SANTIS, D. JONES, A. PARISINI, V. PALERMO,
Applied Surface Science **254**(7), 2162 (2008)

2007

(10) [3.32] « Self-similarity during growth of the Au/TiO2(110) model catalyst as seen by the scattering of x-rays at grazing-angle incidence "
R. LAZZARI, G. RENAUD, J. JUPILLE, AND F. LEROY
Phys. Rev. **B 76** (2007) 125412

(9) [3.32] "Grazing-incidence small-angle x-ray scattering from dense packing of islands on surfaces: Development of distorted wave Born approximation and correlation between particle sizes and spacing "
R. LAZZARI, F. LEROY, AND G. RENAUD
Phys. Rev. **B 76** (2007) 125411

(10) [3.32] "Size and temperature dependent epitaxy for a strong film substrate mismatch : the case of Pt/MgO(001)"
J. OLANDER, R. LAZZARI, J. JUPILLE, B. MANGILI, J. GONIAKOWSKI, G. RENAUD
Phys. Rev. **B 76** (2007) 075409

(1) [3.32] "*Structure and magnetic properties of Mn/Pt(110)-(1x2): a joint x-ray diffraction and theoretical study"*
M. DE SANTIS, Y. GAUTHIER, H. C. N. TOLENTINO, G. BIHLMAYER, S. BLÜGEL, V. LANGLAIS,
Phys. Rev. B **75**, 205432 (2007)

(1) [3.32] *"Role of hydrogen interaction in two-dimensional molecular packing with strong molecule-substrate bonding"*
V. LANGLAIS, X. TORRELLES, Y. GAUTHIER, M. DE SANTIS,
Phys. Rev. B **76**, 035433 (2007).

(7) [1.73] "X-ray scattering from stepped and kinked surfaces: An approach with the paracrystal model »
LEROY F, LAZZARI R, RENAUD G
Surf. Sci. **601** (2007) 1915-1929

(4) [1.73] "Nanostructuration of a CoO film by misfit dislocations"
P. TORELLI, E. A. SOARES, G. RENAUD, S. VALERI, X. X. GUO AND P. LUCHES
Surf. Sci. **601** (2007) 2651-2655

(6) [1.73] "Structural and morphological evolution of Co on faceted Pt/W(111) surface upon thermal annealing"
C. REVENANT, F. LEROY, G. RENAUD, R. LAZZARI, A. LETOUBLON, T. MADEY
Surf. Sci. **601** (2007) 3431

[1.73] *"Chlorine chemisorption on Cu(001) by surface X-ray diffraction: Geometry and substrate relaxation"*
H. C. N. TOLENTINO, M. DE SANTIS, Y. GAUTHIER, V. LANGLAIS,
Surf. Science **601** (2007) 2962-2966

[1.73] *"Surface structure and composition of the missing-row reconstruction of $VC_{0.8}$(110): A LEED, GIXRD and photoemission study"*
Y. GAUTHIER, I. ZASADA, M. DE SANTIS, V. LANGLAIS, C. VIROJANADARA,
Surf. Science **601** (2007) 3383-3394

"*Structure of the 3C-SiC(100)-5x2 Surface Reconstruction Investigated by Synchrotron Radiation Based Grazing Incidence X-ray Diffraction"*
M. SILLY, H. ENRIQUEZ, J. ROY, M. D'ANGELO, P. SOUKIASSIAN, T. SCHÜLLI, M. NOBLET AND G. RENAUD
Mater. Sci. Forum **556-557**, 533 (2007).

2006

[7.18] *Comment on "Destructive effect of disorder and bias voltage on interface resonance transmission in symmetric tunnel junctions*"
TUSCHE, C; MEYERHEIM, HL; JEDRECY, N; RENAUD, G; ERNST, A; HENK, J; BRUNO, P; KIRSCHNER, J
Phys. Rev. Lett. **96** (2006) 119602

(1) [1.73] *"The epitaxial sexiphenyl (001) monolayer on TiO2(110): A grazing incidence Xray diffraction study"*
R. RESEL, M. OEHZELT, O. LENGYEL, T. HABER, T. SCHÜLLI ET AL.,
Surf. Sci. **600** (2006) 4645

(0) [2.20] *"Strain and composition of ultrasmall Ge quantum dots studied by xray scattering and in situ surface xray absorption spectroscopy"*
DUJARDIN, R; POYDENOT, V; SCHULLI, TU; RENAUD, G; ULRICH, O; BARSKI, A; DERIVAZ, M; COLONNA, S; METZGER, T
J. Appl. Phys. **99** (2006) 063510

(2) [3.7398] *"In situ resonant xray study of vertical correlation and capping effects during GaN/AIN quantum dot growth"*
CORAUX, J; RENEVIER, H; FAVRENICOLIN, V; RENAUD, G; DAUDIN, B
Appl. Phys. Lett. **88** (2006) 153125

(3) [1.00] *"Growth of Ag on MgO(001) studied in situ by grazing incidence small angle Xray scattering"*
REVENANT, C; RENAUD, G; LAZZARI, R; JUPILLE, J
Nucl. Inst. & Meth. Phys. Res. **B**, **246** (2006) 112

(0) [0.97] *"In situ and ex situ grazing incidence diffraction anomalous fine structure study of GaN/AIN quantum dots"*
CORAUX, J; RENEVIER, H; PROIETTI, MG; FAVRENICOLIN, V; DAUDIN, B; RENAUD, G
Phys. Stat. Sol. B **243** (2006) 1519

(1) [1.00] *"In situ investigation by GISAXS and GIXD of the growth mode, strain state and shape of Ge islands during their growth on Si(001)"*
RICHARD, MI; SCHULLI, TU; WINTERSBERGER, E; RENAUD, G; BAUER, G
Nucl. Inst. & Meth. Phys. Res. **B 246** (2006) 35

(2) [1.67] *"Growth mode, strain state and shape of Ge islands during their growth at different temperatures: a combined in situ GISAXS and GIXD study"*
RICHARD, MI; SCHULLI, TU; WINTERSBERGER, E; RENAUD, G; BAUER, G
Thin Solid Films **508** (2006) 213

(6) [3.32] *"Growth sequence and interface formation in the Fe/MgO/Fe(001) tunnel junction analyzed by surface x-ray diffraction"*
C. TUSCHE, H. L. MEYERHEIM, N. JEDRECY, G. RENAUD AND J. KIRSCHNER
Phys. Rev. **B 74** (2006) 195422

(0) [2.20] *"Strain and composition of ultrasmall Ge quantum dots studied by x-ray Scattering and in situ surface xray absorption spectroscopy"*
R. DUJARDIN, V. POYDENOT, T. U. SCHÜLLI, G. RENAUD, O. ULRICH, A. BARSKI, M. DERIVAZ, S. COLONNA AND T. METZGER
J. Appl. Phys. **99** (2006) 063510

(2) [3.98] "*In situ investigation of the island nucleation of Ge on Si(001) using xray scattering methods"*
T. U. SCHÜLLI, M.I. RICHARD, G. RENAUD, AND V. FAVRENICOLIN, E. WINTERSBERGER AND G. BAUER
Appl. Phys. Lett. **89** (2006) 143114

(2) [1.73] *"Ge quantum dots growth on nanopatterned Si(001) surface: Morphology and stress relaxation study"*
PASCALE A, GENTILE P, EYMERY J, MEZIERE J, BAVARD A, SCHULLI T U, FOURNEL F
Surf. Sci. (2006) **600** (16): 3187-3193

(1) [1.73] "*Temperature- and coverage-dependent evolution of the Au/Pd(110) surface structure* ",
KRALJ M, BAILLY A, SAINT-LAGER MC, DEGEN S., KRUPSKI A., BECKER C., DOLLE P., DE SANTIS M., WANDELT K.,
Surf. Sci. **600**, 2614 (2006)

(110) [23.13] former beamlime staff and equipements only
« High-Curie-temperature ferromagnetism in self-organized Ge1-xMn nanocolumns"
JAMET, M; BARSKI, A; DEVILLERS, T; POYDENOT, V; DUJARDIN, R; BAYLE-GUILLEMAUD, P; ROTHMAN, J; BELLET-AMALRIC, E; MARTY, A; CIBERT, J; MATTANA, R; TATARENKO, S
Nature Materials, Vol. **5**, P. 653-659 (2006)

Multitechnique Goniometer (GMT)

2010

[1.94] "*Supported bilayers: combined specular and diffuse x-ray scattering*"
L. MALAQUIN, T. CHARITAT, J. DAILLANT
to appear in to Eur. Phys. J. E
cond-matt http://arxiv.org/abs/0910.1275

[2.20]*"Study of the formation, evolution and dissolution of interfacial defects in silicon direct bonding"*
S. VINCENT, JD PENOT, I RADU, F. LETERTRE,F. RIEUTORD
J. Appl. Phys. (2010) Accepted

2009

(1) [3.73] "*X-ray measurements of the strain and shape of dielectric/metallic wrap-gated InAs nanowires*"
J. EYMERY, V. FAVRE-NICOLIN, L. FROBERG, L. SAMUELSON
Appl. Phys. Lett. **94** 131911 (2009)

(1) [3.73] «*A model of interface defect formation in silicon wafer bonding* »
S. VINCENT, I. RADU, D. LANDRU, F. LETERTRE, F. RIEUTORD
Appl. Phys. Lett. **94** (10) 101914 (2009)

[2.44] "*Prebonding Thermal Treatment in Direct Si-Si Hydrophilic Wafer Bonding*"
C. VENTOSA, F. RIEUTORD, L. LIBRALESSO, F. FOURNEL, C. MORALES, H. MORICEAU, H
J. Electrochem. Soc. **156** (11) H818 (2009)

(2) [2.20] "*Elastic relaxation in patterned and implanted strained silicon on insulator*"
S. BAUDOT, F. ANDRIEU, F. RIEUTORD, J. EYMERY
J. Appl. Phys. **105** (11) 114302 (2009)

[2.01] "*Mechanism of Thermal Silicon Oxide Direct Wafer Bonding*"
C. VENTOSA, C. MORALES, L. LIBRALESSO, F. FOURNEL, A.M. PAPON, D. LAFOND, H. MORICEAU, J.D. PENOT, F. RIEUTORD,
Electrochem. Solid State Lett. **12** (10) H373 (2009)

"*Fluctuations and destabilization of single phospholipid bilayers*"
T. Charitat, S. Lecuyer, G. Fragneto
Biointerphases **3**, Issue 2, pp. 3-15 (2008)

2008

[3.73] "*Germanium oxynitride (GeOxNy) as a back interface passivation layer for Germanium-on-insulator substrates*"
T. SIGNAMARCHEIX, F. ALLIBERT, F. LETERTRE, T. CHEVOLLEAU, L. SANCHEZ, E. AUGENDRE, C. DEGUET, H. MORICEAU, L. CLAVELIER, F. RIEUTORD
Appl. Phys. Lett. **93**(2), 022109 (2008)

(11) [3.73] "*Spontaneous compliance of the InP/$SrTiO_3$ heterointerface*"
G. SAINT-GIRONS, C. PRIESTER, P. REGRENY, G. PATRIARCHE, L. LARGEAU, V. FAVRE-NICOLIN, G. XU, Y. ROBACH, M. GENDRY, G. HOLLINGER
Appl. Phys. Lett. **92**, 241907 (2008)

(3) [1.90] "*Effects of thermal annealing on C/FePt granular multilayers: in situ and ex situ studies*"
D. BABONNEAU, G. ABADIAS, J. TOUDERT, T. GIRARDEAU, E. FONDA, J.-S. MICHA and F. PETROFF,
J. Phys : Cond. Mat. **20**, 035218 (2008)

[2.00] « *Looking by grazing incidence small angle x-ray scattering at gold nanoparticles supported on rutile TiO2(110) during CO oxidation* »
M.C. SAINT-LAGER, A. BAILLY, M. MANTILLA, S. GARAUDEE, R. LAZZARI, P. DOLLE, O. ROBACH, J. JUPILLE, I. LAOUFI, P. TAUNIER

Gold Bulletin **41**, 159 (2008)

(3) [2.20] “Hydrophilic low temperature direct wafer bonding”
C. VENTOSA, F. RIEUTORD, L. LIBRALESSO, C. MORALES, F. FOURNEL, H. MORICEAU,
J. Appl. Phys. **104** 123524 (2008).

2007

(20) [10.37] “*Grazing incidence X-ray measurements of epitaxial InAs/InP nanowires*.”
J. EYMERY, F. RIEUTORD, V. FAVRE-NICOLIN, O. ROBACH, L. FRÖBERG, T. MÅRTENSSON, and L. SAMUELSON
Nano Letters **7** (2007) 2596–2601

[4.10]*"Unexpected stability of phospholipid langmuir monolayers deposited on triton X-100 aqueous solutions*”.
P. FONTAINE, M.C. FAURE, F. MULLER, M. POUJADE, J.S. MICHA, F. RIEUTORD, M. GOLDMANN
Langmuir **23**(26), 12959 (2007)

(11) [3.73] "*Strain field in silicon on insulator lines using high resolution x-ray diffraction* »
GAILHANOU M, LOUBENS A, MICHA JS, CHARLET B., MINKEVICH AA, FORTUNIER R., THOMAS O.
Appl. Phys. Lett. **90** (2007) 111914

(8) [3.32] "*Inversion of the diffraction pattern from an inhomogeneously strained crystal using an iterative algorithm* »
MINKEVICH AA, GAILHANOU M, MICHA JS, CHARLET B., CHAMARD V., THOMAS O.
Phys. Rev. B **76** (2007) 104106

(1) [2.20] “*Quantitative study of hydrogen-implantation-induced cavities in silicon by grazing incidence small angle x-ray scattering* »
L. CAPELLO, F. RIEUTORD, A. TAUZIN, F. MAZEN
J. Appl. Phys. **102** (2007) 026106

(4) [1.74] “*New reactor dedicated to in operando studies of model catalysts by means of surface x-ray diffraction and grazing incidence small angle x-ray scattering*”
M.-C. SAINT-LAGER, A. BAILLY, P. DOLLE, R. BAUDOING-SAVOIS, P. TAUNIER, S. GARAUDÉE, S. CUCCARO, S. DOUILLET, O. GEAYMOND, G. PERROUX, O. TISSOT, J.-S. MICHA, O. ULRICH, and F. RIEUTORD
Rev. Sci. Instrum. **78** (2007) 083902

(1) [1.45] “*Water penetration mechanisms in nuclear glasses by X-ray and neutron reflectometry*”
REBISCOUL D, RIEUTORD F, NE F, FRUGIER P,CUBITT R, GIN S
J. Non Cryst. Solids **353** (2007) 2221-2230

(5) [1.21] "*Investigation by High Resolution X-ray Diffraction of the local strains induced in Si by periodic arrays of oxide filled trenches* »
EBERLEIN M, ESCOUBAS S, GAILHANOU M, THOMAS O., MICHA JS, ROHR P., COPPARD R.
Phys. Stat. Sol.**A 204** (2007) 2542-2547

2006

(30) [1.96] “*Effect of macromolecular parameters and processing conditions on supramolecular organisation, morphology and electrical transport properties in thin layers of regioregular poly(3hexylthiophene)*“
VERILHAC JM, LEBLEVENNEC G, DJURADO D, F. RIEUTORD, M. CHOUIKI, J.-P. TRAVERS, A. PRON
Synthetic Metals **156** (1113) 815-823 2006

(11) [2.20] “ *X-ray scattering study of hydrogen implantation in silicon*“
SOUSBIE N, CAPELLO L, EYMERY J, ET AL.
J. Appl. Phys. **99** (2006) 103509

(1) [1.23] “*Surface plasma treatments enabling low temperature direct bonding*“
MORICEAU H, RIEUTORD F, MORALES C, ET AL..
Microsyst. Techn: Micro and Nanosyst. Inform. Stor. Proc. Syst. **12** (2006) 378382

(1) [3.64] “*Long range molecular organization of an organic monolayer grafted on a mineral substrate*“
STRUTH B, TERECH P, RIEUTORD F
Chem. Phys. Chem. **7** (2006) 756-761

(3) [1.94] “*Extension of the resonant scattering technique to liquid crystals without resonant element*“
FERNANDES P, BAROIS P, GRELET E, ET AL.

Eur. Phys. J. **E 20** (2006) 81-87

(143) [12.93] "*Nanowirebased onedimensional electronics*"
THELANDER C, AGARWAL P, BRONGERSMA S, ET AL.
Materials Today **9** (2006) 28-35

(1) [1.58] "*X-ray scattering: A powerful probe of lattice strain in materials with small dimensions*"
THOMAS O, LOUBENS A, GERGAUD P, ET AL.
Appl. Surf. Sci. **253** (2006) 182-187

(1) [0.16] "*Residual stress analysis in micro and nanostructured materials by Xray diffraction*"
GERGAUD P, GOUDEAU P, SICARDY O, ET AL.
Int. J. Mat. Prod. Tech. **26** (2006) 354- 371

"*Stresses in copper damascene lines: insitu measurements and finite element analysis*"
GERGAUD P, BALDACCI A, RIVERO C, SICARDY O, BOIVIN P, MICHA JS, THOMAS O
AIP CONFERENCE PROCEEDINGS.
(2006) (**816**): 205-210

"*Evolution of Lattice Strain in Hydrogenimplanted Silicon Prior to layer Splitting: An Xray Scattering study*"
L. CAPELLO, F. RIEUTORD, A. TAUZIN, F. MAZEN, N. SOUSBIE, F. LETERTRE
ECS Transactions, vol. **6**, 119-127 (2006)

(5) [1.73] "*Ge quantum dots growth on nanopatterned Si(001) surface: Morphology and stress relaxation study*"
PASCALE A, GENTILE P, EYMERY J, MEZIERE J, BAVARD A, SCHULLI T U, FOURNEL F
Surf. Sci. (2006) **600** (16): 3187-93

"*Rough Surface Adhesion Mechanisms for Wafer Bonding*"
F. RIEUTORD, L. CAPELLO, R. BENEYTON, C. MORALES, A.M. CHARVET, H. MORICEAU
Semiconductor Wafer Bonding 9: Science, Technology, And Applications
ECS Transactions, vol. **3**, ECS Transactions, 2006, 205-215

"*Effect of prebonding surface treatment on SiSi Direct Bonding: Bonding void decrease*"
R. BENEYTON, F. FOURNEL, F. RIEUTORD, C. MORALES, H. MORICEAU
ECS Transactions, vol. **6**, pp. 239-248, 2006

Theses

mdiff

G. DAVEAU. "Size effect in plasticity: simulations and experiments", Ecole Centrale Paris (ECP), (2009-2012)

A. RICHARD , Université de Poitiers " Local strain in implanted Uranium oxides " (2009-2012)

INS

M. I. RICHARD « "The growth of Ge islands on nominal and pre-patterned Si(001) surfaces: in situ and ex situ X-ray studies" Univ. Joseph Fourier, December 14, 2007

-M. M. SOARES, grant RTRA Fondation Nanosciences, 2008-2011

-R. DAUDIN, CEA-CFR "Supercooling in metal-semiconductor eutectic droplets on different semiconductors surfaces" (2008-2011)

GMT

C. VENTOSA, "Mechanisms of wafer bonding" Univ. Joseph Fourier,OCTOBER 02 2009

J.-D PENOT , " Implantation and splitting" Univ. Joseph Fourier (2007-2010)

T. SIGNAMARCHEIX, "Germanium on Insulator (GeOI)" Inst. Nat. Polytech. Grenoble (INPG), DEFENDED IN 2007

S. VINCENT, " Direct bonding " Inst. Nat. Polytech. Grenoble (INPG) 25 SEPTEMBRE 2009

R. FEILLEUX, " Polysilicon bonding" Inst. Nat. Polytech. Grenoble (INPG) (2007-2010)

Books and book chapters

INS

-"Chapter 10: Nanostructures in the light of synchrotron radiation: Surface sensitive x-ray techniques and anomalous scattering"
T. METZGER, V. FAVRE-NICOLIN, G. RENAUD, H. RENEVIER, T. SCHÜLLI
Chapitre de livre: « Characterization of Semiconductor Heterostructures and Nanostructures »
Edited by C. Lamberti, Elsevier 2008, p 361-403

GMT

F. Rieutord "The phase problem in x-ray reflectivity", in X-ray and neutron reflectivity edited by A. Gibaud and J. Daillant (Springer, Berlin, 2008)

mdiff

"X-ray diffraction analysis of elastic strains at the nanoscale"
O. Thomas, O. Robach, S. Escoubas, N. Vaxelaire, O. Perroud
in : Mechanical stress on the nanoscale : simulation, material systems and characterization techniques,
Ed. : M. Hanbücken, P. Müller, U. Gösele, R. B. Wehrspohn, Wiley, 2010 (in preparation)

ESRF highlights and newsletters

ESRF Highlights 2007: "From now to then: real-time studies, nanoscale surface faceting", p 79
C. REVENANT, F. LEROY, G. RENAUD, R. LAZZARI, A. LETOUBLON, T. MADEY

ESRF Highlights 2007: "Determination of the complete stress state of sub-micrometric Cu grains by microdiffraction", p 77
O. SICARDY, X. BIQUARD, J.S. MICHA, F. RIEUTORD, O. ROBACH, O. ULRICH, O. GEAYMOND, V. CARREAU

Conference talks

mdiff

P. Gergaud et al, « Synchrotron-bases Laue MicroTomography for 3D strain imaging" MECASENS V, November 10-12, 2009,mito, japan

P. Gergaud et al, «In situ Sub-micrometer grain analysis within copper lines by synchrotron Laue Diffraction" MECASENS V, November 10-12, 2009,mito, japan

P. Bleuet et al « Towards synchrotron-based nanocharacterization » AIP Conf. (Albany, NY, 11-14th may 2009)

J. Villanova et al " Residual stresses in SOFC" International Fuel Cell Conference Lucern, Switzerland 29th June – 2nd July 2009

J. Villanova et al "Determination of global and local residual stresses in SOFC by X-ray diffraction" spring E-MRS Strasbourg, France, 9-11th June 2009

INS

Meeting of the French Crystallographic Association AFC in Rennes, France. “Relaxation and Intermixing Behavior in SiGe Islands Grown on Prepatterned Si(001)”
T. Schülli et al

X-top 2008, Linz, Austria: Enhanced Relaxation and Intermixing in Ge Islands Grown on Pit-Patterned Si(001) Substrates
T. Schülli et al

Joint annual meeting of the Austrian and Swiss Physical Societies in Innsbruck, Austria. *“X-ray light on SiGe islands and new growth methods – results and challenges for in situ studies of nanostructures”*
T. Schülli et al

GISAS 2009 in Hamburg, Germany. Title: *“Investigation of the growth of Ge islands on nominal and patterned Si(001) substrates”*
T. Schülli et al

“*Evolution of the composition and relaxation of Ge(Si) islands during their growth on nominal and patterned Si(001) substrates by in situ X-ray anomalous scattering*”
3S’09 (International Symposium on the Structure of Surfaces, 2009), St Moritz, 8-14 March 2009
G. Renaud et al.

« *Etudes in situ de la croissance de germanium sur silicium par diffusion des rayons X synchrotron en incidence rasante* ».INSP (Institut des NanoSciences de Paris), March 26, 2009
G. Renaud et al.
«*Monitoring growing nanoparticles with in Situ GISAXS and GIXD* »
Catalysis workshop » ESRF Users’s meeting 2008 Grenoble, Tuesday 5 February 2008
G. Renaud et al.
« Relaxation and Intermixing of Ge Islands on nominal and pit-patterned Si(001) surfaces from kinetics to equilibrium thermodynamics »
ICSOS9 Brésil (International Conference on the Structure of Surfaces, Salvador, Août 2008, Brésil)
G. Renaud et al.
« *Evolution of the composition of Ge islands during their growth on Si(001) by in situ grazing incidence x-ray anomalous scattering*”
ICSOS9 Brésil (International Conference on the Structure of Surfaces, Salvador, Août 2008, Brésil)
G. Renaud et al.
« *Combined in situ GISAXS and GIXD study of the growth of Ge islands on nominal and patterned Si(001) surfaces*”
MRS Fall meeting 2008, Boston
G. Renaud et al.
« *Diffraction de surface: un aperçu* »
3ième Ecole Française de Réflectivité, SAXS, GISAXS et Diffraction de Surface Giens, Mai 2008
G. Renaud et al.
« *Structure et morphologie des nano-objets par diffusion/diffraction des rayons X en incidence rasante GISAXS / GIXD (/ EXAFS)* »
Cours : Ecole thématique CNRS « Nano-Objets », Villeneuve D’Ascq, 3-6 nov. 2008
G. Renaud et al.
« *The growth of nanoparticle on surfaces, organized or not, investigated by in situ GISAXS and GIXD in UHV* «
Exposé invité au Institut für Hableiter-und Festkörperphysik de Johannes Kepler Universitât Linz, Austria, Décembre 2008.
G. Renaud et al.

“Structure and magnetism of thin films by Surface X-ray Diffraction” 5th Brazilian Materials Research Society Meeting (SBPMat), Florianopolis, Brazil, October 8-12, 2006

“Profil d’aimantation perpendiculaire dans une bicouche AF/F par réflectivité magnétique résonante des rayons X”Congrès de la SFP, Grenoble, France. 8 au 13 Juillet 2007. Hélio C.N. Tolentino et al.

“Surface structure and magnetism in a perpendicular exchange bias [NiO/CoO]/[PtCo]/Pt(111) system” E-MRS, Warsaw, Polland, 17 to 21 September 2007 Hélio C.N. Tolentino et al.

“Structure and magnetic properties of a NiO/CoO/Pt−Co film epitaxially grown on Pt(111).” ECSCD−9 • 9th European Conference on Surface Crystallography and Dynamics, Vienna, Austria, September 2-5, 2007 , M. De Santis, H. C. N. Tolentino, J. M. Tonnerre, A. Bailly, M. C. Saint−Lager

“Structure and Magnetism of ultra thin films by surface X-ray diffraction” Rencontre Franco-brésilienne de Nanoscience, Nanotechnologie et Bionanotechnologie, Brasilia, Brésil. 18 au 23 Novembre 2007. Hélio C.N. Tolentino

“Atomic structure and magnetic properties of nanostructures by surface X-ray scattering and absorption techniques using synchrotron light”. NSEQO - Workshop on Nanomagnetism, Spin-Electroncis and Quantum Optics, Rio de Janeiro, Brazil, November 11-13, 2009. Hélio C.N. Tolentino et al

GMT

“Strain determination in nanostructures via X-ray scattering measurements”
O. Thomas et al.
SizeDepEn Workshop Size-dependent materials behaviour: Challenges in miniaturisation and materials characterisation - March 15th -16th 2007, Fraunhofer Institut für Werkstoffmechanik Freiburg (Allemagne)

“Local strains in micro and nanostructures using synchrotron radiation”
O. Thomas et al.
ICMCTF 2007, International Conference on Metallurgical Coatings and Thin Films, April 23-27, 2007 San Diego, USA

“Diffraction analysis of elastic strains in micro- and nano-structures (keynote lecture)”
O. Thomas et al.
Size&Strain V 2007, "Diffraction analysis of the microstructure of materials", October 7-9 2007, Garmisch-Partenkirschen (Allemagne).

4 lectures on: Deducing strains and stresses from X-ray diffraction
Advanced synchrotron techniques and small dimensions
O. Thomas et al.
CISM - International Centre for Mechanical Sciences -Mechanical Size-Effects of Materials: Processing, Characterization and Modeling - Udine, May 12 - 16, 2008.

“ La diffraction des rayons X et la mécanique des nano-objets : état de l'art et perspectives » (Conférence semi-plenière)
O. Thomas et al.
11ème Journées de la Matière Condensée - Strasbourg août 2008

« Strain measurements at the nanoscale: micro-beam Laue scattering and coherent x-ray diffraction »
O. Thomas et al.
EPDIC 11, European Powder Diffraction Conference, Varsovie, 18 septembre 2008

« Local strains in micro and nanostructures using synchrotron radiation »
O. Thomas et al.
NANOSTRESS school, Cargese, 29 septembre - 5 octobre 2008

« X-ray structural studies of nanowires »
. J. Eymery
3SN'2008, Summer School on Semiconductor Nanowires, GDR Nanofils Nanotubes Semiconducteurs, june 15-20, 2008, Roscoff, France

“Guided growth on templates – Use of strain”
J. Eymery
Nanostress, Cargese Summer School, CNRS-Max Planck-Fraunhofer-Carnot, 29 Sept. – 5 Oct. 2008

“Structure and dynamic of DNA confined between non cationic lipid membranes”
L. Navailles, E. Andreoli de Oliveira, F. Nallet, E. Grelet, A. Fevrier & J. Dobrindt
2nd French Brazilian Polymer Meeting FBPOL2008, 20-25 April 2008, Florianòpolis, Brazil.

“ Organization of DNA fragments between lipid bilayers”
E. Andreoli de Oliveira, L. Navailles, , F. Nallet, E. Grelet, A. Fevrier & J. Dobrindt
Workshop of application of synchrontron radiation on soft matter, fev. 2008, LNLS- Campinas –Brasil

“Study of Fluctuation and Destabilization of Single Phospholipidic Bilayer by Neutron and X-ray Scattering”
T. Charitat et al
54th AVS Meeting,
Seattle, 14-19 Octobre 2007

“Neutron and X-ray scattering to investigate supported bilayer's physical Properties”
T. Charitat et al
Biological Physics at Large Facilities, 19-23 Grenoble, Octobre 2008

Patents

L. LIBRALESSO, C. MORALES, H. MORICEAU, F. RIEUTORD,
« Traitement de surface par plasma d'azote dans un procédé de collage direct » DD10510 (2008)

F. RIEUTORD
« Monochromateur rayons X ou neutron par collage moléculaire » DD2878 (2006)

Prizes

mdiff

J. Villanova
“Young scientist award”, symposium R , E-MRS Strasbourg 2009

GMT

L. Capello
Best contributed paper prize , Wafer Bonding International Symposium, Cancun (2006)

C.Ventosa
“Best student paper prize” ElectroChemical Society International Conference, Hawaii USA (Oct08)

INS

R.Daudin
prix master de la SF2M Octobre 2009

Annex 3a: Reprints of selected publications

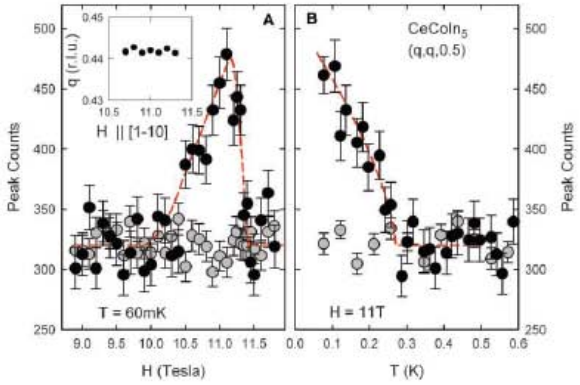

Fig. 3. Neutron-scattering intensity at (*q*, *q*, 0.5), (**A**) as a function of field at $T = 60$ mK and (**B**) as a function of temperature at $H = 11$ T. The gray circles represent the background scattering taken from the two nearest to the center channels of the psd. The dashed red line in (A) is a guide to the eye, whereas the dashed line in (B) describes the background and the onset of the magnetic order in a second-order phase transition with $\beta = 0.365$ fixed to the critical exponent of the three-dimensional Heisenberg universality class. The inset shows that the *q* is field-independent.

The intimate link between superconductivity and magnetic order in $CeCoIn_5$ suggests the presence of a specific coupling between these order parameters (*23*). The multicomponent magneto-superconducting phase can be reached via two second-order phase transitions through a suitable path in the *H-T* phase diagram, which justifies the construction of a phenomenological Landau coupling theory. If one assumes that the superconducting gap at zero field Δ_d has d_{x2-y2} symmetry, the possible coupling terms for magnetic fields in the basal plane that preserve time-reversal symmetry and conserves momentum can be written as $V_1 = \Delta^*_d M_q (H_x\Delta^{(5)}_{y,-q} + H_y\Delta^{(5)}_{x,-q}) + c.c.$, $V_2 = \Delta^*_d M_q (H_xD_x - H_yD_y)\Delta^{(2)}_{-q} + c.c.$, and $V_3 = \Delta^*_d M_q (H_xD_y - H_yD_x)\Delta^{(3)}_{-q} + c.c.$ Here, $(\Delta^{(5)}_{x,-q}, \Delta^{(5)}_{y,-q})$ belongs to the two-component even-parity Γ^+_5 state, $\Delta^{(2)}_{-q}$ and $\Delta^{(3)}_{-q}$ are the Γ^-_2 and Γ^-_3 odd-parity states (*24*), *c.c.* stands for the complex conjugate of the preceding term, and M_q is the magnetic-order parameter. These additional superconducting order parameters include a finite momentum $-q$. (D_x, D_y) is the gauge invariant gradient. Introducing the magnetic field allows one to couple M_q in linear order to preserve time-reversal symmetry. These combinations allow for a second-order phase transition within the superconducting phase and a first-order transition to the nonmagnetic normal state. For the coupling term V_2, no magnetic structure is induced for fields **H** || [100]. Given the weak dependence of the **Q** phase on the magnetic field orientation in the basal plane, our measurements suggest the presence of a V_1 or V_3 coupling term, inducing the finite-momentum even-parity Γ^+_5 state or the odd-parity Γ^-_3 state.

This Landau theory shows that incommensurate magnetic order induces a superconducting gap function that carries a finite momentum—the first experimental evidence of a superconducting condensate that carries a momentum. However, we show that this state may not arise purely from Pauli paramagnetic effects and the formation of a new pairing state between exchange-split parts of the Fermi surface, a state commonly known as the FFLO state (*16*, *17*). In the FFLO state, the pairing state carries a momentum of the Cooper pair that depends on the magnetic field via $|q| = 2\mu_B H/\hbar v_F$, where v_F is the Fermi velocity. However, the inset of Fig. 3A shows that $|q|$ is field-independent in $CeCoIn_5$, at odds with this prediction, which indicates that an additional superconducting pairing channel with finite momentum is induced in conjunction with the cooperative appearance of magnetic order.

A superconducting order that carries momentum illustrates the wealth of quantum phases that can exist in solid matter. The important microscopic role of magnetic fluctuations in the formation of Cooper pairs in $CeCoIn_5$ is self-evident because superconductivity emerges at $H_{c2}(0)$ simultaneously with ordered magnetism.

References and Notes

1. C. Petrovic *et al.*, *J. Phys. Condens. Matter* **13**, L337 (2001).
2. A. D. Bianchi, R. Movshovich, I. Vekhter, P. G. Pagliuso, J. L. Sarrao, *Phys. Rev. Lett.* **91**, 257001 (2003).
3. J. Paglione *et al.*, *Phys. Rev. Lett.* **91**, 246405 (2003).
4. K. Izawa *et al.*, *Phys. Rev. Lett.* **87**, 057002 (2001).
5. N. J. Curro *et al.*, *Phys. Rev. B* **64**, 180514 (2001).
6. R. Movshovich *et al.*, *Phys. Rev. Lett.* **86**, 5152 (2001).
7. A. Vorontsov, I. Vekhter, *Phys. Rev. Lett.* **96**, 237001 (2006).
8. D. Hall *et al.*, *Phys. Rev. B* **64**, 212508 (2001).
9. R. Settai *et al.*, *J. Phys. Condens. Matter* **13**, L627 (2001).
10. A. D. Bianchi *et al.*, *Phys. Rev. Lett.* **89**, 137002 (2002).
11. A. D. Bianchi, R. Movshovich, C. Capan, P. G. Pagliuso, J. L. Sarrao, *Phys. Rev. Lett.* **91**, 187004 (2003).
12. A. D. Bianchi *et al.*, *Science* **319**, 177 (2008).
13. K. Kakuyanagi *et al.*, *Phys. Rev.* **94**, 047602 (2005).
14. T. Watanabe *et al.*, *Phys. Rev. B* **70**, 020506 (2004).
15. H. A. Radovan *et al.*, *Nature* **425**, 51 (2003).
16. P. Fulde, R. A. Ferrell, *Phys. Rev.* **135**, A550 (1964).
17. A. I. Larkin, Y. N. Ovchinnikov, *Sov. Phys. JETP* **20**, 762 (1965).
18. P. Monthoux, D. Pines, G. G. Lonzarich, *Nature* **450**, 1177 (2007).
19. J. Flouquet *et al.*, *C. R. Phys.* **7**, 22 (2006).
20. B. L. Young *et al.*, *Phys. Rev. Lett.* **98**, 036402 (2007).
21. Materials and methods are available as supporting material on *Science* Online.
22. C. Stock, C. Broholm, J. Hudis, H. J. Kang, C. Petrovic, *Phys. Rev. Lett.* **100**, 087001 (2008).
23. A. Aperis, G. Varelogiannis, P. B. Littlewood, B. D. Simons, *J. Phys. Cond. Mat.*, in press; preprint available at http://arxiv.org/PS_cache/arxiv/pdf/0804/0804.2460v1.pdf.
24. M. Sigrist, K. Ueda, *Rev. Mod. Phys.* **63**, 239 (1991).

25. Work at ETH was supported by the Swiss National Science Foundation under contract PP002-102831. This work is based on experiments performed at the Swiss spallation neutron source SINQ, Paul Scherrer Institute, Villigen, Switzerland, and was supported by the Swiss National Center of Competence in Research program Materials with Novel Electronic Properties. Work at Los Alamos was performed under the auspices of the U.S. Department of Energy and supported in part by the Los Alamos Laboratory Directed Research and Development program. A.D.B. received support from the Natural Sciences and Engineering Research Council of Canada (Canada), Fonds Québécois de la Recherche sur la Nature et les Technologies (Québec), and the Canada Research Chair Foundation.

Supporting Online Material

www.sciencemag.org/cgi/content/full/1161818/DC1
Materials and Methods
References

16 June 2008; accepted 7 August 2008
Published online 21 August 2008;
10.1126/science.1161818
Include this information when citing this paper.

Shape Changes of Supported Rh Nanoparticles During Oxidation and Reduction Cycles

P. Nolte,[1] A. Stierle,[1]* N. Y. Jin-Phillipp,[1] N. Kasper,[1] T. U. Schulli,[2] H. Dosch[1]

The microscopic insight into how and why catalytically active nanoparticles change their shape during oxidation and reduction reactions is a pivotal challenge in the fundamental understanding of heterogeneous catalysis. We report an oxygen-induced shape transformation of rhodium nanopartides on magnesium oxide (001) substrates that is lifted upon carbon monoxide exposure at 600 kelvin. A Wulff analysis of high-resolution in situ x-ray diffraction, combined with transmission electron microscopy, shows that this phenomenon is driven by the formation of a oxygen–rhodium–oxygen surface oxide at the rhodium nanofacets. This experimental access into the behavior of such nanoparticles during a catalytic cycle is useful for the development of improved heterogeneous catalysts.

Many industrial chemicals and fuels are synthesized with the use of heterogeneous, solid-phase catalysts that often contain metals in the form of nanoparticles (NPs). The direct study of these catalysts is challenging, and model catalysts such as single crys-

tals and vicinal surfaces have been extensively investigated and have provided important insights (*1*–*3*). The emerging challenge for fundamental research is to provide a detailed microscopic understanding of the different physical and chemical processes that take place at NPs during catalytic reactions. Although there is a consensus that NPs should exhibit enhanced catalytic activity because (i) they posses an increased number of undercoordinated atoms and (ii) different low-index facets coexist [which should facilitate mass transport and thereby lift kinetic barriers known from single crystal surfaces (*4*)], it is still an open question as to whether the metallic or the oxidized state of the particle is the catalytically more active phase [Langmuir-Hinshelwood versus Mars–van Krevelen mechanism (*5*, *6*)]. During catalytic cycling experiments, NPs undergo reversible size changes that are associated with cyclic shape changes, material redispersion, and sintering (*7*, *8*).

Among the many catalytically active metals, the 4d transition metals [Ru, Rh, Pd, and Ag (*1*)] are finding increased use in organic reactions, the synthesis of biologically active compounds under sufficiently mild conditions, and the treatment of contaminated water. Rh is a well-known catalyst for hydrocarbon and CO oxidation, as well as for NO_x reduction in three-way car catalysts (*9*). Recent experimental and theoretical studies of 4d transition metal single-crystal surfaces carried out near atmospheric pressures suggest that their catalytic activities are related to an ultrathin metal oxide film on the surface (*5*, *10*–*12*). In the case of Rh, a hexagonal O–Rh–O trilayer structure forms basically independently of the surface orientation whenever the oxygen chemical potential is near that of the bulk oxide (*11*, *13*, *14*). To date, it is not clear if such surface oxides do also form on the different facets of NPs and, if so, whether they are relevant in industrial catalysis.

In the past, transmission electron microscopy (TEM) has shown that metal NPs undergo shape changes as a function of the gas composition (*15*–*17*). Scanning tunneling microscopy experiments on the top facet of flat NPs have illustrated oxygen-induced superstructures at the edges of different facets (*18*), and recently, the shape of unsupported Pd and Rh NPs was investigated by density functional theory as a function of the oxygen chemical potential using the Wulff construction (*19*). The results of these experiments prove that surface oxides stabilize the low-index (100), (110), and (111) facets at chemical potentials near that for bulk oxide formation, which results in an overall rounding of the NPs.

To upgrade our microscopic understanding of the catalytic activity of NPs, the interplay between the shape and size change of the NPs and the oxidation/reduction process must be established. Here, we report an in situ high-resolution x-ray diffraction (XRD) study of epitaxial Rh NPs on MgO(001) during oxidizing and reduction reactions, which uncovers a reversible facet rearrangement of the NP in direct relation to the formation of oxygen-induced superstructures. From a quantitative analysis of the extended reciprocal-space maps that have been recorded from the Rh nanofacets at elevated temperatures and under varying gas atmospheres, we can access the average NP shape and size with atomic resolution and obtain robust atomic insights into the structure of the surface oxide forming on the facets.

The XRD experiments were performed at beamline BM32 of the European Synchrotron Radiation Facility and at the Max Planck beamline of the Angström Quelle Karlsruhe. The photon energies were 11.04 and 10.5 keV, respectively. The in situ x-ray analysis was complemented by high-resolution TEM (HRTEM) performed on a JEOL 1250 atomic-resolution microscope that is operated at 1250 kV (*20*).

In the first experimental setup, we deposited the Rh NPs in situ at a substrate temperature of 670 K in the BM32 ultrahigh vacuum (UHV) surface XRD chamber, after cleaning the MgO substrates by sputtering and annealing under oxygen atmosphere (*20*). After the growth and an initial oxidation/reduction cycle, the sample was annealed at 970 K to achieve the equilibrium shape of the NPs. Wide-angle diffraction reciprocal-space mapping and grazing-incidence small-angle scattering (GISAXS) were performed simultaneously (*20*). In the second experimental setup, Rh was deposited on MgO in a laboratory UHV chamber, annealed at 870 K, and the sample was subsequently transferred into a portable UHV XRD chamber, which was shipped to the synchrotron radiation facility while maintaining UHV conditions. The epitaxial relation between the Rh NPs and the MgO substrate was determined from reciprocal-space scans in high-symmetry directions. We find that the Rh NPs grow in a cube-on-cube epitaxy on MgO(001), with an in-plane angular distribution of 1.7°. After the annealing, the average lattice constant of the particles is equal to the bulk value for Rh (a_{fcc} = 0.380 nm, where fcc is face-centered cubic), resulting in a misfit of 9% to the MgO substrate. The particles exhibit a typical size distribution of ~30%.

Figure 1A is a schematic view of the NP model together with the four shape parameters N_P, N_T, N_B, and N_E, which can be interrogated by XRD (*21*). N_P describes the particle diameter given by $a_{fcc}/\sqrt{2}\cdot N_P$; N_T and N_B describe the number of atomic layers involved in the top and bottom part of the particle, respectively. The parameter N_E gives the number of layers removed from the particle corners to form the side [100] type facets. The extended reciprocal-space maps contain detailed information about the shape and size of nanoscale objects (*22*). This is illustrated in Fig. 1B, which shows an experimental wide-range reciprocal-space map of the (110) plane taken at 600 K. The (111) Bragg reflection in the center of the map is interconnected with the neighboring Bragg reflections by broad intensity ridges along the [001], [–1,1,1], and [1,–1,1] directions that emanate perpendicularly from the associated facets. The observation and quantitative analysis of these so called "crystal truncation rods" (*23*) in four symmetry-equivalent directions gives direct evidence for the truncated pyramidal shape of the nano-objects under investigation.

To obtain detailed information on the size and shape of the NPs, high-resolution reciprocal-space maps have been recorded from $(H,K) = (-0.5,0.5)$ to (0.5,–0.5) and from $L = 0.6$ to 0.84, as indicated by the white box in Fig. 1B (here, H, K, and L represent the Miller indices of the bulk reciprocal lattice). In Fig. 2A (top) a high-resolution map of

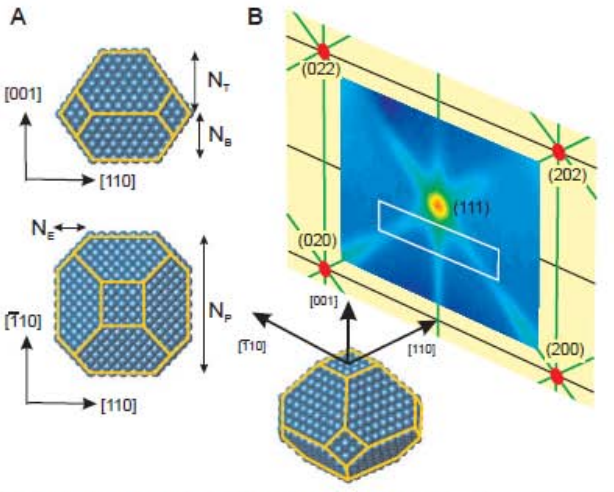

Fig. 1. (**A**) Schematic representation of the particle shape for fcc-based NPs. The lateral particle size is characterized by $a_{fcc}/\sqrt{2}\cdot N_P$, its height by $a_{fcc}/2\cdot(N_T + N_B)$, and the missing edge atoms by N_E. For a Wulff shaped particle (without substrate), $N_T = N_B$ and $N_E = N_P - N_T$ (*25*). (**B**) (110) plane reciprocal-space map of clean Rh NPs on MgO(001) with an average lateral size of 8 nm. Fcc bulk coordinates are used throughout the text, if not otherwise indicated. The white box indicates the area for high-resolution scans used for the quantitative analysis. The reciprocal-space area close above the Bragg peaks cannot be used, because it contains, on the (111) type rods, signal from internal twinning of the particles at ($^4/_3$,$^2/_3$,$^4/_3$), ($^2/_3$,$^4/_3$,$^4/_3$), and equivalent positions (Fig. 4).

[1]Max-Planck-Institut für Metallforschung, Heisenbergstrasse 3, D-70569 Stuttgart, Germany. [2]Institut Nanosciences et Cryogénie/Service de Physique des Matériaux et des Microstructures, Commissariat à l'Energie Atomique, Grenoble, 38054 Grenoble Cedex 09, France.

*To whom correspondence should be addressed. E-mail: stierle@mf.mpg.de

the clean particles is plotted, as observed at 600 K under UHV conditions. The data can be understood in a straightforward way within a kinematical diffraction theory that discloses NPs with truncated octahedral shape (*20*). Figure 2A (middle) shows the best intensity fits associated with the average particle shape presented in Fig. 2A (bottom).

A straightforward understanding of the shape of a NP is provided by the Wulff construction, which is based on the rule $\frac{\gamma_i}{h_i}$ = constant (here, γ_i is the surface energy of facet plane i with distance h_i from the center of the unsupported particle) (*24*). From the fit to the data, we obtain the following parameter values: $N_P = 31 \pm 1$, $N_T = 20 \pm 1$, $N_B = 5 \pm 1$, and $N_E = 3 \pm 1$, corresponding to an average NP diameter of 8.3 nm and an average NP height of 4.8 nm. For the ratios of the surface energies, we deduce $\frac{\gamma_{100}}{\gamma_{111}} = \frac{h_{100}}{h_{111}} = \sqrt{3}\cdot\frac{N_T}{N_P} = 1.12 \pm 0.09$ for the top facets, which agrees well with the theoretical value of $(\gamma_{100}/\gamma_{111})^* = 1.16$ (*19*), but $\frac{\gamma_{100}}{\gamma_{111}} = \sqrt{3}\frac{N_P - N_E}{N_P} = 1.56 \pm 0.06$ for the side facets (the asterisk indicates theoretical values). This marked deviation from the expected value of $(\gamma_{100}/\gamma_{111})^*$ means that the side facets are noticeably smaller than predicted by the Wulff argument. We suggest that this observation is related to strain and/or NP edge effects (line tensions) neglected in the Wulff approach. The Rh NP adhesion energy $E_{ad} = \gamma_{100}\cdot\frac{N_T - N_B}{N_T} = 108 \pm 10$ meV/Å^2 (*25*) is less than the theoretical value $E_{ad}^* = 130$ meV/Å^2 associated with one extended monolayer of Rh on MgO(001), which is in-line with the trend that the adsorption energy decreases as a function of the Rh coverage (*26*).

In the next step, the Rh NPs were exposed to 3×10^{-5} mbar O_2 at 600 K [i.e., above the oxygen chemical potential for Rh_2O_3 bulk oxide formation (*27*)], and we simultaneously recorded the XRD pattern (Fig. 2, B and C). We observed a distinct change in the XRD signal (see difference map in Fig. 2B) that essentially consists of an intensity enhancement along the (001) rod and an intensity loss along the (111) rods, which can also be observed in the large area difference map in fig. S2B (*28*). The best fit to this x-ray intensity change (Fig. 2B) results in an average NP shape as characterized by $N_P = 31 \pm 1$, $N_T = 16 \pm 1$, $N_B = 5 \pm 1$, and $N_E = 7 \pm 1$ (Fig. 2C), with an unchanged average NP diameter of 8.3 nm and a reduced average height of 4 nm. These reconfigured Rh NPs now have a nanosized oxide skin composed of an ultrathin hexagonal surface oxide layer, as we explain below.

An unexpected result of this analysis is that the area of both the (100) side facets and the (001) top facet increases upon oxidation (*29*). This result implies that only intraparticle mass transport takes place during oxidation, which removes Rh atoms from the (100) side and top facets with an average amount that corresponds to the number of atoms incorporated into the surface oxide layers on all facets. However, the strong increase of the (110) facet area, which is predicted by theory (*19*) for the conditions applied, was not observed. Furthermore, no additional facets are formed in between the top (001) and (111) facets (they would readily be observable via additional diffraction intensities).

To get a microscopic insight into the forces that drive this NP shape transformation, we interrogated the atomistic structure of the oxidized (001) and (111) facets by quantitative surface XRD. Figure 3A shows a line scan along the (1,–1,0) direction ($L = 0.3$) associated with clean NPs and NPs exposed to 2×10^{-5} mbar oxygen at 500 K, which witnesses the formation of an oxygen-induced (3x1) superstructure at the top (001) nanofacet that progressively disappears upon further oxidation. The intensity of these superstructure reflections cannot be explained by a simple oxygen chemisorption structure; it is rather in line with a shifted-row structure that creates threefold adsorption sites for oxygen (Fig. 3B). The two-dimensional character of this structure can be inferred from the rodlike diffraction pattern (fig. S4). A similar structure appears during the oxidation of $Pt_{25}Rh_{75}$(100) single crystals (*30*) as a precursor for the surface oxide formation on Rh(100) (*13*).

When the sample temperature was only slightly increased to 550 K, a fast transformation takes place on the (001) top facets from the (3×1) adsorption structure to the hexagonal surface oxide that forms a c(2×8) coincidence structure with the underlying Rh lattice (Fig. 3, C and E) (*13*). At the same time, on the (111) side facets a hexagonal surface oxide is formed with a p(9×9) coincidence structure. The c(2×8) coincidence structure on the (001) facets and the p(9×9) structure on the (111) facets give rise to additional peaks that can be readily identified (Fig. 3C).

In the presence of the surface oxide on both the (111) and (100) facets, the theoretical value of the surface free energy ratio is lowered to $(\gamma_{100}/\gamma_{111})^* = 0.9$ (*19*). This value needs to be compared with our experimental data $(\gamma_{100}/\gamma_{111}) = \sqrt{3}\cdot\frac{N_T}{N_P} = 0.89 \pm 0.09$ and $(\gamma_{100}/\gamma_{111}) = \sqrt{3}\frac{N_P - N_E}{N_P} = 1.34 \pm 0.07$ for the top and side (100) facets, respectively. Thus, the observed increase of the total (100) type facet surface area is in good agreement with the Wulff prediction and can be directly related to the slightly higher stability of the surface oxide on the (100) facets, as compared with the (111) facets. Although bulk oxide formation is thermodynamically favored under the conditions applied (*27*), the surface oxide at

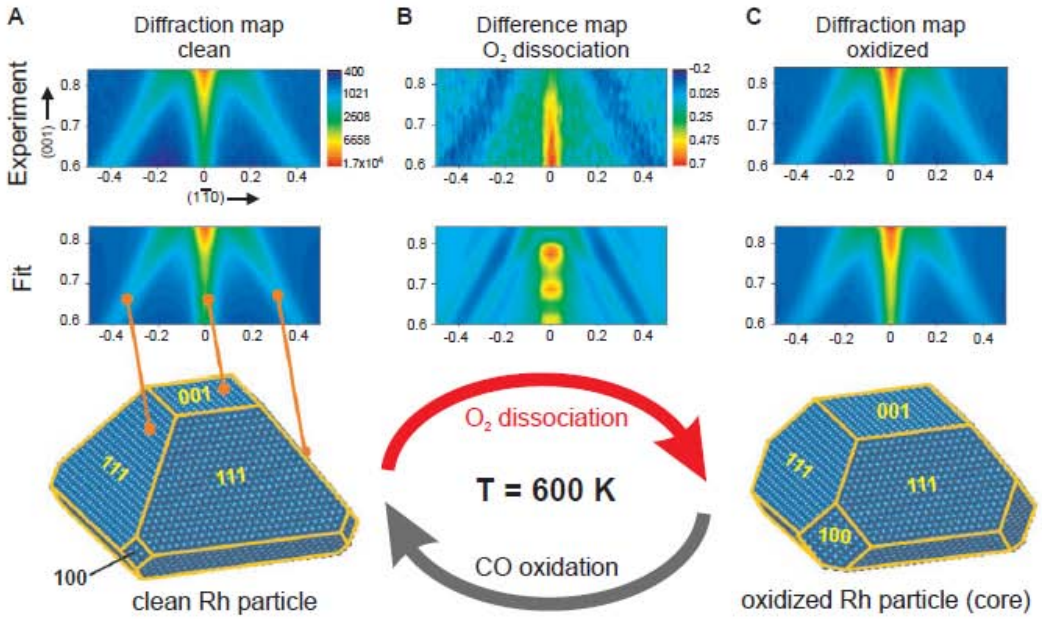

Fig. 2. (**A**) (Top) (110) diffraction map of clean Rh particles at 600 K. (Middle) Fitted diffraction map corresponding to the average particle shape given below. (**B**) (Top) oxygen-induced signal change in the (110) plane. (Middle) Simulated signal change for particles with increased (100) side facet area. (**C**) (Top) Experimental (110) diffraction map at 600 K and 2×10^{-5} mbar O_2 pressure. (Middle) Fitted diffraction map for particles under oxygen exposure. (Bottom) Best-fit core particle shape after oxidation.

the Rh nanofacets is metastable and prevents bulk oxide growth.

A further key observation is that the oxygen-induced shape change of the Rh NPs is fully reversible when the surface oxide is removed by CO exposure (at 1×10^{-5} mbar). The observed x-ray intensity line scans (Fig. 3, C and E) obtained after reduction are identical to the clean particle scans, which is evidence for decomposition of the facet oxide layers. Simultaneously, the oxygen-induced intensity change of the scattering from the (111) and (001) facets (Fig. 2B) is reversible, as can be inferred from the line scans in fig. S3, demonstrating the reformation of the clean particle facets.

Complementary information on the shape of the Rh NPs has been obtained by GISAXS (*31*), which has been carried out parallel to the above surface XRD experiment and by cross-section HRTEM (*20*). The observed marginal changes of the GISAXS patterns and associated line scans for two different azimuths confirm that the average particle size does not change during the oxidation and reduction process (fig. S5). The cross-section TEM image (Fig. 4) taken of a Rh NP on MgO(001) along the (110) direction uncovers a NP shape that corresponds very well with the x-ray results (dashed line in Fig. 4A). We also observed structures with a different periodicity on the particle facets that can be identified as oxide over layers. In some cases (for instance, on the right facet of the particle in Fig. 4A), a one-monolayer-thick oxide layer can be observed with atomic resolution. The zoomed-in view of the white box in Fig. 4A reveals a surface layer on the (111) facet with a different periodicity, a finding that is strongly supported by the simulated TEM image contrast for the O–Rh–O surface oxide trilayer (box in Fig. 4B). The observation that the surface oxide is present, even after exposure of the sample to ambient conditions and the rather destructive TEM specimen preparation, gives us the first evidence for the presence of noticeable kinetic barriers toward bulk oxide formation once the surface oxide is formed.

Our high-resolution in situ oxidation experiments demonstrate that the surface oxide O–Rh–O trilayer stabilizes Rh NPs with low-index facets. We assume that this reversible shape transformation also occurs for smaller particles [as long as they have (111) and/or (100) facets] and that the observed surface oxide formation at the facets of the NPs also takes place in oxidation catalysis involving Rh NPs under technologically relevant conditions.

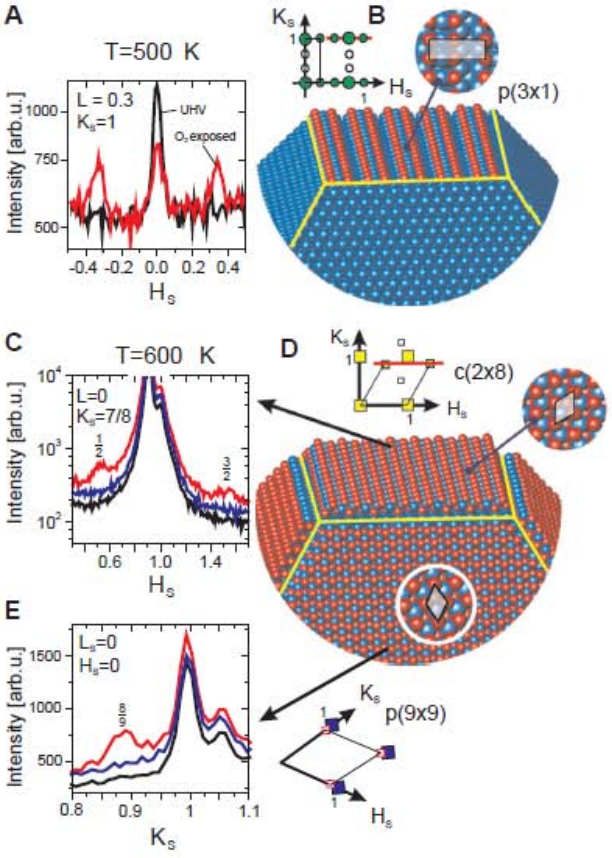

Fig. 3. (**A**) Line scans along the H_S direction in (100) surface coordinates (*13*). Black line, clean particles; red line, under oxygen exposure. (**B**) Reciprocal- and real-space lattice of the (3×1) shifted-row superstructure on the (001) particle top facet. The scans in (A) were performed at $K_S = 1$; see red line. The peaks at $H_S = -1/3$ and $1/3$ are characteristic for the (3×1) superstructure. (**C**) H_S scan in (100) surface coordinates ($K_S = 7/8$) along the red line in the top reciprocal lattice in (D). Satellite peaks at $H_S = 1/2$ and $H_S = 3/2$ give evidence for the c(2×8) coincidence structure of the hexagonal surface oxide (*13*) (hexagonal real- and reciprocal-space unit cells are indicated). (**D**) Structural model of a Rh NP on MgO, covered on all facets by a O–Rh–O trilayer surface oxide. (**E**) K scan along the (01) direction in surface coordinates (*11*) of the (111) side facet pictured in (D). The reflection at $K_S = 8/9$ stems from the surface oxide. (C and E) Black lines, clean surface; red lines, under oxygen exposure; blue lines, after CO reduction.

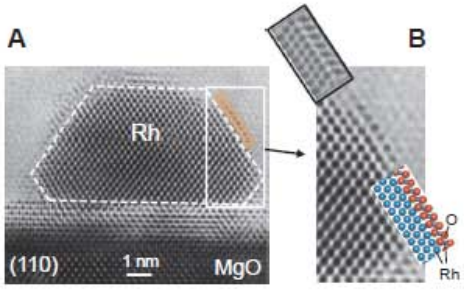

Fig. 4. (**A**) HRTEM micrograph of a Rh particle on MgO(001) in (110) view. On the left side, close to the substrate, a small twin is present with (111) twinning plane. From the XRD data, we can infer that ~5% of the particles are twinned. The dashed line represents the particle shape derived from the XRD data for the oxidized particles. The white box denotes the zoomed-in area of the surface oxide on (111) facets plotted in (B). (**B**) Atomically resolved structure of the O–Rh–O trilayer surface oxide on the (111) facets. In the box, a TEM image simulation is plotted as obtained from the structural model in the second inset. The dark spots correspond to Rh atom rows.

References and Notes

1. G. Ertl, H. Knözinger, F. Schüth, J. Weitkamp, *Handbook of Heterogeneous Catalysis* (Wiley-VCH, Weinheim, Germany, 2008).
2. M. D. Ackermann *et al.*, *Phys. Rev. Lett.* **95**, 255505 (2005).
3. J. G. Wang *et al.*, *Phys. Rev. Lett.* **95**, 256102 (2005).
4. E. Lundgren *et al.*, *Phys. Rev. Lett.* **92**, 046101 (2004).
5. B. L. M. Hendriksen, S. C. Bobaru, J. W. M. Frenken, *Surf. Sci.* **552**, 229 (2004).
6. C. H. F. Peden *et al.*, *J. Phys. Chem.* **92**, 1563 (1988).
7. M. A. Newton, C. Belver-Coldeira, A. Martinez-Arias, M. Fernandez-Garcia, *Angew. Chem. Int. Ed.* **46**, 8629 (2007).
8. M. Bäumer *et al.*, *Phys. Chem. Chem. Phys.* **9**, 3541 (2007).
9. H. S. Gandhi, G. W. Graham, R. W. McCabe, *J. Catal.* **216**, 433 (2003).
10. H. Over *et al.*, *Science* **287**, 1474 (2000).
11. J. Gustafson *et al.*, *Phys. Rev. Lett.* **92**, 126102 (2004).
12. J. Rogal, K. Reuter, M. Scheffler, *Phys. Rev. Lett.* **98**, 046101 (2007).
13. J. Gustafson *et al.*, *Phys. Rev. B* **71**, 115442 (2005).
14. C. Dri *et al.*, *J. Chem. Phys.* **125**, 094701 (2006).
15. P. L. Hansen *et al.*, *Science* **295**, 2053 (2002).
16. G. Rupprechter, K. Hayek, H. Hofmeister, *J. Catal.* **173**, 409 (1998).
17. C. R. Henry, *Surf. Sci. Rep.* **31**, 231 (1998).
18. K. Hojrup Hansen, Z. Sljivancanin, E. Laegsgaard, F. Besenbacher, I. Stensgaard, *Surf. Sci.* **505**, 25 (2002).
19. F. Mittendorfer, N. Seriani, O. Dubay, G. Kresse, *Phys. Rev. B* **76**, 233413 (2007).
20. See the supporting online material for details.
21. N. Kasper *et al.*, *Surf. Sci.* **600**, 2860 (2006).
22. U. Pietsch, V. Holy, T. Baumbach, *High-Resolution X-Ray Scattering* (Springer, New York, 2004).
23. I. K. Robinson, D. J. Tweet, *Rep. Prog. Phys.* **55**, 599 (1992).
24. G. Wulff, *Z. Kristallogr.* **34**, 445 (1901).
25. W. L. Winterbottom, *Acta Metall.* **15**, 303 (1967).
26. S. Nokbin, J. Limtrakul, K. Hermansson, *Surf. Sci.* **566–568**, 977 (2004).
27. This corresponds to a chemical oxygen potential (*19*) $\mu = -1.04$ eV. $\mu(Rh_2O_3)$ is -1.23 eV.
28. Noticeable oxygen-induced lattice distortions lead to intensity asymmetries between the low-Q and high-Q side of the associated Bragg point (where Q is the x-ray momentum transfer). Inspection of fig. S2B shows that this is not observed.

29. For slightly larger particles (diameter D = 9 nm), the formation of (100) side facet rods, in addition to (110) side facet rods, is observed upon oxidation. The latter is not observed for particles with D = 8 nm; for both see fig. S2.
30. M. Sporn *et al.*, *Surf. Sci.* **416**, 384 (1998).
31. G. Renaud *et al.*, *Science* **300**, 1416 (2003).

32. We thank G. Richter and M. Pudleiner for the preparation of Rh/MgO reference samples, N. Jeutter for help with the x-ray experiments, and the European Union for financial support under contract no. NMP3-CT-2003-505670 (NANO2).

Supporting Online Material

www.sciencemag.org/cgi/content/full/321/5896/1654/DC1
Materials and Methods
SOM Text
Figs. S1 to S5
References

22 May 2008; accepted 12 August 2008
10.1126/science.1160845

PRL 102, 025502 (2009) PHYSICAL REVIEW LETTERS week ending 16 JANUARY 2009

Enhanced Relaxation and Intermixing in Ge Islands Grown on Pit-Patterned Si(001) Substrates

T. U. Schülli,[1,*] G. Vastola,[3] M.-I. Richard,[1,2] A. Malachias,[2] G. Renaud,[1] F. Uhlík,[3] F. Montalenti,[3] G. Chen,[4] L. Miglio,[3] F. Schäffler,[4] and G. Bauer[4]

[1]*CEA Grenoble, INAC/SP2M, 17 rue des martyrs, F-38054 Grenoble, France*
[2]*ESRF, Grenoble 6 rue J. Horowitz, F-38043 Grenoble, France*
[3]*L-NESS and Materials Science Department, University of Milano-Bicocca, Via R. Cozzi 53, I-20125 Milano, Italy*
[4]*Johannes Kepler Universität Linz, A-4040 Linz, Austria*

(Received 24 October 2008; published 16 January 2009)

We compare elastic relaxation and Si-Ge distribution in epitaxial islands grown on both pit-patterned and flat Si(001) substrates. Anomalous x-ray diffraction yields that nucleation in the pits provides a higher relaxation. Using an innovative, model-free fitting procedure based on self-consistent solutions of the elastic problem, we provide compositional and elastic-energy maps. Islands grown on flat substrates exhibit stronger composition gradients and do not show a monotonic decrease of elastic energy with height. Both phenomena are explained using both thermodynamic and kinetic arguments.

DOI: 10.1103/PhysRevLett.102.025502 PACS numbers: 81.16.Nd, 61.46.−w, 71.15.Pd, 81.07.−b

Ordering, shape and size uniformity of epitaxial Ge (or SiGe) islands on Si(001) is very important whenever microelectronic applications based on such nanostructures are concerned [1]. Island formation is known to follow the Stranski-Krastanow (SK) growth mode [2], allowing for partial elastic energy relaxation. Significant intermixing between Si and Ge within the islands has been reported [3–8], and the role of alloying for growth has been theoretically investigated [9–13]. Since on flat substrates islands tend to nucleate randomly, substrate patterning can be used to achieve controlled positioning [14]. Remarkably, patterning was also shown to increase size uniformity, possibly because of a more regular distribution of capture areas [15]. The growth of ordered nanometric islands with a narrow distribution in shape and size is already exciting *per se*, but recent results [15,16] indicate that the influence of patterning can be even more far reaching. Self organized patterning in ultra high vacuum (UHV) may also be used in the future, in order to control size and relaxation in SiGe islands [17]. We recall that SiGe islands on Si are coherent up to a critical volume V_c, characteristic for the onset of the formation of misfit dislocations [18]. In Ref. [15], it was demonstrated that patterning of Si(001) extends the allowed volume range for coherent islands. According to atomistic and finite element method (FEM) calculations reported in the same paper, this can be explained by an extra relaxation, caused by the pit, which lowers the substrate or island misfit. The possibility of controlling also the relaxation level of the islands by growth on patterned substrates appears extremely intriguing. In this Letter, we report an experimental proof of the abovementioned effect, and we show that the pits influence both, average relaxation and distribution of Ge within the islands.

Pit-patterned substrates were prepared by lithography, following the procedure used in [19]. Seven ML of Ge were deposited at 650Â °C on a Si(001) substrate with a 900 × 900 μm^2 part of it being patterned with pits at a periodic spacing of 495 nm. The growth of a Si buffer prior to Ge deposition leaves periodic downward pyramid-shaped {1110} pits [19]. The sample was transferred under N_2 atmosphere into the UHV chamber of beam line BM32 at the ESRF in Grenoble. AFM analysis shows that Ge islands nucleate at the bottom of these pits and form dome-shaped islands with identical facets as on the flat part of the substrate. The average island density per surface unit area is 5 μm^{-2} for the patterned part and 20 μm^{-2} for the flat one. The domes on the patterned (flat) part have an average height of 28 nm (23 nm) and a diameter of 130 nm (110 nm).

The islands were characterized by grazing incidence x-ray diffraction (GIXD) at an x-ray energy of 11.04 keV. The incident beam and the collimation on the detection side were translated in order to select between patterned and flat regions. Reciprocal space maps in the vicinity of the (400) Bragg reflection were recorded, as shown in Figs. 1(a) and 1(b) together with corresponding AFM images (insets). The intensity distribution along the radial direction clearly extends to higher lattice parameters for the patterned region. The islands grown on the flat have their main lattice parameter around 5.465 Å (in reciprocal lattice units of $H = 3.975$) whereas for the patterned part, the lattice parameters are stretched in reciprocal space, showing a maximum at ~5.51 Å ($H = 3.943$).

To understand the observed differences, we related the lattice-parameter to the local Ge content inside the islands by exploiting anomalous x-ray scattering. By monitoring the scattered intensity when varying the x-ray energy in the vicinity of the Ge K edge ($E_e = 11.103$ keV) at a fixed momentum tranfer Q, the corresponding average Ge concentration can be determined, so that in-plane lattice parameter $a_{\|}$ vs Ge content (c_{Ge}) data are extracted without any model assumption [5,20]. It is found that for the islands

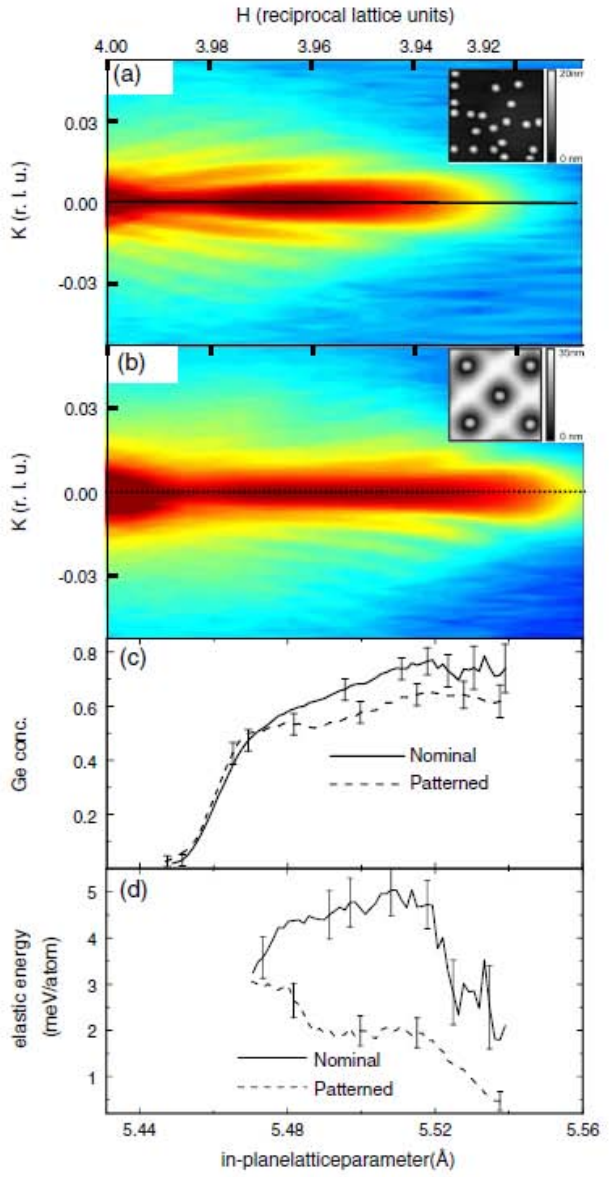

FIG. 1 (color online). Logarithmic intensity distribution in the vicinity of the (400) Bragg reflection for Ge islands grown on the flat (a) and patterned (b) sample part. Corresponding AFM images (1 μm^2 in size) are shown as insets. (c) Ge content inside the islands as a function of lattice parameter for growth on the flat (full line) and on the patterned part (dashed line). (d) elastic energy as a function of lattice parameter as extracted from the x-ray data. All figures correspond to the same lattice-parameter scale.

grown on the flat, the maximum Ge concentration for highest lattice parameters is slightly higher than for the patterned case [Fig. 1(c)]. However, as visible from the intensity distribution in Figs. 1(a) and 1(b), these relaxed regions contribute little to the total diffracted intensity. The combined analysis of the x-ray size oscillations, and the island shape as resolved by AFM, yield that the major part of the island volume is situated at lattice parameters below 5.48 Å for islands on the flat. Combining x-ray diffraction and AFM, the mean Ge content is determined to be $c_{Ge} \simeq (60 \pm 5)\%$ for both island types. Hence, the presence of the pits does neither influence the shape nor the mean SiGe composition of the islands. Let us see where, instead, differences exist. Figure 1(c) shows c_{Ge} vs $a_{\parallel}$ for the flat (full lines) and the patterned region (dashed lines). The continuous broadening of H-constant profiles for lower H values points to a monotonic lattice parameter increase as a function of height in the islands [21]. The flatness of the dashed curve indicates lower gradients for c_{Ge} inside the islands grown in pits in comparison to the flat case. It is thus clear that the elastic energy at comparable c_{Ge} must be significantly lower for islands nucleating in the pits, as the intensity in reciprocal space stretches out to much higher lattice parameters. The volumetric elastic energy can be extracted from these data, as performed in Refs. [7,20]. It is plotted as a function of lattice parameter in Fig. 1(d). In the narrow region that forms the interface between island and substrate, and hence the region where the in-plane strain $\epsilon_{\parallel}$ changes sign from expansive to compressive nature, our method does not allow for a precise determination of the elastic energy since regions with similar lattice parameter and slightly different composition will have a mean $\bar{\epsilon}_{\parallel}$ that amounts to zero. However, with the elastic energy $E_e \propto \epsilon_{\parallel}^2$, its mean value does not average to zero. In the region of validity, our method yields a remarkable decrease of elastic energy throughout the islands grown on the pit-patterned part. One has to state that such x-ray measurements carry information on the in-plane lattice parameter, but effects of local hydrostatic compression cannot be taken into account when determining the elastic energy directly from the data.

More insights can be gained by extracting the actual 3D Ge distribution and the elastic-energy profile throughout the island. Over the last ten years, x-ray methods have been developed, coupling lattice parameter with lateral size [21] and chemical composition of an object, to reconstruct a concentration profile inside nanostructures [4,5,22]. These methods are limited, however, by model assumptions concerning the shape of the considered isostrain regions. A combination of x-ray methods and FEM calculations is thus necessary in order to overcome the lack of experimentally accessible information. We have used a fitting procedure that exploits a FEM-based treatment of nonuniform concentration profiles, to determine the local Ge content without any constraint. After the island and substrate geometry is created based on AFM images, nonuniform concentration values are assigned on a discrete mesh [13]. The elastic problem is then solved exploiting linear interpolation, (c_{Ge}, $a_{\parallel}$) data are extracted, and the statistical χ^2 is evaluated by comparison with the corresponding x-ray data. Using an iterative procedure based on local concentration exchanges, χ^2 is minimized. Technical details on the way we handle nonuniform distributions within FEM can be found in [13] where the elastic energy was

minimized. In the present work, the deviation from the experimental data is minimized. It is important to emphasize that particular care is required in assigning the correct statistical weight to the data. During the fit, (c_{Ge}, $a_{\parallel}$) pairs from the FEM grid were computed from the island interior and from a surrounding region in the substrate with a lateral extension inferred from the experimental island density, and a depth of 12 nm, i.e., the estimated penetration depth of the x-rays in our setup. This allowed us to filter out the substrate contribution from the experimental data which, as shown in Fig. 1(c) for the flat case, causes a sudden drop of the average Ge content at low lattice parameters, due to the strong scattering contribution from the Si-substrate. From the x-ray data, it is thus difficult to analyze the region of the substrate-island interface. Another difficulty stems from the vanishing experimental scattering volume of the regions with lattice parameters close to bulk Ge. In the fit shown in Fig. 2, the local value of c_{Ge} was extrapolated from experiments, assigning a large error bar in order not to bias the region where real data were present. Finally, a satisfactory fit (requiring $\sim 10^4$ iterations) is obtained, the full solution of the elastic problem being required at each step. The FEM fitted data (small dots in Fig. 2) show that several concentration values can be associated with a single value of lattice parameter, which is not obvious from the experimental curve which averages them out.

The 3D compositional maps corresponding to our best fits are displayed in Figs. 3(a)–3(d) together with their horizontally averaged values [Fig. 3(e)], while the elastic energy per atom is reported in Fig. 3(f), where a comparison with the uniform composition case is also shown. In the flat case—Figs. 3(a) and 3(b)—an almost pure Si region is found close to the base edges, a result fully compatible with selective-etching data [23]. From Figs. 3(c) and 3(d), one sees that Si enrichment at the base is less evident in the pit case where the overall Ge distribution is more uniform, but for more localized irregularities. This is particularly evident from the horizontally averaged c_{Ge} values displayed in Fig. 3(e). The different Ge distribution of the island apex along the [100] and [110] cross sections is due to the fact that the island boundary is composed by a set of facets and edges which is different for the two sections. It has thus a direct influence on the local elastic relaxation and hence the Ge concentration profile [24]. The above observations can be justified using both thermodynamic and kinetic arguments. The edges of the islands grown on flat substrates are the most compressed regions in case a uniform Ge distribution is considered [25], so that replacing Ge with Si atoms produces significant relaxation. Comparing the elastic energy in flat vs pit-patterned substrates [Fig. 3(f)] in the case of a uniform distribution, one sees that the driving force for Si segregation at the island base is weaker in pits, since the energy difference between base and top is smaller. Entropy of mixing could then prevail over elastic relaxation, forcing enhanced intermixing. While this thermodynamic argument supports our

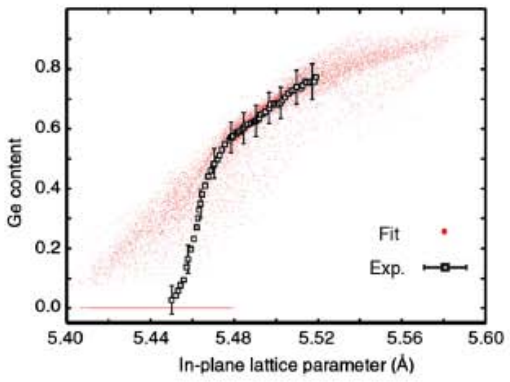

FIG. 2 (color online). Experimental data of the Ge-content as a function of lattice parameter together with FEM fitted data after proper separation of the Si substrate contribution (flat case).

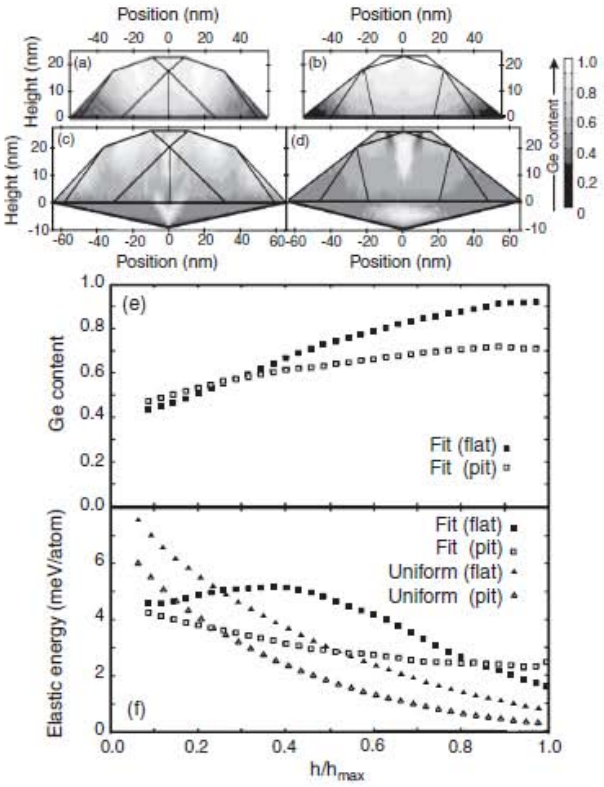

FIG. 3. Cross section map of the 3D-reconstructed Ge content profile for islands grown on flat (a), (b) and patterned (c), (d) samples. Sections are shown along the [100] (a), (c) and the [110] (b), (d) crystallographic directions. Panel (e) displays the average Ge content as a function of height. Panel (f) reports the elastic energy profile corresponding to the fitted Ge distribution on flat (filled box) and patterned (empty box) substrates. Plots made for the case of uniform concentration are analogously displayed for flat (filled triangles) and pit (empty triangles) case. The quantity h/h_{max} is a normalized height to allow the proper comparison between both island types at every height h.

results, it is important to consider that during growth, kinetic limitations are present, so that one should always check whether the proposed scenario is favored or simply made possible by plausible kinetic paths. On flat substrates, large amounts of Si become available during growth when the strong compressive stress at the edges produces trenches penetrating the Si substrate [26]. These Si atoms coming out close to the island periphery could easily be incorporated in the regions which are most favorable from the energetic point of view. As a result, the final profile resembles the minimum-energy one [13]. In the initial stages of growth, trenches are not yet present, providing a kinetic justification for the limited lateral extension of the external Si-rich region. Our results do not confirm the formation of a central Si-rich region ([4,7]), whose presence seems to be difficult to explain from both the thermodynamic and kinetic point of views. In pits, the Si-supply mechanism could be different. In Ref. [27], data collected on pit-patterned samples similar to ours indicated that the condition of a perfect WL completed prior to island formation is not fulfilled. Since preliminary results on the present samples confirm this observation, we believe that in pits, enhanced Si supply prior to trench formation is possible, i.e., from detachment of uncovered Si atoms from the steps of the pits' facets. These could reach the growing islands by surface diffusion, leading to a more uniform intermixing profile.

Let us now analyze quantitatively the main differences between the flat and the patterned case in terms of elastic energy. From Fig. 3(f), one sees that the presence of the pit allows for a significant decrease (~30% on average) in elastic energy. Since this effect is confirmed also for uniform Ge distributions [triangles in Fig. 3(f)], the key role must be played by the different geometry. Before island formation, the pit is filled by Ge forming an inverted pyramid. This redistributes the load between Ge and the surrounding Si resulting in better strain relaxation with respect to a flat WL so that islands on pits nucleate on a substrate with a lower effective misfit. This relaxation mechanism was demonstrated in [15]. Additionally, the behavior of the elastic energy shows that the usual picture of a base-to-top stress relaxation breaks down in the case of a flat substrate [25]: the curve displayed in Fig. 3(f) clearly displays a maximum. Combining this with Fig. 3(e), one sees that Si enrichment at the base guarantees a lowering of the elastic energy. As soon as c_{Ge} approaches its average value (at around $h/h_{max} = 0.3$), elastic-energy lowering becomes less efficient: the strong elastic load determined by the high Ge content cannot be relieved by the limited deformation in regions still close to the base. In the proximity of the island top, instead, the elastic energy is nicely lowered in spite of the maximum Ge content in the island.

If prepatterning is already seen as a powerful tool to control positioning and homogeneity of heteroepitaxial islands, we have shown that it also allows one to control elastic-energy release and thus to grow islands with the desired relaxation. The kinetics of Si supply seems to be also influenced by the pit, calling for further studies for achieving full control.

Financial support by the EU-funded project "D-DotFET" and the FWF (Vienna, project SFB025) and GMe (Vienna) are gratefully acknowledged, together with technical help received from R. Gatti.

*schulli@esrf.fr

[1] F. Schäffler, Semicond. Sci. Technol. **12**, 1515 (1997).
[2] V. A. Shchukin and D. Bimberg, Rev. Mod. Phys. **71**, 1125 (1999).
[3] G. Capellini, M. De Seta, and F. Evangelisti, Appl. Phys. Lett. **78**, 303 (2001).
[4] A. Malachias *et al.* Phys. Rev. Lett. **91**, 176101 (2003).
[5] T. U. Schülli *et al.*, Phys. Rev. Lett. **90**, 066105 (2003).
[6] G. Medeiros-Ribeiro *et al.*, Appl. Phys. A **80**, 1211 (2005).
[7] G. Medeiros-Ribeiro and R. S. Williams, Nano Lett. **7**, 223 (2007).
[8] A. Rastelli *et al.*, Nano Lett. **8**, 1404 (2008).
[9] C. Lang, D. J. H. Cockayne, and D. Nguyen-Manh, Phys. Rev. B **72**, 155328 (2005).
[10] G. Hadjisavvas and P. C. Kelires, Phys. Rev. B **72**, 075334 (2005).
[11] Y. Tu and J. Tersoff, Phys. Rev. Lett. **98**, 096103 (2007).
[12] N. V. Medhekar, V. Hegadekatte, and V. B. Shenoy, Phys. Rev. Lett. **100**, 106104 (2008).
[13] R. Gatti, F. Uhlík, and F. Montalenti, New J. Phys. **10**, 083039 (2008).
[14] Z. Zhong and G. Bauer, Appl. Phys. Lett. **84**, 1922 (2004).
[15] Z. Zhong *et al.*, Phys. Rev. Lett. **98**, 176102 (2007).
[16] H. Hu, H. J. Gao, and F. Liu, Phys. Rev. Lett. **101**, 216102 (2008).
[17] G. Katsaros *et al.*, Phys. Rev. Lett. **101**, 096103 (2008).
[18] A. Marzegalli *et al.*, Phys. Rev. Lett. **99**, 235505 (2007).
[19] G. Chen *et al.*, Phys. Rev. B **74**, 035302 (2006).
[20] R. Magalhães-Paniago *et al.*, Phys. Rev. B **66**, 245312 (2002).
[21] I. Kegel *et al.*, Phys. Rev. Lett. **85**, 1694 (2000).
[22] A. Letoublon *et al.*, Phys. Rev. Lett. **92**, 186101 (2004).
[23] G. Katsaros *et al.*, Phys. Rev. B **72**, 195320 (2005).
[24] In Figs. 3(c) and 3(d), the calculations show Ge rich regions of the pit bottoms which do not appear in 3(e). In this figure, we make the comparison between the average composition between islands on flat and patterned substrates. Since the material at the bottom of the pit is of course not present in the island on flat substrate, the averaged compositions of Fig. 3(e) do not take into account this volume.
[25] G. Vastola, R. Gatti, A. Marzegalli, F. Montalenti, and Leo Miglio, *Detailed Analysis of the Shape-Dependent Deformation Field in 3D Ge Islands on Si(001)* (Springer, Berlin, 2008), pp. 421–438.
[26] S. A. Chaparro, Y. Zhang, and J. Drucker, Appl. Phys. Lett. **76**, 3534 (2000).
[27] T. Stoica *et al.*, Nanotechnology **18**, 455307 (2007).

PRL 100, 115502 (2008) PHYSICAL REVIEW LETTERS week ending 21 MARCH 2008

Controlling Structure and Morphology of CoPt Nanoparticles through Dynamical or Static Coalescence Effects

J. Penuelas,[1] P. Andreazza,[1,*] C. Andreazza-Vignolle,[1] H. C. N. Tolentino,[2] M. De Santis,[2] and C. Mottet[3]

[1]*Centre de Recherche sur la Matière Divisée, UMR 6619 Université d'Orléans & CNRS, 1 bis, rue de la Férollerie, 45071 Orléans Cedex, France*

[2]*Institut Néel, CNRS & UJF, 25 avenue des Martyrs BP 166, 38042 Grenoble Cedex 9, France*

[3]*Centre de Recherche en Matière Condensée et Nanosciences-CNRS, Campus de Luminy, case 913, 13288 Marseille Cedex 9, France*

(Received 12 November 2007; published 18 March 2008)

The structure and morphology of 1 to 3 nm size CoPt nanoparticles have been investigated *in situ* and in real time under different conditions: growth at 500 °C or at room temperature (RT) followed by annealing at 500 °C. The small-angle x-ray scattering measurements show size and temperature dependent growth mode with particle motions on the surface, while wide-angle scattering results, supported by Monte Carlo simulations, allow structure identification. If icosahedra are systematically detected at the first growth stages at RT, annealing at 500 °C yields the decahedral structure from the quasistatic coalescence of icosahedral morphology. Meanwhile, growth at 500 °C proceeds by a dynamical coalescence mechanism at the early stage, yielding truncated octahedral cubic structures.

DOI: 10.1103/PhysRevLett.100.115502 PACS numbers: 61.46.Df, 61.82.Bg, 64.70.Nd, 68.55.A−

Magnetic nanoparticles (NPs) have attracted a lot of interest because of their applications in ultrahigh density recording media. In particular, FePt and CoPt NPs are especially promising due to the combination of size reduction and alloying effects, which lead to an enhancement of both their magnetic moment and anisotropy [1,2]. Apart from size effects, their magnetic behavior is governed by chemical composition [2,3] and influenced by the degree of chemical order or segregation and by morphology [4–6]. These latter parameters are highly dependent on kinetic processes during the NPs formation. Indeed, metastable multitwinned structures, such as large icosahedra or decahedra [7], as well as metastable chemical arrangements, such as onionlike clusters [8], may occur. To achieve suitable magnetic performances, thermal annealing, during or after the NPs growth, is often required [1]. Such thermal assistance may induce morphological changes [9] or important chemical rearrangements in the NPs [10,11]. Moreover, in the case of supported NPs, it may also modify their size and dispersion on the substrate by coalescence or Ostwald ripening. Thus, it is of primary importance to understand temperature effects on the NPs formation mechanisms since their properties are directly connected to their structure and spatial organization.

In this Letter we focus on the morphology and structure of 1 to 3 nm supported CoPt NPs studied *in situ* and in real time by grazing incidence small-angle x-ray scattering (GISAXS) and grazing incidence x-ray diffraction (GIXD). The growth temperature effect, and the result of 500 °C annealing, is reported in terms of the mobility of atoms and particles and in terms of their structural evolution. For such temperature and cluster size ranges, morphological and structural changes occur without long range chemical ordering [6,11,12]. GISAXS and GIXD can make a statistical analysis of the morphology, structure and chemical order of NPs over the whole sample [13]. Grazing incidence ensures a minimum probing depth, so that surface mechanisms may be studied with high sensitivity. *In situ* analysis under ultrahigh vacuum (UHV) is also of prime importance because of the high reactivity of CoPt NPs with their environment that affects their morphology and structure [12]. Time scales for each growth step (nucleation, coarsening, or coalescence) are large enough to allow real time experiments and to study dynamical processes. We demonstrate that irrespective of the chemical ordering, the role of coalescence prevails over size-dependent morphology and structure and yields decahedral or face centered cubic (fcc) structures according to the thermal treatment.

The experiments were performed using the UHV setup of the French-CRG (BM32) beam line at the European Synchrotron Radiation Facility, which combines molecular beam epitaxy (MBE) growth with GISAXS and GIXD techniques [13]. The 18 keV monochromatic x-ray beam was set at a grazing incidence angle α_i of 0.07° with respect to the sample surface. Two-dimensional GISAXS patterns were recorded with a CCD camera mounted at 1 m behind the sample. For the GIXD measurements, a standard scintillator detector was set at a fixed exit angle related to the sample surface ($\alpha_e = \alpha_i$) and the scattering vector q was changed by scanning the in-plane angle. Co and Pt atoms were codeposited by MBE under a pressure varying from 2 to 5×10^{-10} mbar depending on the deposition or annealing temperature. The amorphous SiO_2 substrate was covered with a 10 nm-thick amorphous carbon (a-C) film. Such film limits cluster-to-substrate interactions and allows comparisons with our previous transmission electron microscopy (TEM) results [11]. Co and Pt deposition rates [0.26×10^{15} atoms/(cm^2 h) for each kind of atom] were adjusted to yield a composition close to $Co_{50}Pt_{50}$ with a constant flux of atoms during all the growth stages.

PRL 100, 115502 (2008) PHYSICAL REVIEW LETTERS week ending 21 MARCH 2008

Real time GISAXS measurements were performed with an interval of 30 min between each recording. Beyond 1 h of deposition time on the substrate held at 500 °C, the 2D GISAXS pattern exhibits two distinct lobes of scattered intensity [Fig. 1(a)] that are proportional to the form factor $F(q)$ and the interference function $S(q)$ of cluster assembly. $F(q)$ represents the Fourier transform (FT) of the particle shape and $S(q)$, the FT of the cluster-cluster pair correlation function so that the size, shape, and correlation distance Λ of the NPs can be extracted by simulations using ISGISAXS software [14] from the $q_\perp$ and $q_\parallel$ cross sections [Fig. 1(b)]. The form factor is calculated in the distorted-wave Born approximation, which includes substrate reflections of the scattered intensity and allows fitting the Yoneda peak [15]. The NPs have a truncated spherical shape with an aspect ratio $H/D < 1$ at the beginning of the growth, where D and H are the NPs diameter and height, respectively. The size distribution has been fitted using a narrow Gaussian function with a geometrical standard deviation of $\sigma(D)/D = 0.3$ according to our previous TEM results [11]. The evolution of D and H with time for NPs grown at 500 °C was derived [Fig. 2(a)] from that of the cross sections [Figs. 1(c) and 1(d)]. D increases as a power law during the deposition, the exponent (0.3) is in good agreement with theoretical predictions in the case of Volmer-Weber growth [16]. The NPs aspect ratio increases from 0.63 (truncated sphere) in the early stage to almost 1 at the end [Fig. 2(b)]. The shape goes to a more stable morphology (isotropic) similar to that obtained without support effect. In order to validate the GISAXS simulations, we performed *ex situ* TEM observations [Fig. 2(c)]. Statistical measurements gave an average diameter of 3.2 nm and an aspect ratio of 0.95. These measurements reported in Figs. 2(a) and 2(b) are in a remarkable agreement with the GISAXS results. The NPs density d is derived from the mean interparticle distance, by assuming one particle per Λ^2 surface. For small amounts of CoPt deposits, we observe a decrease of the NPs density [Fig. 2(b)] that we interpret as a dynamical coalescence, because their diffusion length is larger than their average separation Λ. Since the cluster mobility decreases as a power law when their size increases [17], it is understandable that dynamic coalescence stops after 4 h and the density remains almost constant until the end of the deposition.

GIXD patterns were obtained simultaneously with GISAXS measurements (Fig. 3). The background contribution ($t = 0$ h) is mainly the scattering of the amorphous substrate. Beyond 1 h deposition time, which corresponds to 0.52×10^{15} atoms/cm^2, the metal contribution to the scattered signal can be clearly distinguished from the background and increases with time. For the lowest deposited quantities, background subtraction is a crucial aspect of the data analysis. At these very low deposition times (insert in Fig. 3), the position of the main peak (29–30 nm^{-1}) is shifted, whereas beyond 4 h deposition time, a shoulder develops at 33 nm^{-1} simultaneously with the occurrence of another contribution around 47 nm^{-1}. In the early deposition steps, i.e., during the dynamical coalescence stage, we never observe the fcc structure but rather a noncrystalline atomic arrangement instead (amorphous or multitwinned). For longer deposition times, when the NPs density is nearly constant, the diffraction patterns exhibit the characteristic fcc peaks with an interatomic

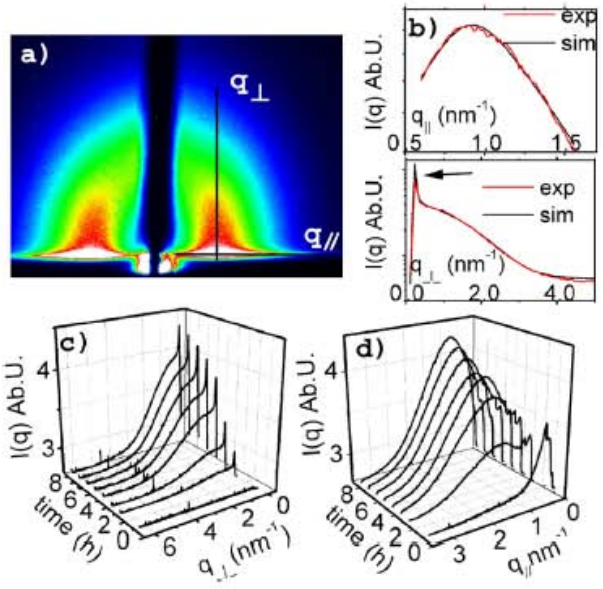

FIG. 1 (color online). (a) Measured GISAXS pattern of sample grown at 500 °C, after five hours corresponding to 2.6×10^{15} atoms/cm^2. The scattering vector q is separated in reciprocal space coordinates $q_\perp$ and $q_\parallel$, perpendicular and parallel to the sample surface, respectively. (b) corresponding cross sections and fits. The arrow shows the Yoneda peak. (c) and (d) graphs show the evolution of $q_\perp$ and $q_\parallel$, respectively, with deposition time.

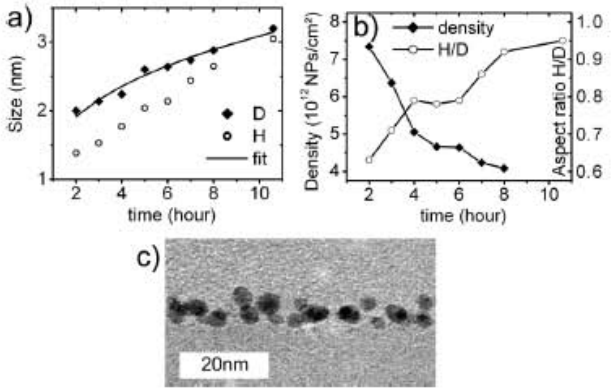

FIG. 2. From the fit of cross sections we deduce the evolution of (a) the mean diameter D and height H ($\pm 5\%$) and (b) the density d of CoPt NPs on the surface (the values at 10.6 h was deduced from TEM measurements) together with the aspect ratio H/D. (c) shows *ex situ* cross section TEM image of the sample.

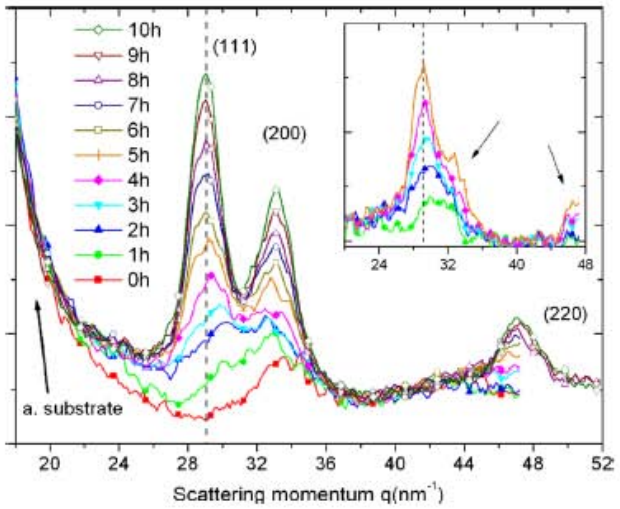

FIG. 3 (color online). Evolution of the GIXD patterns as a function of deposition time. 0 h diffraction data correspond to the background. The inset displays the first scans (up to 5 h) after background subtraction, arrows show fcc additional peaks.

distance of 0.265 nm, close to the fcc disordered bulk value [18], clearly pointing to Co and Pt alloying. However, one may wonder if the structure evolution from a noncrystalline arrangement at the beginning of deposition to a cubic structure after 4 h deposition is linked to the growth mode.

Further interpretation of these measurements requires better knowledge of size and structural effects on the diffraction pattern. The wide-angle scattering intensity for a model cluster i is calculated quantitatively on the basis of the Debye equation [19]:

$$I_{i,N}(q) = \sum_j \sum_{j' \neq j} \exp(-\sigma^2 q^2) f_j f_{j'} \frac{\sin(q r_{jj'})}{q r_{jj'}} + S_{\mathrm{inc}}(q),$$

where f_j is the atomic scattering factor of the jth atom. $r_{jj'}$ is the distance between atom j and atom j', and σ^2 is the mean-square displacement in the Debye-Waller prefactor, which expresses the attenuation of the interference term in the Debye equation, due to thermal vibrations or/and static random defects. $S_{\mathrm{inc}}(q)$ is the incoherent scattering function. Preliminary, calculations of the polarization and absorption evolution effects were made but were neglected due to their weak change with q. We have used three structure types in our cluster models: truncated octahedral (TOh) based on face-centered-cubic structure, decahedral (Dh) and icosahedral (Ih) according with Wulff, Marks, and Ino constructions [20], respectively. To fit the diffraction patterns, we used either single size and single cluster type, or a weighted sum of the intensities from several sizes or structures [7]. Models composed of clusters (between 50 and 2000 atoms) with complete shells have been found to be sufficient for data analysis. Monte Carlo simulations of a representative small number of relaxed CoPt cluster structures (TOh, Dh, and Ih illustrated in the inset of Fig. 4) were performed using a semiempirical tight-binding potential [6], to validate the diffraction profiles of these geometrical models [7]. It is worth noting that the possible ordering of the clusters in their low temperature phase has been taken into account in the analysis. However, as mentioned above, in the *in situ* experiments performed at 500 °C, chemical disorder is more probable for NPs smaller than 3 nm as predicted by the Monte Carlo simulations [6].

Figures 4(a) and 4(c) show two stages (5 and 10 h deposition times) of the growth at 500 °C with diameters centered at $D = 2.5$ and 3.2 nm, respectively. For the largest dimension, i.e., cluster with about 1300 atoms, the sample is dominated by fcc clusters, with a small fraction of icosahedral ones (less than 10%). For the smallest dimension, the best fit is obtained with a mix of Ih and TOh-fcc models (around 50% each in atomic fraction) with about 309 and 405 atoms, respectively. Decahedral models were also considered, but no improvement in the fit quality was found. These results show a structural evolution with the NPs size that is predicted in first approximation by energetic stability calculations in metallic clusters [21]. The icosahedral shape is the most energetically stable structure for small dimensions, while fcc clusters are favored for larger ones. Thus, one possible interpretation is that this continuous shape transition, from Ih to TOh structure, is only due to a size effect and the clusters reaching their equilibrium shape during the growth [6].

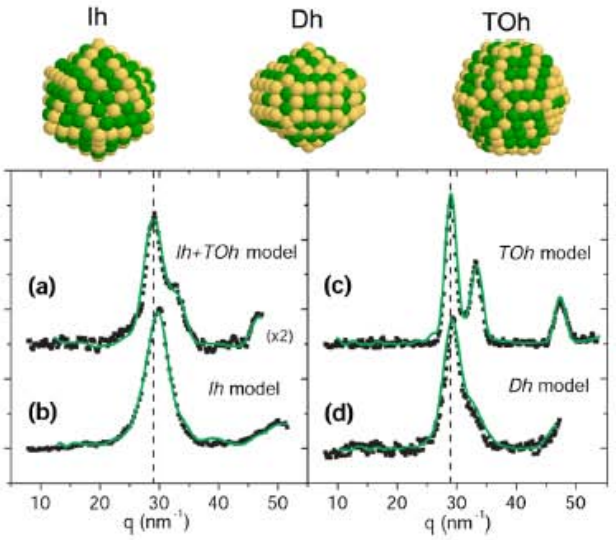

FIG. 4 (color online). Snapshots of icosahedral (Ih), decahedral (Dh) and truncated octahedral (TOh) clusters, and experimental (square marks) and calculated (green or gray solid line) diffraction patterns of similar size distribution samples: $D = 2.5$ nm (a) growth at 500 °C (2.6×10^{15} at/cm^2) and (b) growth at RT (5.2×10^{15} at/cm^2); $D = 3.2$ nm (c) growth at 500 °C and (d) annealing the sample (b) at 500 °C during 1 h. Profiles were offset vertically, and a magnification was applied in one case (in parentheses). A vertical dashed line corresponding to the fcc (111) line of 500 °C grown sample is given for comparison.

However, for small sizes, the 50:50 Ih and TOh-fcc mixture indicates that the sample is still under nonequilibrium conditions. Indeed, the GISAXS results concerning the evolution of the shape and cluster density suggest a coalescence process during the early growth stage. Such events can provide sufficient internal morphological disruption [22] to allow the NPs transformation to the minimum energy morphology, i.e., the TOh shapes at larger sizes [23].

These results have been compared with those obtained for a sample grown at room temperature and then annealed at 500 °C, whose spectra have been chosen to correspond to equivalent cluster sizes:

(i) At room temperature (RT), assuming a size distribution with Gaussian shape (centered between $N = 309$ and 561 atoms), the icosahedral model alone fits the data quite well [Fig. 4(b)]. The growth mechanism at RT is completely different from that at 500 °C: the NPs density is higher (11×10^{12} NP s/cm^2) and the dynamical coalescence is inhibited. After the nucleation stage, the growth at RT corresponds to an atom-by-atom impingement and the initial Ih structure is preserved without transition towards TOh structures [23]. In addition, a shift in the diffraction profile is observed, corresponding to a contraction of the average interatomic distance ($r_i = 0.263$ nm) with respect to the fcc model ($r_i = 0.268$ nm) in the 500 °C sample. Indeed, the contraction is too large to be explained by a thermal effect [6], but is coherent with the denser packing of the Ih structure. For similar NPs size and deposition temperature (RT), Favre *et al.* [4,12] found TOh NPs rather than Ih ones, which could be explained by a matrix effect. Indeed, their NPs were subsequently covered by a thin amorphous silicon layer or embedded in a matrix, thus favoring fcc structures.

(ii) After annealing this sample at 500 °C for 1 h, an average NPs size of 3.2 nm is reached. GIXD refinements [Fig. 4(d)] are consistent with decahedral clusters (centered at $N = 967$) with an average interatomic distance of 0.265 nm. The diffraction signature of Ih and TOh models does not show any similarity with the experimental data. GISAXS measurements indicate that the annealing process induces a decrease of the particle density (6×10^{12} clusters/cm^2) simultaneously with the increase of the particle size from 2.5 to 3.2 nm, which are characteristic of the Ostwald-ripening or static coalescence process [11]. The present structure differs from that of the 500 °C grown sample [Fig. 4(c)] because the kinetic and dynamic history of the samples are different. In the first case (500 °C growth), dynamical coalescence occurs at the early stage of the growth. After this stage, the fcc resulting morphology is locked in and the size increase is dominated by an atom-by-atom growth mechanism. In the second case, the coalescence occurs upon annealing, when the particle size is larger and simultaneously the interparticle distance smaller. Thus, the Dh structure is the result of a quasistatic coalescence [23,24] of Ih structures.

In summary, we have shown, experimentally and with the support of Monte Carlo simulations, the effect of temperature on the structure and morphology of CoPt nanoparticles. Dynamical coalescence in the early stage ($N < 300$ atoms) of growth at 500 °C yields the formation of fcc clusters, while atom-by-atom growth at room temperature produces almost exclusively the nonequilibrium icosahedral morphology. On the other hand, the coalescence from Ih particles (>300 atoms) induced by annealing, yields the formation of decahedral rather than fcc morphology. These *in situ* and real time results bring new understanding of the coalescence versus size effect on small (<3 nm) bimetallic nanoparticle structural transitions at different temperatures.

We acknowledge beam time by the French-CRG of ESRF as well as the help of the BM32 beam line staff. Special thanks to G. Renaud (BM32) for GISAXS training and to T. Sauvage (CERI-Orleans) for RBS facilities.

*Corresponding author.
Pascal.Andreazza@univ-orleans.fr

[1] S. Sun *et al.*, Science **287**, 1989 (2000).
[2] S. Rohart *et al.*, Phys. Rev. B **74**, 104408 (2006).
[3] P. Imperia *et al.*, Phys. Status Solidi (a) (to be published).
[4] P. Moskovkin *et al.*, Eur. Phys. J. D **43**, 27 (2007).
[5] N. Jaouen *et al.*, Phys. Rev. B **76**, 104421 (2007).
[6] G. Rossi, R. Ferrando, and C. Mottet, Faraday Discuss. **138**, 193 (2008).
[7] D. Reinhard *et al.*, Phys. Rev. B **55**, 7868 (1997).
[8] F. Baletto, C. Mottet, and R. Ferrando, Phys. Rev. Lett. **90**, 135504 (2003).
[9] K. Koga, T. Ikeshoji, K. I. Sugawara, Phys. Rev. Lett. **92**, 115507 (2004).
[10] D. Alloyeau *et al.*, Nanotechnology **18**, 375301 (2007).
[11] J. Penuelas *et al.*, Surf. Sci. **602**, 545 (2008).
[12] L. Favre *et al.*, Phys. Rev. B **74**, 014439 (2006).
[13] G. Renaud *et al.*, Science **300**, 1416 (2003).
[14] R. Lazzari, J. Appl. Crystallogr. **35**, 406 (2002).
[15] Y. Yoneda, Phys. Rev. **131**, 2010 (1963).
[16] M. Zinke-Allmang, L. C. Feldman, and M. H. Grabow, Surf. Sci. Rep. **16**, 377 (1992).
[17] P. Jensen, Rev. Mod. Phys. **71**, 1695 (1999).
[18] J. M. Bugnard, Y. Gauthier, and R. Baudoing-Savois, Surf. Sci. **344**, 42 (1995).
[19] B. E. Warren, *X-Ray Diffraction* (Dover, New York, 1990).
[20] L. D. Marks, Rep. Prog. Phys. **57**, 603 (1994).
[21] F. Baletto and R. Ferrando, Rev. Mod. Phys. **77**, 371 (2005).
[22] S. Hendy, S. A. Brown, and M. Hyslop, Phys. Rev. B **68**, 241403(R) (2003).
[23] G. Grochola *et al.*, J. Chem. Phys. **126**, 164707 (2007).
[24] S. Tsyganov *et al.*, Phys. Rev. B **75**, 045421 (2007).

Electrochemical and Solid-State Letters, **12** (10) H373-H375 (2009) H373
1099-0062/2009/12(10)/H373/3/$25.00 © The Electrochemical Society

Mechanism of Thermal Silicon Oxide Direct Wafer Bonding

C. Ventosa,[a] C. Morales,[a] L. Libralesso,[a] F. Fournel,[a] A. M. Papon,[a] D. Lafond,[a] H. Moriceau,[a,*] J. D. Penot,[b] and F. Rieutord[b,z]

[a]*Commissariat à l'Energie Atomique, LETI, Minatec, 38054 Grenoble Cedex 9, France*
[b]*Commissariat à l'Energie Atomique, Institut Nanoscience et Cryogénie, Service de Physique des Matériaux et Microstructures, Nanostructures et Rayonnement Synchrotron, 38054 Grenoble Cedex 9, France*

Thermal silicon oxide-to-oxide bonding was investigated at the nanometer level using X-ray reflectivity, transmission electron microscopy, and infrared absorption spectroscopy. The measurements reveal the stages of the closure mechanism, which are different from standard silicon bonding. Upon annealing, interface water pockets are formed, the contents of which are further dissolved into the oxide, demonstrating that the buried thermal oxide–silicon interface acts as a barrier against water reaction with silicon.
 [DOI: 10.1149/1.3193533]

Manuscript submitted March 31, 2009; revised manuscript received July 11, 2009. Published August 4, 2009.

Direct wafer bonding consists in joining two wafers at room temperature without any adhesive or additional materials, followed by annealing. Despite a wide technological interest, the detailed mechanism of the sealing of such model solids is poorly known due to the lack of experimental tools to investigate a nanometer-wide interface buried under millimeter-thick materials. Yet, the bonding technology is increasingly used in microelectronics, e.g., for silicon-on-insulator mass production, microelectromechanical systems manufacturing, or in three-dimensional level integration. In many cases, it represents an alternative to deposition for building heterostructures with additional capabilities. For most applications, high quality bonding is required, driving many studies on bonding interfaces.[1-4] Water removal has been widely described in the literature through H_2 outgassing due to a low temperature oxidation occurring through the native oxide. We show here that although macroscopically oxide/oxide, silicon/oxide, and silicon/silicon bondings show similar behavior, the interface evolutions at the nanometer scale are entirely different. We used interfacial X-ray reflectivity (XRR),[5] high resolution transmission electron microscopy (HR-TEM), and Fourier transform infrared spectroscopy in multiple internal reflection (FTIR-MIR)[6] to demonstrate our point. The results of similar techniques applied to silicon/silicon or silicon/oxide bonding can be found for comparison in Ref. 7.

The wafers used were 100 mm in diameter (001)-oriented Czochralski-grown Si wafers. HF-etch was first performed on the wafers to remove the native oxide from the surface. Then the oxide films were thermally grown on the Si–H terminated wafers at 800°C in dry O_2 flow. The typical SiO_2 thickness used in this study was 10 nm. Wafers were then cleaned in sulfoperoxide mixture (H_2SO_4,H_2O_2) and rinsed in deionized water. An RCA cleaning treatment was then performed, followed by a deionized water rinse and spin-drying. Finally, hydrophilic wafers were bonded at room temperature in a clean room atmosphere and annealed at various temperatures in the range from room temperature to 400°C for 2 h.

Figure 1 presents the evolutions of (a) bonding interface density and (b) width as a function of the annealing temperature, obtained from XRR analyses. Above 100°C, together with the bonding energy, our data show that the interface density sharply increases corresponding to interface closure. This mechanism of interface sealing in wafer bonding has been described using rough surface adhesion models.[8] The increase in interface density from 100 to 300°C is driven by the formation of siloxane bonds through the reaction

$$\text{Si–OH} + \text{Si–OH} \rightarrow \text{Si–O–Si} + H_2O \qquad [1]$$

The formation of the covalent bonds between the two wafers increases the local adhesion energy, and contact points tend to spread, closing the interface in analogy to a ziplock mechanism. Being a reaction product, water concentration is of course important in this mechanism. In silicon bonding, water is eliminated via silicon oxidation after diffusion through the thin native oxide.[7,9] In the thermal oxide case, the evolution is completely different.

This is already evident considering w (width), the second parameter extracted from the XRR experiment. w is the interface width, i.e., the width of the interwafer zone where the two asperity systems overlap (Fig. 1b). We can observe that, contrary to the silicon bonding case where it stayed constant, the width increases from 1 to 4 nm at 300°C. This increase is coincident with the density rise at the interface. Considering then the product $P = w\Delta\rho$, where $\Delta\rho$ is the difference of the bonding interface density with the silicon density (Fig. 1c), this value is quite constant (P represents the total electron deficit at the interface per unit area). Therefore, during sealing, a volume-conservative mechanism is to be considered, where wider unbonded (pockets) zones are created to store water on a reduced surface area (Fig. 2).

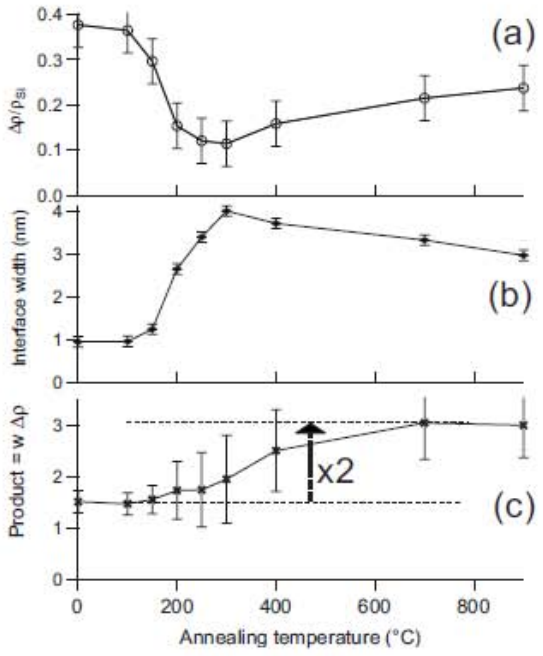

Figure 1. Parameters of the electron density profile obtained from XRR results: (a) Evolution of the bonding interface density $\Delta\rho$, (b) evolution of the bonding interface width w, and (c) P, product of w and $\Delta\rho$, as a function of the postbonding annealing temperature.

* Electrochemical Society Active Member.
z E-mail: francois.rieutord@cea.fr

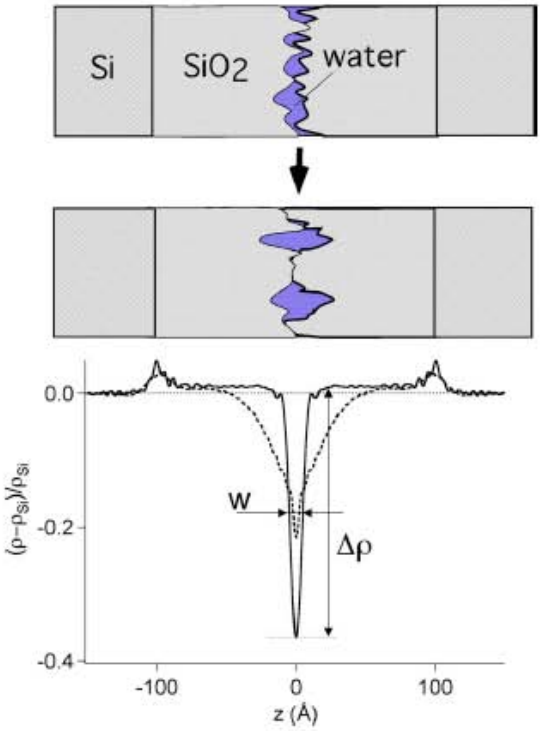

Figure 2. (Color online) Sealing mechanism of the oxide–oxide bonding (top). The electron density profiles are shown on the bottom curve, at room temperature (solid line) and after annealing at 400°C for 2 h (dashed line).

The higher temperature behavior of the interface can be similarly studied. Considering again the P value, an increase is visible at $T > 300$°C. The ratio between high and low temperature P values is close to 2, a value consistent with the removal of water (the electron density of water is half that of silicon or silicon oxide). One can consider that water leaves the 4 nm high pockets, diffusing into the oxide. The driving forces for this diffusion are the water concentration gradient and the possibility for water to hydrolyze siloxane bonds according to the reverse Reaction 1 taking place in the oxide bulk. That two opposite reactions take place at the same temperature is just a matter of the concentration of the reacting species: The large amount of interface silanols tends to favor the creation of interwafer siloxane bonds, while water diffusing in a silanol-poor oxide (thermal oxide) tends to favor siloxane hydrolysis in the oxide bulk.

The location of the Si/SiO_2 buried interfaces for each initial wafer is clearly visible on the electron density profile presented in Fig. 2 as small humps in electron density (due to some denser structure of the oxide close to the silicon). Hence the total thickness of the oxide can also be accurately measured from the data. These data show no thickness increase, whatever the initial thermal oxide thickness. This indicates that, contrary to silicon/silicon or silicon/oxide bondings where the native oxide growth was clearly visible, the Si/SiO_2 buried interface remains watertight up to 400°C. This result is also confirmed by measuring the hydrogen release when mechanically opening the interface in a vacuum vessel connected to a mass spectrometer. Contrary to the standard silicon bonding, oxide–oxide bondings show no released hydrogen for interfaces annealed up to 400°C.

To assert these XRR results, structures with various oxide thicknesses were stacked and observed by HRTEM. Cross section observations were performed using a 200 keV Akashi 002B transmission electron microscope (TEM). The observation of a 4 nm $SiO_2 \parallel$ 7 nm SiO_2 bonded structure is shown in Fig. 3. A mean 11 nm buried oxide total thickness can be measured. The bonding interface is only lightly visible. It can be located thanks to the thinnest, flat unbonded areas. Its location agrees with the initial thickness values of each oxide layer (i.e., 4 and 7 nm). The predicted increase in unbonded zone heights has been put into evidence. These pockets extend symmetrically relative to the bonding interface. Their height is up to 4.3 nm (Fig. 3), which is very consistent with the values obtained by XRR measurements (Fig. 1).

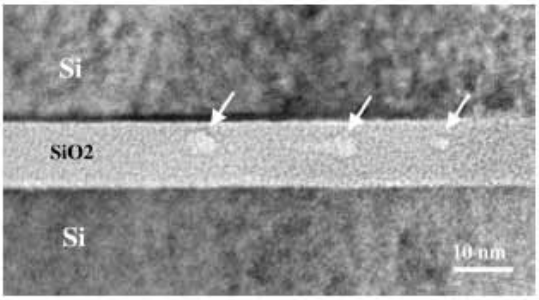

Figure 3. TEM image of a 4 nm $SiO_2 \parallel$ 7 nm SiO_2 bonded structure. Unbonded zones (white arrows) are clearly visible in this cross section observation.

To confirm this mechanism, FTIR-MIR spectroscopy experiments were performed on different samples after postbonding anneal to investigate water evolution at the bonding interface. For this, we focused our study on the O–H stretching absorption band (3200–3700 cm^{-1}), which is composed of two regions: molecular water (3225–3400 cm^{-1}) and hydroxyl groups (–OH) (3500–3700 cm^{-1}). Figure 4 shows the O–H absorption spectra of the samples before and after annealing at different temperatures. First, we observe that from room temperature to 250°C, the O–H absorption band remains almost unchanged. However, the contribution of O–H vibrations in the molecular water region is less intense. This decrease in molecular water contribution comes with the apparition of a shoulder at 3640 cm^{-1} attributed to Si–OH vibrations in silica glass. This evolution is not comparable to the behaviors of the Si–Si and $Si–SiO_2$ structures, where the O–H absorption band has disappeared from room temperature to 250°C because of water consumption necessary for silicon oxidation.[7] Here, most of the water

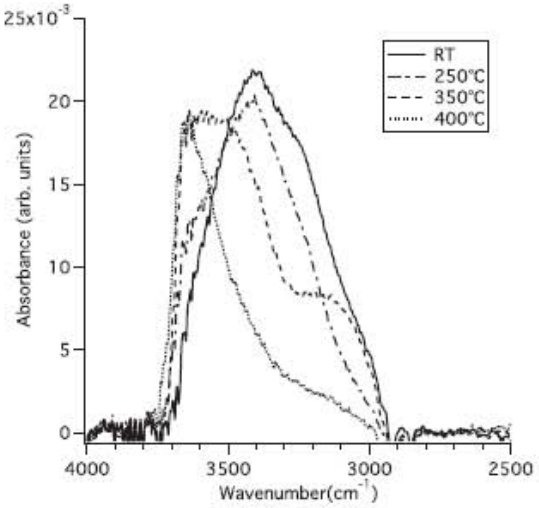

Figure 4. Evolution of the O–H absorption band in FTIR-MIR experiments measured after postbonding anneal at different temperatures.

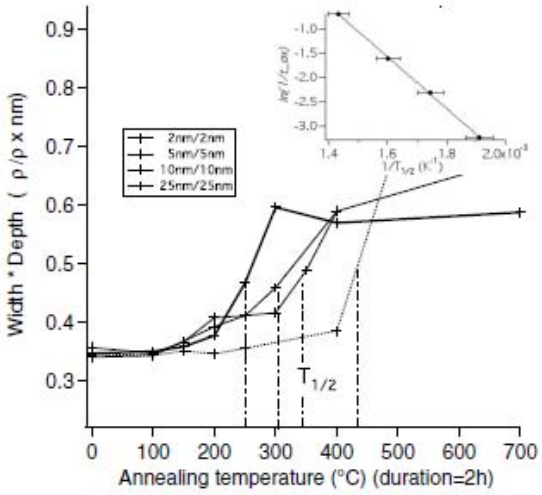

Figure 5. Interface electron deficit as a function of temperature for different oxide thicknesses. The temperature $T_{1/2}$ corresponds to water departure from the interface. Insert: Arrhenius plot of concentration vs $T_{1/2}$.

stays trapped into the bonding interface while the bonding interface closes up. From 250 to 350°C, the 3640 cm^{-1} shoulder becomes more intense and is finally the main component of the O–H absorption band after annealing at 400°C. The molecular water contribution drastically decreased in the same temperature range. It means that above a critical temperature T_e, molecular water could diffuse into the thermal silicon oxide volume and be stored under Si–OH form.

The process of diffusion/reaction of water into silicon oxide was studied by Rigo et al.[10] and Doremus et al.[11] The order of magnitude of both diffusion coefficients and reaction rates given in Ref. 11 is in accordance with our observations of an interface that is still full of water after 2 h at 200°C while nearly empty at 400°C.

The hydrolysis rate of siloxane bonds into silanols decreases with increasing silanol concentration. We observed that higher temperature anneals T_e were necessary to empty the interfaces of thinner oxides (Fig. 5). Assuming from the room temperature X-ray data that the same amount of interfacial water is diluted into different oxide thicknesses t_{ox} and plotting the concentration $[\ln(1/t_{ox})]$ as a function of the inverse T_e (insert of Fig. 5), we could observe a linear dependence with an activation energy of 0.88 eV/mol, which agrees with the activation energy of the siloxane hydrolysis reaction.[12]

To summarize, bonding mechanisms in the SiO_2–SiO_2 structure can be separated in two steps. The first one is a standard sealing phase ($T < 300$°C) where bonding interface closes up through the enlargement of contact points, which explains the interface density increase. Contrary to Si–Si and Si–SiO_2 bondings, there is no water evacuation from the bonding interface in this phase, leading to a wider profile with a higher density. Most of the water stays at the bonding interface trapped in higher unbonded zones. A more important surface area is bonded, and thus the bonding energy increases.

Then, at higher temperatures, the interface density decreases, which is associated with water diffusion out of the interface and reaction into thermal oxide films, leading to the formation of Si–OH groups within the oxide. There is no increase in the oxide thickness, suggesting that the Si/SiO_2 interface (which exhibits a high density oxide layer) remains impermeable to water diffusion.

Acknowledgment

We thank Dr. I. Radu for fruitful discussions and Soitec for financial support.

The Commissariat à l'Energie Atomique (CEA) assisted in meeting the publication costs of this article.

References

1. J. B. Lasky, *Appl. Phys. Lett.*, **48**, 78 (1986).
2. D. Feijoó, Y. J. Chabal, and S. B. Christman, *Appl. Phys. Lett.*, **65**, 2548 (1994).
3. H. Takagi, K. Kikuchi, R. Maeda, T. R. Chung, and T. Suga, *Appl. Phys. Lett.*, **68**, 2222 (1996).
4. Q.-Y. Tong, G. Fountain, and P. Enquist, *Appl. Phys. Lett.*, **89**, 042110 (2006).
5. F. Rieutord, J. Eymery, F. Fournel, D. Buttard, R. Oeser, O. Plantevin, H. Moriceau, and B. Aspar, *Phys. Rev. B*, **63**, 125408 (2001).
6. C. Maleville, O. Rayssac, H. Moriceau, B. Biasse, L. Baroux, B. Aspar, and M. Bruel, in *Semiconductor Wafer Bonding 4: Science, Technology, and Applications*, U. Gösele, H. Baumgart, T. Abe, C. E. Hunt, and S. Iyer, Editors, PV 1997-36, The Electrochemical Society Proceedings Series, Pennington, NJ (1997).
7. C. Ventosa, F. Rieutord, L. Libralesso, C. Morales, F. Fournel, and H. Moriceau, *J. Appl. Phys.*, **104**, 123524 (2008).
8. F. Rieutord, H. Moriceau, R. Beneyton, L. Capello, C. Morales, and A.-M. Charvet, *ECS Trans.*, **3**(6), 205 (2006).
9. M. K. Weldon, V. E. Marsico, Y. J. Chabal, D. R. Hamann, S. B. Christman, and E. E. Chaban, *Surf. Sci.*, **368**, 163 (1996).
10. S. Rigo, F. Rochet, B. Agius, and A. Straboni, *J. Electrochem. Soc.*, **129**, 867 (1982).
11. R. H. Doremus, *J. Mater. Res.*, **10**, 2379 (1995).
12. J. K. West and L. L. Hench, *J. Mater. Sci.*, **29**, 5808 (1994).

NANO LETTERS

2007
Vol. 7, No. 9
2596−2601

Strain and Shape of Epitaxial InAs/InP Nanowire Superlattice Measured by Grazing Incidence X-ray Techniques

Joël Eymery,* François Rieutord, Vincent Favre-Nicolin, Odile Robach, Yann-Michel Niquet, Linus Fröberg, Thomas Mårtensson, and Lars Samuelson

CEA Grenoble, Département de Recherche Fondamentale sur la Matière Condensée, Service des Matériaux et Microstructures, 17 rue des Martyrs, 38054 Grenoble Cedex 9, France, and Solid State Physics, Lund University, Box 118, S-221 00 Lund, Sweden

Received April 16, 2007; Revised Manuscript Received July 26, 2007

ABSTRACT

Quantitative structural information about epitaxial arrays of nanowires are reported for a InAs/InP longitudinal heterostructure grown by chemical beam epitaxy on an InAs $(111)_B$ substrate. Grazing incidence X-ray diffraction allows the separation of the nanowire contribution from the substrate overgrowth and gives averaged information about crystallographic phases, epitaxial relationships (with orientation distribution), and strain. In-plane strain inhomogeneities, intrinsic to the nanowires geometry, are measured and compared to atomistic simulations. Small-angle X-ray scattering evidences the hexagonal symmetry of the nanowire cross-section and provides a rough estimate of size fluctuations.

The development of vertical semiconductor nanowires (NW) as new building blocks for future nanoscale electronics and photonics devices is strongly dependent on the crystalline quality. For some applications (like field effect transistors), the properties of individual (and identical) NWs must be mastered, whereas in other applications, device operation depends on the characteristics of a number of NW in parallel and therefore on the distribution width of the assembly. For example, resonant sensors or optical microcavities containing many NWs must have well-matched diameters to obtain a high quality factor.

To characterize the structural properties of these new materials, transmission electron microscopy (TEM) is a standard tool that gives first-rate information about individual objects or small assemblies including the determination of the growth directions, heterostructure cross sections, surface facets, dislocations, or stacking faults.[1,2] In spite of their very strong complementarities with TEM, X-ray diffraction techniques are up to now very seldom used to get averaged quantitative information important for practical use. Experiments on epitaxial arrays to study defects, disorientations, and strains are very limited,[3−6] and only powder diffraction or texture methods are routinely performed on broadly oriented NW growths. In this paper, we will show that with the development of the growth control, epitaxial NW heterostructures can now be effectively studied by conventional synchrotron X-ray scattering techniques,[7] i.e., grazing incidence X-ray diffraction (GIXRD) and small-angle X-ray scattering (SAXS). It will be shown that statistical quantitative information can be obtained concerning epitaxial relationships, orientation distributions, strain relaxation, and stacking defects. These points will be illustrated by the detailed analysis of a 20 period InAs/InP nanowire superlattice, including comparison to simulation.

The nanowire growth is Au-assisted and takes place in a chemical beam epitaxy (CBE) system using trimethylindium, precracked *tert*-butylarsine, and precracked *tert*-butylphosphine as growth precursors.[8] Prior to growth, size-selected Au aerosol particles are deposited on a InAs(111)B substrate and the sample is deoxidized in the growth chamber at 520 °C under As pressure. Growth is started at 425 °C for about 530 nm of InAs and then further lowered to 390 °C for the superlattice growth with 20 segments of 20 nm (InAs) and 10 nm (InP). The structure is ended with an InAs segment of about 65 nm.

Figure 1 shows scanning electron microscopy (SEM) images of the sample, indicating that most of the NWs are perpendicular to the surface with a standard hexagonal cross section. TEM analysis shows $\langle 11\bar{2} \rangle$ side facets referred to the cubic substrate and a Wurtzite structure of the nanowire; we have never seen any cubic insertion at the bottom of the nanowire or anywhere else.[8] On top of the surface, small pyramidal hillock overgrowths can be observed (see Figure 1b,e). The narrow NW orientation distribution allows studying the NW reciprocal space according to the substrate lattice, and the (*hkl*) Miller indexes, corresponding to the InAs $(111)_B$

* Corresponding author. E-mail: joel.eymery@cea.fr. Équipe Mixte CEA-CNRS-UJF, Nanophysique et Semiconducteurs, CEA Grenoble.

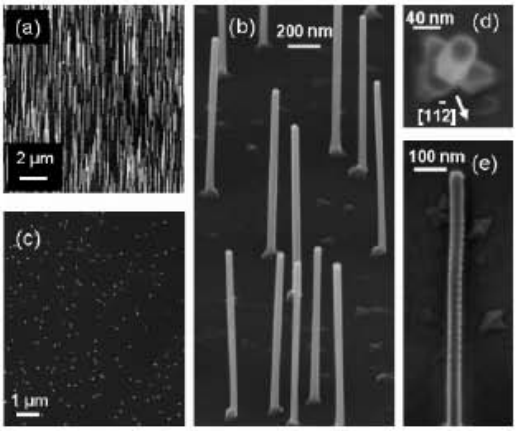

Figure 1. Scanning electron microscopy images of CBE grown epitaxial nanowires. (a,b) tilted views, (c,d) top views, showing the vertical alignment and the hexagonal cross section with facets corresponding to the [11$\bar{2}$] direction indexed in the cubic substrate lattice; (e) side view, where the superlattice periods are barely seen (see cover picture for a SEM picture in the transmission geometry).

surface unit cell, can be used as a reference. The surface unit cell lattice vectors have a hexagonal basis $\mathbf{a}_1$, $\mathbf{a}_2$, $\mathbf{a}_3$ with $\mathbf{a}_1 = {}^1/_2[\bar{1}10]$, $\mathbf{a}_2 = {}^1/_2[0\bar{1}1]$ in the surface plane, and $\mathbf{a}_3 = [111]$ perpendicular to the surface. The corresponding reciprocal lattice vectors are along three h,k,l axes with h and k in the surface plane, making an angle of 60° and l normal to the surface. In these coordinates, InAs $(111)_B$ bulk Bragg reflections are found at $l = 1, 4, 7, \ldots$ for $(h,k) = (1,0)$ and at $l = 2, 5, 8, \ldots$ for $(h,k) = (0,1)$. X-ray experiments were performed at the European Synchrotron Radiation Facility (ESRF, Grenoble France) under helium flow to prevent sample degradation and to avoid background diffuse scattering from the air. Diffraction (respectively, small angle) data were collected on the BM32 French CRG beamline using 10 (respectively, 18) keV photon energy. The beam footprint on the sample surface, which is about 5×0.5 (0.1) mm^2, integrates the intensities of a very large number of NWs.

Figure 2 shows the measurements of the (01l) crystal truncation rod (CTR) for several grazing incidence angles α. Close to the substrate critical angle for total external reflection ($\alpha_c = 0.29°$), we measure at $l = 2$ and 5 the sharp and intense diffraction peaks of the InAs substrate (labeled S). Their intensities decrease with decreasing α and vanish in the "transmission" geometry ($\alpha = 0°$). The extra peaks may come either from the NWs or from other surface overgrowths. Peak intensities at $l \approx 1.5$, 3, and 4.5 (labeled NW in Figure 2) do not depend on the incidence angles, whereas some "satellites" at $l \approx 1$, 2, 4, and 5 (labeled TW, for twinned overgrowth) do. This strongly suggests that noninteger peaks can be attributed to the NWs. It is confirmed by the peak-shape dependence on the incidence shown in the inset of Figure 2. In the transmission geometry and for α close to the critical angle, only a single peak is measured. In intermediate cases, a second peak is measured. Its larger-angle position depends on α, and at $\alpha = 0.1°$, the two peaks overlap. These observations can be explained by using the distorted-wave Born approximation (DWBA). In

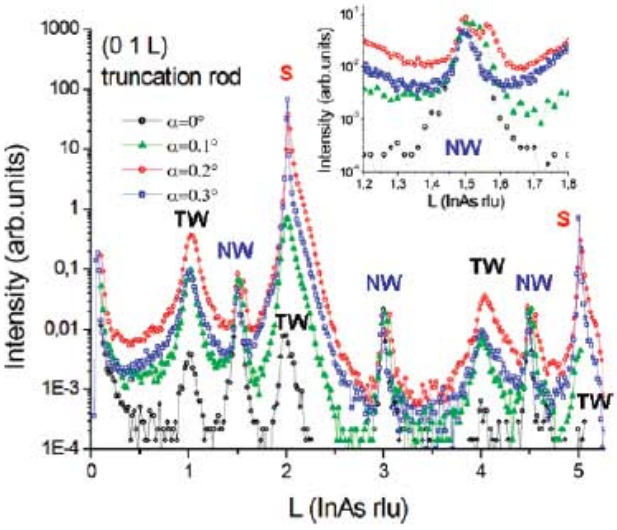

Figure 2. (01l) crystal truncation rod measurement for several grazing incidences ($\alpha = 0$, 0.1, 0.2, 0.3°). l is in reciprocal lattice units (rlu) of the cubic InAs(111) substrate (marked by S). NW (TW) correspond to the nanowires (substrate overgrowths) peaks. Inset: splitting of NW-peak at $l = 1.5$ in two contributions as the function of α. This effect is explained in the text by the coexistence of several scattering processes at very grazing angle.

this formalism, the scattered wave amplitude is composed of four terms, including all combinations of scattering from the NW and reflection from the substrate.[9] At very low grazing incidence (transmission geometry), the incident beam is scattered by the NW and collected by the detector, whereas at larger α (but lower than α_c), a second contribution comes from the reflection by the surface toward the NW. This reflection acts as a second "incident beam" with a wave vector pointing slightly upward. The surface reflection is sharply decreased for $\alpha > \alpha_c$, which explains why the two terms are observed only at very grazing angle. The third and fourth term considered in DWBA, coming respectively from the beam scattered by the NW and reflected by the surface and from both incident and scattered beam reflected by the surface, are negligible because downward scattered beams have an angle much larger than α_c with respect to the surface. This multiple scattering effect also applies to the TW peaks, and a small shift is observed with α, but peak broadness causes the two contributions to overlap. The TW peaks intensities decrease with the incidence suggesting a different origin.

To have more insights about the nature of these peaks, we measure for $\alpha = 0.3°$ several CTRs in the ($h0l$), ($0kl$), and (hhl) reciprocal planes (see some examples in Figure 3b,c). Figure 3a summarizes the ($h0l$) measurements referred to the InAs cubic substrate lattice. Zinc-blende InAs substrate and hexagonal NWs peaks are easily indexed by considering the stacking sequence of (111) planes.[6] Note that two variants having the same peak intensities are measured for the hexagonal NWs. They correspond to "equivalent" 60° rotations domains, which can be probably attributed to different NWs orientations on the (111) surface. TEM observations rule out defects in individual NWs, moreover, this kind of defect should not give identical domains

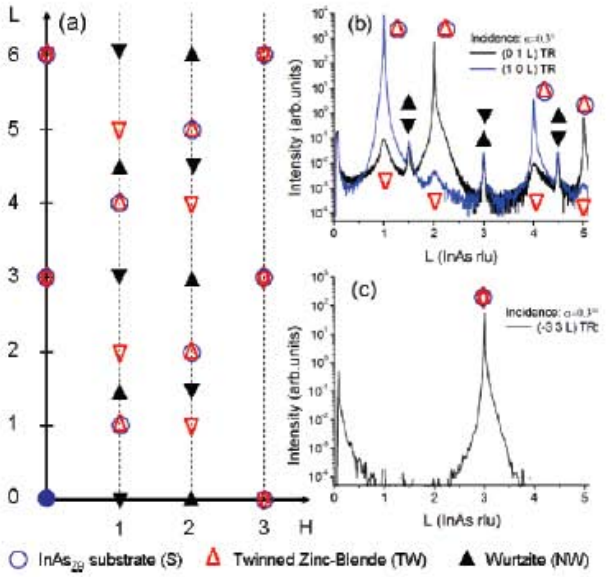

Figure 3. (a) Schematics of the (*h*0*l*) reciprocal plane of the sample shown in Figure 1 (*h*,*l* scales and peak positions are only indicative): (○) InAs cubic substrate, (▲▼) hexagonal NW variants obtained by 60° in-plane rotations, (△▽, in red) twinned cubic substrate overgrowth (ACB stacking of the (111) planes instead of ABC). (b,c) Truncation rod measurements examples (*l* scans) for $\alpha = 0.3°$: (b) along (10*l*) and (01*l*) (equivalent to (20*l*) in (a)), and (c) along (−33*l*).

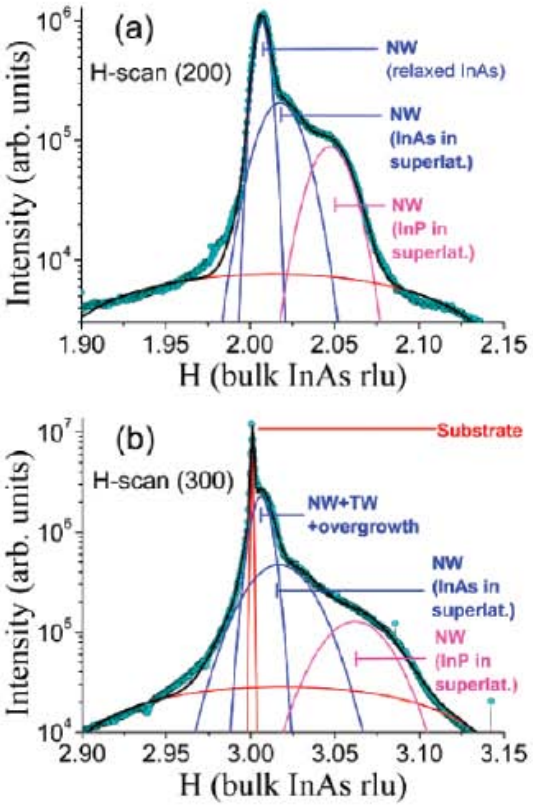

Figure 4. In-plane measurements along *h* (see the definition in Figure 3) for the (a) (200) and (b) (300) reflections. Points correspond to measurements and thick curves to the best fits of the nanowires (NW), twinned overgrowth (TW), and substrate (S) contributions. *h* is in reciprocal lattice units (rlu) of the cubic InAs-(111) substrate.

intensities. The TW peaks are consistent with twins of a cubic phase having a lattice parameter close to the substrate. They can be attributed to the pyramidal hillocks observed by SEM (see Figure 1b,e) in agreement with the α-dependence shown in Figure 2 and with the in-plane orientation distribution (mosaicity) discussed later. The hillock morphology is commonly observed in zinc-blende (111) epilayers for II−VI and III−V compounds. This structure may be nucleated on a surface defect (for example on a gold contamination coming with the aerosol catalysts). The stable cubic phase is obtained due to the strong coupling with the surface. Indeed, we do not have the influence of the NW geometry (dimension and surface effects) that could stabilize the metastable hexagonal structure. The NW and TW lattice parameters are deduced both from in-plane ⟨200⟩, ⟨300⟩, and out-of-plane ⟨01*l*⟩ measurements according to the cubic phase reference ($a^{\mathrm{InAs}}_{\mathrm{Subst}} = 0.60583$ nm and $a^{\mathrm{InP}}_{\mathrm{Subst}} = 0.58687$ nm).

As shown in Figure 4, the fit of in-plane measurements (reflections perpendicular to the surface) allows determination of the different contributions to the measured intensity: the substrate overgrowths, the relaxed InAs segments at the bottom and the top of the nanowire, and the average InAs and InP insertions in the superlattice. For the sake of simplicity, we chose a Gaussian function to model the Bragg peak shape. This choice is adequate to describe the center position and the width of the peak, but it is surely not enough to describe the peak tails. A more complicated description (with more parameters to fit) should take into account these features. It should probably decrease the background below the signal (see the red curve in Figure 4), but up to now no strong physical argument can be given to select the function type (Lorentz, Voigt, Pearson...). Wurtzite InAs NW position (shown in (200) *h* scan and in Figure 3) is slightly larger than the cubic InAs substrate. It corresponds to the bottom and to the top of the NW and should be relaxed due to the small NW diameter and to the small lattice mismatch: the in-plane lattice parameter is only decreased of about 0.32% ± 0.03 according to the substrate reference. For the (003) measurement (see Figure 4b), the relaxed InAs NW signal is superposed to the TW contribution and eventually to planar (and not twinned) substrate overgrowth. The fit of this composite peak gives 0.17% ± 0.03, suggesting that the two last phases are very close to bulk cubic InAs. For the NW superlattice, the InAs and InP average in-plane lattice parameters can be estimated by the positions of the peak maxima of (002) and (003) *h* scans: $a^{\mathrm{InAs}}_{\mathrm{NW}}/a^{\mathrm{InAs}}_{\mathrm{Subst}} = 0.9936 \pm 0.001$ and $a^{\mathrm{InP}}_{\mathrm{NW}}/a^{\mathrm{InAs}}_{\mathrm{Subst}} = 0.9787 \pm 0.001$ (see also the Table 1). It was difficult to assess accurately $c^{\mathrm{InP}}_{\mathrm{NW}}$ due to the low experimental resolution used in CTR measurements and to the low signal, but for InAs, we measured $c^{\mathrm{InAs}}_{\mathrm{NW}} \approx a^{\mathrm{InAs}}_{\mathrm{NW}}/\sqrt{2}$. Note that no clear signals due to the NW superlattice periodicity have been measured in these experiments. It may be due to several reasons, the effects of which are probably combined: strain relaxation distribution along the NWs, disorientations, section variations induced by the catalyst particle's diameter distribution and growth fluctuations (the

Table 1. Calculated Averaged In-Plane Deformation $\langle \epsilon_{yy} \rangle$ for Nanowire Superlattices with Radius $R = 22$ nm Consisting of 20 nm InAs/7 or 10 nm InP Layers[a]

		20 nm InAs/ 7 nm InP NW	20 nm InAs/ 10 nm InP NW
$\langle \epsilon_{yy} \rangle$ (%)	InAs (-0.64 ± 0.1):	-0.46	-0.61
	InP (-2.13 ± 0.1):	-1.82	-2.15
σ_{yy} (%)	InAs:	0.37	0.42
	InP:	0.50	0.43

[a] The atomic positions are relaxed with the valence force field described in the text. The deformations are calculated with respect to the cubic InAs reference and the experimental values are parenthesized. The standard deviations (σ_{yy}) of these deformations show the intrinsic broadening of this longitudinal nanowire structure.

longitudinal growth rate, and therefore the insertion thickness, varies with the NW diameter), or to a height (i.e., phase) shift coming from a nucleation delay before the beginning of the growth of individual NW.

The diffraction peak broadening may have several origins: (i) the NW size along the momentum transfer, (ii) the NW mosaicity corresponding to the in-plane (twist) and out-of-plane (tilt) rotations of the individual NWs, (iii) a nonuniform strain field with a local lattice parameter variation, including heterostructure strain relaxation and bending of the growth axis. (ii) and (iii) depend on the modulus of the momentum transfer, whereas (i) does not.

In-plane mosaicity is measured from transverse scans along (h00) reflections (rocking scan of the sample along its surface normal). It gives a full width at half-maximum (fwhm of a Gaussian function) of the TW peaks lower than 0.02°, whereas the NW peaks have an in-plane mosaicity of about $0.5 \pm 0.1°$. The fwhm of in-plane radial scans along [h00] (for example, for the relaxed InAs peak of Figure 4a) is 0.143 ± 0.006 nm^{-1}, which can be attributed to a NW cross-section diameter between hexagonal facets of about 44 ± 2 nm. This value, consistent with Figure 1, will be confirmed by SAXS measurements below.

The experimental results can be compared to atomistic simulations. We consider hexagonal [0001]-oriented InAs/InP nanowires superlattices with the wurtzite structure. The edge length (and radius) of the regular hexagon ($\{10\bar{1}0\}$ facets in hexagonal notation) is $R = 22$ nm, and the period of the superlattice is $l \approx 30$ nm. The thickness of the InAs layer is 20 nm, while the thickness of the InP layer is varied from 7 to 10 nm. The relaxed atomic positions are computed using Keating's valence force field (VFF model).[10] In this model, the elastic energy depends on the nearest-neighbor bond lengths and bond angles through bond stretching and bond bending constants. These parameters are fitted to the bulk modulus and Poisson ratio ν_{111} of the zinc-blende materials,[11-12] assuming that the elastic constants of the wurtzite phases fulfill Martin's relations.[13] The elastic energy is then minimized with respect to the atomic positions and period of the superlattice using a conjugate gradients algorithm, and the strain tensor is computed from the atomic positions in the $x = [2\bar{1}\bar{1}0]$, $y = [01\bar{1}0]$, and $z = [0001]$ axis set. Within this axis set, the k scans of GIXRD correspond to the y direction perpendicular to the hexagonal facets.

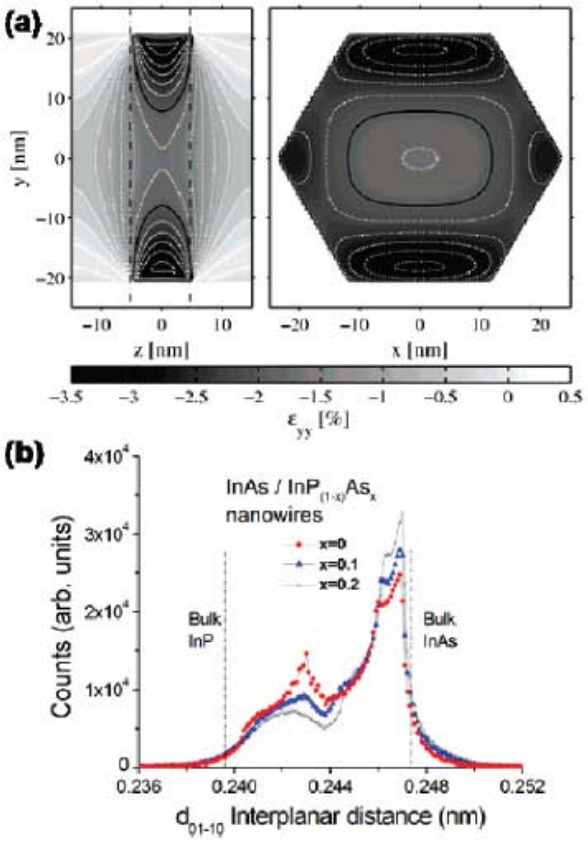

Figure 5. (a) In-plane deformations ϵ_{yy} (with reference to bulk InAs) for a 20 nm InAs/10 nm InP nanowires superlattice (cross sections at $x = 0$ and $z = 0$, respectively). The atomic positions are relaxed with the valence force field model described in the text. The black line is $\epsilon_{yy} = -2\%$, the difference between white dotted lines being $\Delta\epsilon_{yy} = 0.25\%$. (b) Histogram of the distances between $(01\bar{1}0)$ planes (perpendicular to the y direction; i.e., parallel to the hexagonal facets) for a 20 nm InAs/10 nm $InAs_xP_{1-x}$ nanowires superlattices with $x = 0$, 0.1, 0.2.

The in-plane deformation ϵ_{yy}, computed with reference to bulk InAs,[15] is shown in Figure 5a for the 20 nm InAs/10 nm InP structure. The InP layer, whose elastic constants are close to InAs, is heavily compressed by the latter. The surface of the nanowires can, however, bulge to relieve part of the stresses, which leads to a very inhomogeneous strain distribution (see for example refs 12 and 14 for a discussion of the electronic and optical properties of InAs/GaAs nanowire superlattices). The average in-plane deformations in InAs and InP are reported in Table 1 for two InP thicknesses (7 and 10 nm). The standard deviations of these values are very large even for ideal objects, indicating that the strain inhomogeneity is an intrinsic source of the peak broadening observed in GIXRD. These distributions must be taken into account to optimize band gap strain engineering in complex heterostructures. The strains are, moreover, very close to those computed in similar zinc-blende nanowire superlattices.

The calculated average in-plane deformations in InAs and InP (inside the 20 nm InAs/10 nm InP NW superlattice) are in very good agreement with the experimental values parenthesized in Table 1. The impact of various structural

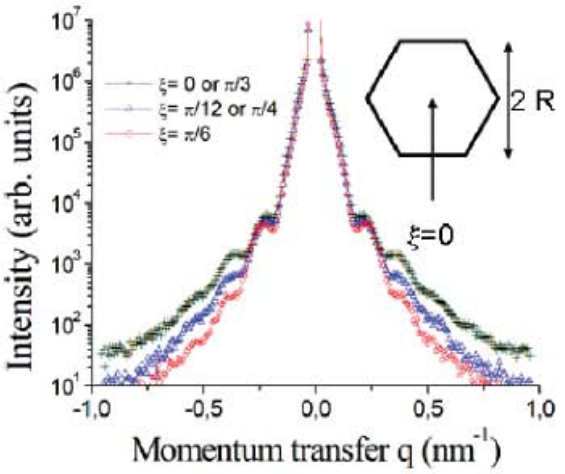

Figure 6. Small-angle X-ray scattering measurements for several azimuth ξ (see inset for definition) as the function of the momentum transfer $q = 4\pi \sin(\theta)/\lambda$ (θ is half of the scattered angle, λ is the wavelength). Grazing and emergence angles are very low (a few hundredths of a degree). Only three measurements (i.e., azimuths) are drawn, representative of the $\pi/6$ symmetry of the scattered intensity.

parameters (thickness of the InP layer, presence of an InAs shell, interdiffusion) has been investigated. The deformations in thinner (7 nm) InP layers are actually too small. The calculated deformations in core/shell 20 nm InAs/10 nm InP NW superlatices remain quite close: for a 1 nm thick InAs shell around a core with radius $R = 21$ nm, we get $\langle \epsilon_{yy} \rangle_{InAs} = -0.60\%$ and $\langle \epsilon_{yy} \rangle_{InP} = -2.04\%$, while for a 2 nm thick shell around a core with radius $R = 20$ nm, we get $\langle \epsilon_{yy} \rangle_{InAs} = -0.57\%$ and $\langle \epsilon_{yy} \rangle_{InP} = -1.94\%$. The interdiffusion is very limited for the low-temperature growth used in this study (390 °C): TEM energy dispersive spectrometry experiments estimate that the P atom concentration in InAs is lower than 2% (i.e., the noise level). For higher growth temperature, the influence of the substitution of P atoms by As in the InP layer (i.e., the insertion material) can be assessed by the distance between the $(01\bar{1}0)$ planes parallel to the nanowires edge (i.e., perpendicular to the k direction). Figure 5b gives the histogram of this distribution for 20 nm InAs/10 nm $InAs_xP_{1-x}$ superlattices with $x = 0$, 0.1, 0.2. It shows that a small substitution of P atoms largely shifts and broadens the initially "peaked" InP contribution, which can also contribute to an increase of the width of the in-plane diffraction peaks. Experimentally, the separation of interdiffusion and elastic relaxation contributions should be obtained by X-ray anomalous measurements around the As k absorption edge (11.868 keV).

After having analyzed the in-plane deformation with X-ray diffraction, we can also access to the average NW shape and size of this assembly by using small-angle X-ray scattering (SAXS)[15] at very grazing incidence and emergence ($\alpha = \beta \approx 0.1°$). Figure 6 shows selected intensity measurements $I(q)$ as a function of the in-plane scattering vector q for several sample orientations (azimuth) around the surface normal. Contrary to what is measured for cylindrical cross sections, we observe the dependence on the azimuth ξ of the

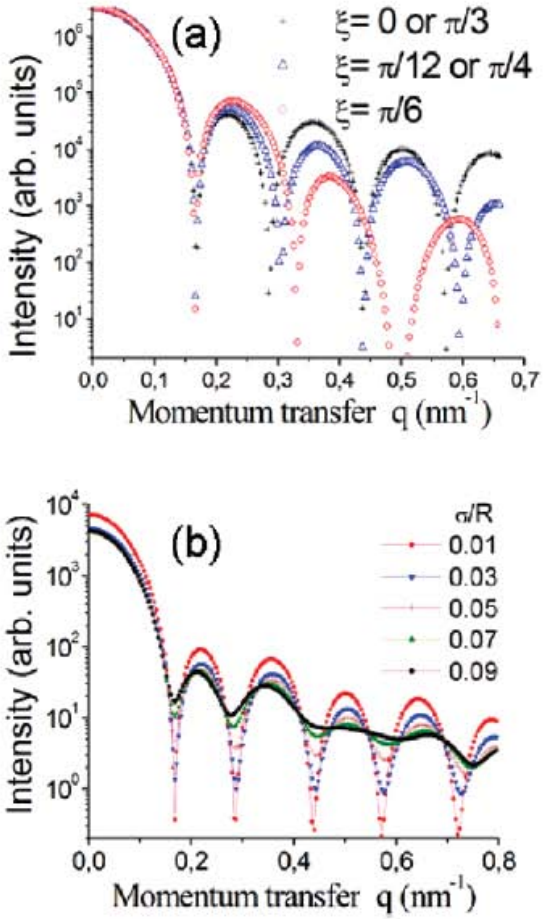

Figure 7. (a) DWBA calculation[10] of the in-plane intensity scattered by uncorrelated regular hexagonal NW of radius $R = 22$ nm at grazing incidence and emergence angles ($\alpha = \beta = 0.1°$). No size distribution is included in these calculations, and the azimuth ξ is defined by the inset of Figure 6. (b) Small-angle intensity calculated at $\xi = 0$ for a Gaussian distribution of the radius R of hexagonal NW. σ is the standard deviation of the R distribution ($\exp[-(x - x_0)^2/(2\sigma^2)]/[(2\pi)^{1/2}\sigma]$), and σ/R indicates the broadening.

oscillation fringes due to the NW size in a direction perpendicular to the beam both in position and intensity. The origin $\xi = 0$ is defined by a direction perpendicular to the NW facets (k direction in the diffraction experiments), as shown in the inset of Figure 6. The systematic measurement of $I(q)$ as a function of ξ (over $\pi/2$, every $\pi/36$) has shown a $\pi/6$ symmetry. The main features of the azimuth−angle dependence consist of the damping and the shift of the second-order fringe from $\xi = 0$ to $\pi/6$ and of the disappearance of the third oscillation at $\xi = \pi/6$. The center part of the experimental curve comes from the surface and overgrowth scattering. Note that in this sample, the NW density is very low (only about 2.5 NWs/μm^2 from Figure 1) so that synchrotron radiation is necessary. For higher densities, this method should be applied with a laboratory setup. Because no interparticle−position interactions have to be considered (see Figure 1c where the distribution of distances between nearest-neighbors NWs is very broad), the X-ray pattern can be analyzed as a convolution of the NW form factor by the

size distribution function. This form factor, derived in the simplest approximation from the Fourier transform of the NW shape,[15−17] can be calculated with the DWBA for a regular hexagon of height H and facet width R. As seen in Figure 7a, all the main features of the experimental measurements can be simulated by a monodisperse size distribution with $R = 22$ nm. The sharp interferences fringes appearing at roughly $q_{||} \sim 2\pi/R$ are associated to the zero of the sine cardinal or Bessel function for simple shapes like parallelepiped or cylinder. As observed in electron microscopy, the growth distribution involves both size and shape variations of the hexagonal cross sections with eventually a variation along the wire length. In a first approximation, only the R variation will be considered, giving a fringe smoothening with the increase of the width of the size distribution. This distribution can be modeled by a Gaussian function (fwhm σ) in the DBDA calculations. The calculated intensity for $\xi = 0$ is drawn in Figure 7b as a function of σ/R. Because the experimental measurements still show the third oscillation fringe, the maximum of the size distribution can be roughly estimated to be lower than $\sigma/R < 8\%$. This variation is mainly imposed by the aerosol particle size distribution and by fluctuations of the catalyst-assisted growth. More accurate measurements with 2D detectors in the grazing incidence SAXS geometry are presently under way to decrease the error bars and to study facets distribution.

In summary, this letter demonstrates the interest of X-ray grazing incidence techniques to get quantitative structural information on epitaxial NWs assemblies. The change of grazing incidence angle in surface diffraction experiments allows separating the different contributions of the signal, i.e., the nanowires from parasitic substrate overgrowths. More generally, these methods could be advantageous when studying samples grown by molecular beam epitaxy, which is a less selective growth method, leading to a larger overgrowth at the nanowires base. The crystalline phases (cubic or hexagonal) as well as growth defects (stacking faults) are determined from the direct analysis of crystal truncation rods. In the present study, the InAs/InP heterostructure was entirely hexagonal with equivalent variants, and a second twinned phase is present only as a substrate overgrowth. The same method could also be applied to inhomogeneous NW (for example GaAs) having a mixture of hexagonal and cubic phases. The in-plane epitaxial disorientations of the NW are small (fwhm $\approx 0.5°$), indicating a very good control of the initial growth stage consistent with classical mosaicity observed in metal (aerosol)/semiconductor substrate epitaxy. The strain distribution resulting from the relaxation in the NW geometry, measured from the position and broadening of the diffraction peaks, is in agreement with atomistic calculations of ideal structures. Complementary experiments using small-angle scattering have shown the possibility to check the size and shape of the objects. This method seems to be very promising in homogeneous assemblies to estimate such geometrical fluctuations, in particular with colloid-assisted growth, where synchrotron experiments are not necessary for dense assemblies. Last, grazing incidence X-ray techniques can be developed to study and to optimize the NW growth mechanisms or the technological processes. They will be helpful to integrate well-controlled NW building blocks into functional assemblies, and ultimately into systems.

Acknowledgment. This work has been performed under the EU program NODE 015783. We thank the French CRG-IF and ID01 ESRF beamlines for their technical help.

References

(1) Bell, D. C.; Wu, Y.; Barrelet, C. J.; Gradečak, S.; Xiang, J.; Timko, B. P.; Lieber, C. M. *Microsc. Res. Techn.* **2004**, *64*, 373.
(2) Johansson, J.; Karlsson, L. S.; Swensson, C. P. T.; Mårtensson, T.; Wacaser, B. A.; Deppert, K.; Samuelson, L.; Seifert, W. *Nat. Mater.* **2006**, *5*, 574.
(3) Bakkers, E. P. A. M.; Van Dam, J. A.; De Franceschi, S.; Kouwenhoven, L. P.; Kaiser, M.; Verheijen, M.; Wondergem, H.; Van Der Sluis, P. *Nat. Mater.* **2004**, *3*, 769.
(4) Svensson, C. P. T.; Seifert, W.; Larsson, M. W.; Wallenberg, L. R.; Stangl, J.; Bauer G.; Samuelson, L. *Nanotechnology* **2005**, *16*, 936.
(5) Kawamura, T.; Bhunia, S.; Watanabe, Y.; Fujikawa, S.; Matsui, J.; Kagoshima, Y.; Tsusaka, Y. *J. Appl. Phys.* **2005**, *97*, 084318.
(6) Mandl, B.; Stangl, J.; Märtensson, T.; Mikkelsen, A.; Eriksson, J.; Karlsson, L. S.; Bauer, G.; Samuelson L.; Seifert, W. *Nano Lett.* **2006**, *6*, 1817.
(7) Metzger, T. H.; Schülli, T. U.; Schmidbauer, M. *C. R. Phys.* **2005**, *6*, 47.
(8) Larsson, M. W.; Wagner, J. B.; Wallin, M.; Håkansson; Fröberg, L. E.; Samuelson, L.; Wallenberg, L. Reine *Nanotechnology* **2007**, *18*, 015504.
(9) Rauscher, M.; Panagio, R.; Metzger, H.; Kovats, Z.; Domke, J.; Peisl, J.; Pfannes, H. D.; Schulze, J.; Eisele, I. *J. Appl. Phys.* **1999**, *86*, 6763.
(10) Keating, P.-N. *Phys. Rev.* **1966**, *145*, 637.
(11) Niquet, Y.-M. *Phys. Rev. B* **2006**, *74*, 155304.
(12) *Physics of Group IV Elements and III-V Compounds*, Madelung, O., Schulz, M., Weiss, H., Eds.; Landolt-Börnstein, New Series, Group III, Vol. 17, Part A; Springer-Verlag: New York, 1982.
(13) Martin, R. M. *Phys. Rev. B* **1972**, *6*, 4546.
(14) Niquet, Y.-M. *Nano Lett.* **2007**, *7*, 1105.
(15) Lazzari, R. *J. Appl. Crystallogr.* **2002**, *35*, 406.
(16) Vargas, R.; Louër, D.; Langford, J. I. *J. Appl. Crystallogr.* **1983**, *16*, 512.
(17) Boulle, A.; Conchon, F.; Guinebretière, R. *Acta Crystallogr., Sect. A: Found. Crystallogr.* **2006**, *A62*, 11.

NL070888Q

Annex 3b: Impact and most cited publications

Publications in journals with impact factor higher than 3 (2006-2010):

Nature	[31.94]	1
Science	[28.10]	1
Materials Today	[12.93]	1
Surf. Sci. Reports	[12.80]	1
Nano Letters	[10.37]	1
Phys. Rev. Lett.	[7.18]	3
Langmuir	[4.10]	1
Appl. Phys. Lett.	[3.73]	8
Nanotechnology	[3.44]	1
Phys. Rev. B	[3.32]	16

Most cited articles (2006), number of citations higher than 10

Thelander et al, Materials Today, 2006	143
Verilhac et al, Synthetic Metals, 2006	30
Nolte et al, Science, 2008	22
Eymery et al, Nano Letters, 2007	20
Sousbie et al, J. Appl. Phys., 2006	11
Gailhanou et al, Appl. Phys. Lett., 2007	11
St-Girons et al, Appl. Phys. Lett., 2008	11
Lazzari et al, Phys. Rev. B, 2007	10
Olander et al, Phys. Rev. B, 2007	10

Annex 4 : 2005' BLRP recommendations

Report of BLRP BM32

The committee was impressed by the high quality of research carried out over the review period. We strongly recommend that the existing programmes continue to be pursued along with new developments. These are seen as complementary activities to those that could be pursued at Soleil, exploiting the high energy beams and unique experimental facilities on BM32 at the ESRF.

Research by Staff and Users

There have been two strands to the work carried out on BM32. The first involves the use of the SUV end station to study the structure of surfaces and the in situ growth of nanoparticles on surfaces using a combination of SXRD and GISAXS. This has been world leading research. The second is the use of the general purpose diffractometer end station to study buried interfaces. Studies here have been quite diverse, and much of this work is internationally competitive. A particular strength of the BM32 activities has arisen from strong collaboration with the French and international communities. This high level of collaboration means that it is difficult to separate the research carried out by staff and users.

There have been a number of highlights. These include the study of high energy X-ray reflectivity of buried interfaces created by wafer bonding [Phys. Rev. B 63 (2001) 125408] and the investigation of the structure and fluctuations of a single floating lipid bilayer [Proc. Nat. Acad. Sci. USA 102 (2005) 11639]. As for work on the SUV, we see the in-situ GISAXS towards a real time modeling of growing nanoparticles as a particular highlight [Science 300 (2003) 1416]. The study of self organized growth of nanoparticles on a surface patterned by a buried dislocation network [Phys.Rev.Lett. 95 (2005) 185501] is a significant advance. Finally, we include the study of two-dimensional oxide on Pd(111) [Phys.Rev.Lett. 88 (2002) 246103] as an example of highly cited ESRF-beamtime work.

Future Scientific Directions

The continued use of SUV for world leading studies of in situ growth is very strongly supported. The combination of SXRD, GISAXS, anomalous diffraction and in situ scanning probe studies is unique. The panel perceives that this activity could lead the field for at least 5 years, particularly as applied to nanostructures on semiconductor and oxide substrates.

As regards the GMT endstation, the panel supports microfocus Laue diffraction as the major new development. This exploits the pink beam facility to study systems of technological relevance linked to the local nanotechnology industry. As an example, the strain associated with Cu grains in interconnects could be evaluated. The use of the 'catalysis' GISAXS chamber is seen as another important development. The panel also anticipates that the use of hard X-rays to study buried interfaces will continue, for instance bonding problems at Si-Si interfaces.

G Bauer, W de Jeu, S Ferrer, U Pietsch, G Thornton

Technical Status of the beamline and future developments

The planned upgrade to the optics is seen as appropriate, especially in achieving harmonic rejection and the focusing conditions needed for the Laue project. Completion of the microfocus setup requires a new CCD detector. This item, which is an essential element of the development, is not presently funded. Moreover, the panel recommends installation of a new goniometer that is better suited to microdiffraction as well as additional control systems.

Continuation of the successful in situ GISAXS studies requires short and midterm additional investment. In particular, new 1D and 2D fast detectors are needed. To take full advantage of the GISAXS facilities requires an extension of the hutch to allow an increased sample-detector distance. In the midterm we encourage refurbishment of the UHV system and electronics as well as installation of an in situ CVD facility. The latter would expand the capabilities to different growth systems.

Staff

The panel was impressed by the quality of the beamline staff. The level of support is adequate apart from the computing and electronics area. The panel recommends that additional technical support is provided in this area.

Summary

. Science at BM32 should be continued as complementary activities to those that could be pursued at Soleil, exploiting the high energy beams and unique experimental facilities on this beamline.

. The quality of the in situ studies with the SUV instrument is outstanding and should be fully supported.

. The panel supports the development of the microfocus project along with funding to complete the development.

G Bauer, W de Jeu, S Ferrer, U Pietsch, G Thornton